Optimal Design of
Natural and Hybrid Laminar Flow Control
on Wings

by

Jan Pralits

Typsatt i $\mathcal{A}_{\mathcal{M}}\mathcal{S}$-LaTeX.

Optimal design of natural and hybrid laminar flow control on wings.

Jan Pralits
Department of Mechanics, Royal Institute of Technology
SE-100 44 Stockholm, Sweden.

Abstract

Methods for optimal design of different means of control are developed in this thesis. The main purpose is to maintain the laminar flow on wings at a chord Reynolds number beyond what is usually transitional or turbulent. Linear stability analysis is used to compute the exponential amplification of infinitesimal disturbances, which can be used to predict the location of laminar-turbulent transition. The controls are computed using gradient-based optimization techniques where the aim is to minimize an objective function based upon, or related to, the disturbance growth. The gradients of the objective functions with respect to the controls are evaluated from the solutions of adjoint equations.

Sensitivity analysis using the gradients of the disturbance kinetic energy with respect to different periodic forcing show where and by what means control is most efficiently made. The results are presented for flat plate boundary layer flows with different free stream Mach numbers.

A method to compute optimal steady suction distributions to minimize the disturbance kinetic energy is presented for both incompressible and compressible boundary layer flows. It is shown how to formulate an objective function in order to minimize simultaneously different types of disturbances which might exist in two, and three-dimensional boundary layer flows. The problem formulation also includes control by means of realistic pressure chambers, and results are presented where the method is applied on a swept wing designed for commercial aircraft.

Optimal temperature distributions for disturbance control are presented for flat plate boundary layer flows. It is shown that the efficiency of the control depends both on the free stream Mach number, and whether the wall downstream of the control domain is insulated, or heat transfer occurs.

Shape optimization is presented with the aim of reducing the aerodynamic drag, while maintaining operational properties. Results of optimized airfoils are presented for cases where both the disturbance kinetic energy, and wave drag are reduced simultaneously while lift, and pitch-moment coefficients as well as the volume are kept at desired values.

Descriptors: fluid mechanics, laminar-turbulent transition, boundary layer, laminar flow control, natural laminar flow, adjoint equations, optimal control, objective function, PSE, APSE, ABLE, HLFC, e^N-method, Euler equations

Preface

The thesis is based on and contains the following papers:

Paper 1. PRALITS, J. O., AIRIAU, C., HANIFI, A. & HENNINGSON, D. S. 2000 Sensitivity analysis using adjoint parabolized stability equations for compressible flows. *Flow, Turbulence and Combustion*, **65**(3), 312–346

Paper 2. PRALITS, J. O., HANIFI, A. & HENNINGSON, D. S. 2002 Adjoint-based optimization of steady suction for disturbance control in incompressible flows. *Journal of Fluid Mechanics*, **467**, 129–161

Paper 3. PRALITS, J. O. & HANIFI, A. 2003 Optimization of steady suction for disturbance control on infinite swept wings. *Physics of Fluids*, **15**(9), 2756–2772

Paper 4. PRALITS, J. O. & HANIFI, A. 2003 Optimization of steady wall temperature for disturbance Control. To be submitted.

Paper 5. AMOIGNON, O., PRALITS, J. O., HANIFI, A., BERGGREN, M. & HENNINGSON, D. S. 2003 Shape optimization for delay of laminar-turbulent transition. *Technical Report FOI-R–0919–SE, at the Swedish Defence Research Agency, FOI, Aeronautics Division, FFA.*

The papers are re-set in the present thesis format.

Reports and proceedings related to the content of the thesis

PRALITS, J. O., HANIFI, A. & HENNINGSON, D. S. 2000 Adjoint-based Suction Optimization for 3D Boundary Layer Flows. *Technical Report FFA TN 2000-58, at the Swedish Defence Research Agency, FOI, Aeronautics Division, FFA.*

AIRIAU C., PRALITS, J. O., BOTTARO, A. & HANIFI, A. 2001 Adjoint PSE and boundary layer equations for HLFC. *Technical Report TR 10, ALTTA Deliverable No D3.1.4-1.*

HANIFI, A., PRALITS, J. O., ZUCCHER, S, DONELLI, R. & AIRIAU, C. 2001 Adjoint-based Sensitivity Analysis: Validation and Comparison. *Technical Report TR 22, ALTTA Deliverable No D3.1.4-2.*

PRALITS, J. O., HANIFI, A. & MUGHAL, S. 2002 Optimal suction design for HLFC applications. *Technical Report TR 57, ALTTA Deliverable No D3.1.4-6.*

PRALITS, J. O.& HANIFI, A. 2002 Optimization of Steady Suction for Disturbance Control on Infinite Swept Wings. *In proceeding no. FEDSM2002-31055 at ASME Fluids Engineering Division Summer Meeting, Montreal, Canada.*

PRALITS, J. O.& HANIFI, A. 2003 Optimal Suction Design for HLFC Applications. *AIAA paper 2003-4164, 33rd AIAA Fluid Dynamics Conference and Exhibit, Orlando, Florida.*

Contents

Part 1

Summary

CHAPTER 1

Introduction

The final design of an aircraft wing is always a compromise in the intersection of feasibility imposed by various requirements. Aerodynamics is one important aspect as it enables calculations of operational properties such as lift, moments and drag. Traditionally, the design work has been an iterative process between theory and experiments, in which the latter has often been costly. Orville and Wilbur Wright[1] spend many hours in the laboratory using their home made wind tunnel to test different types of wings in order to increase the lift coefficient enough enabling their first controlled flight in 1903. Nowadays, when available computer power increases rapidly and numerical tools increase in accuracy and modeling capability, both experiments and numerical calculations are part of the total design process. For a computational method to be reliable as a tool, it must be based on a mathematical model which provides an appropriate representation of the significant features of the flow, such as shock waves, boundary layers and laminar-turbulent transition.

The total drag of an aircraft is mainly given by the sum of pressure or wave drag, related to the existence of shock waves for transonic and supersonic flows, and viscous drag, whose magnitude depends on whether the flow is laminar or turbulent. Turbulent flow, in some cases, produces a much larger drag; thus important research efforts have been devoted to find efficient means to keep the flow laminar over the largest possible portion of the wing surface. A similar situation is encountered in other industrial applications (wind-turbine blades, diffuser inlets), where less turbulence means less energy spent to achieve the same motion, which in turn translates directly to less pollution and reduced expenses.

Control of fluid flow can be made by means of *active* or *passive* control devices. A natural passive device is the shape of the wing itself, and reduction of drag is obtained by a properly made design. An approach in which the aim is to increase the laminar portion of the wing is usually called Natural Laminar Flow (NLF) design. Other examples are found looking at the surface structure where roughness elements or cavities, such as on golf-balls, are sometimes used. An active device which has been investigated extensively is suction of air through the whole or parts of the wing which have been equipped with a porous surface. This technique falls into the category of Laminar Flow Control (LFC) which

---

[1] The 17th of December 2003 is the 100 year anniversary of the first controlled flight performed by O. and W. Wright in 1903 which had a duration of 59 seconds.

means to maintain the laminar flow at a chord Reynolds number beyond what is usually transitional or turbulent when no control is used. With this definition it does not cover cases where the aim is to relaminarize already turbulent flow. A combination of NLF and LFC in which the active control is imposed only on a part of the wing is usually called Hybrid Laminar Flow Control (HLFC). A distinctive feature of any flow design process as opposed to one not involving fluids is that the computation is often very costly, or even totally out of reach of any existing computer when turbulent flow in complex geometries is involved. It is therefore common practice to introduce approximations. Once a reliable and efficient numerical tool is available, a straight-forward approach for design of passive or active devices is a vast parameter study in order to find the control which best meets certain criteria set on the operational properties, and decreases the drag. In most cases the number of possible designs is large, and it is very unlikely that a truly optimal design can be found without assistance of automatic tools. For this reason, there is a growing interest in utilizing numerical optimization techniques to assist in the aerodynamic design process.

The aim of the work presented in this thesis is to integrate physical modeling of the flow and modern optimization techniques in order to perform optimal NLF and HLFC design. Gradient-based optimization techniques are used and the gradients of interest are derived using adjoint equations. When one considers highly streamlined bodies such as wings, there is often a substantial laminar portion, thus a correct transition prediction becomes essential for a good estimate of the total drag. The governing equations for the physical problem are introduced in chapter 2, and transition prediction is covered in chapter 3. Means of control laminar-turbulent transition is discussed in 4, and the approach taken here to perform optimal HLFC and NLF is given in chapter 5. A summary and conclusions are given in chapter 6, and papers related to the work presented in these chapters are given in the second part.

CHAPTER 2

Modeling the flow

2.1. Governing equations

The motion of a compressible gas is given by the conservation equations of mass, momentum and energy and the equation of state. The conservation equations in dimensionless form and vector notation are

$$\frac{\partial \rho}{\partial t} + \nabla \cdot (\rho \mathbf{u}) = 0, \qquad (2.1)$$

$$\rho \Big[\frac{\partial \mathbf{u}}{\partial t} + (\mathbf{u} \cdot \nabla) \mathbf{u} \Big] = -\nabla p + \frac{1}{Re} \nabla \Big[\lambda (\nabla \cdot \mathbf{u}) \Big] + \frac{1}{Re} \nabla \cdot \Big[\mu (\nabla \mathbf{u} + \nabla \mathbf{u}^{\mathrm{T}}) \Big], \quad (2.2)$$

$$\rho c_p \Big[\frac{\partial T}{\partial t} + (\mathbf{u} \cdot \nabla) T \Big] = \frac{1}{Re \, \mathrm{Pr}} \nabla \cdot (\kappa \nabla T) + (\gamma - 1) M^2 \Big[\frac{\partial p}{\partial t} + (\mathbf{u} \cdot \nabla) p + \frac{1}{Re} \Phi \Big], \quad (2.3)$$

$$\gamma M^2 p = \rho T, \qquad (2.4)$$

with viscous dissipation given as

$$\Phi = \lambda (\nabla \cdot \mathbf{u})^2 + \frac{1}{2} \mu \Big[\nabla \mathbf{u} + \nabla \mathbf{u}^{\mathrm{T}} \Big]^2 .$$

Here t represents time, ρ, p, T stand for density, pressure and temperature, $\mathbf{u}$ is the velocity vector. The quantities λ, μ stand for the second and dynamic viscosity coefficients, γ is the ratio of specific heats, κ the heat conductivity and c_p the specific heat at constant pressure. All flow quantities are made dimensionless by corresponding reference flow quantities at a fixed streamwise position $x_0^\star$, except the pressure which is made dimensionless with two times the corresponding dynamic pressure. The reference length scale is fixed and taken as

$$l_0^\star = \sqrt{\frac{\nu_0^\star x_0^\star}{U_0^\star}}.$$

The Mach number, M, Prandtl number, Pr and Reynolds number, Re are defined as

$$M = \frac{U_0^\star}{\sqrt{\Re \gamma T_0^\star}}, \quad \mathrm{Pr} = \frac{\mu_0^\star c_{p0}^\star}{\kappa_0^\star}, \quad Re = \frac{U_0^\star l_0^\star}{\nu_0^\star},$$

where $\Re$ is the specific heat constant and superscript * refers to dimensional quantities. In order to generalize the equations for geometries with curved surfaces an orthogonal curvilinear coordinate system is introduced. The transformation from Cartesian coordinates X^i to curvilinear coordinates x^i is made

using the scale factors h_i. The definition of the scale factors and corresponding derivatives m_{ij} are given as

$$h_i^2 = \sum_{j=1}^{3} \left(\frac{\partial X^j}{\partial x^i}\right)^2 \quad \text{and} \quad m_{ij} = \frac{1}{h_i h_j}\frac{\partial h_i}{\partial x^j}.$$

Using the scale factors, an arc length in this coordinate system can be written as

$$ds^2 = \sum_{i=1}^{3} \left(h_i dx^i\right)^2.$$

Here, x^1, x^2 and x^3 are the coordinates of the streamwise, spanwise and wall normal directions respectively[1].

2.2. The steady boundary layer flow

In this thesis flat plate boundary-layer flows with and without pressure gradient are considered as well as the flow past a swept wing with infinite span. All these different flows are special cases of the flow past a swept wing with infinite span. They are here given in dimensionless primitive variable form as

$$\frac{1}{h_1}\frac{\partial(\rho U)}{\partial x^1} + \frac{\partial(\rho W)}{\partial x^3} = 0, \tag{2.5}$$

$$\frac{\rho U}{h_1}\frac{\partial U}{\partial x^1} + \rho W\frac{\partial U}{\partial x^3} = -\frac{1}{h_1}\frac{dP_e}{dx^1} + \frac{1}{Re}\frac{\partial}{\partial x^3}\left(\mu\frac{\partial U}{\partial x^3}\right), \tag{2.6}$$

$$\frac{\rho U}{h_1}\frac{\partial V}{\partial x^1} + \rho W\frac{\partial V}{\partial x^3} = \frac{1}{Re}\frac{\partial}{\partial x^3}\left(\mu\frac{\partial V}{\partial x^3}\right), \tag{2.7}$$

$$c_p\frac{\rho U}{h_1}\frac{\partial T}{\partial x^1} + c_p\rho W\frac{\partial T}{\partial x^3} = \frac{1}{RePr}\frac{\partial}{\partial x^3}\left(\kappa\frac{\partial T}{\partial x^3}\right)$$

$$+ (\gamma-1)M^2\left\{\frac{U}{h_1}\frac{dP_e}{dx^1} + \frac{\mu}{Re}\left[\left(\frac{\partial U}{\partial x^3}\right)^2 + \left(\frac{\partial V}{\partial x^3}\right)^2\right]\right\}, \tag{2.8}$$

where U, V, W are the streamwise, spanwise and wall-normal velocity components, respectively[2]. Under the boundary-layer assumptions, the pressure is constant in the direction normal to the wall, i. e. $P = P_e(x^1)$. The equation of state can then be expressed as

$$\gamma M^2 P_e = \rho T,$$

and the streamwise derivative of the pressure is given by the inviscid flow as

$$\frac{dP_e}{dx^1} = -\rho_e U_e\frac{dU_e}{dx^1}.$$

---

[1]In the second paper the coordinates are given as $x^1 = x$, $x^2 = z$ and $x^3 = y$, where x, y, z are the streamwise, wall normal and spanwise coordinates, respectively.
[2]In the second paper U, V, W are the streamwise, wall normal and spanwise velocity components respectively.

The corresponding boundary conditions with no-slip conditions and assuming an adiabatic wall condition are

$$U = V = W = \frac{\partial T}{\partial x^3} = 0, \qquad \text{at} \qquad x^3 = 0,$$

$$(U, V, T) \rightarrow (U_e, V_e, T_e), \qquad \text{as} \qquad x^3 \rightarrow +\infty.$$

The variables with subscript e are evaluated at the boundary layer edge and are calculated from well known fundamental relations using respective free stream values found either from measurements or inviscid flow calculations. The first relation is that the total enthalpy is constant along a streamline in an inviscid, steady, and adiabatic flow. The second is the isentropic relations which are used to obtain the relation between pressure, density and temperature expressed as ratios between total and static quantities.

2.3. Linear stability equations

In order to derive the linear stability equations, we decompose the total flow field q and material quantities into a mean $\bar{q}$, and a perturbation part $\tilde{q}$ as

$$q(x^1, x^2, x^3, t) = \bar{q}(x^1, x^2, x^3) + \tilde{q}(x^1, x^2, x^3, t) \qquad (2.9)$$

where $\bar{q} \in [U, V, W, p, T, \rho]$ and $\tilde{q} \in [\tilde{u}, \tilde{v}, \tilde{w}, \tilde{p}, \tilde{T}, \tilde{\rho}]$. The mean flow quantities were introduced in the previous sections and the lower case variables correspond the the disturbance quantities. It is assumed that c_p, μ and κ are functions of the temperature only and are divided into a mean and perturbation part. The latter are expressed as expansions in temperature as

$$\tilde{c}_p = \frac{dc_p}{dT}\tilde{T}, \qquad \tilde{\mu} = \frac{d\mu}{dT}\tilde{T}, \qquad \tilde{\kappa} = \frac{d\kappa}{dT}\tilde{T}.$$

The ratio of the coefficients of second and dynamic viscosity is given as

$$\frac{\lambda}{\mu} = \frac{\mu_v}{\mu} - \frac{2}{3}, \qquad (2.10)$$

were the bulk viscosity μ_v is given as

$$\frac{\mu_v(T)}{\mu(T)} = \left(\frac{\mu_v}{\mu}\right)_{T=293.3\ K} \exp\left(\frac{T - 293.3}{1940}\right),$$

and is taken from Bertolotti (1998). Note here that Stokes' hypothesis is used setting $\mu_v = 0$ in expression (2.10). We introduce the flow decomposition (2.9) into the governing equations (2.1)–(2.4), subtract the mean flow, and neglect non-linear disturbance terms. The result can be written as

$$\frac{\mathrm{D}\tilde{\rho}}{\mathrm{D}t} + \rho\nabla\cdot\tilde{\mathbf{u}} + \tilde{\rho}\nabla\cdot\mathbf{u} + \tilde{\mathbf{u}}\cdot\nabla\rho = 0, \qquad (2.11)$$

$$\rho\left[\frac{\mathrm{D}\tilde{\mathbf{u}}}{\mathrm{D}t} + (\tilde{\mathbf{u}}\cdot\nabla)\mathbf{u}\right] + \tilde{\rho}(\mathbf{u}\cdot\nabla)\mathbf{u} = -\nabla\tilde{p} + \frac{1}{Re}\nabla\left[\lambda(\nabla\cdot\tilde{\mathbf{u}}) + \tilde{\lambda}(\nabla\cdot\mathbf{u})\right]$$
$$+ \frac{1}{Re}\nabla\cdot\left[\mu(\nabla\tilde{\mathbf{u}} + \nabla\tilde{\mathbf{u}}^{\mathrm{T}}) + \tilde{\mu}(\nabla\mathbf{u} + \nabla\mathbf{u}^{\mathrm{T}})\right], \quad (2.12)$$

$$\rho c_p \Big[\frac{\mathrm{D}\tilde{T}}{\mathrm{D}t} + (\tilde{\mathbf{u}} \cdot \nabla)T \Big] + (\rho \tilde{c}_p + \tilde{\rho} c_p)(\mathbf{u} \cdot \nabla)T = \frac{1}{Re\,\mathrm{Pr}} \nabla \cdot (\kappa \nabla \tilde{T})$$

$$+ \frac{1}{Re\,\mathrm{Pr}} \nabla \cdot (\tilde{\kappa} \nabla T) + (\gamma - 1)M^2 \Big[\frac{\mathrm{D}\tilde{p}}{\mathrm{D}t} + (\tilde{\mathbf{u}} \cdot \nabla)p + \frac{1}{Re}\tilde{\Phi} \Big], \quad (2.13)$$

$$\gamma M^2 \tilde{p} = \rho \tilde{T} + \tilde{\rho} T, \qquad\qquad\qquad (2.14)$$

where

$$\frac{\mathrm{D}}{\mathrm{D}t} = \frac{\partial}{\partial t} + \mathbf{u} \cdot \nabla$$

and

$$\tilde{\Phi} = \tilde{\lambda}(\nabla \cdot \mathbf{u})^2 + 2\lambda \Big[(\nabla \cdot \mathbf{u})(\nabla \cdot \tilde{\mathbf{u}}) \Big] + \mu(\nabla \mathbf{u} + \nabla \mathbf{u}^{\mathrm{T}}) : (\nabla \tilde{\mathbf{u}} + \nabla \tilde{\mathbf{u}}^{\mathrm{T}})$$

$$+ \frac{1}{2}\tilde{\mu}(\nabla \mathbf{u} + \nabla \mathbf{u}^{\mathrm{T}}) : (\nabla \mathbf{u} + \nabla \mathbf{u}^{\mathrm{T}}), \quad (2.15)$$

with the definition $A : B = A_{ij}B_{ij}$. These equations are subject to the following boundary conditions:

$$\tilde{u} = \tilde{v} = \tilde{w} = \tilde{T} = 0, \qquad \text{at} \qquad x^3 = 0,$$

$$(\tilde{u}, \tilde{v}, \tilde{w}, \tilde{T}) \rightarrow 0, \qquad \text{as} \qquad x^3 \rightarrow +\infty.$$

2.4. Parabolized stability equations

In most cases a boundary layer grows in the downstream direction. In classical or quasi-parallel stability theory the parallel-flow assumption is made which means that the growth of the boundary layer is not taken into account. Setting the non-parallel terms to zero is commonly made on grounds that the growth of the boundary layer is small over a wave length of the disturbances and that the local boundary layer profiles will determine the behavior of the disturbances. This is an additional approximation made on the linearized equations which for instance has to be considered in comparisons between theory and experiments. Theoretical investigations of the instability of growing boundary layers can be found in e. g. Gaster (1974); Saric & Nayfeh (1975) who used a method of successive approximations and a multiple-scales method, respectively. In Hall (1983), the idea of solving the parabolic disturbance equations was introduced to investigate the linear development of Görtler vortices. Parabolic equations for the development of small-amplitude Tollmien-Schlichting waves was developed by Itoh (1986). Further development was done by e. g. Herbert & Bertolotti (1987); Bertolotti *et al.* (1992) who derived the non-linear Parabolized Stability Equations (PSE). Simen (1992) developed independently a similar theory for the development of convectively amplified waves propagating in non-uniform flows. The PSE has since its development been used to investigate different kind of problems such as stability analysis of different types of flows (Bertolotti *et al.* 1992; Malik & Balakumar 1992), receptivity studies (Hill 1997a; Airiau 2000; Dobrinsky & Collis 2000), sensitivity analysis (Pralits *et al.* 2000) and optimal control problems (Hill 1997b; Pralits *et al.* 2002; Walther *et al.* 2001; Pralits & Hanifi 2003; Airiau *et al.* 2003). In the

following sections an outline based on Hanifi *et al.* (1994) is given on the derivation of the parabolized stability equations used in this thesis. A review of the PSE can be found in Herbert (1997).

2.4.1. *Assumption and derivation*

The disturbance equations are derived for mean flows which are independent of the x^2 direction i. e. quasi-three dimensional flows. Two assumptions are used in the derivation:

1. The first is of WKB (Wentzel, Kramers and Brillouin) type in which the dependent variables are divided into a amplitude and a oscillating part as

$$\tilde{\mathbf{q}}(x^i, t) = \hat{\mathbf{q}}(x^1, x^3) e^{i\theta} \tag{2.16}$$

where $\tilde{\mathbf{q}}$ is the complex amplitude function and i the imaginary unit,

$$\theta = \int_{X_0}^{x^1} \alpha(x')\, dx' + \beta x^2 - \omega t$$

the complex wave function with angular frequency ω, streamwise and spanwise wave numbers α and β, respectively. Note that both the amplitude and wave functions depend on the x^1-direction.

2. The second assumption is a scale separation Re_0^{-1} between the weak variation in the x^1-direction and the strong variation in the x^3-direction. Here, Re_0 is the local Reynolds number at a streamwise position x_0. Further, the wall normal component of the mean flow W and the derivatives of the scale factors m_{ij} are also assumed to scale with Re_0^{-1}. A slow scale $x_S^1 = x^1 Re_0^{-1}$ is introduced which gives the new dependent variables

$$\begin{aligned}
h_i &= h_i(x_S^1, x^3 Re_0^{-1}), \\
\bar{\mathbf{q}} &= \bar{\mathbf{q}}(x_S^1, x^3), \qquad W = W_S(x_S^1, x^3) Re_0^{-1}, \\
\hat{\mathbf{q}} &= \hat{\mathbf{q}}(x_S^1, x^3), \qquad \alpha = \alpha(x_S^1).
\end{aligned} \tag{2.17}$$

If the ansatz (2.16) and the scalings (2.17) are introduced in the linearized governing equations, keeping terms up to (Re_0^{-1}), we obtain the linear parabolized stability equations. They can be written in the form

$$\mathcal{A}\hat{\mathbf{q}} \; + \; \mathcal{B}\frac{1}{h_3}\frac{\partial \hat{\mathbf{q}}}{\partial x^3} \; + \; \mathcal{C}\frac{1}{h_3^2}\frac{\partial^2 \hat{\mathbf{q}}}{(\partial x^3)^2} \; + \; \mathcal{D}\frac{1}{h_1}\frac{\partial \hat{\mathbf{q}}}{\partial x^1} \; = \; 0, \tag{2.18}$$

where $\hat{\mathbf{q}} = (\hat{\rho}, \hat{u}, \hat{v}, \hat{w}, \hat{T})^{\mathrm{T}}$. These equations describe the non-uniform propagation and amplification of wave-type disturbances in a non-uniform mean flow. The non-zero coefficients of the 5×5 matrices $\mathcal{A}, \mathcal{B}, \mathcal{C}$ and $\mathcal{D}$ are found in Pralits *et al.* (2000). Equation (2.18) is a set of nearly parabolic partial differential equations (see section 2.4.2). The boundary conditions of the disturbances at the wall and in the freestream are

$$\begin{aligned}
\hat{u} = \hat{v} = \hat{w} = \hat{T} = 0, &\qquad \text{at} \qquad x^3 = 0, \\
(\hat{u}, \hat{v}, \hat{w}, \hat{T}) \to 0, &\qquad \text{as} \qquad x^3 \to +\infty.
\end{aligned}$$

Note that in the ansatz (2.16), both the amplitude and wave functions given above depend on the x^1-direction. To remove this ambiguity, a *normalization* or *auxiliary* condition is introduced such that the streamwise variation of the amplitude function remains small. This is in accordance with the WKB type assumption where the amplitude function should vary slowly on the scale of a wavelength. Various forms of the normalization condition exist (see Hanifi *et al.* 1994). In the investigations presented here we have used the following condition

$$\int_0^{+\infty} \hat{\mathbf{q}}^{\mathrm{H}} \frac{\partial \hat{\mathbf{q}}}{\partial x^1} \, dx^3 = 0, \tag{2.19}$$

where superscript H denotes the conjugate transpose. The stability equation (2.18) is integrated in the downstream direction initiated at an upstream position $x^1 = X_0$ with the initial condition $\tilde{q} = \tilde{q}_0$ given by the local stability theory. At each streamwise position the streamwise wavenumber α is iterated such that the normalization condition (2.19) is satisfied. When a converged streamwise wave number has been obtained the disturbance growth rate σ can be calculated. For an arbitrary disturbance component ξ the growth rate is given as

$$\sigma = -\alpha_i + \mathrm{Real}\left\{\frac{1}{\xi} \frac{\partial \xi}{\partial x^1}\right\}$$

where the first term on the right hand side is the contribution from the exponential part of the disturbance and the second part due to the changes in the amplitude function. The variable ξ is usually $\hat{u}, \hat{v}, \hat{w}, \hat{T}$ or $\bar{\rho}\hat{u} + \hat{\rho}\bar{u}$ taken at some fixed wall normal position or where it reaches its maximum. In addition, the growth rate can be based on the disturbance kinetic energy

$$E = \int_0^{+\infty} \bar{\rho}(|u|^2 + |v|^2 + |w|^2) \, dx^3,$$

and is then written

$$\sigma_E = -\alpha_i + \frac{\partial}{\partial x^1} \ln(\sqrt{E})$$

2.4.2. *Step-size restriction*

In the parabolized stability equations presented here no second derivatives of $\hat{\mathbf{q}}$ with respect to x^1 exist. The ellipticity has however not entirely been removed. This is known to cause oscillations in the solution as the streamwise step size is decreased. The remaining ellipticity is due to disturbance pressure terms or viscous diffusion terms. Several investigations (see Haj-Hariri 1994; Li & Malik 1994, 1996; Andersson *et al.* 1998) have been performed regarding this problem. Li & Malik showed that the limit for the streamwise step size in order to have stable solution is $1/|\alpha|$. Haj-Hariri proposed a relaxation of the term $\partial \hat{p}/\partial x^1$ in order to allow smaller streamwise steps. Li & Malik showed however that this approach is not sufficient to eliminate the step-size restriction. They showed instead that eliminating $\partial \hat{p}/\partial x^1$ relaxes the step-size restriction. The approach which best removes the ellipticity while still producing an accurate
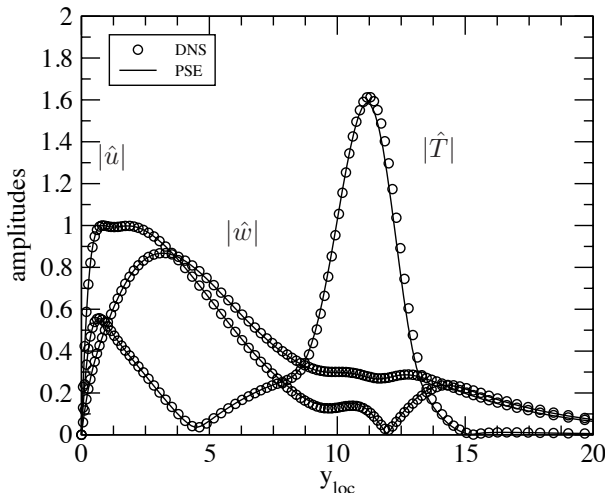
FIGURE 2.1. Comparison of amplitude functions for a second
mode instability with $F = 122 \times 10^{-4}$ at $Re = 1900$ between
DNS by Jiang *et al.* (2003) and the NOLOT/PSE code for
the flow past a flat plate at M_∞=4.5, T_∞=61.11 K, Pr = 0.7,
Sutherland's law for viscosity, Stokes hypothesis for the second
viscosity.

result is the technique introduced by Andersson *et al.* (1998), where some of
the originally neglected higher order terms, $O(Re^{-2})$, are reintroduced in the
stability equations. This method is used in the second paper where more details
can be found regarding the modifications of the parabolized stability equations.

2.4.3. *Comparison with DNS*

Since the development of the Parabolized Stability Equations, several verifica-
tions have been made in which the PSE has been compared with the results
of Direct Numerical Simulations (DNS), see for instance the investigations by
Pruett & Chang (1993); Hanifi *et al.* (1994) and Jiang *et al.* (2003). An example
is given here for the case of a flat plate boundary layer with a free stream Mach
number M_∞=4.5 and temperature T_∞=61.11 K. The disturbance analyzed is a
second mode[3] with reduced frequency $F = 122 \times 10^{-6}$. Here, $F = 2\pi f^* \mu_e^*/U_e^{*2}$
where f^*, μ^* and U^* are the dimensional frequency, kinematic viscosity and
streamwise velocity, respectively. In Figure 2.1, a comparison can be seen be-
tween the amplitude functions $\hat{u}, \hat{w}$ and $\hat{T}$ obtained with the NOLOT/PSE
code[4] used for the calculations in this thesis and the DNS data provided by
Jiang *et al.* (2003). The data has been normalized with the maximum value of
$|\hat{u}|$. As can be seen from the figure the agreement is very good.

---

[3]The second mode is defined in chapter 4.
[4]NOLOT was developed by the authors given in Hanifi *et al.* (1994) and Hein *et al.* (1994)

Transition prediction

Even though linear theory cannot describe the non-linear phenomena prior and after transition, it has been widely used for transition prediction. Using the linear stability equations previously described, we can calculate the ratio between the amplitudes A_2 and A_1 which are given at two streamwise positions X_1 and X_2 as

$$\frac{A_2}{A_1} = \exp\left(\int_{X_1}^{X_2} \sigma dx^1\right).$$

A problem then arises if we say that transition occurs when 'the most dangerous disturbance' reaches a certain threshold amplitude, as the values of A_1 and A_2 remain unknown. Some empirical methods exist however, where the linear amplification of a disturbance is correlated with the experimentally measured onset of transition. The one which has been mostly used is the e^N-method (see van Ingen 1956; Smith & Gamberoni 1956) and a brief review is given here. For an excellent overview of this method see Arnal (1993). As an example we consider the two-dimensional disturbances superimposed on the Blasius boundary layer. If we perform a stability analysis for each streamwise position and for a large number of frequencies $f_1, f_2, \cdots, f_n$ we can draw a neutral curve in the $f - Re$ plane which defines the intersection between the regions where these disturbances are damped and amplified. If the upstream position of the neutral curve (branch one) of a frequency f_1 is denoted X_0 with its 'initial' amplitude A_0, then we can calculate any downstream amplitude A related to the initial one as

$$\frac{A}{A_0} = \exp\left(\int_{X_1}^{X} \sigma dx^1\right) \qquad \text{or} \qquad \ln\left(\frac{A}{A_0}\right) = \int_{X_1}^{X} \sigma dx^1.$$

The frequencies f_i are amplified in different streamwise regions, and the corresponding maximum amplification and streamwise position will therefore vary with frequency. If we take the envelope of the amplification curves over all frequencies as

$$N = \max_f \left[\ln\left(\frac{A}{A_0}\right)\right], \tag{3.1}$$

then at each x^1, N represents the maximum amplification factor of these disturbances. Expression (3.1), which is commonly denoted the N-factor, cannot however determine the position of transition without additional information.
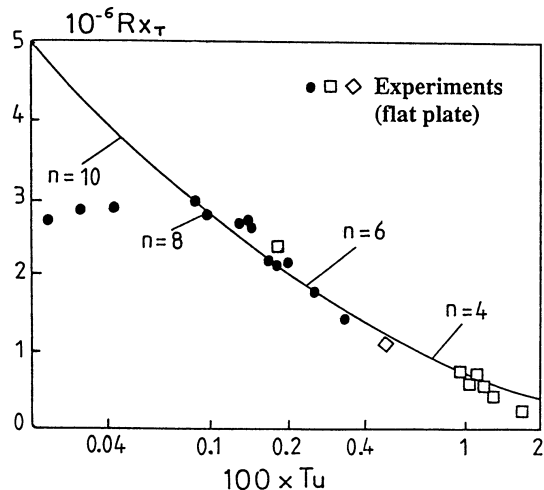
FIGURE 3.1. Comparison between e^N-method using expression (3.2) (line), and wind tunnel data (symbols) for a flat plate incompressible boundary layer flow. *(Arnal 1993)*.

It was early found in experiments by Smith & Gamberoni (1956) and van Ingen (1956) that the N-factor at the transition position was nearly constant ($N_{tr} \approx 7-9$). This is unfortunately not universal and does only apply under certain conditions. The disturbances inside the boundary layer can be triggered by acoustic waves, surface roughness, and free stream turbulence. The mechanisms which explain how disturbance enter the boundary layer are commonly called receptivity. Since the route to transition is preceded by receptivity and transition itself involves non-linear mechanisms, their absence in this approach is a shortcoming. Mack (1977) proposed the following expression for the transition N-factor to account for dependence of N_{tr} on the free stream turbulence level Tu

$$N_{tr} = -8.43 - 2.4 \ln Tu, \tag{3.2}$$

This relation was derived to fit numerical results to low speed zero pressure gradient wind tunnel data. Results of a comparison between expression (3.2) and wind tunnel data can be seen in Figure (3.1). For values of Tu between 0.1% and 1% transition is probably due to exponential instability waves. For higher values of Tu, and especially for $Tu > 3\%$ transition occurs at $N = 0$ indicating that transition is not caused by exponential instabilities. In several experiments, (see e. g. Westin *et al.* 1994; Matsubara & Alfredsson 2001), performed at moderate to high free stream turbulence levels, streamwise elongated structures have been observed with streamwise scales much larger than the spanwise scales. A model for transition prediction which correlates well with experimental data from e. g. Matsubara & Alfredsson (2001) for $Tu > 1\%$ was derived by Levin & Henningson (2003). They calculated both exponential

and spatial transient (non-modal) growth of disturbances. For sufficiently large disturbance amplitudes, the latter can lead to the so called bypass transition, which is not associated with exponential instabilities (see e. g. Brandt 2003).

An important issue in applying the e^N-method to more complex geometries, where the flow is three dimensional, is the choice of the integration path. For results presented in this thesis we follow the suggestions by Mack (1988). There, applying the condition that the wave number vector is irrotational together with the assumption of a wing with infinite span implies that β (spanwise wavenumber) is constant. The N-factor is then computed maximizing over ω and β. This is here denoted envelope of envelopes (EoE). Due to the shortcomings and limitations of the e^N-method mentioned before, better transition prediction models are needed. However, in this thesis the N-factor curves should be seen as capturing the trends of variation of the amplification rather than exact prediction of the transition position.

CHAPTER 4

Disturbance control

The linear stability analysis presented in chapter 2 can be used to calculate the growth of a disturbance superimposed on the mean flow for a given geometry and flow condition. The growth rate can then be used as outlined in chapter 3 for the purpose of transition prediction. In many applications it is also of interest to know how to affect the disturbance growth in order to control the position of laminar-turbulent transition and thus the laminar portion of a given geometry.

The linear stability of compressible boundary layers is different from that of incompressible boundary layers in many ways. The incompressible Blasius boundary layer is stable to inviscid disturbances, as opposed to the compressible boundary layer on an adiabatic flat plate which has a so called *generalized inflection point* and is therefore unstable to inviscid disturbances. The generalized inflection point y_s is defined as the wall normal position where $D(\rho D(U)) = 0$, $(D = \partial/\partial x^3)$. As the Mach number is increased the generalized inflection point moves away from the wall and hence the inviscid instability increases. The viscous instability becomes less significant when $M > 3$, so the maximum amplification rate occurs at infinite Reynolds number and viscosity has a stabilizing instead of destabilizing effect. In incompressible flows there is at most one unstable wave number (frequency) at each Re, whereas multiple unstable modes exist whenever there is region of supersonic flow relative to the disturbance phase velocity. The first unstable mode (first mode) is similar to the ones in incompressible flows. The additional modes, which do not have a counter part in incompressible flows, were discovered by Mack (1984) who called them higher modes. The most unstable first-mode waves in supersonic boundary layers are three dimensional, whereas the two-dimensional modes are the most unstable in incompressible boundary layer flows. The most unstable higher mode (second mode) is two-dimensional.

A brief review is made in this chapter on different active and passive methods to act on, or control disturbances in order to affect their amplification. The expression active control implies that energy is added to the flow in order to control, for example suction and blowing at the wall. A passive control on the other hand is made without additional energy added, and an example is changing the curvature of the wall. The review is restricted to methods which will be used later on in the thesis for the purpose of optimal laminar flow

control using blowing/suction, wall temperature distributions, and shape optimization. Other methods which can be used to affect the disturbance growth are e. g. surface roughness, transpiration cooling, nose bluntness and MHD (magneto-hydro-dynamic) flow control.

4.1. Suction/blowing

When steady suction is applied, a second inflection point y_{s1} appear close to the wall. This additional inflection point does not destabilize the inviscid disturbances. Masad *et al.* (1991) showed that the suction level needed to remove the generalized inflection point increases with increasing Mach number. They further found that suction is more effective in stabilizing the viscous instabilities and therefore more effective at low Mach numbers. Al-Maaitah *et al.* (1991) showed that suction is more effective in stabilizing second-mode waves at low Mach numbers. They also found that the most unstable second mode remains two-dimensional when suction is applied. In Masad *et al.* (1991) and Al-Maaitah *et al.* (1991) it was found that the variation of the maximum growth rate with suction level is almost linear for both first and second-mode disturbances. Studies have also been performed using discrete suction strips in order to approach a more 'realistic' case where it is assumed that only certain parts of a geometry are available for the implementation of control devices. Masad & Nayfeh (1992) presented results using suction strips for control of disturbances in subsonic boundary layers. They found that suction strips should be placed just downstream of the first neutral point for an efficient control of the most dangerous frequency[1]. However, no such conclusion can be made if all frequencies are considered which is the case in a real experiment. For further reading regarding disturbance control by means of steady suction see the extensive review on numerical and experimental investigations by Joslin (1998).

A different approach to control compared to modifying the mean flow, is to aim the control efforts at the instability wave itself. This is usually called wave cancellation or wave superposition. An advantage of this method is the small amount of control that is needed, of order $O(\epsilon^2)$, in order to obtain considerable reduction of a disturbance with amplitude of order $O(\epsilon)$. The concept of wave superposition has been used in a number of experimental investigations. Milling (1981) used an oscillating wire in water to both introduce and cancel waves. Other investigations concerns elements of heating (Liepmann *et al.* 1982), vibrating ribbons (Thomas 1983), acoustic waves introduced by loudspeakers (Gedney 1983), and suction/blowing (Kozlov & Levchenko 1985). A draw back of this method is that exact information about the amplitude and phase of the disturbance is needed.

---

[1]The frequency which first reach an N-factor which corresponds to laminar-turbulent transition is sometimes denoted 'the most dangerous frequency'.
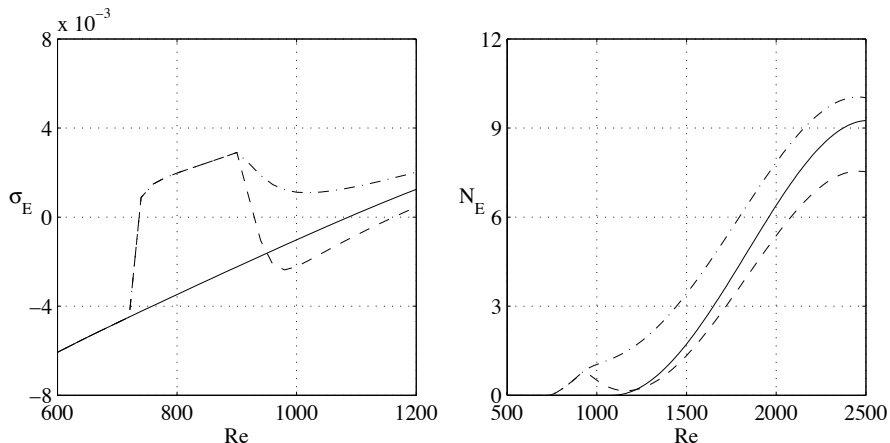
FIGURE 4.1. Disturbance control on a flat plate boundary layer using a heating strip with a temperature of 1.5 times the adiabatic temperature when no control is applied, located at $720 \leq Re \leq 900$. Left: Streamwise variation of the local growth rate of a 2D disturbance with $F = 15 \times 10^{-6}$, for the cases of zero control (solid), compared to the cases when the heating strip is used and the plate downstream of the heating strip is assumed insulated (dash-dot), and heat transfer occurs (dash), $M = 0.8$, $T_\infty = 300$ K, $\mathrm{Pr} = 0.72$. Right: corresponding N-factors.

4.2. Wall cooling

It was early recognized that uniformly distributed cooling has a damping effect on viscous instabilities of boundary-layer flows at various Mach number, see experiments by e. g. Diaconis *et al.* (1957) and Jack *et al.* (1957). Liepmann & Fila (1947) showed that at low subsonic speeds the transition location on a flat plate moves upstream as it is heated. The destabilizing effect of wall-heating on boundary-layer disturbances is due to the increase of the viscosity of air near the wall, which creates inflectional velocity profiles there. Cooling the wall on the other hand, decrease the viscosity near the wall which results in a thicker velocity profile and thus a more stable flow. Lees & Lin (1946) and Mack (1984) used inviscid and viscous stability theory, respectively, and found that subsonic air boundary layers can be completely stabilized by uniformly distributed wall-cooling. Mack (1984) also showed that uniformly distributed cooling has a destabilizing effect on the higher modes. The results by Mack (1984) have also been confirmed in experiments for supersonic flows by Lysenko & Maslov (1984). In the work by Masad *et al.* (1992) similar results were found using the spatial stability equations for compressible flows. Cooling has an effect on the compressible boundary layer similar to the one found

in boundary layers subject to suction. As cooling is applied an additional inflection point appear close to the surface which is not destabilizing the inviscid disturbances. Masad *et al.* (1992) showed that the cooling level needed to remove the general inflection point increases as the Mach number is increased. They further showed that cooling is always stabilizing the first-mode waves and destabilizing the second-mode waves. Several investigations have also been performed with localized heat-transfer strips. It was found by Masad & Nayfeh (1992) that a properly placed heating strip, close to the first neutral position, has a stabilizing effect on first-mode disturbances. They further showed that a cooling strip at the same location has a destabilizing effect on the first-modes. This effect appear as the flow leaves the cooling strip it encounters a relatively hotter surface downstream, which is destabilizing. The opposite occurs in the case of heating strips. Similar results were found in the numerical investigation by Lo *et al.* (1995) and experiments by Maestrello & Nagabushana (1989). Our investigations showed that this stabilizing effect is found only when the wall-temperature downstream of the strip is set to the adiabatic temperature in the uncontrolled case, T_{ad_0}. If the wall is insulated also downstream of the heating strip, the wall-temperature will be larger than T_{ad_0}. That is due to the fact that extra heat has been added to the flow as it passes the heating strip. This higher wall-temperature will increase the instability of the flow. This is presented in figure 4.1 and the details regarding these calculations are found in paper 4.

4.3. Wall-shaping

Shaping the wall results in two different effects which affect the disturbance instability. The first one is the creation of a pressure gradient and the second one is the effect of surface curvature.

4.3.1. *Pressure gradient*

Modification of the pressure gradient can be made by changing either the geometry itself or surrounding conditions. The latter is usually made in wind tunnels by placing a curved geometry above a flat plate. It was early found in experiments for incompressible flows by Schubauer & Skramstad (1948) that a favorable pressure gradient has a stabilizing effect on the boundary layer while the opposite was found for adverse pressure gradients. Malik (1989) investigated the effect of the pressure gradient on second-mode waves at $M = 4.5$. He found that favorable pressure gradients stabilizes the second-mode waves and the band of unstable disturbances moves to higher frequencies. A more thorough investigation was performed by Zurigat *et al.* (1990) in which the pressure gradient was generated assuming a power-law edge Mach-number distribution ($M_e = cx^n$). They analyzed the effects on both the first and second-mode waves at different Mach numbers. They showed that a favorable pressure gradient has a stabilizing effect on both first and second-mode waves. For lower Mach numbers ($M = 2$) oblique first-modes are more efficiently damped than
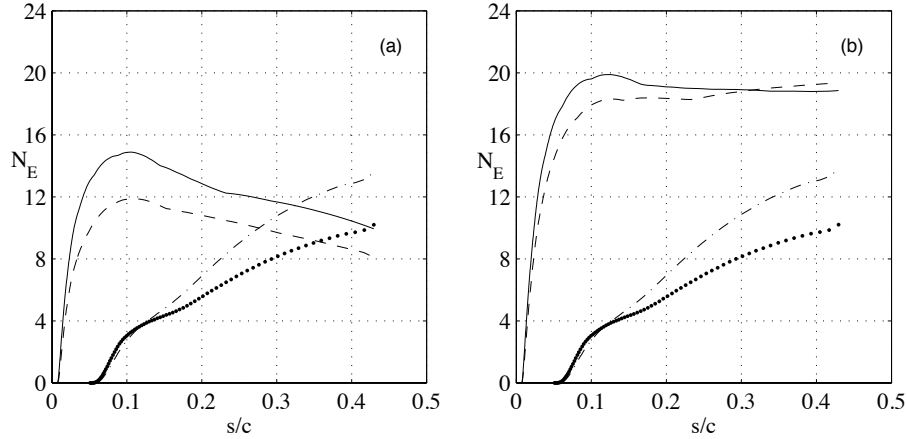
FIGURE 4.2. Effect of including curvature terms in the PSE on the disturbance growth. Envelope of envelopes of N-factor curves for cross-flow (CF) and Tollmien-Schlichting (TS) waves. (a) with curvature included; (b) without curvature in the PSE. Traveling CF (Solid), stationary CF (dashed), 2D TS (dotted) and 3D TS (dash-dotted). Mean flow over infinite swept wing with leading edge sweep angle $\psi_{le} = 30.2^o$, Mach number $M_\infty = 0.8$ and temperature $T_\infty = 230$ K.

two-dimensional ones. For higher Mach-numbers ($M = 4 - 8$) it was shown for 2D second-mode waves that the damping effect of a favorable pressure gradient decreases with increasing Mach number. For both disturbance types it was shown that the maximum growth rate varies almost linearly with n.

4.3.2. *Curvature*

The effects of the curvature on the disturbance growth can roughly be divided into two categories, i. e. those by *concave* surfaces and those by *convex* surfaces. The interest here lies mainly in the case of convex surfaces as such geometries have been analyzed in this thesis. It should however be mentioned that stability analysis of boundary layer flows over concave surfaces has been the topic of many investigations as it concerns the problem of so called Görtler vortices, i. e. stationary counter-rotating vortices arising from centrifugal effects (see e. g. Hall 1983; Spall & Malik 1989). The case of convex surfaces was studied by Masad & Malik (1994) for three-dimensional incompressible flows over an infinite swept cylinder. They found that curvature is stabilizing both stationary and traveling disturbances. Including nonparallel terms, on the other hand, is known to be destabilizing and will therefore have an opposite effect on the disturbance growth compared to curvature. Masad & Malik (1994) found however that the changes in disturbance growth in an analysis accounting for both these effects will be controlled by the convex curvature part.
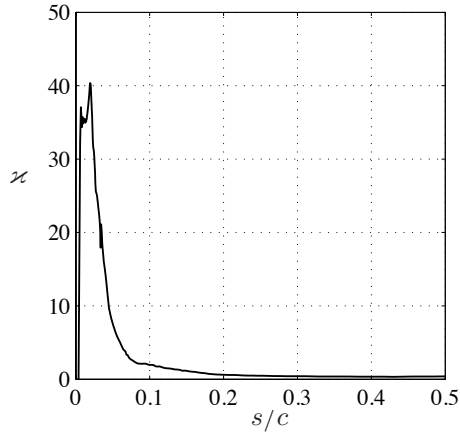
FIGURE 4.3. Curvature, $\varkappa$, of the wing analyzed in Figure 4.2 which is used to calculate the curvature radius $1/\varkappa$.

In the parabolized stability equations used in this thesis, (2.18), the scale factors h_i and corresponding derivatives m_{ij} are all functions of the curvature $\varkappa$. An example on the effect of including curvature in (2.18) or not, is given here. The latter is obtained by setting $h_1 = h_3 = 1$, and corresponding derivatives to zero. The case is the mean flow on the upper surface of an infinite swept wing (see Pralits & Hanifi 2003). Here the envelope of envelopes (EoE) of the N-factors for a large number of convectively unstable disturbances have been computed both with and without curvature terms in the linear stability equations. The results are given in Figure 4.2 where the horizontal axis shows the arc-length of the surface divided by the chord length.

The mean flow pressure gradient is strong and negative upstream of $s/c \approx$ 0.4 and weak and positive downstream of this position. Due to the inflection point in the velocity profile perpendicular to the inviscid streamline in the region of a favorable pressure gradient, cross-flow (CF) waves are amplified. Further downstream, in the zero or weakly adverse pressure gradient region, Tollmien-Schlichting type of waves are amplified. The curvature $\varkappa$ of the wing can be seen in Figure 4.3. Close to the leading edge the curvature is large and then decreases rapidly downstream until approximately $s/c = 0.05$. Downstream of this position the curvature is an order of magnitude smaller compared to the leading edge. As the region of large curvature coalesce with the region of favorable pressure gradient it is clear that the disturbance growth of CF waves, here given by the N-factors, will be mostly affected by the presence of the curvature terms in the linear stability equations.

CHAPTER 5

Optimal design for disturbance control

The knowledge obtained from the analysis regarding disturbance control, which was previously described, can be used in design of different active and passive devices in order to affect the laminar portion of a geometry such as an aircraft wing. Using suction and blowing, or the wall temperature for control purposes can be considered as active devices. The term design here refers to how the mass flux or temperature should be distributed along the surface. The knowledge regarding the effect of the pressure distribution and curvature on disturbance growth can also be related to the design of the geometry itself. For a rigid body this is made once and can be regarded as a passive control device. A straight forward design approach is, for a given number of design variables, to perform a parameter study in order to find the "best" design. If we take the example of design of a mass flux distribution, this means in practice to test different control domains, mass flux amplitudes, distributions and further more, for each case compute the effect on the disturbance growth. This can be an extremely time-consuming approach if the number of degrees of freedom is large. The word "best" is not objective and its meaning depends on the specific case. For mass flux design it might be to decrease disturbance growth using the least amount of suction power, while for wing design the best could be to decrease disturbance growth while maintaining operational properties such as given lift, and pitch-moment coefficients, and volume. The best solution from a parameter analysis however does not rule out the possibility that an even better solution might exist.

A different design approach is to define an optimization problem with an *objective function* which includes the costs of the design that one wants to minimize using certain *control* or *design variables*. Conditions which should be satisfied while minimizing the objective function are introduced as *constraints*. The advantage of the latter approach is that a number of different optimization techniques such as e. g. gradient-based and generic algorithms exist which depending on the problem can be used to efficiently compute an optimal solution. Gradient-based algorithms are especially efficient when the number of objective functions is small compared to the number of degrees of freedom.

5.1. Background
The work related to design of active and passive control devices for disturbance control and transition delay dates back several centuries, and a review

23

is therefore not made here. Instead an attempt is made to cover representative investigations where optimization techniques have been used for the purpose of disturbance control.

5.1.1. *Natural laminar flow*

Design of a geometry such that the laminar portion is increased or maximized is commonly denoted Natural Laminar Flow (NLF) design. In terms of practical implementations, NLF is probably the simplest approach. Once a feasible geometry is found no additional devices such as e. g. suction systems, sensors or actuators need to be mounted. One approach to NLF design is, in a first step, to generate a pressure distribution (target) that delays transition, then, in a second step, design a wing that results in a pressure distribution as close as possible to the target. In addition constraints on e. g. lift, pitch, volume, minimum thickness et cetera must be handled. Green & Whitesides (1996) took an iterative approach which uses a target pressure-N-factor relationship to compute the desired pressure distribution, and an inverse method to find the geometry which satisfies the computed pressure distribution. The N-factor method has also been used in multidisciplinary optimization problems of whole aircraft configurations where aerodynamics is considered as one discipline. In Lee *et al.* (1998), it was used to predict the onset of transition in order to determine where to turn on a chosen turbulence model in the Reynolds-Averaged-Navier-Stokes equations, enabling calculation of the friction drag. In Manning & Kroo (1999), a surface panel method was coupled with an approximative boundary layer calculation, and stability analysis. Note however, that none of these investigations explicitly calculates the sensitivity of a quantity obtained from the stability analysis such as the N-factor or disturbance kinetic energy, with respect to variations of the geometry. In paper 5, the sensitivity of the disturbance kinetic energy with respect to the geometry is used for the purpose of optimal NLF design.

5.1.2. *Laminar flow control*

Laminar flow control (LFC) is an active control technique, commonly using steady suction, to maintain the laminar state of the flow beyond the chord Reynolds number at which transition usually occurs. It is one of the few control techniques which has been attempted in flight tests. A combination of NLF and LFC, where the active control is employed on a just a part of the surface is called hybrid laminar flow control, HLFC. For an extensive review of these techniques see Joslin (1998). Most investigations of HLFC concerns suction but also wall-cooling have been used for control purposes. Balakumar & Hall (1999) used an optimization procedure to compute the optimal suction distribution such that the location of a target N-factor value was moved downstream. The theory was derived for two-dimensional incompressible flows and the growth of the boundary layer was not taken into account. In Airiau *et al.*

(2003), a similar problem was solved for the purpose of minimizing the disturbance kinetic energy, accounting for the non-parallel effects using the Prandtl equations and the PSE for incompressible two-dimensional flows. The same problem is extended to three-dimensional incompressible flows in paper 2, and compressible flows on infinite swept wings in paper 3. Similar investigations for the purpose of optimizing temperature distributions are, to the best of our knowledge, not found in the literature. In Masad & Nayfeh (1992), a parameter test was performed to find the "best" location for a predefined temperature distribution in order to reduce the N-factor of a given disturbance. In Gunzburger *et al.* (1993) an optimal control problem using boundary controls for the incompressible full Navier-Stokes equations was derived. An application to control by heating and cooling was given with the wall heat flux as the control and a target wall temperature as the objective. In paper 4, a problem is formulated for the purpose of minimizing the disturbance kinetic energy by optimizing the wall temperature distribution. In Hill (1997b) an inverse method was mentioned to compute the optimal suction distributions, and cooling/heating distributions, however no details were given there.

5.1.3. *Control by blowing and suction*

In a large number of investigations, different optimal control strategies in a temporal frame work have been investigated. A recent thesis by Högberg (2001) on the topic of optimal control of boundary layer transition provides a good overview of this field. The investigations considered here are performed for spatially developing flows. In Högberg & Henningson (2001), an extension to spatially developing incompressible flows was made for previously developed optimal feedback control through periodic blowing and suction at the wall. Even though parallel flow assumptions are needed for their formulation, successful results are shown for control of TS waves in Blasius flow and cross-flow vortices in Falkner-Skan-Cooke flow. Cathalifaud & Luchini (2000) formulated an optimal control problem for laminar incompressible flows over flat-, and concave walls with optimal perturbations. They successfully minimized both the disturbance kinetic energy at a terminal position, and as streamwise integrated quantity, by optimizing distributions of blowing and suction. In Walther *et al.* (2001) an optimal control problem was derived for two-dimensional incompressible flows with the focus on minimizing the disturbance kinetic energy of TS waves. They accounted for the developing boundary layer using the PSE. In both of the latter investigations, adjoint equations were used to obtain sensitivities of the chosen objective function with respect to the control. A global framework for feedback control of spanwise periodic disturbances, for spatially developing flows, was presented by Cathalifaud & Bewley (2002). In paper 1, we compute the sensitivity of the disturbance kinetic energy in a spatially developing boundary layer flow, with respect to periodic forcing at the wall and inside the boundary layer. The formulation is made using the PSE for compressible flows and the sensitivities are computed using the adjoint of the PSE. The sensitivity of the disturbance kinetic energy with respect to the

wall normal velocity component of the perturbation is used in section 5.4.2 to formulate an optimal control problem for cancellation of instability waves.

5.2. Gradient evaluation using adjoint equations

In gradient based optimization, there are different ways to compute the gradients of interest. To discuss this we consider the following problem. Let the state vector $\mathbf{q}$ satisfy the state equation

$$\frac{\partial \mathbf{q}}{\partial x} + A\mathbf{q} = 0; \quad \mathbf{q}(X_0, y) = \mathbf{q}_0, \quad \mathbf{q}(x, 0) = 0, \quad \lim_{y \to \infty} \mathbf{q}(x, y) = 0 \qquad (5.1)$$

where A is a matrix. Equation (5.1) is parabolic and solved by integration between $x = X_0$ and $x = X_1$. We wish to find the initial value of $\mathbf{q}(X_0, y) = \mathbf{q}_0$ such that the norm of $\mathbf{q}$ at some downstream position $x = X_1$ defined as

$$\|\mathbf{q}_1\|^2 = \langle \mathbf{q}_1, \mathbf{q}_1 \rangle = \int_0^\infty |\mathbf{q}(X_1, y)|^2 \, dy. \qquad (5.2)$$

is maximized. This can be written as an optimization problem where the aim is to maximize an objective function

$$\mathcal{J} = \int_0^\infty |\mathbf{q}(X_1, y)|^2 \, dy, \qquad (5.3)$$

where the initial condition $\mathbf{q}_0$ is the control. The gradient of the objective function $\mathcal{J}$ with respect to the control $\mathbf{q}_0$ can be defined through the directional derivative as

$$\delta \mathcal{J} = \langle \nabla \mathcal{J}(\mathbf{q}_0), \delta \mathbf{q}_0 \rangle = \lim_{s \to 0} \frac{\mathcal{J}(\mathbf{q}_0 + s\delta \mathbf{q}_0) - \mathcal{J}(\mathbf{q}_0)}{s} \qquad (5.4)$$

A straight forward approach to compute the gradient of interest, $\nabla \mathcal{J}(\mathbf{q}_0)$, is to perturb each degree of freedom of the control and for each perturbation, solve the state equations (5.1) and evaluate the objective function. A finite difference approximation of the gradient can then be made from these results. For a first order finite difference approximation, this is written

$$\nabla \mathcal{J}(\mathbf{q}_0)_i \approx \frac{\mathcal{J}(\mathbf{q}_0 + \epsilon_{\mathbf{q}_0} \mathbf{e}_i) - \mathcal{J}(\mathbf{q}_0)}{\epsilon_{\mathbf{q}_0}} \qquad (5.5)$$

where the vector $\mathbf{e}_i$ has component i equal to one and all other components zero, and $\epsilon_{\mathbf{q}_0}$ is a small real-valued parameter. If we denote the number of degrees of freedom M, then for a first order approximation of the gradient, the state equations have to be solved M times, for a second order approximation $2M$ times et cetera. If M is large then this procedure can be very time consuming. Another approach which has been shown successful in different optimization problems in fluid dynamics is to use adjoint equations. An example will be given below. For a compact notation of the adjoint equations, we will use the *formal adjoint* L^* for the differential operator L defined by the relation

$$\langle \mathbf{u}, L\mathbf{v} \rangle = \langle L^*\mathbf{u}, \mathbf{v} \rangle + \text{ boundary terms}, \qquad (5.6)$$

where the inner product $\langle \cdot, \cdot \rangle$ is defined as

$$\langle \mathbf{u}, \mathbf{v} \rangle = \int_{X_0}^{X_1} \int_0^\infty \mathbf{u}^{\mathrm{T}} \mathbf{v} \; dx \; dy \tag{5.7}$$

for $\mathbb{R}^n$-valued vectors $\mathbf{u}$ and $\mathbf{v}$. Here, the superscript * stands for the adjoint quantities and T for the transpose. The derivation of the adjoint equations is made in the following steps: the first variation of equations (5.3) and (5.1) gives

$$\delta \mathcal{J}(\mathbf{q}_0) = 2 \int_0^\infty \mathbf{q}(X_1, y)^{\mathrm{T}} \delta \mathbf{q}(X_1, y) \; dy, \tag{5.8}$$

$$\frac{\partial \delta \mathbf{q}}{\partial x} + A \delta \mathbf{q} = 0, \quad \delta \mathbf{q}(X_0, y) = \delta \mathbf{q}_0, \quad \delta \mathbf{q}(x, 0) = 0, \quad \lim_{y \to \infty} \delta \mathbf{q}(x, y) = 0 \tag{5.9}$$

Then (5.9) is multiplied with the co-state or adjoint variable $\mathbf{r}$ and used in the inner product given by (5.7). The right hand side of (5.6) is derived by removing the derivatives from $\delta \mathbf{q}$ using partial integration

$$\langle \mathbf{r}, \frac{\partial \delta \mathbf{q}}{\partial x} + A \delta \mathbf{q} \rangle = \langle -\frac{\partial \mathbf{r}}{\partial x} + A^{\mathrm{T}} \mathbf{r}, \delta \mathbf{q} \rangle + \left[\int_0^\infty \mathbf{r}^{\mathrm{T}} \; \delta \mathbf{q} \; dy \right]_{X_0}^{X_1}. \tag{5.10}$$

We now require $\mathbf{r}$ to satisfy the adjoint equation with the initial and boundary conditions

$$-\frac{\partial \mathbf{r}}{\partial x} + A^{\mathrm{T}} \mathbf{r} = 0, \quad \mathbf{r}(X_1, y) = 2\mathbf{q}(X_1, y), \quad \mathbf{r}(x, 0) = 0, \quad \lim_{y \to \infty} \mathbf{r}(x, y) = 0. \tag{5.11}$$

Equation (5.11) is integrated from $x = X_1$ to $x = X_0$ and the initial condition for $\mathbf{r}$ at $x = X_1$ is chosen such that the remaining boundary terms can be written

$$\int_0^\infty \mathbf{r}(X_0, y)^{\mathrm{T}} \; \delta \mathbf{q}(X_0, y) \; dy. = 2 \int_0^\infty \mathbf{q}(X_1, y)^{\mathrm{T}} \; \delta \mathbf{q}(X_1, y) \; dy = \delta \mathcal{J}(\mathbf{q}_0) \tag{5.12}$$

Since the left hand side of (5.12) is equal to $\delta \mathcal{J}$, the gradient of $\mathcal{J}$ with respect to $\mathbf{q}_0$ is identified as

$$\nabla \mathcal{J}(\mathbf{q}_0) = \mathbf{r}(X_0, y) \tag{5.13}$$

Compared to the finite-difference approach, the gradient (5.13) is now evaluated by solving the state equation (5.1) and the corresponding adjoint equation (5.11) once, independent of the size of M. The right hand side of (5.6) can be derived using either a continuous or discrete approach. A continuous approach means that the adjoint equations are derived from the continuous state equation and then discretized. In the discrete approach, the adjoint equations are derived directly from the discretized state equation. The gradient which is later identified from the adjoint equations, should in the latter case have an accuracy close to machine precision. The accuracy of the gradient derived using the continuous approach increases as the resolution of the computational domain is increased. This is well explained in Högberg & Berggren (2000). The continuous approach has been used through out the thesis except for the work in paper 5 where the adjoint of the inviscid flow equations are derived using

the discrete approach. The accuracy of the numerically calculated gradients is discussed in papers 1, 2 and 5.

5.3. Outline of the current approach

In this section the optimal design problems considered in this thesis are outlined. Gradient-based optimization is used in all cases and the gradients of interest are evaluated from the solution of the adjoint equations. The aim is to use different control or design variables in order to achieve a decrease in disturbance growth and therefore an increase in the laminar portion, thus a decrease in friction drag.

5.3.1. Objective function

The objective function is given as the sum of the different costs of the state which we want to minimize in order to achieve some desired goal. The costs, or cost functions, can be given different weights depending on their respective importance for the goal. In the analysis given here, the cost of friction drag is not given as a measure of the shear stress. It is instead based on the idea that an increase in the laminar portion of the body will result in a decrease of the friction drag. This can also be seen as moving the position of laminar-turbulent transition further downstream. The cost function is therefore a measure which can be related to the transition position. One choice is to measure the kinetic energy of a certain disturbance at a downstream position, say X_f. This can be written as

$$E_f = \frac{1}{2} \int_{Z_0}^{Z_1} \int_0^{+\infty} \tilde{\mathbf{q}}^{\mathrm{H}} M \tilde{\mathbf{q}} \ h_1 dx^2 dx^3 \bigg|_{x^1 = X_f}, \tag{5.14}$$

where $\tilde{\mathbf{q}} = (\tilde{\rho}, \tilde{u}, \tilde{v}, \tilde{w}, \tilde{T})^{\mathrm{T}}$ and $M = \mathrm{diag}(0, 1, 1, 1, 0)$ which means that the disturbance kinetic energy is calculated from the disturbance velocity components. If the position X_f is chosen as the upper branch of the neutral curve, then the measure can be related to the maximum value of the N-factor as

$$N_{max} = \ln \sqrt{\frac{E_f}{E_0}}, \tag{5.15}$$

where E_0 is the disturbance kinetic energy at the first neutral point. If in addition, the value of the N-factor of the measured disturbance is the one which first reaches the transition N-factor, then the position can be related to the onset of laminar-turbulent transition. It is however not clear, a priori, that such a measure will damp the chosen disturbance or other ones in the whole unstable region, especially if different types of disturbances are present. For Blasius flow, it has been shown that a cost function based on a single TS wave is sufficient to successfully damp the growth of other TS waves (see Pralits *et al.* 2002; Airiau *et al.* 2003). On a swept wing however, it is common that both TS and cross-flow waves are present and moreover can be amplified in different streamwise regions. An alternative is therefore to measure the

kinetic energy as the streamwise integral over a defined domain. Using such an approach several different disturbances, with respective maximum growth rate at different positions, can be accounted for in one calculation. Here, the size of K disturbances superimposed on the mean flow at an upstream position X_0, is measured by their total kinetic energy as

$$E_\Omega = \sum_{k=1}^{K} \frac{1}{2} \int_{X_{ms}}^{X_{me}} \int_{Z_0}^{Z_1} \int_0^{+\infty} \tilde{\mathbf{q}}_k^{\mathrm{H}} M \tilde{\mathbf{q}}_k h_1 dx^1 dx^2 dx^3. \qquad (5.16)$$

We now define the objective function as the sum of all the cost functions based on the disturbance kinetic energy as

$$\mathcal{J}_{\tilde{\mathbf{q}}} = \xi E_\Omega + (1 - \xi) E_f, \qquad (5.17)$$

where the parameter ξ can be chosen between zero and one, depending on the quantity we want to minimize. An alternative approach to decrease the disturbance growth and thus increase the laminar portion of the wing was investigated in Airiau *et al.* (2003) to optimize the mean flow suction distribution in a given domain. They minimized the streamwise integral of the shape factor, which for 2D disturbances in a 2D boundary layer should result in a suppression of disturbance amplification. Minimizing the shape factor is a more heuristic approach based on the knowledge that in such flows the two-dimensional disturbances are stabilized by any thinning of the boundary layer. Their results showed that an optimal suction distribution based on minimizing the shape factor does have a damping effect on the disturbance growth. A negative aspect of not explicitly minimizing a measure of the disturbances is that one cannot know if the optimized control will have a damping effect on the disturbances. This has to be calculated after wards. A cost function based on the streamwise integral of the shape factor is here written as

$$\mathcal{J}_{\mathbf{Q}} = \int_{X_{ms}}^{X_{me}} H_{12} h_1 dx^1 = \int_{X_{ms}}^{X_{me}} \frac{\delta_1}{\delta_2} h_1 dx^1, \qquad (5.18)$$

where both the displacement δ_1, and momentum-thickness δ_2 are based on the velocity component which is in the direction of the outer streamline. In paper 3 we present results which show that optimal suction distributions obtained by minimizing expression (5.18) does not have a damping effect, but instead amplifies disturbances in the case of swept wing flows.

5.3.2. *Optimal design cases*

With the objective functions defined, different optimal design cases can be outlined. We consider the flow over a body decomposed into three different parts: a steady inviscid part provides a pressure distribution P for a given geometry $\mathbf{x}$, a steady mean flow $\mathbf{Q}$ is the solution for a given pressure distribution and geometry, and the solution $\tilde{\mathbf{q}}$ emerging from the stability analysis calculated for a given mean flow and geometry. From the latter, the objective function based on the disturbance kinetic energy can be evaluated. If the objective function

Design variables	Euler	BLE	PSE	Obj. fcns.	Gradients
$\tilde{w}_{\mathrm{w}}$	$P_0 \rightarrow$	$\mathbf{Q}_0 \rightarrow$	$\tilde{\mathbf{q}} \rightarrow$	$\mathcal{J}_{\tilde{\mathbf{q}}}$	$\nabla J_{\tilde{\mathbf{q}}}(\tilde{w}_{\mathrm{w}})$
$\dot{m}_{\mathrm{w}}, T_{\mathrm{w}}$	$P_0 \rightarrow$	$\mathbf{Q} \rightarrow$	$\tilde{\mathbf{q}} \rightarrow$	$\mathcal{J}_{\tilde{\mathbf{q}}}$	$\nabla J_{\tilde{\mathbf{q}}}(\dot{m}_{\mathrm{w}}),\ \nabla J_{\tilde{\mathbf{q}}}(T_{\mathrm{w}})$
$\dot{m}_{\mathrm{w}}, T_{\mathrm{w}}$	$P_0 \rightarrow$	$\mathbf{Q} \rightarrow$		$\mathcal{J}_{\mathbf{Q}}$	$\nabla \mathcal{J}_{\mathbf{Q}}(\dot{m}_{\mathrm{w}}),\ \nabla \mathcal{J}_{\mathbf{Q}}(T_{\mathrm{w}})$
$\mathbf{x}$	$P \rightarrow$	$\mathbf{Q} \rightarrow$	$\tilde{\mathbf{q}} \rightarrow$	$\mathcal{J}_{\tilde{\mathbf{q}}}$	$\nabla J_{\tilde{\mathbf{q}}}(\mathbf{x})$
$\mathbf{x}$	$P \rightarrow$	$\mathbf{Q} \rightarrow$		$\mathcal{J}_{\mathbf{Q}}$	$\nabla \mathcal{J}_{\mathbf{Q}}(\mathbf{x})$
$\mathbf{x}$	$P \rightarrow$			$\mathcal{J}_P$	$\nabla \mathcal{J}_P(\mathbf{x})$

TABLE 5.1. Table of state equations involved in the possible optimal design cases. The arrows indicates the order in which the equations are solved, and P, $\mathbf{Q}$, and $\tilde{\mathbf{q}}$ are the states obtained by solving the Euler, BLE and PSE respectively. The subscript 0 means that the solution is fixed during the optimization procedure.

is based on the shape factor, only the inviscid and mean flow parts are considered. Three different types of control or design variables are used. In the first, we consider unsteady forcing such as periodic blowing/suction at the wall, $\tilde{w}_{\mathrm{w}}$, for a fixed geometry. In this case, only the stability equations are affected by the control as the inviscid flow and mean flow are both time-independent and non-linear effects are not accounted for. As a second case we consider control of disturbances by modifications of the mean flow on a fixed geometry. This is made using either a mass flux distribution $\dot{m}_{\mathrm{w}}$ or a wall temperature distribution T_{w}. Here both the mean flow and disturbances are affected by the control, which means that an objective function can be based on either $\mathbf{Q}$ or $\tilde{\mathbf{q}}$. The last case considers optimal design by changing the geometry and will affect all states, i. e. the inviscid flow, the mean flow, and the disturbances. It is therefore possible to consider objective functions based on either of the three states P, $\mathbf{Q}$ or $\tilde{\mathbf{q}}$.

If we denote the objective functions based on the three different states P, $\mathbf{Q}$, and $\tilde{\mathbf{q}}$ as $\mathcal{J}_P$, $\mathcal{J}_{\mathbf{Q}}$, and $\mathcal{J}_{\tilde{\mathbf{q}}}$ respectively, a chart of possible optimal design problems can be made. This is shown in table 5.1. The solution of the inviscid flow, mean flow and disturbances are here denoted Euler, BLE and PSE, respectively. Depending on the design case, one or several states will change during the optimization. The states which are not changed (kept fixed) in respective case are given subscript 0. The different gradients required to solve respective optimization problem are given in the column on the right hand side of table 5.1.

5.4. Optimal laminar flow control

5.4.1. *Sensitivity analysis using periodic forcing*

The concept of wave cancellation was discussed in section 4.1 and examples were given of experimental results using different types of forcing, or actuators such as heating plates, vibrating ribbons, and blowing and suction. Before deciding which actuator to use in order to control the instability waves, it can be of interest to investigate the sensitivity of different types of forcing $\tilde{\zeta}$ on a measure of the disturbance growth of a given disturbance. The latter is here given by the objective function $\mathcal{J}_{\tilde{\mathbf{q}}}$, expression (5.17). A small variation of the forcing $\delta\tilde{\zeta}$ will cause a small variation of the objective function $\delta\mathcal{J}_{\tilde{\mathbf{q}}}$ and the gradient $\nabla\mathcal{J}_{\tilde{\mathbf{q}}}(\tilde{\zeta})$ express the sensitivity of $\mathcal{J}_{\tilde{\mathbf{q}}}$ with respect to $\tilde{\zeta}$. The different forcing considered here are the disturbance velocity components $\tilde{u}_{\mathrm{w}}$, $\tilde{v}_{\mathrm{w}}$, $\tilde{w}_{\mathrm{w}}$ and temperature $\tilde{T}_w$ at the wall, and a momentum force $\tilde{\mathbf{S}}$ inside the boundary layer as the model of a vibrating ribbons. When a low amplitude periodic forcing such as blowing/suction at the wall is applied, only the linear stability equations need to be considered, as neither the mean flow nor the inviscid flow is affected if non-linear interaction of the disturbances are neglected. The state equations solved here are the parabolized stability equations outlined in section 2.4, which including the above mentioned periodic forcing are written

$$L_P\,\hat{\mathbf{q}} = \hat{\mathbf{S}}, \tag{5.19}$$

$$\int_0^{+\infty} \hat{\mathbf{q}}^{\mathrm{H}}\frac{\partial\hat{\mathbf{q}}}{\partial x^1}dx^3 = 0. \tag{5.20}$$

The forcing given at the wall are introduced as boundary conditions in (5.19). The gradients of the objective function with respect to each forcing are derived using adjoint equations. This is described in detail in paper 1 and the gradients with respect to the wall forcing are

$$\nabla\mathcal{J}_{\tilde{\mathbf{q}}}(\tilde{u}_{\mathrm{w}}) = \frac{\mu D_3(u^*)}{\bar{\Theta}Re}, \qquad \nabla\mathcal{J}_{\tilde{\mathbf{q}}}(\tilde{v}_{\mathrm{w}}) = \frac{\mu D_3(v^*)}{\bar{\Theta}Re},$$

$$\nabla\mathcal{J}_{\tilde{\mathbf{q}}}(\tilde{w}_{\mathrm{w}}) = \frac{\rho\rho^*}{\bar{\Theta}}, \qquad \nabla\mathcal{J}_{\tilde{\mathbf{q}}}(\tilde{T}_{\mathrm{w}}) = -\frac{\kappa D_3(\theta^*)}{\bar{\Theta}\,\mathrm{Pr}\,Re},$$

where $\Theta = e^{i\theta}$, and with respect to the momentum forcing

$$\nabla\mathcal{J}_{\tilde{\mathbf{q}}}(\tilde{\mathbf{S}}) = \frac{\mathbf{q}^*}{\bar{\Theta}} \qquad \text{where} \qquad \mathbf{q}^* = (\rho^*,u^*,v^*,w^*,\theta^*)^{\mathrm{T}}.$$

Here, the over bar denotes the complex conjugate and superscript $*$ denote adjoint variables. The latter satisfy the adjoint of the parabolized stability equations (APSE), here given as

$$L_P^*\,\mathbf{q}^* = \mathbf{S}_P^* \tag{5.21}$$

$$\frac{\partial}{\partial x^1}\int_0^{+\infty} \mathbf{q}^{*\mathrm{H}}\frac{\partial L_P}{\partial\alpha}\,\hat{\mathbf{q}}\,h_1 h_2 h_3\,dx^3 = f^*, \tag{5.22}$$
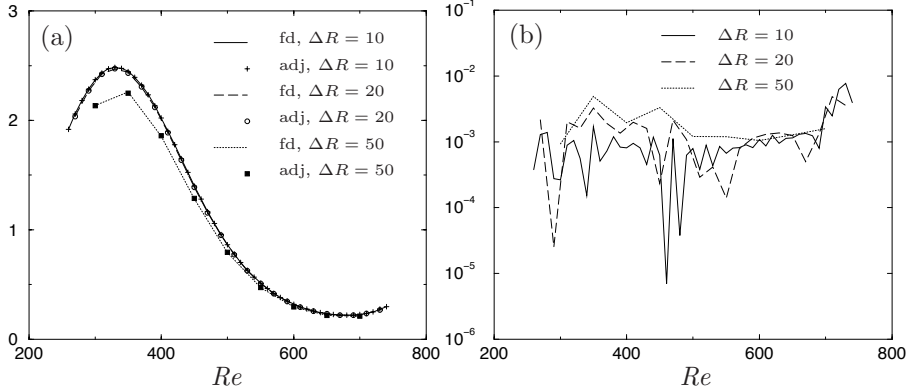
FIGURE 5.1. Comparison between adjoint (adj) and central difference (fd) calculations for different ΔR. Mach number $M = 0.7$, $\beta = 0$. (a) lines denote $||(\partial \mathcal{J}_{\tilde{\mathbf{q}}}/\partial \tilde{w}_r, \partial \mathcal{J}_{\tilde{\mathbf{q}}}/\partial \tilde{w}_i)/\Delta_n||$ and symbols $|\nabla \mathcal{J}_{\tilde{\mathbf{q}}}(\tilde{w}_{\mathrm{w}})_n|$. (b) relative error.

Details regarding equations (5.21)–(5.22) are found in paper 1 for the case of $\mathcal{J}_{\tilde{\mathbf{q}}} = \mathcal{J}_{\tilde{\mathbf{q}}}(\xi = 0)$. The adjoint equations shown here are derived from the continuous state equations. An alternative is to first discretize the state equations and then derive the adjoint equations. It was concluded by Högberg & Berggren (2000) that a continuous formulation is a good enough approximation if control is performed on a problem with a dominating instability. This type of analysis can be made with the PSE and a continuous approach is therefore used here. In order to verify the accuracy of the gradient, we compare the gradients computed using the adjoint equations with those obtained using a finite-difference approximation. In the latter, the gradient of the objective function with respect to each forcing is approximated by a second-order accurate central finite-difference scheme. To compare the gradients given by the adjoint and finite-difference approaches let us consider the example of a wall normal velocity perturbation $\delta \tilde{w}_{\mathrm{w}}$ at $x^3 = 0$. The variation of $\mathcal{J}_{\tilde{\mathbf{q}}}$ with respect to this wall perturbation is :

$$\delta \mathcal{J}_{\tilde{\mathbf{q}}} = \frac{\partial \mathcal{J}_{\tilde{\mathbf{q}}}}{\partial \tilde{w}_r} \delta \tilde{w}_r + \frac{\partial \mathcal{J}_{\tilde{\mathbf{q}}}}{\partial \tilde{w}_i} \delta \tilde{w}_i$$

The subscripts r and i denote the real and imaginary parts of a complex number. In the finite-difference approach, the variation of $\mathcal{J}_{\tilde{\mathbf{q}}}$ is obtained by imposing the inhomogeneous boundary condition $\tilde{w}_{\mathrm{w}} = \pm \varepsilon$ at $x^1 = x_n^1$. Here, ε is a small number and index n refers to n-th streamwise position. Then, the approximative gradients are calculated using a second-order accurate finite-difference scheme. The expression for $\delta \mathcal{J}_{\tilde{\mathbf{q}}}$ in the adjoint approach, for a flat plate geometry, is in discretized form given as

$$\delta \mathcal{J}_{\tilde{\mathbf{q}}} = \int_{Z_0}^{Z_1} \sum_{n=2}^{N-1} \frac{1}{2} (\nabla \mathcal{J}_{\tilde{\mathbf{q}}}(\tilde{w}_{\mathrm{w}})_n^{\mathrm{H}} \delta \tilde{w}_{\mathrm{w}_n} + c.c.) \Delta_n \, dx^2,$$
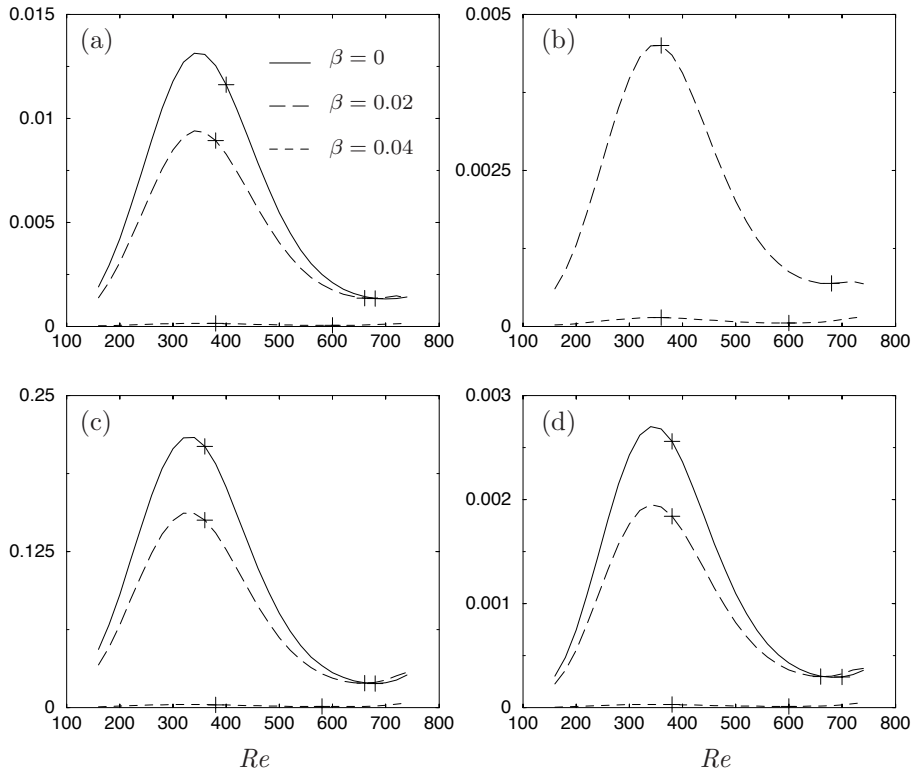
FIGURE 5.2. Modulus of the gradients (sensitivities) due to 2D and 3D wall forcing as a function of the Reynolds number for a flat plate boundary layer at Mach number $M = 0.7$. (a) $|\nabla\mathcal{J}_{\tilde{\mathbf{q}}}(\tilde{u}_{\mathrm{w}})|$, streamwise velocity component; (b) $|\nabla\mathcal{J}_{\tilde{\mathbf{q}}}(\tilde{v}_{\mathrm{w}})|$ spanwise velocity component; (c) $|\nabla\mathcal{J}_{\tilde{\mathbf{q}}}(\tilde{w}_{\mathrm{w}})|$ normal velocity component; (d) $|\nabla\mathcal{J}_{\tilde{\mathbf{q}}}(\tilde{T}_{\mathrm{w}})|$ temperature component. The $+$ marks the first and second neutral point for each case.

where $\Delta_n = (x_{n+1}^1 - x_{n-1}^1)/2$ and *c.c.* is the complex conjugate. In the following, the quantity $\nabla\mathcal{J}_{\tilde{\mathbf{q}}}(\tilde{w}_{\mathrm{w}})_n$ is compared to those of the finite-difference approach. The case is a flat plate boundary layer with free stream Mach number of 0.7, and the streamwise domain used here is $Re \in [250, 750]$. The modulus $||(\partial\mathcal{J}_{\tilde{\mathbf{q}}}/\partial\tilde{w}_r, \partial\mathcal{J}_{\tilde{\mathbf{q}}}/\partial\tilde{w}_i)/\Delta_n||$, as a function of x_n^1, is shown in figure 5.1a and is compared to $|\nabla\mathcal{J}_{\tilde{\mathbf{q}}}(\tilde{w}_{\mathrm{w}})_n|$ for different resolution of the streamwise step ΔR. A good agreement is found between the approaches for a given ΔR, and both values converge as ΔR is decreased. The relative error given in figure 5.1b is below half a percent for all cases and decreases as ΔR is decreased. Sensitivity results for a flat plate boundary layer at Mach number $M = 0.7$ subject to two-, and three dimensional wall forcing by $\tilde{u}_{\mathrm{w}}$, $\tilde{v}_{\mathrm{w}}$, $\tilde{w}_{\mathrm{w}}$ and $\tilde{T}_{\mathrm{w}}$ can be seen in figure 5.2. Here the modulus of each component have been plotted as a function of the local Reynolds number. For all cases except the spanwise
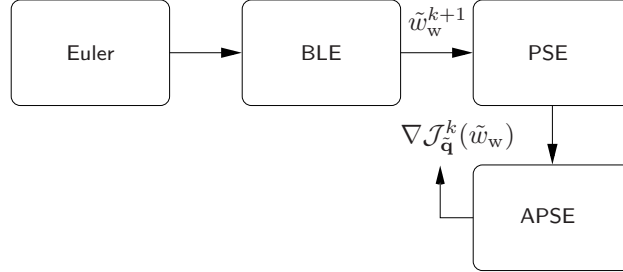
FIGURE 5.3. Flow chart for the case of minimizing the disturbance kinetic energy using the wall normal disturbance velocity at the wall $\tilde{w}_{\mathrm{w}}$.

component, the largest sensitivity is obtained for two-dimensional wall forcing and the maximum value occurs close to the first neutral point of analyzed disturbance. It can also be seen that the magnitude of the wall normal velocity component is about 15 times that of the streamwise component for this case and the ratio is even larger compared to the spanwise velocity component and the temperature. This implies that blowing/suction is the most efficient mean of controlling instability waves. However, as shown in paper 1, the sensitivity decreases with increasing Mach number.

5.4.2. *Wave cancellation*

In principle, any periodic forcing considered in section 5.4.1 can be optimized. However, as an example we choose the wall normal velocity component because it has been shown to give the highest sensitivity, and also because it is a good model for periodic blowing/suction. In order to find the optimal solution for a limited cost of the control, and also to bound the control amplitude we define an objective function which balances the cost of the kinetic energy and the control as

$$\tilde{\mathcal{J}}_{\tilde{\mathbf{q}}} = \mathcal{J}_{\tilde{\mathbf{q}}} + l^2 \int_{X_0}^{X_1} |\tilde{w}_{\mathrm{w}}|^2 \, h_1 \, dx^1. \tag{5.23}$$

The term l^2 serve as a penalty on the control such that $l^2 = 0$ means unlimited control and vice verse. The gradient of the objective function (5.23) with respect to the control is given as

$$\nabla \tilde{\mathcal{J}}_{\tilde{\mathbf{q}}}(\tilde{w}_{\mathrm{w}}) = \nabla \mathcal{J}_{\tilde{\mathbf{q}}}(\tilde{w}_{\mathrm{w}}) + 2 \, l^2 \tilde{w}_{\mathrm{w}} \tag{5.24}$$

As the optimization problem is defined for a given geometry and mean flow, the only state equation which is updated in the optimization procedure is the PSE (5.19)-(5.20). The optimization procedure can now be described considering the chart given in figure 5.3 where k is the iteration number of the optimization loop. An initial disturbance $\tilde{\mathbf{q}}_0$ is superimposed on the mean flow at an initial position X_0. The PSE is integrated from $x = X_0$ to $x = X_1$ and the objective function is evaluated. The adjoint equations, APSE are then integrated from $x = X_1$ to $x = X_0$. The gradient is evaluated from the solution of the APSE
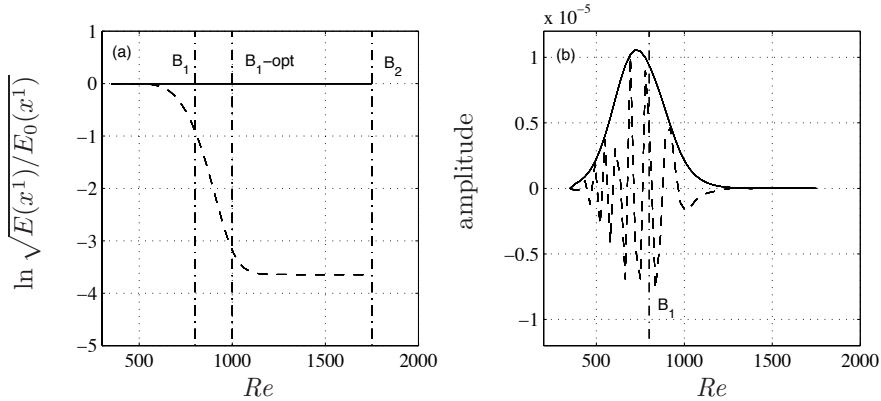
FIGURE 5.4. Control of a two-dimensional wave with $F = 30 \times 10^{-6}$ in a zero pressure gradient flat plate boundary layer where $M_\infty = 0$. (a) energy for zero (solid) and optimal (dashed) control, (b) the optimal suction/blowing distribution given as $|\tilde{w}_{\mathrm{w}}|$ (solid) and $\mathrm{Real}(\tilde{w}_{\mathrm{w}})$ (dashed). B_{i} and B_{i}-opt mark the branch points for zero and optimal control

and the new boundary condition for the PSE is calculated using a chosen optimization algorithm. In the next loop, the PSE is solved with a new $\tilde{w}_{\mathrm{w}}$ followed by the APSE. The optimization loop is continued until the variation of the objective function is less than a prescribed value. Results of the optimal design problem described above are given in figure 5.4 for the case when $\mathcal{J}_{\tilde{\mathbf{q}}} = \mathcal{J}_{\tilde{\mathbf{q}}}(\xi = 0)$. Here we consider a flat plate boundary layer with free stream Mach number $M_\infty = 0$ and zero pressure gradient. The computational domain in the streamwise direction is $Re = [350, 1750]$. A two-dimensional disturbance with reduced frequency $F = 30 \times 10^{-6}$ is superimposed on the meanflow at $Re = 350$. The control is imposed along the whole plate and the penalty has value of $l = 10^4$. The objective function is evaluated at $Re = 1750$ which is close to the second branch of the neutral curve, i. e. where the disturbance kinetic energy is close to its maximum. In figure 5.4a the reduction in energy has been plotted as the natural logarithm of the ratio between the square root of optimal-, and initial disturbance kinetic energy, $\ln \sqrt{E(x^1)/E_0(x^1)}$. Branch 1 and 2 of the uncontrolled case have been marked with vertical lines as B_1 and B_2, respectively. The downstream shift of branch one in the case of optimal control is shown with a vertical line marked $B_1 - opt$. In figure 5.4b the optimal distribution of suction and blowing is plotted both as the real part and absolute value. Here it is seen that the control acts most strongly in the vicinity of the first neutral point and then decays rapidly both in the upstream and downstream direction. Results showing that the disturbance kinetic energy measured close to the second branch of the neutral curve is most sensitive to periodic forcing close to the first branch of the neutral curve can be seen in paper 1 for different Mach numbers.

5.4.3. *Hybrid laminar flow control*

The motivation for using optimal control theory for the purpose of hybrid laminar flow is that in many industrial applications (see Joslin 1998), the design of e. g. suction systems rely on the experience of the engineers which may not always give the largest delay of laminar-turbulent transition at a given suction power. Design using steady forcing implies that given a fixed geometry, the mean flow will change during the optimization procedure. The analysis here is made using either the wall mass flux $\dot{m}_{\mathrm{w}} = \rho_{\mathrm{w}} W_{\mathrm{w}}$, or the wall temperature T_{w} as design variables. This particular choice is made as both $\dot{m}_{\mathrm{w}}$ and T_{w} have been investigated for the purpose of Hybrid Laminar Flow Control. As outlined in table 5.1, several different cases can be considered depending on which combination of objective function and control variable that is used. Gradient based optimization is used in all cases analyzed here and the gradients are evaluated from the solution of adjoint equations. When the objective function is evaluated from the solution of the mean flow, $\mathcal{J}_{\mathbf{Q}}$, then only the BLE is used in the optimization and the gradient of $\mathcal{J}_{\mathbf{Q}}$ with respect to the chosen control variable is evaluated from the adjoint of the boundary layer equations (ABLE). Minimization of $\mathcal{J}_{\tilde{\mathbf{q}}}$ on the other hand, requires the solution of both the BLE and PSE and the respective gradients are evaluated from the ABLE which in turn is forced by the solution of the APSE. A summary on how to compute the gradient for the different cases is given in table 5.2 where W^* and T^* are solutions of the ABLE. Details regarding respective equation are given in papers 3 and 4. Note that for the cases presented in table 5.2 the assumption is made that the streamwise domain of the forcing and the objective function is the same. If this is not the case, changes occur in the boundary conditions of both the BLE and ABLE. This is covered in paper 3 and 4.

5.4.3.1. *Limiting the control*

In many optimization problems it is of interest to bound or limit the control, and in such a way compute the optimal solution using the least effort. Other arguments for bounding the control come from issues regarding validity of the state equations or avoiding ill-posed problems. This can be made using e. g. a regularization parameter such that the objective function express the sum of the original measure, expression (5.17) or (5.18), and a parameter times a defined measure of the control. An example was given in section 5.4.2 for the case of optimizing periodic blowing/suction. As an example here, we consider the case of optimization the wall mass flux to minimize the disturbance kinetic energy. A new objective function can be written

$$\tilde{\mathcal{J}}_{\tilde{\mathbf{q}}} = \mathcal{J}_{\tilde{\mathbf{q}}} + l^2 \int_{X_0}^{X_1} \dot{m}_{\mathrm{w}}^2 \, h_1 \, dx^1. \tag{5.25}$$

The only difference compared to the equations given in table 5.2 appear in the expression of the gradient which is now given as

$$\nabla \tilde{\mathcal{J}}_{\tilde{\mathbf{q}}}(\dot{m}_{\mathrm{w}}) = \nabla \mathcal{J}_{\tilde{\mathbf{q}}}(\dot{m}_{\mathrm{w}}) + 2 \, l^2 \dot{m}_{\mathrm{w}}. \tag{5.26}$$

Des.	Euler	BLE	PSE	Obj.	APSE	ABLE	Gradients
$\dot{m}_\mathrm{w}$	$P_0 \rightarrow$	$\mathbf{Q} \rightarrow$	$\tilde{\mathbf{q}} \rightarrow$	$\mathcal{J}_{\tilde{\mathbf{q}}}$	$\mathbf{q}^* \rightarrow$	$\mathbf{Q}^* \rightarrow$	$\nabla \mathcal{J}_{\tilde{\mathbf{q}}}(\dot{m}_\mathrm{w}) = W_\mathrm{w}^*$
$\dot{m}_\mathrm{w}$	$P_0 \rightarrow$	$\mathbf{Q} \rightarrow$		$\mathcal{J}_{\mathbf{Q}}$		$\mathbf{Q}^* \rightarrow$	$\nabla \mathcal{J}_{\mathbf{Q}}(\dot{m}_\mathrm{w}) = W_\mathrm{w}^*$
T_w	$P_0 \rightarrow$	$\mathbf{Q} \rightarrow$	$\tilde{\mathbf{q}} \rightarrow$	$\mathcal{J}_{\tilde{\mathbf{q}}}$	$\mathbf{q}^* \rightarrow$	$\mathbf{Q}^* \rightarrow$	$\nabla \mathcal{J}_{\tilde{\mathbf{q}}}(T_\mathrm{w}) = \dfrac{\kappa}{Re\,\mathrm{Pr}} \dfrac{\partial T_\mathrm{w}^*}{\partial x^3}$
T_w	$P_0 \rightarrow$	$\mathbf{Q} \rightarrow$		$\mathcal{J}_{\mathbf{Q}}$		$\mathbf{Q}^* \rightarrow$	$\nabla \mathcal{J}_{\mathbf{Q}}(T_\mathrm{w}) = \dfrac{\kappa}{Re\,\mathrm{Pr}} \dfrac{\partial T_\mathrm{w}^*}{\partial x^3}$

TABLE 5.2. Table of state and adjoint equations to evaluate respective gradient in the optimal design cases using steady forcing. The arrows indicates the order in which the equations are solved. P, $\mathbf{Q}$, and $\tilde{\mathbf{q}}$ are the states obtained by solving the Euler, BLE and PSE respectively, and $\mathbf{Q}^*$ and $\tilde{\mathbf{q}}^*$ are solutions of the ABLE and APSE respectively. The subscript 0 defines that the solution is fixed during the optimization procedure.

If the regularization parameter l is zero then the control is unbounded, and when $l > 0$ then it is bounded. In practice this means that as l is increased, less control effort is allowed, and possibly less decrease in the original state measure is obtained. In some cases it is of interest not only to bound the control but more specifically bound it at a certain value. One example is when the mass flux is optimized for disturbance control purposes. The suction distribution is commonly obtained by a system of pumps and pipes which uses a certain amount of energy. It can therefore be of interest to find an optimal suction distribution which uses a specified amount of energy E_C, which for instance can be written as

$$E_C = \int_{X_0}^{X_1} \dot{m}_\mathrm{w}^2 \, h_1 \, dx^1. \tag{5.27}$$

In this case the problem is not regularized but instead constrained. As shown in papers 3 and 4, this constraint can be fulfilled using a Lagrange multiplier technique. Details on the derivations are found in the papers and the resulting gradient expression is

$$\nabla \tilde{\mathcal{J}}_{\tilde{\mathbf{q}}}(\dot{m}_\mathrm{w}) = \nabla \mathcal{J}_{\tilde{\mathbf{q}}}(\dot{m}_\mathrm{w}) + 2\,\chi^* \dot{m}_\mathrm{w}, \tag{5.28}$$

The constant regularization parameter l^2 in (5.26) has now been replaced by an adjoint variable χ^*. This adjoint variable can be solved as follows: when $\nabla \tilde{\mathcal{J}}(\dot{m}_\mathrm{w}) = 0$ then $\dot{m}_\mathrm{w} = -W_\mathrm{w}^*/(2\chi^2)$ is the corresponding optimal mass flux distribution and usually denoted *optimality condition*, $\dot{m}_\mathrm{w}$ is then substituted
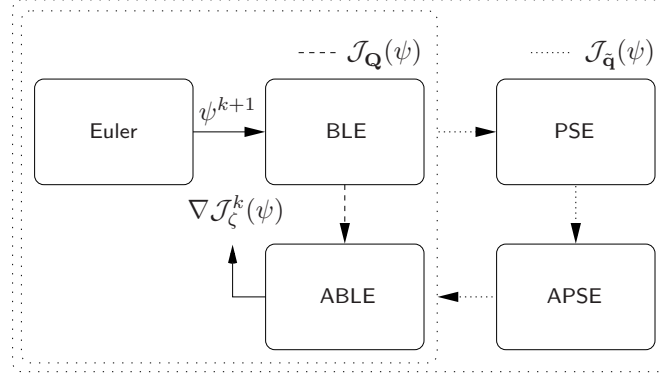
FIGURE 5.5. Optimization procedure using steady forcing. Here, k denotes the iteration number, ψ is the control variable, $\mathcal{J}_{\mathbf{Q}}$ and $\mathcal{J}_{\tilde{\mathbf{q}}}$ are the objective functions evaluated from the solutions of the BLE and PSE respectively.

into (5.27) and an expression for χ^* is evaluated as

$$\chi^* = \left(\frac{1}{4E_C} \int_{X_0}^{X_1} W_{\mathrm{w}}^{*2} h_1 dx^1 \right)^{\frac{1}{2}}. \tag{5.29}$$

It should be noted that using this approach does not mean that expression (5.27) is satisfied in each iteration of the optimization procedure. The constraint on the control energy is derived assuming that $\nabla \tilde{\mathcal{J}}(\dot{m}_{\mathrm{w}}) = 0$. Therefore, as the optimization problem converge, i. e. $\nabla \tilde{\mathcal{J}}(\dot{m}_{\mathrm{w}})$ goes to zero, also the constraint on the control energy will converge.

5.4.3.2. *Solution procedure*

The optimization procedures for the different optimal design problems considered here can be described using the chart in figure 5.5. There, k denotes the iteration number, ψ is the control variable, $\mathcal{J}_{\mathbf{Q}}$ and $\mathcal{J}_{\tilde{\mathbf{q}}}$ are the objective functions evaluated from the solutions of the BLE and PSE respectively. We start by considering the case of minimizing $\mathcal{J}_{\tilde{\mathbf{q}}}$ for a single disturbance, i. e. $K = 1$ if $\mathcal{J}_{\tilde{\mathbf{q}}}$ includes expression (5.16). This case is presented figure 5.5 as the large dotted rectangle. The optimization is performed for a given geometry and inviscid solution in an iterative procedure. During each iteration step, we perform successive calculations of the BLE and PSE from X_0 to X_1; and APSE and ABLE from X_1 to X_0. Then, a new control variable ψ^{k+1} is computed using the gradient evaluated from the solution of the ABLE, in a chosen optimization algorithm. The calculations are repeated until the relative change in the objective function is less than a prescribed value. If the objective function includes expression (5.16) with $K > 1$ then instead of solving both state and adjoint equations K times, we can utilize the fact that the ABLE, here written
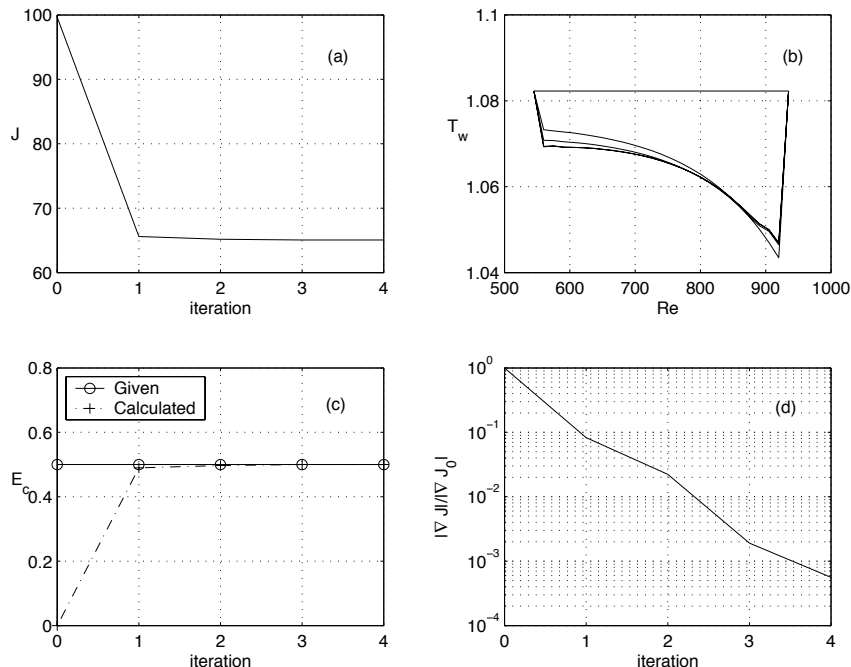
FIGURE 5.6. Convergence history for the case of minimizing the disturbance kinetic energy at a downstream position using the wall temperature. (a) objective function vs. iteration number, (b) wall temperature vs. Reynolds number for all iterations, the arrow shows the direction of increasing iteration number (c) control energy, given and calculated vs. iteration number, (d) gradient norm normalized by its initial value vs. iteration number.

as

$$L_B^* \, \mathbf{Q}^* \quad = \quad S_B^*. \tag{5.30}$$

are linear equations. In this case the gradient is evaluated as follows: the BLE is solved once; the PSE and APSE are solved K times; the right hand side of the ABLE, S_B^*, is calculated as

$$S_B^* = \sum_{k=1}^{K} S_{B_k}^*.$$

Finally, the gradient is evaluated from a single calculation of the ABLE. The case of minimizing $\mathcal{J}_{\mathbf{Q}}$ is computationally less expensive. This case is shown in figure 5.5 as the smaller dotted rectangle. During each iteration step, successive calculations are performed of the BLE from X_0 to X_1; and ABLE from X_1 to X_0. The gradient evaluation and convergence is then as described above.

5.4.3.3. *Convergence*

An example of the convergence history for an optimal design case is shown in figure 5.6. The wall temperature distribution is optimized such that the disturbance kinetic energy at a downstream position is minimized on a flat plate with zero pressure gradient and a free stream Mach number $M_\infty = 0.7$. A disturbance with reduced frequency $F = 50 \times 10^{-6}$ is superimposed on the meanflow at $Re = 500$ and the objective function, given by expression (5.14), is evaluated at $Re = 935$. The wall temperature distribution T_{w} is optimized between $Re = 545$ and $Re = 935$, and the convergence criteria is set as $(\mathcal{J}_{\tilde{\mathbf{q}}}^{k+1} - \mathcal{J}_{\tilde{\mathbf{q}}}^{k})/\mathcal{J}_{\tilde{\mathbf{q}}}^{k} < 10^{-4}$. When control is applied, a deviation of the wall temperature, ΔT_{w}, occur with respect to the case of zero control. The constraint used here is the square of ΔT_{w}, accounting for both heating and cooling, integrated in the control domain. With the reference temperature taken as the adiabatic wall temperature in the case of zero control T_{ad_0}, this is written

$$E_C = \int_{X_{cs}}^{X_{ce}} \left(T_{\mathrm{w}} - T_{ad_0}(x^1, 0) \right)^2 dx^1, \tag{5.31}$$

Here, the start and end of the control domain are denoted X_{cs} and X_{ce}, respectively, and the value of E_C used in this example is 0.5. The optimization algorithm used here is the L-BFGS-B[1] routine and convergence was reached after 4 iterations. The objective function and the norm of the gradient, normalized by its initial value, both as functions of the iteration number can be seen in figures 5.6a and b, respectively. The objective function has reached a plateau while the gradient norm is still decreasing indicates that the solution is getting close to a local minimum. At the last iteration the relative difference between the given and calculated control energy is 10^{-4} (figure 5.6c). If the optimization is continued then finally it would reach a point where the gradient norm would no longer decrease. This might depend on the accuracy of the gradient and/or the search algorithm used. The results from iteration 3 and 4 are not possible to distinguish from each other which can be seen in figure 5.6b, and as efficiency is of importance when a large number of designs are evaluated, the results here are considered converged.

5.4.3.4. *HLFC for an industrial application*

Optimization of the wall temperature or the mass flux distribution without considering how it can implemented and used in a real case might solely be of academic interest or serve as a reference case. This has been addressed in paper 3 for the case of optimizing the mass flux distribution for the purpose of disturbance control on infinite swept wings. The direct application of such an analysis is a tool which could be used in design of HLFC systems. The mass

---

[1]The algorithm is the limited memory quasi-Newton method developed by Zhu *et al.* (1994). It is based on a limited memory BFGS approximation of the Hessian matrix of the functional f, and a gradient projection method is used to account for bounds on the data which makes it suitable for large scale problems where only the gradient of f is available.
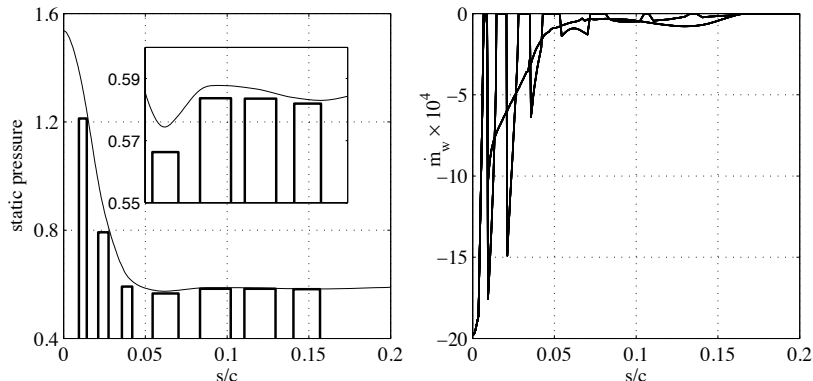
FIGURE 5.7. Optimal suction design for minimization of E_Ω including a TS and a CF wave. The control energy is $E_C = 0.35$ in all cases. Left: optimal static pressures for the case of 7 pressure chambers, the continuous line shows the pressure distribution on the wing. Right: Corresponding suction distributions (thick lines) compared to an optimal suction distribution in a continuous domain (thin lines).

flux distributions on the porous surface of a wing in these systems is commonly obtained using a number of pressure chambers. The surface velocity can be expressed as a function of the surface porosity, hole geometry and the pressure difference between the pressure distribution on the surface and static pressure in the chambers. The relation used here written on dimensionless form is given as

$$
\begin{aligned}
\Delta P_j &= P_e - P_{c_j} \\
&= \frac{C_1}{\rho_w} \dot{m}_w^2 + C_2 \frac{\mu_w}{\rho_w} \dot{m}_w \quad \forall x^1 \in [X_{cs_j}, X_{ce_j}], \quad j = 1, \cdots, K_p \quad (5.32)
\end{aligned}
$$

and is taken from Bieler & Preist (1992). It is based on measurements carried out in the framework of the ELFIN (European Laminar Flow INvestigation) program. The internal static pressure, start and end positions of chamber number j is given by P_{c_j}, X_{cs_j} and X_{ce_j}, respectively, and the coefficients C_1 and C_2 can be found in paper 3. If we use expression (5.32), then the design variable is no longer $\dot{m}_w$ but instead P_{c_j}, and the size and position of the chambers for a given porous surface characterized by C_1 and C_2. As expression (5.32) is differentiable with respect to $\dot{m}_w$ it is possible to formulate an optimal design problem similar to the previous cases. We use the Lagrange multiplier technique and expression (5.32) is used as an additional constraint. The BLE, PSE, APSE and ABLE are used in the optimization procedure and the gradient of the objective function is now evaluated with respect to P_{c_j}. A comparison can now be made between the case of optimizing the mass flux distribution, $\dot{m}_w$, in one continuous domain with the case of optimizing the static pressures
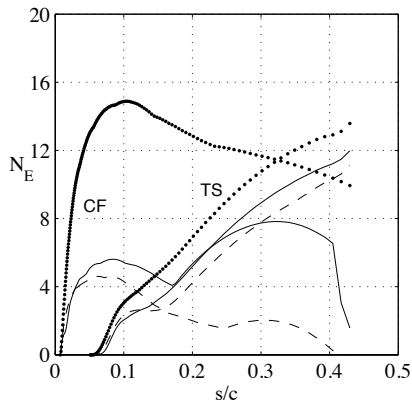
FIGURE 5.8. Envelope of envelopes (EoE) of N-factor curves for the cases of zero control (dotted) and the optimal pressure chambers in figure 5.7 (solid). A comparison is made with the EoE of N_E-factor curves (dashed) obtained with the continuous suction distribution in figure 5.7.

in a number of discrete pressure chambers, with the aim of minimizing the disturbance kinetic energy. In the latter, $\dot{m}_{\mathrm{w}}$ is indirectly optimized through the relation (5.32). Results taken from paper 3 of such a comparison are presented here for the case of minimizing the disturbance kinetic energy calculated as the sum of a Tollmien-Schlichting (TS) and cross-flow (CF) wave. The mean flow studied is the boundary layer on the upper side of a swept wing designed for commercial aircraft. The continuous mass flux distribution is optimized in the whole available control domain. A configuration of seven pressure chambers are used for the comparison and the start of the first, and end of the last pressure chamber are given by the end points of the available control domain. In both the continuous and pressure chamber cases, the control energy (5.27) is kept constant with a value of 0.35. The left hand side of figure 5.7, shows the optimal static pressures for the case of 7 chambers. The pressure distribution of the wing has been added for comparison in the plot. The largest values of ΔP_j occur close to the leading edge and then decrease downstream. This is most evident observing the close up made in each plot on the left hand side. The corresponding suction distributions are shown on the right hand side of the same figure. There a comparison is made with the case of optimizing the mass flux in a continuous control domain. Both the continuous suction distribution and the ones obtained from the optimal static pressures are larger in magnitude upstream and then decrease rapidly and become almost constant downstream. The effect on the disturbance growth is given in figure 5.8 by plotting the envelope of envelopes (EoE) of the N-factor curves both for TS and CF waves, for the cases of zero and the optimal suction distributions shown in figure 5.7. The results using the continuous suction distribution can be seen as a reference case of what best can be achieved. As further constraints are imposed using

the pressure chambers, it is expected that less damping of the disturbances will be achieved.

5.5. Shape optimization for natural laminar flow

The various possible optimal design cases which can be considered in the current frame work, where outlined in table 5.1. In the cases of using the shape of the geometry as design variables, it was shown that the objective function can be based on either the inviscid, mean flow, or stability solution. Note, that in addition, also combinations of the three can be used as an objective function, see paper 5. An objective function based on the solution of the inviscid flow, $\mathcal{J}_P$, is commonly used in the case of shape optimization where the aim is to minimize e. g. the pressure, or wave drag. References to optimization problems regarding inviscid flows can be found in e. g. Jameson (1988). A design problem which accounts for viscous flow effects can be formulated using either $\mathcal{J}_{\mathbf{Q}}$, and/or $\mathcal{J}_{\tilde{\mathbf{q}}}$ as objective function. In particular the latter enables the possibility to account for the physics related to laminar-turbulent transition. In the current approach there are several physical approximations made. A discussion about this is found in paper 5. The goal of the approach taken is to use an iterative gradient-based optimization procedure with the aim of minimizing an objective function based on a measure of the linear disturbance growth by optimizing the shape of the geometry, such as a wing. As a decrease in disturbance growth means a downstream shift of the laminar-turbulent transition location, and thus an increase of the laminar portion of the surface, the approach taken here can be seen as optimal design for natural laminar flow.

5.5.1. *Problem formulation and gradients*

We minimize the objective function based on the disturbance kinetic energy $\mathcal{J}_{\tilde{\mathbf{q}}}$, expression (5.17), which depends explicitly on the solution of the stability equations $\tilde{\mathbf{q}}$ and the mesh, here given by the nodal coordinates $\mathbf{X}$. This is here written as

$$\mathcal{J} \equiv \mathcal{J}(\tilde{\mathbf{q}}, \mathbf{X})\,, \tag{5.33}$$

and is evaluated as follows:

1. The solution of the Euler equations for compressible flows (see paper 5) provides the pressure distribution of a given geometry
2. The viscous mean flow is obtained by solving (2.5)–(2.8) for the given geometry, and the pressure distribution from the Euler solution.
3. The parabolized stability equations (2.18)–(2.19) are solved for the geometry, and mean flow from the boundary layer analysis.
4. The objective function (5.33) is evaluated from the solution of the parabolized stability equations.

If $\mathbf{w}$, $\mathbf{Q}$, and $\tilde{\mathbf{q}}$ are the solutions of the three state equations given above, then $\mathcal{J}$ can be considered to be a functional of $\mathbf{X}$ only and the objective function is then denoted $\mathcal{J}_X(\mathbf{X})$. The nodal coordinates, $\mathbf{X}$, are evaluated from the

displacements, $\mathbf{y}$, of the nodes on the airfoil by a mesh movement algorithm, here denoted $\mathbf{X} \equiv \mathbf{X}(\mathbf{y})$. The displacements are controlled by the parameter $\mathbf{a}$, i. e. $\mathbf{y} \equiv \mathbf{y}(\mathbf{a})$. From these definitions we can now define

$$\mathcal{J}_y\left(\mathbf{y}\right) = \mathcal{J}_X\left(\mathbf{X}\left(\mathbf{y}\right)\right), \quad \text{and} \quad \mathcal{J}_a\left(\mathbf{a}\right) = \mathcal{J}_y\left(\mathbf{y}\left(\mathbf{a}\right)\right), \tag{5.34}$$

which clearly shows that $\mathcal{J}_a\left(\mathbf{a}\right)$ is the objective function depending only on the control parameter $\mathbf{a}$. As the gradient of $\mathcal{J}_a\left(\mathbf{a}\right)$ with respect to $\mathbf{a}$ is used in the optimization procedure, we show in paper 5 that $\nabla \mathcal{J}_a$ can be evaluated from

$$\nabla \mathcal{J}_X \quad \rightarrow \quad \nabla \mathcal{J}_y \quad \rightarrow \quad \nabla \mathcal{J}_a,$$

in the above mentioned order. The gradient of the objective function with respect to the nodal coordinates $\nabla \mathcal{J}_X$ is derived using adjoint equations and is evaluated solving the APSE, ABLE and adjoint of the Euler equations (AEuler) in the mentioned order.

5.5.2. *Mesh displacements, parametrization and geometrical constraints*

All displacements are made with respect to a reference mesh, defined by its vector of nodal coordinates $\mathbf{X}^0$. For a vector $\mathbf{y}^k$ of shape displacements the new grid is obtained as

$$\mathbf{X}^k = \mathbf{X}^0 + \mathrm{L}\mathbf{y}^k. \tag{5.35}$$

Given the gradient ∇J_X of a functional J_X of the nodal coordinates, the gradient of the functional $J_y\left(\mathbf{X}\right) \equiv J_X\left(\mathbf{X}\left(\mathbf{y}\right)\right)$ is obtained by the following matrix–vector product

$$\nabla \mathcal{J}_y = \mathrm{L}^T \nabla \mathcal{J}_\mathbf{X}. \tag{5.36}$$

Smooth shapes, together with geometric constraints, are obtained taking the vectors of displacements $\mathbf{y}$ that are the solutions of a minimization problem (see Amoignon 2003) of the form

$$\mathbf{y} = \begin{cases} \min_{\mathbf{v} \in \mathbb{R}^n} \dfrac{1}{2}\mathbf{v}^T \mathrm{A}_s \mathbf{v} - \mathbf{v}^T \mathrm{M}_s \mathbf{a}, \\ \mathrm{C}^T \mathbf{y} = \mathbf{b}, \end{cases} \tag{5.37}$$

where A_s is the stiffness matrix associated with the Laplace operator, M_s is a mass matrix, C is the matrix whose rows are the gradients of the linear constraints (in $\mathbb{R}^{n \times m}$) and $\mathbf{b}$ is the vector of values imposed to the constraints (in $\mathbb{R}^m$). The solution $\mathbf{y}$ to the above system can be seen as the vector of displacements, which, according to the norm defined by the positive definite matrix A_s, is the closest to the solution of the discretized Laplace equation defined by

$$\mathrm{A}_s \tilde{\mathbf{y}} = \mathrm{M}_s \mathbf{a}, \tag{5.38}$$

and fulfills exactly the constraints

$$\mathrm{C}^T \mathbf{y} = \mathbf{b}. \tag{5.39}$$

Such a parameterization implies that the controls are the vector $\mathbf{a}$, right hand side of equation (5.38), and the vector $\mathbf{b}$, right hand side of the constraints,

$$\mathbf{a}^{k+1} \rightarrow \mathbf{y}^{k+1} \rightarrow \mathbf{X}^{k+1}$$

$$\uparrow$$

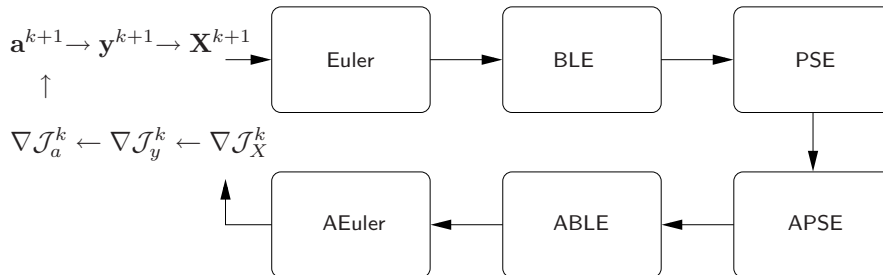$$\nabla \mathcal{J}_a^k \leftarrow \nabla \mathcal{J}_y^k \leftarrow \nabla \mathcal{J}_X^k$$

FIGURE 5.9. Flow chart for the case of minimizing the disturbance kinetic energy using the parameter $\mathbf{a}$ to control the shape of geometry.

relation (5.39). The gradients with respect to $\mathbf{a}$ and $\mathbf{b}$, which are the control variables in our method, can then be obtained by solving an adjoint problem (see Amoignon 2003) of the form

$$\begin{pmatrix} A_s^T & -C \\ -C^T & 0 \end{pmatrix} \begin{pmatrix} \mathbf{y}^* \\ \lambda^* \end{pmatrix} = \begin{pmatrix} \nabla \mathcal{J}_y \\ \mathbf{0} \end{pmatrix} , \qquad (5.40)$$

from which it holds that

$$\nabla \mathcal{J}_a = M_s^T \mathbf{y}^* \quad \text{and} \quad \nabla \mathcal{J}_b = -\lambda^* . \qquad (5.41)$$

Note that $\nabla \mathcal{J}_y$ in (5.40) is obtained by evaluating expression (5.36). All constraints considered so far are equality constraints, and $\mathbf{b}$ is therefore a vector of constants. The only control parameter in this case is therefore $\mathbf{a}$.

5.5.3. *Solution procedure*

A simple chart of the order in which the state and adjoint equations are solved and gradients are evaluated in order to perform optimal NLF is given in figure 5.9. There, k denotes the iteration number and the procedure is as follows:

1. For $k = 1$, we start with an initial Euler mesh $\mathbf{X}^0$
2. The Euler, BLE and PSE are solved in the given order
3. The objective function $\mathcal{J}^k$ is evaluated
4. The adjoint equations, APSE, ABLE and AEuler are solved
5. The gradients $\nabla \mathcal{J}_X^k$, $\nabla \mathcal{J}_y^k$ and $\nabla \mathcal{J}_a^k$ are evaluated in the given order
6. A new control parameter $\mathbf{a}^{k+1}$ is calculated[2] using the gradient $\nabla \mathcal{J}_a^k$
7. If $k > 1$, check convergence: If $|(\mathcal{J}^{k+1} - \mathcal{J}^k)/\mathcal{J}^k| < \epsilon$, else[3] continue
8. A new mesh $\mathbf{X}^{k+1}$ is calculated from the new control parameter $\mathbf{a}^{k+1}$
9. Goto 2.

---

[2]In the computations shown in paper 5, the L-BFGS-B routine was used, normally requiring several functional and gradient evaluations in order to build up the approximative Hessian matrix.

[3]Several convergence criteria exist in the L-BFGS-B routine, (see Zhu *et al.* 1994)

5.5.4. *An optimal design case*

An optimization case in which constraints are not imposed on operational properties such as lift, and pitch-moment coefficients might result in a design which is not useful. Results are shown here for the case of minimizing an objective function including both the disturbance kinetic energy, pressure drag C_D, and in addition penalties on the deviations of the lift, and pitch-moment coefficients, C_L and C_M, from the initial values. This is written

$$\mathcal{J}_C = \lambda_U \mathcal{J} + \lambda_D C_D + \lambda_L \frac{1}{2} \left(C_L - C_L^0 \right)^2 + \lambda_M \frac{1}{2} \left(C_M - C_M^0 \right)^2 , \qquad (5.42)$$

where the coefficients λ_U and λ_D are used to normalize $\mathcal{J}$ and C_D with respective values computed using the initial mesh. The coefficients λ_L and λ_M are used to penalize the deviations of C_L and C_M from respective values computed on the initial mesh. The initial design is the RAE2822 airfoil and the flow is characterized by a free stream Mach number of $M_\infty = 0.734$ and Reynolds number of $Re_\infty = 6.5 \times 10^6$. The disturbance used to evaluate $\mathcal{J}$ has a physical frequency $f^* = 11$ kHz and wave angle of $\psi_w \approx 40°$ and is integrated from close to the leading edge to half chord. As geometrical constraints we impose that the volume should not deviate from its initial value and that a region around the leading edge is kept fixed.
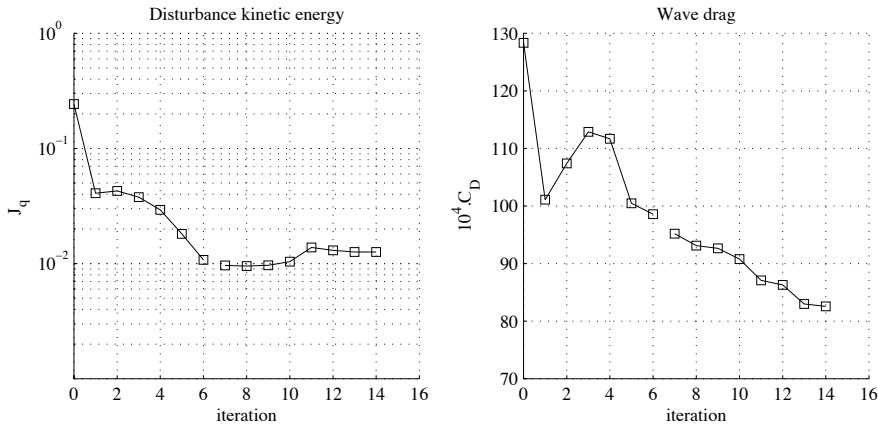

FIGURE 5.10. Left: Disturbance kinetic energy. Right: wave drag. Both as functions of the iteration number.

Results of the convergence history is shown in figures 5.10 and 5.11 for the disturbance kinetic energy, pressure drag, lift, and pitch-moment coefficients as functions of the iteration number. A reduction in the objective function (5.42) is obtained from the first to the last iteration (see paper 5). During a few iterations, however, it can be noted that the pressure drag increase while the deviations of C_D and C_M decrease, figure 5.10. At the final iteration a
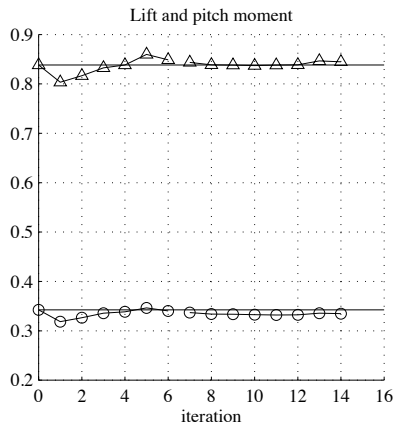
FIGURE 5.11. Lift, (triangle-solid) and pitch-moment (circle-solid) coefficients as functions of the iteration number. The values at initial design are indicated at each step (solid).

reduction has been obtained in both disturbance kinetic energy and pressure drag while C_D and C_M are kept within a few percent, figure 5.11.

A comparison between the pressure coefficients, and geometry for the initial (solid) and last iteration (dash) obtained from the optimization can be seen in figure 5.12. The largest change in the geometry occur in the region on the upper side of the airfoil where $\mathcal{J}$ is evaluated. This can also be seen in the pressure distributions. The relative small change on the lower side is caused in order to satisfy the constant volume constraint. As the upper side of the final design is thinner, and the part around the leading edge is fixed to approximately 4% chord, an increase occur in the curvature of the airfoil around 10% chord. This can be seen in the decrease in the pressure coefficient in that region.

The EoE of the N-factor curves for a large number of modes can be seen in figure 5.13 for the initial and final design. In comparison with figure 5.12 we can note that the pressure gradient in the region where the disturbance become unstable has change from an adverse to zero or weakly favorable. This has a damping effect on the disturbance growth in the whole domain where $\mathcal{J}$ is evaluated, which can be seen in figure 5.13. In order to estimate the change in the total drag computations were performed solving the Reynolds Averaged Navier Stokes equations on the initial and final design. The transition location in these computations was estimated using the EoE curves computed using the pressure distributions from the Euler solutions. The computations showed a decrease in pressure drag of about 25%, viscous drag of about 23%, and total drag of about 24%. In the approach taken here there are still improvements to be made. This can for instance be seen looking at the region $x/c \approx 0.4$ to $x/c \approx 0.6$ of the pressure distributions in figure 5.12 of the final design. The
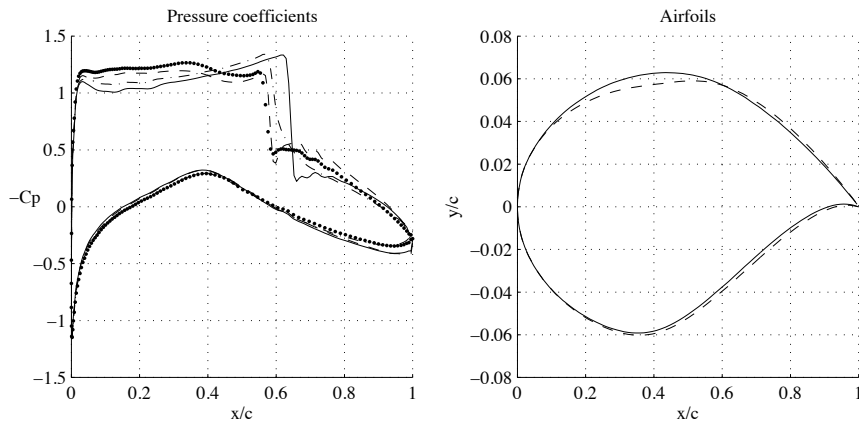
FIGURE 5.12. Left: Pressure coefficients for initial (solid), and final design (dash) obtained from the optimization solving the Euler equations. A comparison is made using the Reynolds Averaged Navier Stokes Equtions to compute the flow of the initial (dash-dot), and final design (dot). Right: initial (solid) and final design (dash).
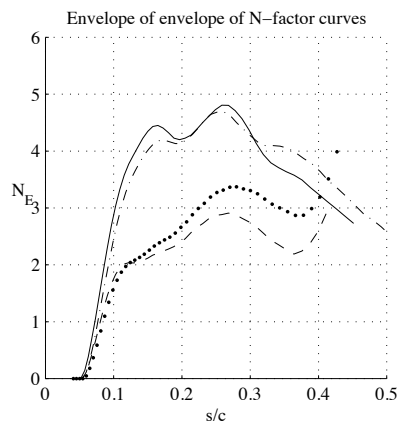

FIGURE 5.13. Envelope of envelopes of N-factor curves. Lines correspond to the cases shown in figure 5.12.

pressure gradient in this region is adverse indicating that separation occurs. More results and discussions are found in paper 5.

CHAPTER 6

Summary & conclusions

The work presented in this thesis concerns the use of gradient-based optimization techniques for the purpose of laminar flow control (LFC), and design of wings for natural laminar flow (NLF). The goal of using this technique is to reduce the viscous drag. Reduction of viscous drag can be seen as an increase of the laminar portion of the wing, thus a delay of laminar-turbulent transition. On wings in low free-stream turbulence environments, the latter is usually caused by break down of small disturbances which grow as they propagate down stream. The fluid flow has been divided into three different parts, namely: an inviscid part providing the pressure distribution for a given geometry, a viscous mean flow which is computed given the pressure distribution and geometry, and finally a linear stability analysis using the PSE providing the growth rate of convectively unstable disturbances superimposed on the viscous mean flow. The growth rate can been used to predict the transition location using the so called e^N-method. Here it is assumed that transition will occur at the location where the total amplification of the disturbance, with respect to the first streamwise position where the disturbance starts to grow, attains an empirically determined value, whose logarithm is generally denoted by N.

Several optimization problems have been defined for the purpose of LFC and NLF with the aim of minimizing an objective function based on measures of, or related to, the growth of unstable disturbances. Here, different control variables, means of control, have been used and the gradients of the objective function with respect to the control has been derived using adjoint equations. Especially the derivation of the adjoint of the PSE (APSE), and the adjoint of the BLE (ABLE) for compressible flows have been of interest, and now accomplished can be used in several applications. An existing optimization routine has been used in most cases as the topic of this research does not concern development of these routines.

The accuracy of the gradients evaluated from the solution of the adjoint equations have been investigated by comparing them with those computed by a finite-difference approximation. The tests have shown that an increased accuracy can be achieved by increasing the spatial resolution of the discretized equations. As the latter is known to cause numerical stability problems for the PSE, a known method to overcome this problem has been used which also alters the APSE and ABLE. A sensitivity analysis using the gradients of the disturbance kinetic energy at the second neutral point with respect to periodic

forcing show that control is most efficiently made in the vicinity of the first neutral point. It was further shown that the disturbance kinetic energy is most sensitive to control by means of periodic blowing and suction, and in general the efficiency decreases with increasing Mach number.

Results of optimal steady suction distributions have been presented for both incompressible and compressible flows. It has been shown that minimizing an objective function based on the disturbance kinetic energy of a single disturbance results in a suction distribution which has a damping effect on a large number of disturbances of the same type, e. g. (TS) Tollmien-Schlichting-, or (CF) cross-flow waves. On swept wings, a situation might occur when both these types of waves exist simultaneously. For such cases it has been shown that both types must be included in the objective function in order to obtain a suction distribution which has a damping effect on other disturbances of these two types. Results of optimal temperature distributions for disturbance control have been presented for various Mach numbers. It has been shown that the efficiency of the optimal control decreases when the wall temperature downstream of the control domain is maintained at its original adiabatic value, compared to the case when the wall there is insulated. It has also been shown that the efficiency decreases with increasing Mach number.

A problem has been formulated to perform optimal NLF design, in which the aim is to minimize a measure of the disturbance kinetic energy. Results have been presented for cases where both the disturbance kinetic energy, and wave drag have been reduced simultaneously while lift, and pitch-moment coefficients as well as the volume have been maintained at desired values.

One of the goals with work presented here was to show that the derived techniques can be used in realistic applications. This was addressed for the case of optimal suction distributions in which the problem was also formulated using discrete pressure chambers, and computations were made on an infinite swept wing designed for commercial aircraft. Also the problem of optimal NLF design was formulated such that airfoils in realistic flow conditions can be optimized.

Acknowledgment

Bibliography

AIRIAU, C. 2000 Non-parallel acoustic receptivity of a Blasius boundary layer using an adjoint approach. *Flow, Turbulence and Combustion* **65**, 347–367.

AIRIAU, C., BOTTARO, A., WALTHER, S. & LEGENDRE, D. 2003 A methodology for optimal laminar flow control: Application to the damping of Tollmien-Schlichting waves in a boundary layer. *Phys. Fluids* **15**, 1131–1145.

AL-MAAITAH, A. A., NAYFEH, A. H. & MASAD, J. A. 1991 Effect of suction on the stability of supersonic boundary layers. part I: Second-mode waves. *J. Fluids Engng* **113**, 591–597.

AMOIGNON, O. 2003 Aerodynamic shape optimization: I. *Tech. Rep.*. Department of Information Technology, Uppsala, Sweden, licenciate thesis to be published, University of Uppsala.

ANDERSSON, P., HENNINGSON, D. S. & HANIFI, A. 1998 On a stabilization procedure for the parabolic stability equations. *J. Engng Maths* **33**, 311–332.

ARNAL, D. 1993 Boundary layer transition: Predictions based on linear theory. Special course on 'progress in transition modeling', March-April 1993. AGARD-R-793, 2-1–2-63.

BALAKUMAR, P. & HALL, P. 1999 Optimum suction distribution for transition prediction. *Theor. Comput. Fluid Dyn.* **13**, 1–19.

BERTOLOTTI, F. P. 1998 The influence of rotational and vibrational energy relaxation on boundary-layer stability. *J. Fluid Mech.* **372**, 93–118.

BERTOLOTTI, F. P., HERBERT, T. & SPALART, S. 1992 Linear and nonlinear stability of the Blasius boundary layer. *J. Fluid Mech.* **242**, 441–474.

BIELER, H. & PREIST, J. 1992 HLFC for commercial aircraft. In *First european forum on laminar flow technology*, pp. 193–199. Hamburg.

BRANDT, L. 2003 Numerical studies of bypass transition in the Blasius boundary layer. PhD thesis, Royal Institute of Technology, Stockholm, Sweden.

CATHALIFAUD, P. & BEWLEY, T. R. 2002 A numerically tractable global framework for the feedback control of boundary-layer perturbations. ASME, ASME Fluids Engineering Division Summer Meeting, Montreal, Canada.

CATHALIFAUD, P. & LUCHINI, P. 2000 Algebraic growth in a boundary layer: optimal control by blowing and suction at the wall. *Eur. J. Mech. B/Fluids* **19** (4), 469–490.

DIACONIS, N. S., JACK, J. R. & WISNIEWSKI, R. J. 1957 Boundary-layer transition

at mach 3.12 as affected by cooling and nose blunting. *NACA Tech. Note No. 3928* .

DOBRINSKY, A. & COLLIS, S. S. 2000 Adjoint parabolized stability equations for receptivity prediction. *AIAA Paper* (2000-2651).

GASTER, M. 1974 On the effect of boundary layer growth in flow stability. *J. Fluid Mech.* **66**, 465–480.

GEDNEY, C. J. 1983 The cancellation of a sound-excited Tollmien-Schlichting wave with plate vibration **26** (5), 1158–1160.

GREEN, B. E. & WHITESIDES, J. L. 1996 A method for the constrained design of natural laminar flow airfoils. *AIAA Paper* (96-2502).

GUNZBURGER, M. D., HOU, L. S. & SVOBODNY, T. P. 1993 The approximation of boundary control problems for fluid flows with an application to control by heating and cooling. *Comp. Fluids* **22** (2/3), 239–251.

HAJ-HARIRI, H. 1994 Characteristics analysis of the parabolized stability equations. *Stud. Appl. Math.* **92**, 41–53.

HALL, P. 1983 The linear development of görtler vortices in growing boundary layers. *J. Fluid Mech.* **130**, 41–58.

HANIFI, A., HENNINGSON, D. S., HEIN, S. & BERTOLOTTI, F. P.and SIMEN, M. 1994 Linear non-local instability analysis - the linear NOLOT code. *FFA TN* **1994-54**.

HEIN, S., BERTOLOTTI, F. P., SIMEN, M., HANIFI, A. & HENNINGSON, D. S. 1994 Linear non-local instability analysis - the linear NOLOT code. *DLR-IB* **223-94 A 43**.

HERBERT, T. 1997 Parabolized stability equations. *Annu. Rev. Fluid Mech.* **29**, 245–283.

HERBERT, T. & BERTOLOTTI, F. P. 1987 Stability analysis of nonparallel boundary layers. *Bull. Am. Phys. Soc.* **32**, 2079.

HILL, D. C. 1997a Receptivity in non-parallel boundary layers. In *ASME Fluids Engineering Division Summer Meeting, FEDSM '97*.

HILL, D. C. 1997b Inverse design for laminar three-dimensional boundary layers. *Bull. Am. Phys. Soc.* **42**, 2120.

HÖGBERG, M. 2001 Optimal control of boundary layer transition. PhD thesis, Royal Institute of Technology, SE-172 90 Stockholm, Sweden.

HÖGBERG, M. & BERGGREN, M. 2000 Numerical approaches to optimal control of a model equation for shear flow instabilities. *Flow, Turbulence and Combustion* **65**, 299–320.

HÖGBERG, M. & HENNINGSON, D. S. 2002 Linear optimal control applied to instabilities in spatially developing boundary layers. *J. Fluid Mech.* **470**, 151–179.

VAN INGEN, J. L. 1956 A suggested semiempirical method for the calculation of the boundary layer transition region. *Tech. Rep.* VTH-74. Department of Aeronautical Engineering, University of Delft.

ITOH, N. 1986 The origin and subsequent development in space of Tollmien-Schlichting waves in a boundary layer. *Fluid Dyn. Res.* pp. 119–130.

JACK, J. R., WISNIEWSKI, R. J. & DIACONIS, N. S. 1957 Effects of extreme surface cooling on boundary-layer transition. *NACA Tech. Note No. 4094* .

JAMESON, A. 1988 Aerodynamic design via control theory. *J. Scientific Computing* **3** (3), 233–260.

JIANG, L., CHANG, C.-L., CHOUDHARI, M. & LIU, C. 2003 Cross-validation of DNS and PSE results for instability-wave propagation in compressible boundary layers past curvilinear surfaces. *AIAA Paper* (2003-3555), 33rd AIAA Fluid Dynamics Conference and Exhibit, Orlando, Florida, 23-26 June, 2003.

JOSLIN, R. 1998 Overview of laminar flow control. *Tech. Rep.* 1998-208705. NASA, Langley Research Center, Hampton, Virginia.

KOZLOV, V. V. & LEVCHENKO, V. Y. 1985 Laminar-turbulent transition control by localized disturbances. *AIAA Paper* (85–0568).

LEE, J.-M., SCHRAGE, D. P. & MAVRIS, D. N. 1998 Development of subsonic transports with laminar flow wings. *AIAA Paper* (98-0406).

LEES, L. & LIN, C. C. 1946 Investigation of the stability of the laminar boundary layer in a compressible fluid. *NACA Tech. Note No. 1115* .

LEVIN, O. & HENNINGSON, D. S. 2003 Exponential vs algebraic growth and transition prediction in boundary layer flow. *Flow, Turbulence and Combustion* Accepted for publication.

LI, F. & MALIK, M. R. 1994 Mathematical nature of parabolized stability equations. In *4th IUTAM Symp. on Laminar-Turbulent Transition, Sendi, Japan* (ed. R. Kobayashi), pp. 205–212. Springer.

LI, F. & MALIK, M. R. 1996 On the nature of PSE approximation. *Theor. Comput. Fluid Dyn.* **8**, 253–273.

LIEPMANN, H. W., BROWN, G. L. & NOSENCHUCK, D. M. 1982 Control of laminar-instability waves using a new technique. *J. Fluid Mech.* **118**, 187–200.

LIEPMANN, H. W. & FILA, G. H. 1947 Investigations of effects of surface temperature and single roughness elements on boundary-layer transition. *NACA Tech. Report No. 890* .

LO, C. F., LAFRANCE, R., MEREDITH, W. S. & WIBERG, C. G. 1995 Laminar flow control with wall temperature distribution for quiet supersonic wind tunnels. *AIAA Paper* (95-2296).

LYSENKO, V. I. & MASLOV, A. A. 1984 The effect of cooling on supersonic boundary-layer stability. *J. Fluid Mech.* **147**, 39–52.

MACK, L. M. 1977 Transition prediction and linear stability theory. Paris: AGARD Report No 224, also JPL Publication 77-15, 1977.

MACK, L. M. 1984 Boundary-layer linear stability theory. *AGARD Report No. 709* .

MACK, L. M. 1988 Stability of three-dimensional boundary layers on swept wings at transonic speeds. In *IUTAM Symp. Transsonicum III* (ed. J. Zierep & H. Oertel). Göttingen: Springer.

MAESTRELLO, L. & NAGABUSHANA, K. A. 1989 Relaminarization of turbulent flow on a flat plate by localized surface heating. *AIAA Paper* (89-0985), 2nd Shear Flow Conference, March 13-16, 1989/Tempe, AZ.

MALIK, M. R. 1989 Prediction and control of transition in supersonic and hypersonic boundary layers. *AIAA J.* **27**, 1487–1493.

MALIK, M. R. & BALAKUMAR, P. 1992 Nonparallel stability of rotating disk flow using PSE. In *Instability, Transition and Turbulence* (ed. M. Hussaini, A. Kumar & C. Streett), pp. 168–180. Springer.

MANNING, V. M. & KROO, I. M. 1999 Multidisciplinary optimization of a natural laminar flow supersonic aircraft. *AIAA Paper* (99-3102).

MASAD, J. A. & MALIK, M. R. 1994 Effects of body curvature and nonparllelism on the stability of flow over a swept cylinder. *Phys. Fluids* **6**, 2363–2379.

MASAD, J. A. & NAYFEH, A. H. 1992 Laminar flow control of subsonic boundary layers by suction and heat-transfer strips. *Phys. Fluids A* **4** (6), 1259–1272.

MASAD, J. A., NAYFEH, A. H. & AL-MAAITAH, A. A. 1991 Effect of suction on the stability of supersonic boundary layers. part II: First-mode waves. *J. Fluids Engng* **113**, 598–601.

MASAD, J. A., NAYFEH, A. H. & AL-MAAITAH, A. A. 1992 Effect of heat transfer on the stability of compressible boundary layers. *Comp. Fluids* **21** (1), 43–61.

MATSUBARA, M. & ALFREDSSON, P. 2001 Disturbance growth in boundary layers subjected to free-stream turbulence. *J. Fluid Mech.* **430**, 149–168.

MILLING, R. W. 1981 Tollmien-Schlichting wave cancellation **24** (5), 979–981.

PRALITS, J. O., AIRIAU, C., HANIFI, A. & HENNINGSON, D. S. 2000 Sensitivity analysis using adjoint parabolized stability equations for compressible flows. *Flow, Turbulence and Combustion* **65** (3), 321–346.

PRALITS, J. O. & HANIFI, A. 2003 Optimization of steady suction for disturbance control on infinite swept wings. *Phys. Fluids* **15** (9), 2756–2772.

PRALITS, J. O., HANIFI, A. & HENNINGSON, D. S. 2002 Adjoint-based optimization of steady suction for disturbance control in incompressible flows. *J. Fluid Mech.* **467**, 129–161.

PRUETT, C. D. & CHANG, C.-L. 1993 A comparison of PSE and DNS for high-speed boundary-layer flows. In *Transitional and Turbulent Compressible Flows* (ed. L. Kral & T. Zang), , vol. 151, pp. 57–67. Washington, D.C.: ASME.

SARIC, W. S. & NAYFEH, A. H. 1975 Non-parallel stability of boundary layer flows. *Phys. Fluids* **18**, 945–950.

SCHUBAUER, G. B. & SKRAMSTAD, H. K. 1948 Laminar-boundary-layer oscillations and transition on a flat plate. *NACA Tech. Note No. 909* .

SIMEN, M. 1992 Local and non-local stability theory of spatially varying flows. In *Instability, Transition and Turbulence* (ed. M. Hussaini, A. Kumar & C. Streett), pp. 181–201. Springer.

SMITH, A. M. O. & GAMBERONI, N. 1956 Transition, pressure gradient and stability theory. *Tech. Rep.* ES 26388. Douglas Aircraft Co.

SPALL, R. E. & MALIK, M. R. 1989 Goertler vortices in supersonic and hypersonic boundary layers. *Phys. Fluids A* **1**, 1822.

THOMAS, A. S. W. 1983 The control of boundary-layer transition using a wave-superposition principle. *J. Fluid Mech.* **137**, 233–250.

WALTHER, S., AIRIAU, C. & BOTTARO, A. 2001 Optimal control of Tollmien-Schlichting waves in a developing boundary layer. *Phys. Fluids* **13**, 2087–2096.

WESTIN, K., BOIKO, A., KLINGMANN, B., KOZLOV, V. & ALFREDSSON, P. 1994 Experiments in a boundary layer subjected to free stream turbulence. part 1. boundary layer structure and receptivity. *J. Fluid Mech.* **281**, 193–218.

ZHU, C., BYRD, R., LU, P. & NOCEDAL, J. 1994 L-BFGS-B: Fortran subroutines for large scale bound constrained optimization. *Tech. Rep.* NAM-11. EECS Department, Northwestern University.

ZURIGAT, Y. H., NAYFEH, A. H. & MASAD, J. A. 1990 Effect of pressure gradient on the stability of compressible boundary layers. *AIAA Paper* (90-1451), 21st Fluid Dynamics, Plasma Dynamics and Lasers Conference, Seattle, WA.

Part 2

Papers

1

Paper 1

Sensitivity Analysis Using Adjoint Parabolized Stability Equations for Compressible Flows

By   Jan O. Pralits[1,3], Christophe Airiau[2],
Ardeshir Hanifi[3] and Dan S. Henningson[1,3]

An input/output framework is used to analyze the sensitivity of two- and three dimensional disturbances in a compressible boundary layer for changes in wall- and momentum forcing. The sensitivity is defined as the gradient of the kinetic disturbance energy at a given downstream position with respect to the forcing. The gradients are derived using the parabolized stability equations (PSE) and their adjoint (APSE). The adjoint equations are derived in a consistent way for a quasi two-dimensional compressible flow in an orthogonal curvilinear coordinate system. The input/output framework provides a basis for optimal control studies. Analysis of two-dimensional boundary layers for Mach numbers between 0 and 1.2 show that wall- and momentum forcing close to branch I of the neutral stability curve give the maximum magnitude of the gradient. Forcing at the wall gives the largest magnitude using the wall normal velocity component. In case of incompressible flow, the two-dimensional disturbances are the most sensitive ones to wall inhomogeneity. For compressible flow, the three-dimensional disturbances are the most sensitive ones. Further, it is shown that momentum forcing is most effectively done in the vicinity of the critical layer.

1. Introduction

Transition from laminar to turbulent flow can be triggered by unstable disturbances inside the boundary layer. The growth of such1 disturbances are known to be sensitive to surface inhomogeneities, forcing inside the boundary layer and external acoustic perturbations, see *e.g.* Nishioka and Morkovin (1986), Saric (1993) and Corke, Bar-Sever and Morkovin (1986). The studies devoted to the birth of disturbances due to such forcing are called receptivity. The acoustic receptivity is explained by Goldstein (1983) as a wavelength conversion mechanism. The long wave length of an acoustic wave can be converted to a shorter wave length of an instability wave at the leading edge or where

---

[1]Department of Mechanics, KTH, SE-100 44 Stockholm, Sweden.
[2]Institut de Mécanique des Fluides de Toulouse, Allée du professeur Camille Soula, F-31 400 Toulouse, France.
[3]Swedish Defence Research Agency, FOI, Aeronautics Division, FFA, SE-172 90 Stockholm, Sweden.

a geometric inhomogeneity is present. Results of boundary layer receptivity are documented by Crouch (1992a, 1992b) and Choudhari and Street (1992) for two-dimensional disturbances in a Blasius boundary layer. Other references may be found in Goldstein (1989) and in Saric (1993).

A disturbance inside the boundary layer may encounter an unsteady wall inhomogeneity (forcing) which changes its growth. This problem can also be viewed as a receptivity to wall perturbations. If the perturbation is appropriate, it can be used to control the development of the disturbance. This is the wave cancellation concept proposed by Thomas (1983). Such study may be formulated as input/output problem where the input is some forcing on the wall or in the boundary layer, and the output is a measure of the disturbance in the domain. The sensitivity can be defined as the gradient of the output with respect to the input. A typical output measure is the disturbance energy at some downstream position or in the whole domain. Such a formulation can easily be extended to a control problem by using the gradient to update the input *i.e.* control variables in order to minimize the output. This analysis can be done with gradient based optimization techniques as shown in Gunzburger (2000) and Bewley, Temam and Ziane (2000).

Here we investigate the sensitivity of disturbances to unsteady wall conditions and source of momentum in a compressible boundary layer in framework of the non-local stability theory. This analysis is formulated as an input/output problem and provides information which is useful for the control of disturbances. The state equations are the so called Parabolized Stability Equations, PSE, and are written in an orthogonal curvilinear coordinates system. For a detailed presentation of PSE see *e.g.* Bertolotti, Herbert and Spalart (1998) and Simen (1992).

The main tool developed here is based on the adjoint equations. The approach of adjoint equations has been used for sensitivity studies in oceanography and atmospheric circulation models, *e.g.* Hall (1986). This approach has also appeared in receptivity studies. Tumin (1996) used it for confined flows. Hill (1995,1997a) applied the adjoint approach for the local and nonlocal stability theories to study the receptivity of Tollmien-Schlichting waves in boundary layer flows. Receptivity of Görtler vortices was studied by Luchini and Bottaro (1998) using backward-in-time integration. The adjoint techniques has also been used for identifying the optimal disturbances in boundary layer flows, *e.g.* Andersson, Berggren and Henningson (1999) and Luchini (2000).

Sensitivity analysis may be performed by forward calculations. For each parameter that is changed (inhomogeneous wall boundary conditions, initial disturbance, momentum source) the forward problem has to be solved. The total time spent will be the product of the number of input parameters and the time spent for each calculation.

The advantage of the adjoint approach is that the sensitivity of a disturbance can be obtained by solving the state and adjoint equations once. This means that the adjoint method can provide an optimal distribution of suction
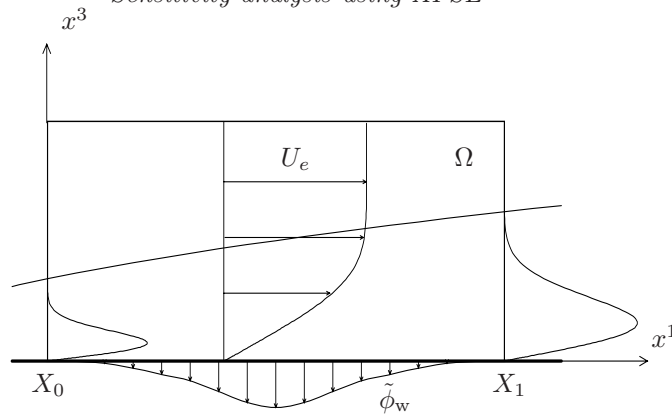
FIGURE 1. Computational domain

to suppress the growth of disturbances with a relatively low computational cost. Such a study was carried out by Cathalifaud and Luchini (2000) for optimal disturbances in a Blasius boundary layer.

The aim of the present work is to derive the adjoint of the parabolized stability equations for a compressible flow in a consistent way. The paper is organized as follows. In section 2 the problem is defined and section 3 gives the adjoint formulation and the gradient expressions. Validation and results of the sensitivity analysis are presented for a two-dimensional compressible boundary layer with two and three dimensional disturbances in section 4. The conclusions appear in section 5. Details of the derivation of nonlocal stability equations and their adjoint are given in the appendix.

2. Problem formulation

2.1. *Definition of the sensitivity*

The sensitivity of two- and three dimensional disturbances in a compressible boundary layer for changes in wall- and momentum forcing is investigated. This analysis is formulated as an input/output problem and will be discussed below considering the domain given in figure 1. Here, x^1, x^2 and x^3 are the streamwise, spanwise and wall normal coordinates, respectively, and U_e the freestream velocity. The computational domain is defined such that $x^1 \in [X_0, X_1]$, $x^2 \in [Z_0, Z_1]$ and $x^3 \in [0, \infty[$. An initial disturbance is superimposed to the boundary layer base flow at an upstream position X_0.

In optimal control theory, sensitivity is defined as the derivative of the state variables (output) with respect to the control variables (input). It is related to the gradient of a functional J (called cost or objective functional) which includes both a measure of a state E and a measure of the control E_c. The measures are weighted together with a positive factor ϵ, so called the regularization parameter, as $J = E + \epsilon E_c$. The regularization parameter serves the purpose of limiting the size of the control. The optimal input can

then be obtained via an optimality condition using gradient based optimization techniques as *e.g.* steepest descent or conjugate gradient, see *e.g.* Bewley *et al.* (2000) and Gunzburger (2000).

Here, the input is defined as the inhomogeneities of velocity $\tilde{\mathbf{u}}_w$ and temperature $\tilde{T}_w$ on the wall $x^3 = 0$ and a source $\tilde{\mathcal{S}}$ in the boundary layer. The output is a function of disturbance variables, here written as the disturbance energy norm

$$E = \frac{1}{2} \int_{Z_0}^{Z_1} \int_0^\infty \tilde{\phi}_1^H \mathcal{M} \tilde{\phi}_1 h_2 h_3 \; dx^3 \; dx^2, \tag{1}$$

or alternatively

$$E = \frac{1}{2} \int_{X_0}^{X_1} \int_{Z_0}^{Z_1} \int_0^{+\infty} \tilde{\phi}^H \mathcal{M} \tilde{\phi} \; h_1 h_2 h_3 \; dx^1 \; dx^2 \; dx^3, \tag{2}$$

where $\tilde{\phi} = (\tilde{\rho}, \tilde{u}, \tilde{v}, \tilde{w}, \tilde{T})^{\mathrm{T}}$ with $\tilde{\rho}$ denoting the density perturbation, $\tilde{u}, \tilde{v}, \tilde{w}$ the streamwise, spanwise and normal velocity perturbations, respectively, and $\tilde{T}$ the temperature perturbation. The superscript ^{H} denotes the transpose complex conjugate, the subscript $_1$ refers to values at $x = X_1$ and h_i the scale factors of the coordinate system. The positive diagonal matrix $\mathcal{M}$ defines the measure of 'size' of disturbances. In this paper $\mathcal{M} = \mathrm{Diag}(0, 1, 1, 1, 0)$ such that disturbances are measured by the modulus of their velocity components. An example of another measure is given in Hanifi *et al.* (1994) where $\mathcal{M} = \mathrm{Diag}(T/\rho\gamma M^2, \rho, \rho, \rho, \rho/\gamma(\gamma - 1)TM^2)$ with T being the mean temperature, ρ the mean density, γ the ratio of the specific heat coefficients and M the Mach number of the flow. We define the sensitivity as the gradient of E with respect to $\tilde{\mathbf{u}}_w$, $\tilde{T}_w$ and $\tilde{\mathcal{S}}$. Here we consider the case with no penalty, *i.e* $\epsilon = 0$, therefore can the output be written $J = E$.

In the present paper the amplitude of the control parameters are assumed to be so small that the nonlinear interaction with the mean flow can be neglected. However, the procedure presented here can be extended to account for the modification of the mean flow, see Pralits *et al.* (2000).

2.2. *State equations*

The governing equations are the non-local stability equations formulated using PSE technique for quasi-three dimensional viscous, compressible flow formulated in primitive variables and general, orthogonal curvilinear coordinates. Here, we consider a general case where the boundary layer is subjected to sources of mass, momenta and energy $\tilde{\mathcal{S}}$, and inhomogeneous boundary conditions on the wall $\tilde{\mathbf{u}}_w$ and $\tilde{T}_w$. The notation, the reference quantities, the assumptions and the derivation of the PSE are given in appendix Appendix A.

The equations in symbolic form are written as

$$
\begin{aligned}
\hat{\mathcal{L}}\,\hat{\phi} &= \hat{\mathcal{S}} && \text{in} \quad \Omega \\
\hat{\phi} &= \hat{\phi}_0 && \text{on} \quad x^1 = X_0 \\
\hat{\mathbf{u}} = \hat{\mathbf{u}}_{\mathrm{w}}(x^1), \quad \hat{T} &= \hat{T}_{\mathrm{w}}(x^1) && \text{on} \quad x^3 = 0 \\
\hat{\mathbf{u}} \to 0, \quad \hat{T} &\to 0 && \text{as} \quad x^3 \to \infty \\
\int_0^\infty \hat{\phi}^H \frac{\partial \hat{\phi}}{\partial x^1}\, h_2 h_3 dx^3 &= 0 && \forall \quad x^1
\end{aligned}
\tag{3}
$$

The disturbance $\tilde{\phi}$, the source $\tilde{\mathcal{S}}$ and the inhomogeneous boundary conditions have been divided into an amplitude function and a wave function

$$
\tilde{\phi}(x^i, t) = \hat{\phi}(x^1, x^3)\Theta, \quad \tilde{\mathcal{S}}(x^i, t) = \hat{\mathcal{S}}(x^1, x^3)\Theta,
\tag{4}
$$

where

$$
\Theta(x^1, x^2) = \exp\, i\, \left(\int_{X_0}^{x^1} \alpha(x')dx' + \beta x^2 - \omega t \right).
\tag{5}
$$

Here, α is the complex streamwise wavenumber, β the real spanwise wavenumber and ω the real angular frequency of the perturbations. The integral expression in equation (3), the so called auxiliary condition, is used to remove the ambiguity from the streamwise dependence that remains between the wave and the amplitude functions.

In accordance to the derivation of the nonlocal stability equations, the input parameters ($\hat{\mathbf{u}}_{\mathrm{w}}$, $\hat{T}_{\mathrm{w}}$ and $\hat{\mathcal{S}}$) are assumed to be weak functions of the streamwise coordinate, *i.e.* $\partial/\partial x^1 \sim \mathcal{O}(R^{-1})$. Note that $\tilde{\phi}_{\mathrm{w}}$ and $\tilde{S}$ have the same x^2, t and main x^1 dependence as the disturbances.

The system of equations (3), which is nonlinear in $(\alpha, \hat{\phi})$, is integrated in the downstream direction using a marching procedure, with the initial condition at $x^1 = X_0$ given by the local stability theory. At each streamwise position, the value of α is iterated such the auxiliary condition is satisfied.

3. Adjoint equations and gradients

The gradient of the output given by (1), is defined through the directional derivative as

$$
\begin{aligned}
\delta J = \quad \texttt{Real} \Bigg\{ &\int_{X_0}^{X_1} \int_{Z_0}^{Z_1} \left(\nabla_{\tilde{\mathbf{u}}_{\mathrm{w}}} J^H \delta \tilde{\mathbf{u}}_{\mathrm{w}} + \nabla_{\tilde{T}_{\mathrm{w}}} J^H \delta \tilde{T}_{\mathrm{w}} \right) h_1 h_2\, dx^2\, dx^1 + \\
&\int_{X_0}^{X_1} \int_{Z_0}^{Z_1} \int_0^\infty \nabla_{\tilde{\mathcal{S}}} J^H \delta \tilde{\mathcal{S}}\, h_1 h_2 h_3\, dx^3\, dx^2\, dx^1 \Bigg\},
\end{aligned}
\tag{6}
$$

where

$$
\nabla_\xi J\, \delta\xi = \lim_{s \to 0} \frac{J(\xi + s\delta\xi) - J(\xi)}{s},
$$

and $\delta \tilde{\mathbf{u}}_{\mathrm{w}}, \delta \tilde{T}_{\mathrm{w}}$ and $\delta \tilde{\mathcal{S}}$ are the variations of the input parameters. The gradient expressions, *i.e.* the sensitivities, are derived in appendix Appendix B, using a perturbation technique together with integration by parts in space. It yields

$$\nabla_{\tilde{u}_{\mathrm{w}}} J = \frac{\mu}{\Theta R} D_3(u^*) \qquad \text{on} \quad x^3 = 0$$

$$\nabla_{\tilde{v}_{\mathrm{w}}} J = \frac{\mu}{\Theta R} D_3(v^*) \qquad \text{on} \quad x^3 = 0$$

$$\nabla_{\tilde{w}_{\mathrm{w}}} J = \frac{\rho \rho^*}{\bar{\Theta}} \qquad \text{on} \quad x^3 = 0 \qquad (7)$$

$$\nabla_{\tilde{T}_{\mathrm{w}}} J = -\frac{\kappa}{\bar{\Theta} \operatorname{Pr} R} D_3(T^*) \qquad \text{on} \quad x^3 = 0$$

$$\nabla_{\tilde{\mathcal{S}}} J = \frac{\phi^*}{\bar{\Theta}} \qquad \text{in} \quad \Omega$$

where the overbar denotes the complex conjugate, μ, κ, R and Pr are the dynamic viscosity, the heat conductivity, the Reynolds and Prandtl numbers, respectively, and

$$D_i = \frac{1}{h_i} \frac{\partial}{\partial x^i}.$$

The co-state variables $\phi^* = (\rho^*, u^*, v^*, w^*, T^*)$ and r^* satisfy the adjoint equations

$$\hat{\mathcal{L}}^* \phi^* = \mathcal{S}^* \qquad \text{in} \quad \Omega$$
$$\mathbf{u}^* = 0, \quad T^* = 0 \qquad \text{on} \quad x^3 = 0$$
$$\mathbf{u}^* \to 0, \quad T^* \to 0 \qquad \text{as} \quad x^3 \to \infty$$
$$\phi^* = \phi_1^*, \quad r^* = r_1^* \qquad \text{on} \quad x^1 = X_1 \qquad (8)$$
$$\frac{\partial}{\partial x^1} \int_0^{+\infty} \phi^{*H} \frac{\partial \hat{\mathcal{L}}}{\partial \alpha} \hat{\phi} \, h_1 h_2 h_3 \, dx^3 = f^* \qquad \forall \quad x^1$$

where

$$\mathcal{S}^* = - \left[\bar{r}^* D_1(\hat{\phi}) - D_1(r^* \hat{\phi}) - (m_{21} + m_{31}) r^* \hat{\phi} \right], \qquad (9)$$

$$f^* = i \int_0^{+\infty} \phi^{*H} \hat{\mathcal{S}} \, h_1 h_2 h_3 \, dx^3 + i h_1 h_2 \left[-\frac{\kappa}{\operatorname{Pr} R} D_3(\bar{T}^*) \hat{T} \right.$$
$$\left. + (\rho \bar{\rho}^*) \hat{w} + \frac{\mu}{R} D_3(\bar{u}^*) \hat{u} + \frac{\mu}{R} D_3(\bar{v}^*) \hat{v} \right] \Big|_{x^3 = 0}. \qquad (10)$$

and

$$m_{ij} = \frac{1}{h_i h_j} \frac{\partial h_i}{\partial x^j}.$$

The co-state equations (8) are integrated in the upstream direction with the initial condition at $x^1 = X_1$ as :

$$\phi_1^* = |\Theta_1|^2 (\mathcal{D}^H)^{-1} (\mathcal{M} - c_1 \mathcal{I}) \hat{\phi}_1, \qquad r_1^* = |\Theta_1|^2 c_1 \qquad (11)$$

where c_1 is given in the appendix and $\mathcal{I}$ is the identity matrix. Equations (8) are solved iteratively to find r^* such that the integral expression is satisfied.

β		0	0.02	0.04
$M = 0,$	$\varphi =$	$0°$	$22.3°$	$41.2°$
$M = 0.7,$	$\varphi =$	$0°$	$23.5°$	$42.5°$
$M = 1.2,$	$\varphi =$	$0°$	$25.9°$	$45.2°$

TABLE 1. Spanwise wavenumber β with corresponding wave angle φ at $R = 160$ for different Mach numbers M. $F = 10^{-4}$

Now, the gradients of J can be obtained in following steps. First, the state variable ϕ is calculated by integrating equations (3) from $x^1 = X_0$ to X_1. Then the co-state equations (8) are integrated backward in the streamwise direction from $x^1 = X_1$ to X_0 to obtain the co-state variables ϕ^*. Finally, equations (7) give the gradients with respect to each control parameter.

It is worth mentioning that the expression for $\mathcal{S}^*$ depends on the choice of the auxiliary condition while the adjoint operator $\hat{\mathcal{L}}^*$ will remain unchanged for other choices of this condition. If the output is defined as in (2) the adjoint system will be

$$
\begin{aligned}
\hat{\mathcal{L}}^* \, \phi^* &= \mathcal{S}^* + \mathcal{M}^H \hat{\phi} |\Theta|^2 && \text{in} \quad \Omega \\
\mathbf{u}^* = T^* &= 0 && \text{on} \quad x^3 = 0 \\
\mathbf{u}^* , T^* &\to 0 && \text{as} \quad x^3 \to \infty \\
\phi^* = r^* &= 0 && \text{on} \quad x^1 = X_1
\end{aligned}
\tag{12}
$$

$$
\frac{\partial}{\partial x^1} \int_0^{+\infty} \phi^{*H} \frac{\partial \hat{\mathcal{L}}}{\partial \alpha} \, \hat{\phi} \, h_1 h_2 h_3 dx^3 + |\Theta|^2 \int_0^{+\infty} \hat{\phi}^H \mathcal{M} \hat{\phi} \, h_1 h_2 h_3 \, dx^3 = f^* \forall x^1
$$

Note that in this case both ϕ^* and r^* are subjected to homogeneous initial conditions.

4. Results

The results presented here are obtained by numerically integrating the discretized state and co-state equations. The x^1-derivatives are approximated by a first-order accurate backward Euler scheme and the x^3-derivatives by a fourth-order accurate compact finite-difference scheme. For details the reader is referred to Hanifi *et al.* (1994).

The calculations are performed for two- and three dimensional disturbances in a two-dimensional compressible boundary layer on an adiabatic flat plate. The gradients express the sensitivity of disturbances to small unsteady inhomgeneities in the steady boundary layer flow. The stagnation temperature is $300 \, K$ and the Prandtl number is held constant to $\mathrm{Pr} = 0.72$. The dynamic viscosity is calculated using Sutherland law and the coefficient of the specific heat c_p is assumed to be constant. The ratio of the coefficients of second and dynamic viscosity is given by the Stoke's hypothesis, *i.e.* $\lambda/\mu = -2/3$. In all figures the reduced frequency, defined as $F = 2\pi f^\star \nu_e^\star / U_e^{\star 2}$, is equal
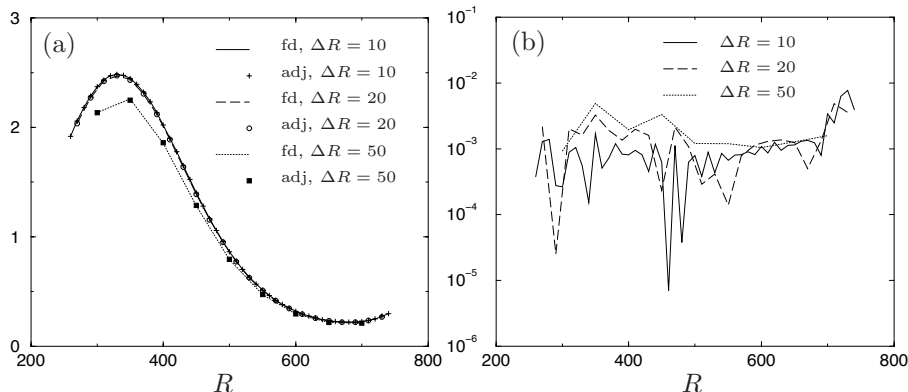
FIGURE 2. Comparison between adjoint (adj) and central difference (fd) calculations for different ΔR. Mach number $M = 0.7$, $\beta = 0$. a) lines denote $\|(\partial J/\partial \tilde{w}_r, \partial J/\partial \tilde{w}_i)/\Delta_n\|$ and symbols $|\nabla_{\tilde{w}_\mathrm{w}} J_n|$. b) relative error.

to 10^{-4}. Here $f^\star$ is the dimensional physical frequency and the subscript $_e$ refers to values at the edge of the boundary layer. The output is measured at $R = \sqrt{U_e^\star x^{1\star}/\nu_e^\star} = 760$. The calculations have been performed for three values of spanwise wavenumbers β at different Mach numbers. Values of the wave angle φ given at $x^1 = X_0$ for the cases studied here are given in table 1. In all calculations, the metric coefficients $h_1 = h_2 = h_3 = 1$.

4.1. *Accuracy of the gradient, validation*

In order to verify the correctness of the gradient, we compare the adjoint based gradients to those obtained using the finite-difference approach. In the latter, the derivative of the output variable with respect to each input parameter is approximated by a second-order accurate central finite-difference scheme.

To compare the gradients given by the adjoint and finite-difference approaches let us consider the example of a wall normal velocity perturbation $\delta \tilde{w}_\mathrm{w}$ at $x^3 = 0$. The variation of a functional J with respect to this wall perturbation is :

$$\delta J = \frac{\partial J}{\partial \tilde{w}_r}\delta \tilde{w}_r + \frac{\partial J}{\partial \tilde{w}_i}\delta \tilde{w}_i \tag{13}$$

The subscripts $_r$ and $_i$ denote the real and imaginary parts of a complex number. In the finite-difference approach, the derivatives of J are obtained by imposing the inhomogeneous boundary condition $\tilde{w}_\mathrm{w} = \pm\varepsilon$ at $x^1 = x_n^1$. Here, ε is a small number and index n refers to n-th streamwise position. Then, the derivatives are calculated using a second-order accurate finite-difference scheme.
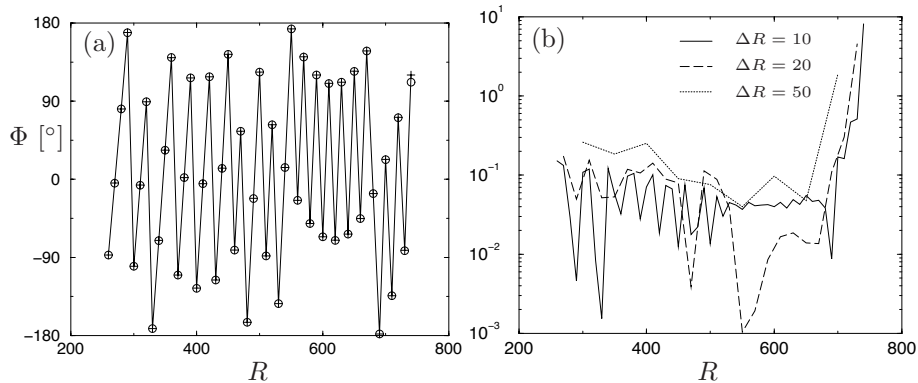
FIGURE 3. Comparison between adjoint and central difference calculations of the phase Φ in degrees for $M = 0.7$, $\beta = 0$. a) $\Delta R = 10$. $+$ denotes central difference, and $\circ$ denotes adjoint calculations. b) absolute error in degrees.

The expression for δJ in the adjoint approach, for a flat plate geometry, is in discretized form given as

$$\delta J = \int_{Z_0}^{Z_1} \sum_{n=2}^{N-1} \frac{1}{2} (\nabla_{\tilde{w}_\mathrm{w}} J_n^H \delta \tilde{w}_{\mathrm{w}_n} + c.c.) \Delta_n \, dx^2, \tag{14}$$

where $\Delta_n = (x_{n+1}^1 - x_{n-1}^1)/2$ and $c.c.$ is the complex conjugate. In the following, the quantity $\nabla_{\tilde{w}_\mathrm{w}} J_n$ is compared to those of the finite-difference approach. The streamwise domain used here is $R \in [250, 750]$. In figure 2a the modulus $||(\partial J/\partial \tilde{w}_r, \partial J/\partial \tilde{w}_i)/\Delta_n||$, as a function of x_n^1, is compared to $|\nabla_{\tilde{w}_\mathrm{w}} J_n|$ for different resolution of the streamwise step ΔR. A good agreement is found between the approaches for a given ΔR, and both values converge as ΔR is decreased. The relative error given in figure 2b is below one percent for all cases and decreases slightly as ΔR is decreased.

The phase Φ of the gradients obtained by adjoint equations and central differences is compared in figure 3a for a given streamwise step, $\Delta R = 10$. The absolute error of the phase shown in figure 3b is less than 0.1 degrees except close to the outlet of the domain.

4.2. *Sensitivity to wall disturbances.*

In figures 4, 5 and 6 the modulus of the gradient for inhomogeneous wall boundary conditions are shown for three different Mach numbers M and spanwise wavenumbers β. As can be seen in there, the maximum value of the gradient is achieved if forcing is situated close to branch I of the neutral stability curve. This is in agreement with receptivity studies of *e.g.* Hill (1995), Airiau, Walther and Bottaro (2001) and Airiau (2000). In Airiau *et al.* the wall gradients were interpreted as wall Green's functions. One should note that
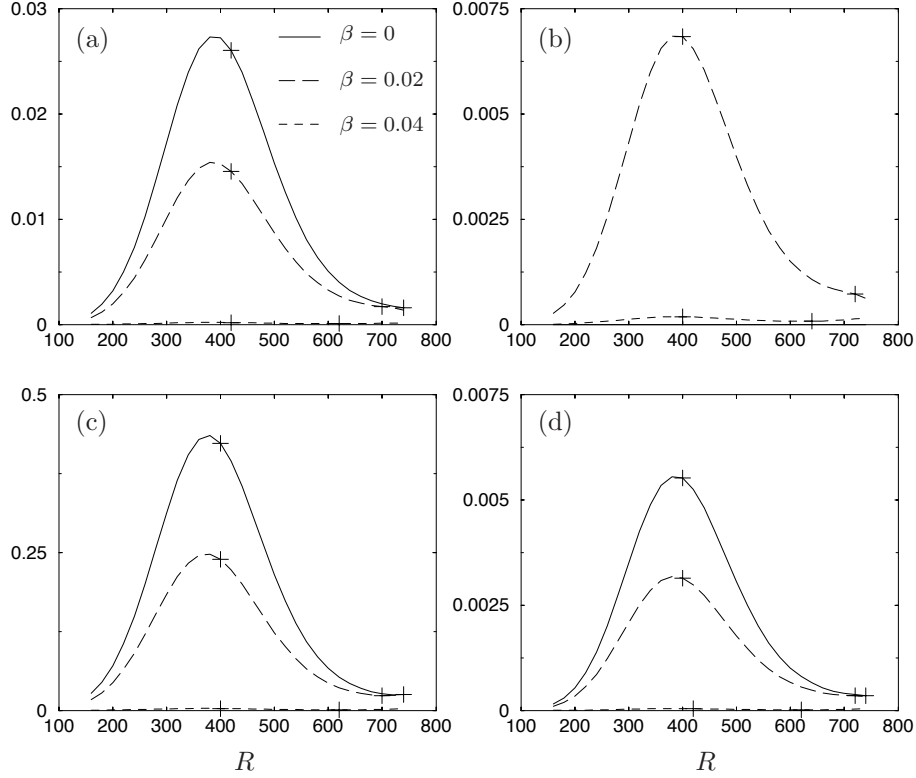
FIGURE 4. Modulus of the gradients due to 2D and 3D wall disturbances as a function of the Reynolds number for a Mach number $M = 0$. a) $|\nabla_{\tilde{u}_w}J|$, streamwise velocity component; b) $|\nabla_{\tilde{v}_w}J|$ spanwise velocity component; c) $|\nabla_{\tilde{w}_w}J|$ normal velocity component; d) $|\nabla_{\tilde{T}_w}J|$ temperature component.

the distance between the maximum value of the gradient and Branch I of the neutral stability curve depends on the Mach number and the input parameter. Branch I and branch II are marked on each curve in the figures with + signs. For low Mach numbers, the two-dimensional waves, $\beta = 0$, give the largest value of the gradient for wall-disturbance components $\tilde{u}, \tilde{v}, \tilde{w}$ and $\tilde{T}$. This can be seen for $M = 0$ and $M = 0.7$ in figures 4 and 5, respectively. As is shown in figure 6, where $M = 1.2$, it is clear that for higher Mach numbers the two-dimensional waves do not have the largest gradient. This observation follows the fact that in compressible boundary layers the three-dimensional disturbances are the most unstable ones (see *e.g.* Mack 1984). The magnitude of the gradient is quite different comparing $\tilde{u}, \tilde{v}, \tilde{w}$ and $\tilde{T}$ in figures 4, 5 and 6. It was noted that the normal velocity component gave the largest gradient for various spanwise wavenumber at Mach numbers between 0 and 1.2. The
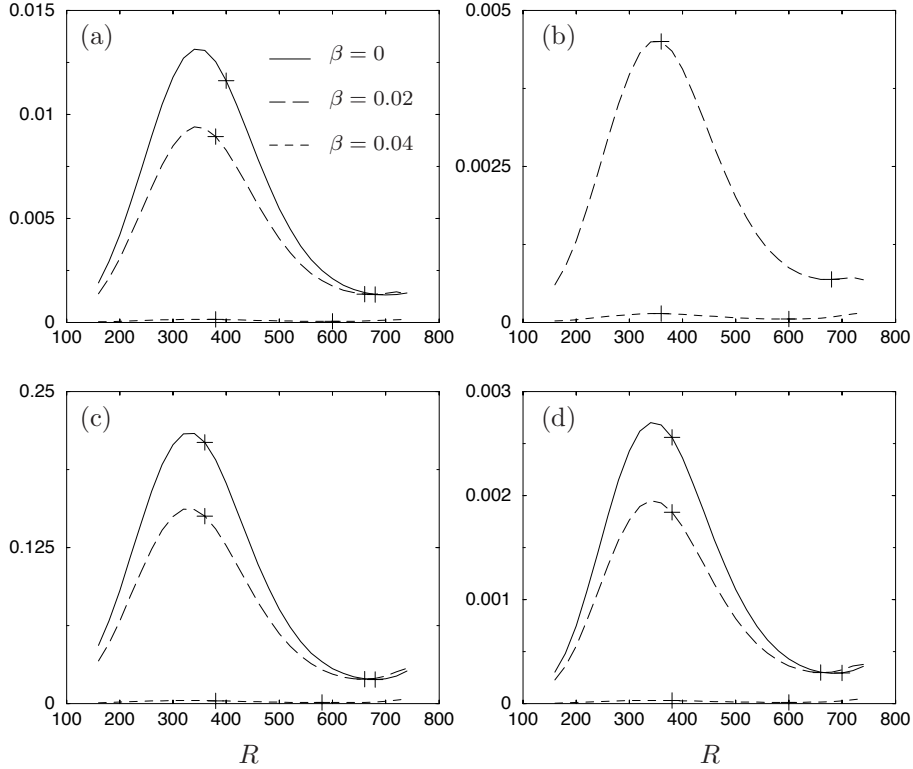
FIGURE 5. Modulus of the gradients due to 2D and 3D wall disturbances as a function of the Reynolds number for a Mach number $M = 0.7$. a) $|\nabla_{\tilde{u}_w} J|$, streamwise velocity component; b) $|\nabla_{\tilde{v}_w} J|$ spanwise velocity component; c) $|\nabla_{\tilde{w}_w} J|$ normal velocity component; d) $|\nabla_{\tilde{T}_w} J|$ temperature component.

response to the wall normal velocity component was one order of magnitude larger than the streamwise and spanwise velocity components. In cases studied here, the normal component is about 15 times that of the streamwise component. This implies that blowing and suction at the wall is the most efficient mean of controlling the instability waves. However, as is shown in the figures, the maximum response to a wall disturbance decreases as the Mach number increases. This means that the efficiency of blowing and suction for control of disturbance growth decreases at higher Mach numbers.

4.3. *Sensitivity to momentum sources.*

In figure 7 the modulus of the gradients for the streamwise and normal momentum forcing are plotted. The Mach number and spanwise wavenumber are both zero in this case. However, the qualitative behavior does not change for higher Mach numbers up to 1.2, and spanwise wavenumbers of 0, 0.02 and
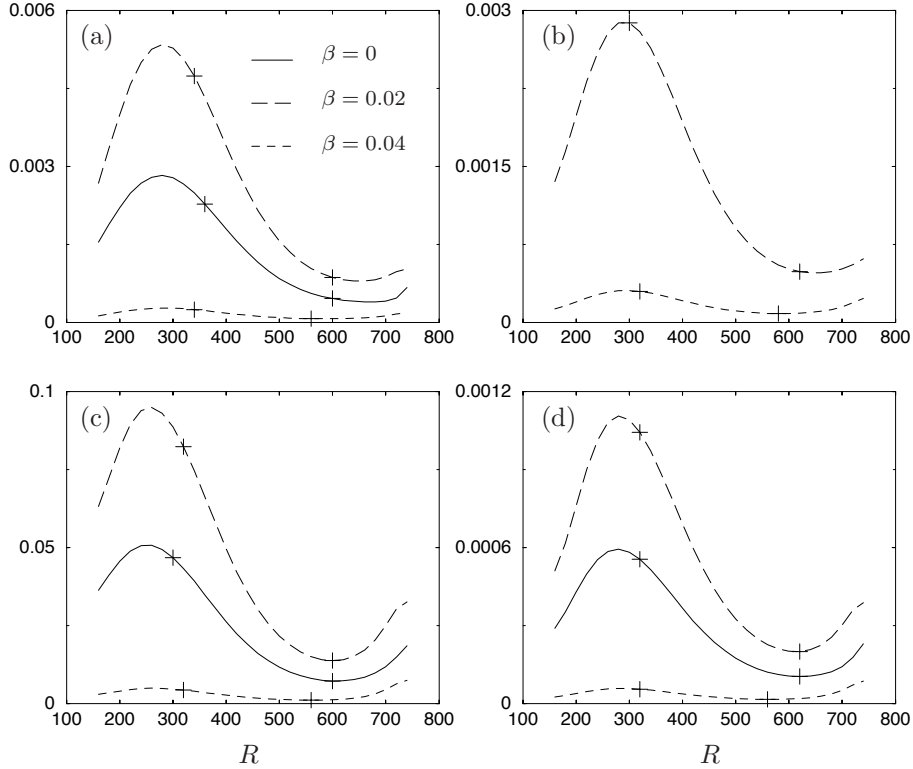
FIGURE 6. Modulus of the gradients due to 2D and 3D wall disturbances as a function of the Reynolds number for a Mach number $M = 1.2$. a) $|\nabla_{\tilde{u}_\mathrm{w}} J|$, streamwise velocity component; b) $|\nabla_{\tilde{v}_\mathrm{w}} J|$ spanwise velocity component; c) $|\nabla_{\tilde{w}_\mathrm{w}} J|$ normal velocity component; d) $|\nabla_{\tilde{T}_\mathrm{w}} J|$ temperature component.

0.04 which were studied here. A first observation is that the gradient for the streamwise component of a source of momentum $|\nabla_{\tilde{\mathcal{S}}_u} J|$ is about 10 times that of the normal component. Further, the maximum value of $|\nabla_{\tilde{\mathcal{S}}_u} J|$ is located near branch I of the neutral stability curve. It was noted by *e.g.* Hill (1995) that forcing most effectively is done in the vicinity of the critical layer, *i.e.* where the streamwise velocity $U(x, y) = \omega/\mathtt{Real}\{\alpha\}$. This was also found in our analysis. The location of the critical layer is marked with a line in figure 7a.

5. Conclusions

The Adjoint Parabolized Stability Equations (APSE) have been derived for quasi three-dimensional compressible flow using an input/output framework. The equations are given for an orthogonal curvilinear coordinate system. The
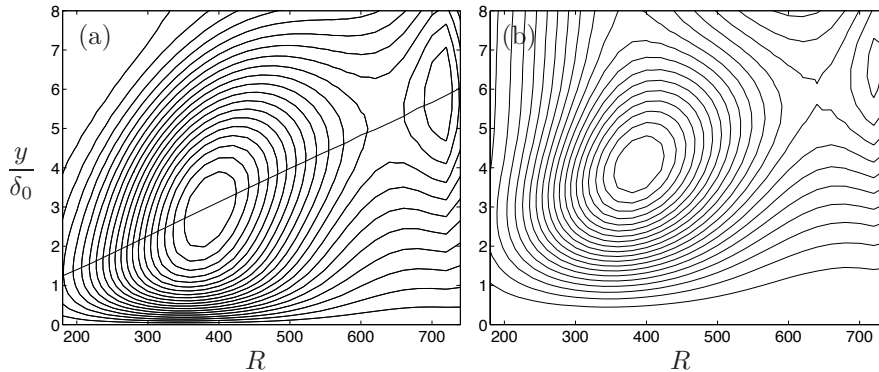
FIGURE 7. Contour plot of the gradients for momentum forcing. δ_0 denotes the boundary-layer thickness at streamwise position $x^1 = X_0$. $F = 10^{-4}$, $M = 0.7$, $\beta = 0$. The line in a) shows the position of the critical layer. a) $|\nabla_{\tilde{\mathcal{S}}_u} J|$, streamwise component with maximum = 1.8. Branch locations: I at $R \approx 400$, II at $R \approx 680$. b) $|\nabla_{\tilde{\mathcal{S}}_w} J|$, normal component with maximum = 0.16. Branch locations: I at $R \approx 360$, II at $R \approx 680$.

adjoint field gives the sensitivity of disturbances to changes in boundary conditions and momentum forcing. These equations provide a basis for optimal control of disturbance growth using unsteady wall perturbation or unsteady momentum forcing.

In the present formulation, the sensitivity of the objective function (output) to all control parameters (input) is found by solving the state equations and their adjoint once. This will drastically reduce the computational costs in an optimal design procedure.

The accuracy of the gradients have been verified by comparing the gradients derived by the adjoint equations with a finite-difference approach. It was shown that as the streamwise resolution is increased the differences between these two methods decrease and the solution of the gradient converges.

Analysis of two-dimensional boundary layers shows that a given disturbance is most sensitive to wall- and momentum forcing close to branch I of the neutral stability curve. The streamwise distance between the maximum of sensitivity and Branch I depends on the input component. This was found to be true for $0 \leqslant M \leqslant 1.2$ studied here. We also found that the response to the inhomogeneities of normal velocity at the wall is at least one order of magnitude larger than those of other the velocity components and temperature. This is in agreement with Hill (1995) for incompressible flow.

For incompressible flows, it has been shown that the two-dimensional disturbances are the most sensitive ones to wall inhomogeneity. However, for compressible flows, the three-dimensional disturbances are the most sensitive ones.

Further, it has been observed that momentum forcing is most effectively done in the vicinity of the critical layer, which has earlier been shown by Hill for incompressible boundary layer.

The results shown here are obtained with an objective function solely defined by the terminal energy. If instead the disturbance energy over the entire domain is used then the peak of the gradient would probably move another streamwise position. Further, if the cost of the control energy is added to the objective function as $J = E + \epsilon E_c$ then the results will most certainly change. One point that has to be made clear when adding the control energy is that the goal is not just to find the gradient for the disturbance energy but also for the control energy used. In the simple case shown in this article it turns out that the gradient appear to be similar to well known stability results, however what will happen in the other cases described above is left for future investigations.

Appendix A. The non-local stability equations

A.1. *Governing equations and assumptions*

A model of convectively unstable waves with curved or divergent wave-rays in a non-uniform flow is described here. The equations are derived from the equations of conservation of mass, momentum and energy and the equation of state governing the flow of a viscous, compressible, ideal gas expressed in primitive variables and curvilinear coordinates. The non-dimensional conservation equations in vector notation are given by

$$\rho\left[\frac{\partial \mathbf{u}}{\partial t} + (\mathbf{u} \cdot \nabla)\mathbf{u}\right] = -\nabla p + \frac{1}{R}\nabla[\lambda(\nabla \cdot \mathbf{u})] + \frac{1}{R}\nabla \cdot [\mu(\nabla\mathbf{u} + \nabla\mathbf{u}^T)], \quad (15)$$

$$\frac{\partial \rho}{\partial t} + \nabla \cdot (\rho\mathbf{u}) = 0, \quad (16)$$

$$\rho c_p\left[\frac{\partial T}{\partial t} + (\mathbf{u} \cdot \nabla)T\right] = \frac{1}{R\,\mathrm{Pr}}\nabla \cdot (\kappa\nabla T) + (\gamma - 1)M^2\left[\frac{\partial p}{\partial t} + (\mathbf{u} \cdot \nabla)p + \frac{1}{R}\Phi\right], \ (17)$$

$$\gamma M^2 p = \rho T, \quad (18)$$

with viscous dissipation given as

$$\Phi = \lambda(\nabla \cdot \mathbf{u})^2 + \frac{1}{2}\mu[\nabla\mathbf{u} + \nabla\mathbf{u}^T]^2.$$

Here t represents time, ρ, p, T stand for density, pressure and temperature, $\mathbf{u}$ is the velocity vector. The quantities λ, μ stand for the second and dynamic viscosity coefficient, γ is the ratio of specific heats, κ the heat conductivity, c_p the specific heat at constant pressure. All flow quantities are made non-dimensional by corresponding reference flow quantities at a fixed streamwise

position $x_0^\star$, except the pressure which is referred to twice the corresponding dynamic pressure. The reference length scale is fixed and taken as

$$l_0^\star = \sqrt{\frac{\nu_0^\star x_0^\star}{U_0^\star}}.$$

The Mach number, M, Prandtl number, Pr and Reynolds number, R are defined as

$$M = \frac{U_0^\star}{\sqrt{\Re \gamma T_0^\star}}, \quad \mathrm{Pr} = \frac{\mu_0^\star c_{p0}^\star}{\kappa_0^\star}, \quad R = \frac{U_0^\star l_0^\star}{\nu_0^\star},$$

where $\Re$ is the specific heat constant and superscript * refers to dimensional quantities.

We decompose the flow and material quantities into a mean flow part Q and a disturbance $\tilde{q}$ as $Q_{tot}(x^i, t) = Q(x^i) + \tilde{q}(x^i, t)$ where x^1, x^2 and x^3 are the streamwise, spanwise and wall normal components respectively. Here $Q \in [U, V, W, p, T, \rho]$ and $\tilde{q} \in [\tilde{u}, \tilde{v}, \tilde{w}, \tilde{p}, \tilde{T}, \tilde{\rho}]$, where U, V, W are the streamwise, spanwise and wall normal components of the mean velocity vector, respectively. u, v, w are those of the perturbation velocity vector. The domain considered is defined as $x^1 \in [X_0, X_1]$, $x^2 \in [Z_0, Z_1]$ and $x^3 \in [0, \infty[$. To simplify the analysis the mean flow is considered to be independent of the spanwise coordinate x^2. Two assumptions are made to derive the non-local stability equations. The first is of WKB type where the disturbance $\tilde{q}$ is divided into an amplitude function and a wave function

$$\tilde{q}(x^i, t) = \hat{q}(x^1, x^3)\Theta, \quad \Theta = \exp\, i\,\left(\int_{X_0}^{x^1} \alpha(x')dx' + \beta x^2 - \omega t\right).$$

Here α is a complex wavenumber, β the real spanwise wavenumber and ω the real angular wave frequency. The second assumption is a scale separation $1/R$ between the weak variation in the x^1 direction and the strong variation in the x^3 direction analogous to the multiple scales method. We assume

$$\frac{\partial}{\partial x^1} \sim \mathcal{O}(R^{-1}), \quad W \sim \mathcal{O}(R^{-1})$$

Furthermore, it is assumed that the metrics are of order $\mathcal{O}(R^{-1})$.

A.2. *The linear non-local stability equations*

The non-local stability equations are derived using Parabolized Stability Equation approach (PSE). We consider a general case where the boundary layer is subjected to sources of mass, momenta and energy, $\tilde{\mathcal{S}}$, and inhomogeneous boundary conditions on the wall. The linearized disturbance equations are obtained by introducing the variable decomposition into the governing equations (15)-(18), subtracting the equations for the mean flow and removing the products of disturbances. We proceed with the derivation of the stability equations by introducing the scaling relations given in section A.1. Finally, collecting terms up to order $\mathcal{O}(R^{-1})$ gives a set of nearly parabolic partial differential equations. A note on the parabolic nature of PSE can be found in *e.g.* Li and

Malik (1996), and Andersson, Henningson and Hanifi (1998). The equation can now be written

$$\hat{\mathcal{L}}\,\hat{\phi}(x^1, x^3) = \hat{\mathcal{S}}(x^1, x^3) \tag{19}$$

where the vector of the amplitude functions is $\hat{\phi} = (\hat{\rho}, \hat{u}, \hat{v}, \hat{w}, \hat{T})^{\mathrm{T}}$. The boundary conditions are

$$\begin{aligned}
\hat{\mathbf{u}}(x^1, 0) &= \hat{\mathbf{u}}_{\mathrm{w}}(x^1), \quad \hat{T}(x^1, 0) = \hat{T}_{\mathrm{w}}(x^1), \\
\lim_{x^3 \to \infty} \hat{\mathbf{u}} &= 0 \quad \text{and} \quad \lim_{x^3 \to \infty} \hat{T} = 0.
\end{aligned} \tag{20}$$

The operator $\hat{\mathcal{L}}$ is defined as

$$\hat{\mathcal{L}} = \mathcal{A} + \mathcal{B}D_3 + \mathcal{C}D_{33} + \mathcal{D}D_1 \tag{21}$$

where

$$D_i = \frac{1}{h_i}\frac{\partial}{\partial x^i}, \qquad D_{ii} = \frac{1}{h_i^2}\frac{\partial^2}{(\partial x^i)^2}.$$

Here, h_i is the scale factor such that a length element is defined as $ds^2 = (h_1 dx^1)^2 + (h_2 dx^2)^2 + (h_3 dx^3)^2$. The coefficients of the 5×5 matrices $\mathcal{A}$, $\mathcal{B}$, $\mathcal{C}$ and $\mathcal{D}$ can be found in appendix Appendix C. Furthermore, as both the amplitude function and the wave function depend on the x^1 coordinate, this ambiguity is removed by specifying an auxiliary condition

$$\int_0^\infty \hat{\phi}^H \frac{\partial\hat{\phi}}{\partial x^1}\, h_2 h_3 dx^3 = 0, \tag{22}$$

where, superscript ^{H} denotes the transpose complex conjugate. This condition also guarantees that x^1-variation of the disturbance amplitude function remains small such that second streamwise derivatives are negligible.

Appendix B. Derivation of the gradient

The gradients are derived using the adjoint equations of the Parabolized Stability Equations. A discrete or a continuous formulation may be used. It was concluded by Högberg *et al.* (2000) that a continuous formulation is a good enough approximation if control is performed on a problem with a dominating instability. This type of analysis can be done with the PSE therefore a continuous approach is used in this paper.

B.1. *Inner product*

For a compact notation of the adjoint equations, we will use the *formal adjoint* $\mathcal{L}^*$ of the differential operator $\mathcal{L}$ defined by the relation

$$(\mathcal{L}^*\Psi^*, \Phi) = (\Psi^*, \mathcal{L}\Phi) + \text{ boundary terms,}$$

where the inner product $(\cdot, \cdot)$ is defined as

$$(\Phi, \Psi^*) = \int_{X_0}^{X_1}\int_{Z_0}^{Z_1}\int_0^{+\infty} \Phi^H\Psi^*\, h_1 h_2 h_3\, dx^3\, dx^2\, dx^1, \tag{23}$$

for $\mathbb{C}^n$-valued functions Φ and Ψ^*. Here, the superscript * stands for adjoint quantities.

B.2. *Derivation of adjoint equations*

At first, the equations (1), (19), (20) and (22) has to be differentiated with respect to the input variables $\hat{\mathbf{u}}_w, \hat{T}_w, \hat{\mathcal{S}}$ and the state variables α and ϕ

$$
\delta J = \texttt{Real} \left\{ \int_{Z_0}^{Z_1} \int_0^\infty |\Theta_1|^2 \hat{\phi}_1^H \mathcal{M} \delta\hat{\phi}_1 h_2 h_3 \; dx^3 \; dx^2 + \right.
$$
$$
\left. \int_{Z_0}^{Z_1} \int_0^\infty |\Theta_1|^2 \hat{\phi}_1^H \mathcal{M} \hat{\phi}_1 \; i \int_{X_0}^{X_1} \delta\alpha dx' \; h_2 h_3 \; dx^3 \; dx^2 \right\} \tag{24}
$$

$$
\begin{aligned}
\hat{\mathcal{L}} \, \delta\hat{\phi} - \delta\hat{\mathcal{S}} + \frac{\partial\hat{\mathcal{L}}}{\partial\alpha} \delta\alpha \, \hat{\phi} &= 0 & \text{in} \quad \Omega \\
\delta\phi_0 &= 0 & \text{on} \quad x^1 = X_0 \\
\delta\hat{\mathbf{u}}(x^1,0) &= \delta\hat{\mathbf{u}}_w(x^1) & \text{on} \quad x^3 = 0 \\
\delta\hat{\mathbf{u}} &\to 0 & \text{as} \quad x^3 \to \infty \\
\delta\hat{T}(x^1,0) &= \delta\hat{T}_w(x^1) & \text{on} \quad x^3 = 0 \\
\delta\hat{T} &\to 0 & \text{as} \quad x^3 \to \infty \\
\int_0^\infty (\delta\hat{\phi}^H \frac{\partial\hat{\phi}}{\partial x^1} + \hat{\phi}^H \frac{\partial\delta\hat{\phi}}{\partial x^1}) \, h_2 h_3 dx^3 &= 0 & \forall \quad x^1
\end{aligned} \tag{25}
$$

Note here that the variation of a disturbance ϕ results in the variation of both the amplitude function $\hat{\phi}$ and the streamwise wave-number α. A complex co-state vector $\phi^* = (\rho^*, u^*, v^*, w^*, T^*)^{\mathrm{T}}$ and complex function $r^*(x^1)$ are introduced. The adjoint equations are derived by taking the inner product of vector ϕ^* with the differentiated state equations, and r^* with the differentiated auxiliary condition according to the inner product (23). The complex conjugate of each term in the equation is added. Then, derivatives are removed from the differentiated variables in equation (26) using integration by parts. After

integrations, it yields (without complex conjugate for clarity)

$$(\phi^*, \ \hat{\mathcal{L}} \, \delta\hat{\phi} - \delta\hat{\mathcal{S}} + \frac{\partial\hat{\mathcal{L}}}{\partial\alpha} \delta\alpha \, \hat{\phi}) +$$

$$\int_{X_0}^{X_1} \int_{Z_0}^{Z_1} \bar{r}^* \int_0^{+\infty} [\delta\hat{\phi}^H D_1(\hat{\phi}) + \hat{\phi}^H D_1(\delta\hat{\phi})] \, h_1 h_2 h_3 dx^3 \, dx^2 \, dx^1 =$$

$$(\hat{\mathcal{L}}^*\phi^*, \delta\hat{\phi}) - (\phi^*, \delta\hat{\mathcal{S}}) -$$

$$\int_{X_0}^{X_1} \int_{Z_0}^{Z_1} \int_0^{+\infty} \frac{\partial}{\partial x^1}(\phi^{*H}\frac{\partial\hat{\mathcal{L}}}{\partial\alpha} \, \hat{\phi} \, h_1 h_2 h_3) \int_{X_0}^{x^1} \delta\alpha dx' \, dx^3 \, dx^2 \, dx^1 +$$

$$\int_{Z_0}^{Z_1} \int_0^{+\infty} \left[\phi^{*H}\frac{\partial\hat{\mathcal{L}}}{\partial\alpha} \, \hat{\phi} \, h_1 h_2 h_3 \int_{X_0}^{x^1} \delta\alpha dx'\right]_{X_0}^{X_1} dx^3 \, dx^2 +$$

$$\int_{Z_0}^{Z_1} \int_0^{+\infty} \left[\phi^{*H} \, \mathcal{D} \, \delta\hat{\phi} \, h_2 h_3\right]_{X_0}^{X_1} dx^3 \, dx^2 +$$

$$\int_{Z_0}^{Z_1} \int_{X_0}^{X_1} \left[\left\{\phi^{*H} \left(\mathcal{B} \, - \, (m_{13} + m_{23} - m_{33}) \, \mathcal{C} \, - \, D_3(\mathcal{C})\right) \delta\hat{\phi} \, + \right.\right.$$

$$\left.\left. -D_3(\phi^{*H}) \, \mathcal{C} \, \delta\hat{\phi} \, + \, \phi^{*H} \mathcal{C} \, D_3(\delta\hat{\phi})\right\} h_1 h_2 \, dx^2 \, dx^1\right]_0^{\infty} +$$

$$\int_{X_0}^{X_1} \int_{Z_0}^{Z_1} \int_0^{+\infty} \left(r^* D_1(\hat{\phi}^H) - D_1(\bar{r}^* \hat{\phi}^H) - \right.$$

$$\left. (m_{21} + m_{31})\bar{r}^* \hat{\phi}^H\right) \delta\hat{\phi} \, h_1 h_2 h_3 dx^3 \, dx^2 \, dx^1 +$$

$$\int_{Z_0}^{Z_1} \int_0^{+\infty} \left[h_2 h_3 \bar{r}^* \hat{\phi}^H \delta\hat{\phi}\right]_{X_0}^{X_1} dx^3 \, dx^2 = 0 \tag{26}$$

where

$$m_{ij} = \frac{1}{h_i h_j}\frac{\partial h_i}{\partial x^j}.$$

Terms of $\delta\alpha$ have also been integrated in equation (26) in order to identify from δJ the boundary terms at X_1. Collecting terms of $\delta\hat{\phi}$ leads to the adjoint equations

$$\hat{\mathcal{L}}^*\phi^* = -\left[\bar{r}^* D_1(\hat{\phi}) - D_1(r^*\hat{\phi}) - (m_{21} + m_{31}) \, r^*\hat{\phi}\right] \tag{27}$$

In order to remove the terms of $\delta\hat{\phi}$ in the equation (26) as $x^3 \to \infty$, the following homogeneous boundary conditions are chosen

$$\begin{array}{llll}
\mathbf{u}^*(x^1, 0) & = & 0 & \quad \text{and} \quad T^*(x^1, 0) & = & 0, \\
\lim_{x^3 \to \infty} \mathbf{u}^* & = & 0 & \quad \text{and} \quad \lim_{x^3 \to \infty} T^* & = & 0,
\end{array} \tag{28}$$

where $\mathbf{u}^* = (u^*, v^*, w^*)^{\mathrm{T}}$. Using the operator matrices of the forward problem, the adjoint operator $\hat{\mathcal{L}}^*$ can be identified

$$\hat{\mathcal{L}}^* = \tilde{\mathcal{A}} + \tilde{\mathcal{B}} \, D_3. + \tilde{\mathcal{C}} \, D_{33}. + \tilde{\mathcal{D}} \, D_1. \tag{29}$$

where $\tilde{\mathcal{A}}, \tilde{\mathcal{B}}, \tilde{\mathcal{C}}$ and $\tilde{\mathcal{D}}$ are

$$
\begin{aligned}
\tilde{\mathcal{A}} &= \mathcal{A}^H - D_3(\mathcal{B}^H) - (m_{13} + m_{23})\, \mathcal{B}^H + D_{33}(\mathcal{C}^H) \\
&+ 2\,(m_{13} + m_{23} - m_{33})\, D_3(\mathcal{C}^H) \\
&- D_1(\mathcal{D}^H) - (m_{21} + m_{31})\, \mathcal{D}^H \\
\tilde{\mathcal{B}} &= -\mathcal{B}^H + 2\, D_3(\mathcal{C}^H) + 2\,(m_{13} + m_{23} - m_{33})\, \mathcal{C}^H \\
\tilde{\mathcal{C}} &= \mathcal{C}^H \\
\tilde{\mathcal{D}} &= -\mathcal{D}^H,
\end{aligned}
$$

The system of equations (27) with corresponding boundary conditions (28) is parabolic in the streamwise direction and must be integrated upstream, from X_1 to X_0. The initial condition at X_1 is found by identifying δJ, equation (24), with the terms defined at X_1 in equation (26). Matching terms of $\delta\hat{\phi}$, and $\delta\alpha$ gives the following system of equations to solve for the initial condition for ϕ^* and r^*

$$
|\Theta_1|^2 \int_0^\infty \hat{\phi}_1^H \mathcal{M} \delta\hat{\phi}_1 h_2 h_3 \, dx^3 = \int_0^{+\infty} (\phi^{*H}\,\mathcal{D} + \bar{r}^*\,\hat{\phi}^H)\, \delta\hat{\phi}\, h_2 h_3 dx^3 \Big|_{X_1}
\tag{30}
$$

$$
i|\Theta_1|^2 \int_0^\infty \hat{\phi}_1^H \mathcal{M} \hat{\phi}_1 h_2 h_3 \, dx^3 = \int_0^{+\infty} \phi^{*H} \frac{\partial\hat{\mathcal{L}}}{\partial\alpha}\, \hat{\phi}\, h_1 h_2 h_3 \, dx^3 \Big|_{X_1}
$$

Solving the above equations gives the initial condition for the adjoint equations at X_1 as

$$
\phi_1^* = |\Theta_1|^2 \mathcal{D}^+ (\mathcal{M} - c_1 \mathcal{I}) \hat{\phi}_1, \qquad r_1^* = |\Theta_1|^2\, c_1,
$$

$$
\bar{c}_1 = \frac{\displaystyle\int_0^\infty (h_1 \hat{\phi}_1^H \mathcal{M}\, D^{+H} \frac{\partial\hat{\mathcal{L}}}{\partial\alpha} \hat{\phi}_1 - i\hat{\phi}_1^H \mathcal{M} \hat{\phi}_1)\, h_2 h_3 \, dx^3}{\displaystyle\int_0^\infty \hat{\phi}_1^H \mathcal{D}^{+H} \frac{\partial\hat{\mathcal{L}}}{\partial\alpha} \hat{\phi}_1\, h_1 h_2 h_3 \, dx^3},
\tag{31}
$$

where $\mathcal{D}^+ = (\mathcal{D}^H)^{-1}$. Since by definition $\delta\phi = 0$ at X_0, the remaining terms of equation (26) together with equation (24) can be written

$$
\delta J = \texttt{Real}\Bigg\{ \int_{X_0}^{X_1} \int_{Z_0}^{Z_1} \int_0^{+\infty} \phi^{*H} \delta\hat{\mathcal{S}}\, h_1 h_2 h_3 \, dx^3 \, dx^2 \, dx^1 +
$$

$$
\int_{X_0}^{X_1} \int_{Z_0}^{Z_1} \int_0^{+\infty} \frac{\partial}{\partial x^1} (\phi^{*H} \frac{\partial\hat{\mathcal{L}}}{\partial\alpha}\, \hat{\phi}\, h_1 h_2 h_3) \int_{X_0}^{x^1} \delta\alpha dx'\, dx^3 \, dx^2 \, dx^1 +
$$

$$
\int_{Z_0}^{Z_1} \int_{X_0}^{X_1} \Big\{ \phi^{*H} \Big[\mathcal{B} - (m_{13} + m_{23} - m_{33})\, \mathcal{C} - D_3(\mathcal{C}) \Big] \delta\hat{\phi} +
$$

$$
-D_3(\phi^{*H})\, \mathcal{C}\, \delta\hat{\phi} + \phi^{*H}\, \mathcal{C}\, D_3(\delta\hat{\phi}) \Big\}\, h_1 h_2 \, dx^2 \, dx^1 \Big|_{x^3=0} \Bigg\}
\tag{32}
$$

The gradient should be identified from the variation of $\tilde{\phi}$ and of $\tilde{\mathcal{S}}$. However in equation (32) the variation of the momentum source and wall boundary

condition is expressed in terms of $\hat{\phi}$ and $\hat{\mathcal{S}}$. The total variation of $\tilde{\phi}$ and $\tilde{\mathcal{S}}$ is written

$$\delta\tilde{\phi} = \delta\hat{\phi}\,\Theta + \tilde{\phi}\,i\int_{X_0}^{x^1}\delta\alpha dx' \,, \qquad \delta\tilde{\mathcal{S}} = \delta\hat{\mathcal{S}}\,\Theta + \tilde{\mathcal{S}}\,i\int_{X_0}^{x^1}\delta\alpha dx' \qquad (33)$$

From equation (33), $\delta\hat{\phi}$ and $\delta\hat{\mathcal{S}}$ are substituted into equation (32). The variation of the functional δJ with respect to the total variation of $\tilde{\phi}$ and $\tilde{\mathcal{S}}$ is now written

$$\delta J = \texttt{Real}\left\{\int_{X_0}^{X_1}\int_{Z_0}^{Z_1}\int_0^{+\infty}\frac{1}{\Theta}\phi^{*H}\delta\tilde{\mathcal{S}}\,h_1h_2h_3\,dx^3\,dx^2\,dx^1+\right.$$

$$\int_{X_0}^{X_1}\int_{Z_0}^{Z_1}h_1h_2\Big[-\frac{\kappa}{\Theta\,\mathrm{Pr}\,R}D_3(\bar{T}^*)\delta T + \frac{(\rho\bar{\rho}^*)}{\Theta}\delta\tilde{w}+$$

$$\left.\frac{\mu}{\Theta R}D_3(\bar{u}^*)\delta\tilde{u} + \frac{\mu}{\Theta R}D_3(\bar{v}^*)\delta\tilde{v}\right]\,dx^2\,dx^1\Big|_{x^3=0}-$$

$$\int_{X_0}^{X_1}\int_{Z_0}^{Z_1}\int_0^{+\infty}\frac{\partial}{\partial x^1}(\phi^{*H}\frac{\partial\hat{\mathcal{L}}}{\partial\alpha}\,\hat{\phi}\,h_1h_2h_3)\int_{X_0}^{x^1}\delta\alpha dx'\,dx^3\,dx^2\,dx^1+ \qquad (34)$$

$$\int_{X_0}^{X_1}\int_{Z_0}^{Z_1}\int_0^{+\infty}\phi^{*H}\hat{\mathcal{S}}\,h_1h_2h_3\,i\int_{X_0}^{x^1}\delta\alpha dx'dx^3\,dx^2\,dx^1+$$

$$\int_{X_0}^{X_1}\int_{Z_0}^{Z_1}h_1h_2\Big[-\frac{\kappa}{\mathrm{Pr}\,R}D_3(\bar{T}^*)\hat{T} + (\rho\bar{\rho}^*)\hat{w} + \frac{\mu}{R}D_3(\bar{u}^*)\hat{u}+$$

$$\left.\frac{\mu}{R}D_3(\bar{v}^*)\hat{v}\Big]\,i\int_{X_0}^{x^1}\delta\alpha dx'\,dx^2\,dx^1\Big|_{x^3=0}\right\}$$

In equation (34) the expression for the wall boundary terms have been expanded to clarify the dependence between each state variable and the adjoint quantities. In the derivation of the adjoint equations the co-state variable $r^*(x)$ has been used in order to incorporate the auxiliary condition. However, equation (27) gives a system with five equations and six co-state variables. Therefore, an additional equation is needed to close the system. Collecting the terms of $\delta\alpha$ in equation (34) provides an additional equation which must be satisfied for each position in x^1

$$\int_0^{+\infty}\frac{\partial}{\partial x^1}(\phi^{*H}\frac{\partial\hat{\mathcal{L}}}{\partial\alpha}\,\hat{\phi}\,h_1h_2h_3)\,dx^3 = i\int_0^{+\infty}\phi^{*H}\hat{\mathcal{S}}\,h_1h_2h_3\,dx^3+$$

$$i\,h_1h_2\Big[-\frac{\kappa}{\mathrm{Pr}\,R}D_3(\bar{T}^*)\hat{T} + (\rho\bar{\rho}^*)\hat{w} + \frac{\mu}{R}D_3(\bar{u}^*)\hat{u} + \frac{\mu}{R}D_3(\bar{v}^*)\hat{v}\Big]\Big|_{x^3=0} \qquad (35)$$

It is denoted 'adjoint auxiliary condition' and is solved with an iterative process for r^* in a similar manner that equation (22) is solved for the streamwise wavenumber α. The gradient of the functional ∇J, with respect to the momentum forcing and wall disturbances can now be identified from the remaining

terms of equation (34) as

$$\nabla_{\tilde{u}_{\mathrm{w}}}J = \frac{\mu}{\Theta R}D_3(u^*) \qquad \text{on} \quad x^3 = 0$$

$$\nabla_{\tilde{v}_{\mathrm{w}}}J = \frac{\mu}{\Theta R}D_3(v^*) \qquad \text{on} \quad x^3 = 0$$

$$\nabla_{\tilde{w}_{\mathrm{w}}}J = \frac{\rho\rho^*}{\bar{\Theta}} \qquad \text{on} \quad x^3 = 0 \qquad (36)$$

$$\nabla_{\tilde{T}_{\mathrm{w}}}J = -\frac{\kappa}{\bar{\Theta}\,\mathrm{Pr}\,R}D_3(T^*) \qquad \text{on} \quad x^3 = 0$$

$$\nabla_{\tilde{\mathcal{S}}}J = \frac{\phi^*}{\bar{\Theta}} \qquad \text{in} \quad \Omega$$

Appendix C. Operator matrices

The non-zero components of matrices $\mathcal{A}, \mathcal{B}, \mathcal{C}$ and $\mathcal{D}$ in equation (21) are

$$a(1,1) = U(m_{31} + m_{21}) + D_3(W) + D_1(U) + i\xi$$

$$a(1,2) = \rho(i\alpha_0 + m_{31} + m_{21}) + D_1(\rho)$$

$$a(1,3) = i\beta_0\rho$$

$$a(1,4) = \rho(m_{13} + m_{23}) + D_3(\rho)$$

$$a(2,1) = \frac{1}{\gamma M^2}(D_1(T) + i\alpha_0 T) + D_1(U)U + D_3(U)W - m_{21}V^2$$

$$a(2,2) = \rho(D_1(U) + i\xi) + \frac{\mu}{R}(\alpha_0^2 l_2 + \beta_0^2)$$

$$a(2,3) = -2\rho m_{21}V + \frac{\mu}{R}\alpha_0\beta_0 l_1$$

$$a(2,4) = \rho(m_{13}U + D_3(U)) - \frac{i\alpha_0}{R}\frac{d\mu}{dT}D_3(T)$$

$$a(2,5) = \frac{1}{\gamma M^2}(D_1(\rho) + i\rho\alpha_0) + \frac{1}{R}(-\frac{d\mu}{dT}D_{33}(U) - D_3(U)\frac{d^2\mu}{dT^2}D_3(T))$$

$$a(3,1) = U(m_{21}V + D_1(V)) + D_3(V)W + \frac{i\beta_0}{\gamma M^2}T$$

$$a(3,2) = \rho(m_{21}V + D_1(V)) + \frac{\mu}{R}\alpha_0\beta_0 l_1$$

$$a(3,3) = \rho(m_{21}U + i\xi) + \frac{\mu}{R}(\beta_0^2 l_2 + \alpha_0^2)$$

$$a(3,4) = \rho(m_{23}V + D_3(V)) - \frac{i\beta_0}{R}\frac{d\mu}{dT}D_3(T)$$

$$a(3,5) = \frac{i\beta_0}{\gamma M^2}\rho + \frac{1}{R}(-\frac{d\mu}{dT}D_{33}(V) - D_3(V)\frac{d^2\mu}{dT^2}D_3(T))$$

$$a(4,1) = \frac{1}{\gamma M^2}D_3(T) - m_{13}U^2 - m_{23}V^2 + \frac{i\mu}{R}\frac{l_2}{\rho}(\beta_0 D_3(V) + \alpha_0 D_3(U))$$

$$a(4,2) \;=\; -2\rho m_{13} U - \frac{i\alpha_0}{R} l_0 \frac{d\mu}{dT} D_3(T) + \frac{D_3(\rho)}{\rho} \frac{i\alpha_0}{R} \mu l_2$$

$$a(4,3) \;=\; -2\rho m_{23} V - \frac{i\beta_0}{R} l_0 \frac{d\mu}{dT} D_3(T) + \frac{D_3(\rho)}{\rho} \frac{i\beta_0}{R} \mu l_2$$

$$a(4,4) \;=\; \rho(D_3(W) + m_{31} U + i\xi) + \frac{1}{R}\mu(\beta_0^2 + \alpha_0^2) + \frac{D_{33}(\rho)}{\rho} \frac{\mu}{R} l_2$$

$$a(4,5) \;=\; \frac{1}{\gamma M^2} D_3(\rho) + \frac{1}{R} \frac{d\mu}{dT} i(-\beta_0 D_3(V) - D_3(U)\alpha_0)$$

$$a(5,1) \;=\; \frac{(\gamma-1)}{\gamma}(U D_1(T) + W D_3(T) + iT\xi) + c_p(-W D_3(T) - U D_1(T))$$

$$a(5,2) \;=\; (\gamma-1)M^2 D_1(p) - \rho c_p D_1(T)$$

$$a(5,4) \;=\; (\gamma-1)M^2 \left[D_3(p) + \frac{2i\mu}{R}(\beta_0 D_3(V) + D_3(U)\alpha_0) \right] - \rho c_p D_3(T)$$

$$a(5,5) \;=\; \rho \left\{ \frac{dc_p}{dT}(-W D_3(T) - U D_1(T)) + i\left[\frac{(\gamma-1)}{\gamma} - c_p\right]\xi \right\} +$$
$$\frac{1}{R\,\mathrm{Pr}} \left[\frac{d\kappa}{dT} D_{33}(T) + \frac{d^2\kappa}{dT^2}(D_3(T))^2 + \kappa(-\beta_0^2 - \alpha_0^2) \right] +$$
$$\frac{(\gamma-1)}{R} \frac{d\mu}{dT} M^2 \left[(D_3(U))^2 + (D_3(V))^2 \right] +$$
$$\frac{(\gamma-1)}{\gamma}(U D_1(\rho) + W D_3(\rho))$$

$$b(1,1) \;=\; W$$

$$b(1,4) \;=\; \rho$$

$$b(2,2) \;=\; \rho W - \frac{1}{R} \frac{d\mu}{dT} D_3(T)$$

$$b(2,4) \;=\; -\frac{i\mu}{R}\alpha_0 l_1$$

$$b(2,5) \;=\; -\frac{1}{R} D_3(U) \frac{d\mu}{dT}$$

$$b(3,3) \;=\; \rho W - \frac{1}{R} \frac{d\mu}{dT} D_3(T)$$

$$b(3,4) \;=\; -\frac{i\mu}{R}\beta_0 l_1$$

$$b(3,5) \;=\; -\frac{1}{R} D_3(V) \frac{d\mu}{dT}$$

$$b(4,1) \;=\; \frac{1}{\gamma M^2} T + \frac{i\mu}{R} \frac{l_2}{\rho} \xi$$

$$b(4,2) \;=\; \frac{i\mu}{R}\alpha_0$$

$$b(4,3) \;=\; \frac{i\mu}{R}\beta_0$$

$$b(4,4) = \rho W + \frac{l_2}{R}\left(2\mu\frac{D_3(\rho)}{\rho} - \frac{d\mu}{dT}D_3(T)\right)$$

$$b(4,5) = \frac{1}{\gamma M^2}\rho$$

$$b(5,1) = \frac{(\gamma-1)}{\gamma}WT$$

$$b(5,2) = 2(\gamma-1)M^2\frac{\mu}{R}D_3(U)$$

$$b(5,3) = 2(\gamma-1)M^2\frac{\mu}{R}D_3(V)$$

$$b(5,5) = \rho W\left[\frac{(\gamma-1)}{\gamma} - c_p\right] + \frac{2}{R\,\mathrm{Pr}}\frac{d\kappa}{dT}D_3(T)$$

$$c(2,2) = -\frac{\mu}{R}$$

$$c(3,3) = -\frac{\mu}{R}$$

$$c(5,5) = \frac{\kappa}{R\,\mathrm{Pr}}$$

$$d(1,1) = U$$

$$d(1,2) = \rho$$

$$d(2,1) = \frac{T}{\gamma M^2}$$

$$d(2,2) = \rho U$$

$$d(2,5) = \frac{\rho}{\gamma M^2}$$

$$d(3,3) = \rho U$$

$$d(4,4) = \rho U$$

$$d(5,1) = \frac{(\gamma-1)}{\gamma}UT$$

$$d(5,5) = \rho U\left[\frac{(\gamma-1)}{\gamma} - c_p\right]$$

where

$$D_i = \frac{1}{h_i}\frac{\partial}{\partial x^i}, \quad D_{ij} = \frac{1}{h_i h_j}\frac{\partial^2}{\partial x^i \partial x^j}, \quad \alpha_0 = \frac{\alpha}{h_1}, \quad \beta_0 = \frac{\beta}{h_2}, \quad l_j = \frac{\lambda}{\mu} + j,$$

and

$$\xi = (\alpha_0 U + \beta_0 V - \omega).$$

References

Airiau, C. 2000. 'Non-parallel acoustic receptivity of a Blasius boundary layer using an adjoint approach.' *to appear in Flow, Turbulence and Combustion.*

Airiau, C., Walther, S., Bottaro, A. 1999. 'Non-parallel receptivity and the adjoint PSE.' to appear in *IUTAM Symposium on Laminar-Turbulent Transition (September 1999, Sedona, AZ), Fasel, H. and Saric, W., eds. Springer.*

Andersson, P., Berggren, M. and Henningson, D.S. 1999. 'Optimal disturbances and bypass transition in boundary layer.' *Phys. Fluids*, **11**, pp. 134–150.

Andersson, P., Henningson, D.S. and Hanifi, A. 1998. 'On a stabilization procedure for the parabolic stability equations.' *J. Eng. Math.*, **33**, pp. 311–332.

Bewley, T.R., Temam, R. and Ziane, M. 2000. 'A general framework for robust control in fluid mechanics.' *Physica D*, **138**, pp. 360–392.

Bertolotti, F.P., Herbert, Th. and Spalart, S.P. 1992. 'Linear and Nonlinear Stability of the Blasius Boundary Layer.' *J. Fluid Mech.*, **242**, pp. 441–474.

Cathalifaud, P. and Luchini, P. 2000. 'Algebraic growth in a boundary layer: optimal control by blowing and suction at the wall.' *Eur. J. Mech. B/Fluids*, **19**(4), pp. 469–490

Choudhari, M. and Street, C.L. 1992. 'A finite reynolds-number approach for the prediction of boundary-layer receptivity in localized regions.' *Phys. Fluids A*, **4**, pp. 2495–2514.

Corke, T.C., Bar-Sever, A. and Morkovin, M.V. 1986. 'Experiments on transition enhancement by distributed roughness.' *Phys. Fluids.* **29**, pp. 3199–3213.

Crouch, J.D. 1992a. 'Localized receptivity of boundary layers.' *Phys. Fluids A* **4**, pp. 1408–1414.

Crouch, J.D. 1992b. 'Non-localized receptivity of boundary layers.' *J. Fluid Mech.* **244**, pp. 567–581.

Goldstein, M.E. 1983. 'The evolution of Tollmien-Schlichting waves near the leading edge.' *J. Fluid Mech.* **127**, pp. 59–81.

Goldstein, M.E. and Hultgren, L.S. 1989. 'Boundary-layer receptivity to long-wave free-stream disturbances.' *Ann. Rev. Fluid Mech.*, **21**, pp. 137–166.

Gunzburger, M. 2000. 'Adjoint equation-based methods for control problems in incompressible, viscous flows.' *in press in Flow, Turbulence and Combustion.*

Hall, M. C. G. 1986. 'Application of Adjoint Sensitivity Theory to an Atmospheric General Circulation Model.' *J. The Atmospheric Sci.* **43**, pp. 2644–2651.

Hanifi, A., Henningson, D.s., Hein, S., Bertolotti, F.P. and Simen, M. 1994. 'Linear Non-local Instability Analysis - the linear NOLOT code.' *FFA TN* 1994-54, See also Hein et al. 1994.

Hanifi, A. and Schmid, P.J., Henningson, D.S. 1996. 'Transient growth in compressible boundary layer flow' *Phys. Fluids* **8**(3), pp. 826–837.

Hein, S., Bertolotti, F.P., Simen, M., Hanifi, A. and Henningson, D.S. 1994. 'Linear Non-local Instability Analysis - the linear NOLOT code.' *DLR-IB* 223-94 A 43.

Herbert, Th. 1994. 'Parabolized Stability Equations.' *AGARD Report* No. 793, pp. 4-1–4-34.

Hill, D. C. 1995. 'Adjoint Systems and their role in the Receptivity Problem for Boundary Layers.' *J. Fluid Mech.* **292**, pp. 183–204.

Hill, D. C. 1997. 'Receptivity in non-parallel boundary layers.' *ASME Fluids Engineering Division Summer Meeting, FEDSM '97, June 22-26, 1997.*

Högberg, M. and Berggren, M. 2000. 'Numerical approaches to optimal control

of a model equation for shear flow instabilities. *, Submitted to Journal of Flow, Turbulence and Combustion.*

LI, F. AND MALIK, M.R. 1996 'On the Nature of PSE Approximation.' *Theoretical and Computational Fluid Dynamics* No.**8**, pp. 253–273.

LUCHINI, P. AND BOTTARO, A. 1998 'Görtler vortices : a backward-in-time approach to the receptivity problem.' *J. Fluid Mech.*, **363**, pp. 1–23.

LUCHINI, P. 2000 'Reynolds-number-independent instability of the boundarylayer over a flat surface: optimal perturbations.' *J. Fluid Mech.*, **404**, pp. 289–309.

MACK, L.M. 1984 'Boundary-layer stability theory.' *AGARD Report* No. 709, pp. 3-1–3-81.

NISHIOKA, M. AND MORKOVIN, M.V. 1986. 'Boundary-layer receptivity to unsteady pressure gradients : experiments and overview.' *J. Fluid Mech.* **171**, pp. 219–261.

PRALITS, J.O., HANIFI, A. AND HENNINGSON, D.S. 2000. 'Adjoint-based suction optimization for 3D boundary layer flows' *FFA TN* 2000-58.

SARIC, W.S. 1993. 'Physical description of boundary-layer transition : experimental evidence' *AGARD report* **793**, pp. 183–204.

SIMEN, M. 1992. 'Local and Nonlocal Stability Theory of Spatially Varying Flows.' *Instability, Transition and Turbulence*, Springer Verlag, pp. 181–201

THOMAS, A. 1983. 'The control of boundary-layer transition using a wave superposition principle.' *J. Fluid Mech.* **137**, pp.233–250.

TUMIN, A. 1996. 'Receptivity of Pipe Poiseuille Flow.' *J Fluid Mech.* **315**, pp. 119–137.

Paper 2

Adjoint-based optimization of steady suction for disturbance control in incompressible flows

By Jan O. Pralits[1,2], **Ardeshir Hanifi**[2],
and Dan S. Henningson[1,2]

The optimal distribution of steady suction needed to control the growth of single or multiple disturbances in quasi three-dimensional incompressible boundary layers on a flat plate is investigated. The evolution of disturbances is analyzed in the framework of the Parabolized Stability Equations (PSE). A gradient based optimization procedure is used and the gradients are evaluated using the adjoint of the parabolized stability equations (APSE) and the adjoint of the boundary layer equations (ABLE). The accuracy of the gradient is increased by introducing a stabilization procedure for the PSE. Results show that a suction peak appears in the upstream part of the suction region for optimal control of Tollmien-Schlichting (T-S) waves, steady streamwise streaks in a two-dimensional boundary layer and oblique waves in a quasi three-dimensional boundary layer subject to an adverse pressure gradient. The mean flow modifications due to suction are shown to have a stabilizing effect similar to that of a favorable pressure gradient. It is also shown that the optimal suction distribution for the disturbance of interest reduce the growth rate of other perturbations. Results for control of a steady cross-flow mode in a three-dimensional boundary layer subject to a favorable pressure gradient show that not even large amounts of suction manages to completely stabilize the disturbance.

1. Introduction

Laminar-turbulent transition in boundary layers on aircrafts causes a rapid increase of the skin friction and consequently a larger drag. Therefore, delay of transition occurrence will reduce the fuel consumption which results in a lower operation cost and less pollution. Transition in the boundary layer on aircraft wings is usually caused by break down of small disturbances which grow as they propagate down stream. It is well known that growth of such disturbances can be suppressed or controlled by steady- or unsteady wall-suction. The latter is sometimes referred to as the wave-cancellation concept and has been investigated both numerically and experimentally by numerous authors, see Joslin (1998) for an excellent overview of earlier experimental and numerical works.

[1]Department of Mechanics, KTH, SE-100 44 Stockholm, Sweden.
[2]Swedish Defence Research Agency, FOI, Aeronautics Division, FFA, SE-172 90 Stockholm, Sweden.

Steady suction implies that a modification of the steady mean flow is done. Here, the aim is to reduce the thickness of the boundary layer and to stabilize the mean velocity profile. The inviscid instability in two-dimensional boundary layers, which is related to the second wall-normal derivative of the streamwise velocity, is stabilized by suction. A similar stabilizing effect is obtained by imposing a favorable pressure gradient given zero suction on the wall. The relation between suction, the pressure gradient and the viscous terms in two-dimensional boundary layers is well explained in e. g. Schlichting (1979). The mean flow obtained using non-zero suction have similarities with those obtained when a negative pressure gradient is applied. In the case of an adverse pressure gradient present in the flow, the superposition of suction will reduce the curvature of the velocity profile at the wall, weakening the inflection in the profile which inhibits the inviscid instability. It should be noted that the discussion above relates primarily to exponential instabilities.

Constant steady suction has been studied both experimentally and numerically by several authors. Iglisch (1949) investigated theoretically the initial length needed for the shape factor (displacement thickness/momentum thickness) to reach a constant value in the case of a flat plate two-dimensional boundary layer. Here, the streamwise velocity profile becomes 'fuller' downstream as suction is applied finally reaching the so called 'asymptotic suction profile'. With the assumption of an asymptotic velocity profile present along the whole plate, the laminar boundary layer is stable with respect to two-dimensional T-S wave instabilities if the constant suction velocity $V_{\mathrm{w}} = V_{\mathrm{w}}^{\star}/U_{\infty}^{\star} = 1.4 \times 10^{-5}$. Here, $V_{\mathrm{w}}^{\star}$ and $U_{\infty}^{\star}$ are the dimensional wall-normal suction velocity at the wall and free-stream velocity components of the mean flow, respectively. For the same case, Ulrich (1944) showed that the critical Reynolds number, Re_{crit}, in fact decreases as one approaches the leading edge. Hence, an increasing amount of suction is required in this region. In Schlichting (1979) it was shown that a correction due to increased amount of suction close to the leading edge leads to a constant suction velocity $V_{\mathrm{w}} = 1.2 \times 10^{-4}$ in order to maintain a laminar flow along the whole plate. The increased suction velocity due to the correction of the initial length is an increased amount of suction energy. If a large amount of suction is applied then the power saved by the reduction in drag might well be lost by the power used for the suction device. Further, if a large amount of suction is used, resulting in a thinning of the boundary layer then this may lead to an increase of the shear stress at the wall. It is therefore of interest to investigate if a more optimal suction distribution can be obtained which meets the objective of reducing the disturbances present in the flow while using the least amount of suction energy.

In the last decade more interest has been focused on optimal control of fluid flows in which optimal control theory has been utilized in different manners. Here, the objective is to minimize some measure of the state with a prescribed amount of suction on the wall. This can mathematically be described by a minimization of an objective function which balances a measure of the state

and a measure of the control. The problem can be solved using the sensitivity information given by the gradient of the objective function with respect to the control in a gradient based optimization routine. An efficient way to calculate the gradients is the adjoint approach which has been shown successful in numerous applications such as shape optimization, optimal control, receptivity, meteorology and optimal perturbations as long as the number of constraints are low and the control-variable space is large. A recent workshop on adjoint systems, see *Flow, Turbulence and Combustion* 2000 Vol. 65 (3/4), indicate some of the progress in the field.

Here the wall-normal velocity component of the steady mean flow on the wall is used as the control, which means that the suction will modify the mean flow to control disturbance growth rather than generating an out-of phase disturbance by time periodic suction. Another investigation was done by Balakumar & Hall (1999) who used a Lagrangian approach to find the optimal suction distribution for Blasius and swept Hiemenz flows. The objective was to move the transition point, given by the e^N-method, downstream. They found that for Blasius boundary layers the optimal suction distribution peaked upstream of the maximum growth rate and decreases to zero at the transition point.

In the present work we use an approach different from that in Balakumar & Hall (1999). The control problem is defined using optimal control theory in which a gradient-based technique is used to update the control during the optimization process. The aim is to minimize a given objective function balancing a measure of the total disturbance kinetic energy and the control energy. The mean flow is found by solving the quasi three-dimensional boundary layer equations for incompressible flows and the growth of disturbances is analyzed for developing boundary layers using the PSE (see Bertolotti *et al.* 1992; Malik & Balakumar 1992; Simen 1992; Herbert 1997). In the frame work of these governing equations we can analyze convective instabilities under the assumption of a slow variation of both the mean flow and the shape function of the disturbances in the streamwise direction. We also assume that the streamwise pressure distribution is not affected by suction at the wall. The mean flow is obtained using the boundary layer equations (see eg. Schlichting 1979). In this approximation, as well as in higher order approximations, the wall normal velocity of the mean flow, V, is of order $O(1/Re)$. Here $Re = U_\infty^\star l^\star / \nu^\star$ is the Reynolds number in which $l^\star$ and $\nu^\star$ denotes the dimensional reference length and kinematic viscosity, respectively. In the optimization one must make sure that this assumption is not violated.

An adjoint-based technique is used to evaluate the gradients (sensitivities). Here, we couple the adjoint of the PSE with the adjoint of the boundary-layer equations in order to find the gradient of the disturbance growth due to modifications of the mean flow. The use of the adjoint PSE (APSE) was first proposed by Herbert (1997) and has then been used for receptivity studies (see Hill 1997a; Airiau 2000; Dobrinsky & Collis 2000), sensitivity analysis (see Pralits *et al.* 2000) and optimal control problems (see Hill 1997b; Pralits

et al. 2000*b*; Walther *et al.* 2001). Hill (1997b) used a similar approach in inverse design for laminar boundary layer. However, no details were given there. The common interest of all these applications lies in the efficient evaluation of receptivity-coefficients and sensitivity information provided by a single solution of the APSE. The major difference between previous works is found in the derivation of the APSE. In Hill (1997a,b); Airiau (2000); Dobrinsky & Collis (2000) the APSE is an approximation of the adjoint of the linearized Navier–Stokes equations given an ansatz similar to the PSE. The additional equation used to find the "adjoint" streamwise wave number comes from an orthogonality relation between the solutions from the APSE and PSE. In Dobrinsky & Collis (2000) it is shown that this condition in fact does not hold in a large part of the domain which means a less accurate result of the adjoint equations. The reason is said to depend on the numerical scheme and approximate inflow conditions. In Pralits *et al.* (2000) the APSE is derived directly from the PSE using a variational technique and the additional equation and inflow conditions are part of the definition of the adjoint operator. The latter technique, which is shown to have good accuracy in the major part of the domain, is also used in Pralits *et al.* (2000*b*) and Walther *et al.* (2001).

The optimization process is dependent on the accuracy of the gradient (search-direction), which can be evaluated to better assess the optimization results. In the present work, the gradient is derived from the continuous state equations which means that its accuracy can be improved if the resolution is increased, see e. g. Högberg & Berggren (2000). However, the PSE is known for its instability for small streamwise steps due to the remaining ellipticity. Several studies on how to stabilize the PSE have been done (see Haj-Hariri 1994; Li & Malik 1994, 1996; Andersson *et al.* 1998). The approach which best removes the ellipticity while still producing an accurate result is the technique introduced by Andersson *et al.* (1998), where originally neglected higher order terms, $O(Re^{-2})$, are reintroduced. This stabilization procedure will also affect the adjoint equations (see §2.4).

In this paper we present a method which involves solving a number of problems regarding the derivation of the gradient, adjoint equations and stabilization of the adjoint equations. For this reason, a large part of the paper is dedicated to explaining the different steps in detail. The optimal control problem and the corresponding equations are presented in §2. In §3, a validation of the adjoint equations is done by analyzing the gradient accuracy. Here we also show results on optimal control of steady streamwise streaks and T-S waves in a two-dimensional boundary layer, and oblique waves and a steady cross-flow mode in a quasi three-dimensional boundary layer. The discussion and concluding remarks are given in §4 and the complete derivation of the gradient and the coupling of the adjoint of the parabolized stability and boundary layer equations are shown in Appendix B. A preliminary version of the work presented here can be found in the report by Pralits *et al.* (2000*b*).

2. Problem formulation

This section presents the optimal control problem for incompressible flows. For simplicity, we restrict our analysis to a plane geometry.

2.1. *State equations*

The flow field is given by the solution of the mass and momentum conservation equations for a viscous flow. The equations are written for a Cartesian coordinate system with streamwise, normal and spanwise coordinates denoted as x, y and z, respectively. The flow field is decomposed into a mean, Q, and a perturbation part, q, as

$$Q_{tot}(x, y, z, t) = Q(x, y) + q(x, y, z, t)$$

where $Q = (U, V, W, P)^T$ and $q = (u, v, w, p)^T$. The mean flow, which has zero variation in the spanwise direction, is a three-component, two-dimensional boundary layer and is here referred to as a quasi three-dimensional boundary layer. The evolution of disturbances is analyzed in the framework of the nonlocal stability theory (see e. g. Bertolotti *et al.* 1992; Malik & Balakumar 1992; Simen 1992; Herbert 1997).

In the following sections the equations for the mean flow and disturbances, in non-dimensional form, are given. The velocity components are made non-dimensional by $U_\infty^\star$, the pressure by $\rho^\star U_\infty^{\star 2}$ and the reference length is taken as $l_0^\star = (\nu^\star x_0^\star / U_\infty^\star)^{\frac{1}{2}}$. Here superscript * denotes dimensional quantities, $\nu^\star$ the kinematic viscosity, $U_\infty^\star$ the free stream velocity and $\rho^\star$ the density.

2.1.1. *Mean flow equations*

The non-dimensional boundary layer equations for a quasi three-dimensional incompressible flow on a flat plate with an external pressure gradient given as $\mathrm{d}P_e/\mathrm{d}x = -U_e \mathrm{d}U_e/\mathrm{d}x$ can be written

$$\frac{\partial U}{\partial x} + \frac{\partial V}{\partial y} = 0, \tag{1}$$

$$U\frac{\partial U}{\partial x} + V\frac{\partial U}{\partial y} - U_e\frac{\mathrm{d}U_e}{\mathrm{d}x} - \frac{1}{Re}\frac{\partial^2 U}{\partial y^2} = 0, \tag{2}$$

$$U\frac{\partial W}{\partial x} + V\frac{\partial W}{\partial y} - \frac{1}{Re}\frac{\partial^2 W}{\partial y^2} = 0, \tag{3}$$

with the boundary conditions

$$U = W = 0, \ V = V_\mathrm{w} \qquad \text{on} \qquad y = 0,$$

$$(U, W) \rightarrow (U_e, W_e) \qquad \text{as} \qquad y \rightarrow \infty, \tag{4}$$

where index e denotes that the variable is evaluated at the boundary layer edge and $Re = l_0^\star U_\infty^\star / \nu^\star$ is the Reynolds number. Note that for the boundary layer approximations to be valid, the normal velocity at the wall, $V_\mathrm{w} = V_\mathrm{w}^\star / U_\infty^\star$, should be of order $O(Re^{-1})$.

2.1.2. *Disturbance equations*

We assume the perturbations to be time and spanwise periodic disturbances as

$$q(x, y, z, t) = \hat{q}(x, y) \exp \mathrm{i}\left(\int_{X_0}^{x'} \alpha \, \mathrm{d}x' + \beta z - \omega t\right) + \text{c.c.,} \tag{5}$$

where α is the complex streamwise wavenumber, β the real spanwise wavenumber and ω the real disturbance angular frequency. We assume a scale separation Re^{-1} between the weak variation in x-direction and the strong variation in the y-direction. It is also assumed that $\partial/\partial x \sim O(Re^{-1})$ and $V \sim O(Re^{-1})$. Introducing (5) and the assumptions above in the linearized governing equations and keeping terms up to order $O(Re^{-1})$, yield a set of nearly parabolic partial differential equations

$$A\hat{q} + B\frac{\partial \hat{q}}{\partial y} + C\frac{\partial^2 \hat{q}}{\partial y^2} + D\frac{\partial \hat{q}}{\partial x} = 0, \tag{6}$$

where the matrices A, B, C and D are given in Appendix A. For a note on the parabolic nature of the PSE see Bertolotti *et al.* (1992); Haj-Hariri (1994); Li & Malik (1994, 1996); Andersson *et al.* (1998). To remove the ambiguity of having x-dependence of both the amplitude function and wave function in (5) and to maintain a slow variation of the amplitude function $\hat{q}$, a so called 'auxiliary condition' is introduced

$$\int_0^\infty \hat{\mathbf{u}}^H \frac{\partial \hat{\mathbf{u}}}{\partial x} \, \mathrm{d}y = 0, \tag{7}$$

where $\hat{\mathbf{u}} = (\hat{u}, \hat{v}, \hat{w})^T$ and superscript ^{H} denotes the complex conjugate transpose. The disturbances are subjected to the following boundary conditions

$$\begin{aligned} \hat{\mathbf{u}} = 0 & \quad \text{on} \quad & y = 0 \\ \hat{\mathbf{u}} \to 0 & \quad \text{as} \quad & y \to \infty. \end{aligned} \tag{8}$$

The system of equations (6) and (7), is integrated in the downstream direction with the initial condition given by the solution of the local stability theory at $x = X_0$. At each streamwise position, the value of α is iterated such that (7) is satisfied.

2.2. *Optimal control of a single disturbance*

In this section, we define an optimal control problem where the mean normal velocity at the wall is optimized to reduce the growth of a single disturbance with a fixed given initital condition. The optimization problem is solved by minimizing an objective function balancing a measure of the state and the control using a gradient based method. We obtain the gradient of the objective function using an adjoint technique. The complete derivation of the equations can be seen in Appendix B.
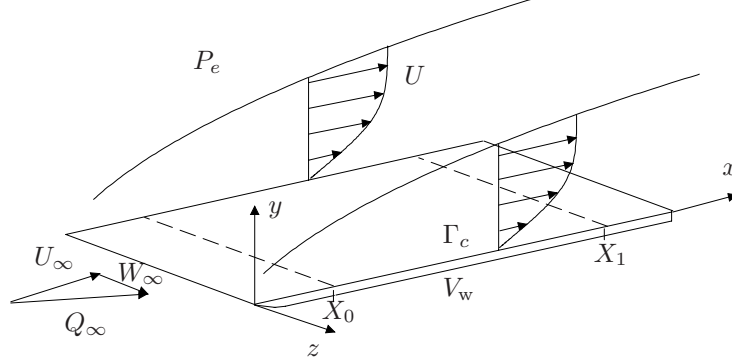
FIGURE 1. Computational domain: flat-plate boundary layer

2.2.1. *Objective function*

We measure the size of a disturbance in domain Ω, defined such that $x \in [X_0, X_1]$, $y \in [0, \infty)$ and $z \in [Z_0, Z_1]$ (see figure 1), by its total kinetic energy defined as

$$E = \frac{1}{2} \int_{Z_0}^{Z_1} \int_{X_0}^{X_1} \int_0^\infty \mathbf{u}^T \mathbf{u} \, \mathrm{d}y \, \mathrm{d}x \, \mathrm{d}z.$$

The objective function to be minimized is

$$J(V_\mathrm{w}) = \frac{1}{2} \int_{Z_0}^{Z_1} \int_{X_0}^{X_1} \int_0^\infty \mathbf{u}^T \mathbf{u} \, \mathrm{d}y \, \mathrm{d}x \, \mathrm{d}z + \frac{l^2}{2} \int_{Z_0}^{Z_1} \int_{X_0}^{X_1} V_\mathrm{w}^2 \, \mathrm{d}x \, \mathrm{d}z \qquad (9)$$

where $l^2 > 0$, is the regularization parameter and is used to insure that the size of the control parameter V_w does not grow unbounded. Now, the control problem can be defined mathematically as

$$\begin{aligned} \text{find} \quad & V_\mathrm{w}^{opt} \in L^2(\Gamma_c) \quad \text{such that} \\ & J(V_\mathrm{w}^{opt}) \leq J(V_\mathrm{w}) \; \forall \; V_\mathrm{w} \in L^2(\Gamma_c) \end{aligned} \qquad (10)$$

where V_w^{opt} is the optimal suction distribution on the wall.

2.2.2. *Adjoint equations and the gradient*

The gradient of the objective function (9) with respect to the control variable is defined through the directional derivative as

$$\delta J = \langle \nabla_{V_\mathrm{w}} J, \delta V_\mathrm{w} \rangle = \lim_{s \to 0} \left| \frac{J(V_\mathrm{w} + s\delta V_\mathrm{w}) - J(V_\mathrm{w})}{s} \right|, \qquad (11)$$

where δV_w is the variation of the control variable. Here, we derive the gradient expression using the adjoint of the state equations. Details of the derivation is given in Appendix B. This yields

$$\nabla_{V_\mathrm{w}} J = l^2 V_\mathrm{w} + V_\mathrm{w}^* \qquad \text{on} \qquad y = 0. \qquad (12)$$

The value of $V_\mathrm{w}^* = V^*(x, 0)$ in (12) is given by the solution of the adjoint of the PSE and boundary layer equations, hereafter referred to as APSE and ABLE,
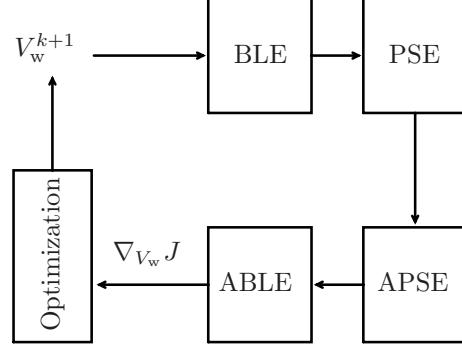
FIGURE 2. Chart of the solution process

respectively. The APSE which is found as (40)–(44) in Appendix B is here written

$$A^H q^* - B^H \frac{\partial q^*}{\partial y} + C^H \frac{\partial^2 q^*}{\partial y^2} - D^H \frac{\partial q^*}{\partial x} = f_{APSE}, \qquad (13)$$

$$\frac{\partial}{\partial x} \int_0^\infty q^{*H} \frac{\partial A}{\partial \alpha} \hat{q} \, dy + i|\Theta|^2 \int_0^\infty |\hat{\mathbf{u}}|^2 \, dy = 0, \qquad (14)$$

with boundary conditions

$$\begin{aligned} u^* = v^* = w^* = 0 \qquad &\text{on} \qquad y = 0, \\ u^*, v^*, w^* \to 0 \qquad &\text{as} \qquad y \to \infty. \end{aligned} \qquad (15)$$

and initial conditions

$$q^* = r^* = 0 \qquad \text{on} \qquad x = X_1. \qquad (16)$$

Here, $q^* = (p^*, u^*, v^*, w^*)^T$ and r^* are the co-state variables and f_{APSE} is the forcing due to the auxiliary condition of the PSE and the objective function. Equations (13)–(14) are integrated in the upstream direction starting at $x = X_1$. At each streamwise position, the value of the scalar r^* is iteratively found such that (14) is satisfied. The ABLE which are found as (45)–(47) in Appendix B, are satisfied by the co-state variables $Q^* = (U^*, V^*, W^*)$. They are here written as

$$L^*_{BLE}(Q)Q^* = f_{ABLE}, \qquad (17)$$

with boundary conditions

$$\begin{aligned} U^* = W^* = 0 \qquad &\text{on} \qquad y = 0, \\ U^*, V^*, W^* \to 0 \qquad &\text{as} \qquad y \to \infty, \end{aligned} \qquad (18)$$

and initial conditions

$$U^* = V^* = W^* = 0 \qquad \text{on} \qquad x = X_1. \qquad (19)$$

The forcing term in (17), f_{ABLE}, is a function of the solutions of both the PSE and the APSE. Equations (17) are integrated in the upstream direction starting at $x = X_1$. The optimization procedure can now be outlined following

the steps below considering the chart given in figure 2 where k denotes the iteration number.

i. The BLE (1)–(3) are integrated from $x = X_0$ to $x = X_1$. If $k = 1$ then $V_\mathrm{w}^k = 0$ (initial guess on the suction distribution).

ii. The PSE (6)–(7) are integrated from $x = X_0$ to $x = X_1$, then the APSE are integrated from $x = X_1$ to $x = X_0$.

iii. f_{ABLE} is calculated from the solution of both the PSE and APSE.

iv. The ABLE (17) are integrated from $x = X_1$ to $x = X_0$ given the forcing, f_{ABLE}, from (iii).

v. If $k < 2$ then goto (vi), else evaluate the convergence criteria: If $J^{k+1} - J^k < err$ then convergence is reached else goto (vi). Here err is a small real-valued parameter defining the convergence.

vi. The gradient, (12), is evaluated and the new boundary condition for the BLE, V_w^{k+1}, is calculated using an optimization routine (here we use a limited-memory quasi-Newton method). Continue: $k = k + 1$, goto (i).

The gradient of the objective function due to a variation of the free stream velocity can be derived in the same manner as for V_w and yields,

$$\nabla_{U_e} J = -U_e \int_0^\infty \frac{\partial U^*}{\partial x}\, \mathrm{d}y. \tag{20}$$

This variation would be the result of a change in the geometry and consequently the pressure distribution. Effects due to geometry changes are not investigated here.

2.3. *Optimal control of multiple disturbances*

In this section we generalize the technique introduced above to find the optimal suction distribution of the steady mean flow that accounts for the growth of more than one disturbance. This is necessary for cases where it is not possible to clearly state which disturbance will grow the most and thus cause laminar-turbulent transition first. An example of this is the two-dimensional Blasius boundary layer where either T-S wave type instabilities or steady streamwise streaks could give the maximum growth at a given streamwise position. The measure of disturbance kinetic energy in Ω, is now taken as the sum of the energy of a chosen number of pre-defined disturbances in a convectively un-stable flow. In this case, the suction distribution will be optimal for the sum of these disturbances. Our approach is however different from non-cooperative strategies (see Bewley & Liu 1998; Bewley & Moin 1997) which analyze worst-case scenarios, so called robust control. There, the strategy is to find the best control in the presence of the worst case external disturbance.

The analysis does not differ much from the one outlined in § 2.2 and is therefore done here on a more compact form. If we denote the total number of

existing disturbances with N then the total kinetic energy is defined as

$$E = \sum_{k=1}^{N} \frac{1}{2} \int_{Z_0}^{Z_1} \int_{X_0}^{X_1} \int_{0}^{\infty} \mathbf{u}_k{}^T \mathbf{u}_k \, \mathrm{d}y \, \mathrm{d}x \, \mathrm{d}z.$$

The objective function to be minimized is now

$$J(V_{\mathrm{w}}) = \sum_{k=1}^{N} \frac{1}{2} \int_{Z_0}^{Z_1} \int_{X_0}^{X_1} \int_{0}^{\infty} \mathbf{u}_k{}^T \mathbf{u}_k \, \mathrm{d}y \, \mathrm{d}x \, \mathrm{d}z + \frac{l^2}{2} \int_{Z_0}^{Z_1} \int_{X_0}^{X_1} V_{\mathrm{w}}{}^2 \, \mathrm{d}x \, \mathrm{d}z. \quad (21)$$

The same procedure to find the gradient of J with respect to V_{w} given in Appendix B for control of single disturbances is now used to account for several disturbances. As the control problem is derived for steady suction, the case of multiple disturbances does not introduce any further complications. Equation (11) is used to define the gradient which can now be written

$$\nabla_{V_{\mathrm{w}}} J = l^2 V_{\mathrm{w}} + \sum_{k=1}^{N} (V_{\mathrm{w}}^*)_k \qquad \text{on} \qquad y = 0. \quad (22)$$

Equation (22) implies that each equation in the solution procedure given in figure 2 must be solved N times, i. e. for each disturbance, before evaluating the gradient. Instead, one can use the fact that the ABLE are linear equations. In this case, for a given solution of the BLE, the PSE and the APSE are solved N times, step (ii) in figure 2. The forcing term of the ABLE, step (iii), is then computed as the sum of N realizations. In step (iv), the ABLE are solved once given the total forcing from all N disturbances. The gradient is finally evaluated from (12) which was given for control of single disturbances. However, now a single evaluation of V_{w}^* accounts for all N disturbances.

It should be mentioned that the evaluation of the initial disturbances far upstream of the neutral point may be difficult. Therefore, if we consider a large number of different disturbances whose neutral points are widely spread in the streamwise direction, care has to be taken when X_0 is chosen.

2.4. Adjoint of the stabilized PSE

In gradient based optimization, an increased accuracy of the gradient will give a result closer to the optimum. The gradient presented here, (12), is derived using a so called continuous approach. This means that the adjoint of a state equation is derived from the continuous equation and then discretized. Another approach is to first discretize the state equation and then derive its adjoint, the so called discrete approach. The latter yields a more accurate gradient in most cases but its derivation is more complicated. However, results of the continuous approach should converge to that of the discrete one as the grid resolution is refined, (see Högberg & Berggren 2000). It is a rather well know problem that the PSE equations become unstable as the grid in the streamwise direction is refined due to a remaining ellipticity in the equations, (see Haj-Hariri 1994; Li & Malik 1994, 1996; Andersson *et al.* 1998). This problem will therefore put a limit on the accuracy of the gradient unless some technique is

used to overcome the instability problem and allow a smaller step-size in the streamwise direction. A stabilization procedure was presented by Andersson *et al.* (1998) in which they add terms proportional to the truncation error of the implicit scheme used in the streamwise direction. These terms are of the same order as some of the originally neglected terms in the PSE. It was shown that the procedure does not alter the PSE results while allowing higher streamwise resolution. The procedure here, does however not only add terms to the PSE but also affects all adjoint equations since we derive the adjoint from the PSE and not the adjoint linearized Navier–Stokes equations. Here, we present the outline on how to derive the PSE, gradient and the adjoint equations, using the stabilization technique given by Andersson *et al.*. The details of the derivation can be seen in B.3. Following Andersson *et al.*, terms of order $O(Re^{-2})$ are introduced in (6). The stabilized PSE can be written

$$-D\frac{\partial \hat{q}}{\partial x} = A\Big[\hat{q} + s\frac{\partial \hat{q}}{\partial x}\Big] + B\Big[\frac{\partial \hat{q}}{\partial y} + s\frac{\partial}{\partial x}\Big(\frac{\partial \hat{q}}{\partial y}\Big)\Big] +$$
$$C\Big[\frac{\partial^2 \hat{q}}{\partial y^2} + s\frac{\partial}{\partial x}\Big(\frac{\partial^2 \hat{q}}{\partial y^2}\Big)\Big] \tag{23}$$

where s is a positive real number. The gradient, (12) and the adjoint equations were derived in Appendix B without the stabilization terms. Now, the derivation has to be done using (23) instead of (6) which yields the following adjoint equations

$$-D^H\frac{\partial q^*}{\partial x} = -\Big[A^H q^* - s\tilde{A}^H\frac{\partial q^*}{\partial x}\Big] + B^H\Big[\frac{\partial q^*}{\partial y} - s\frac{\partial}{\partial x}\Big(\frac{\partial q^*}{\partial y}\Big)\Big] -$$
$$C^H\Big[\frac{\partial^2 q^*}{\partial y^2} - s\frac{\partial}{\partial x}\Big(\frac{\partial^2 q^*}{\partial y^2}\Big)\Big] + f_{APSE} \tag{24}$$

$$\frac{\partial}{\partial x}\int_0^\infty q^{*H}\frac{\partial A}{\partial \alpha}\Big[\hat{q} + s\frac{\partial \hat{q}}{\partial x}\Big]\,\mathrm{d}y + \mathrm{i}|\Theta|^2\int_0^\infty |\hat{\mathbf{u}}|^2\,\mathrm{d}y = 0, \tag{25}$$

$$L_{BLE}^*(Q)Q^* = \tilde{f}_{ABLE}, \tag{26}$$

where f_{APSE} and f_{ABLE} denotes the forcing terms of the APSE and ABLE respectively and the accent˜marks where additional terms due to the stabilization procedure appear. Note here, that there is no influence on the gradient expression or on the boundary conditions of the state and adjoint equations due to the stabilizing terms. The additional terms on the right hand side of (24) resembles the stabilizing terms in (23) apart from the sign difference on s. The APSE resembles the PSE and the new right hand side of (24) will indeed work as a stabilizing term allowing a smaller step-size in the streamwise direction and the calculation of a more accurate gradient.

3. Results

The results presented are obtained by numerically integrating the discretized state and co-state (adjoint) equations. The x-derivatives are approximated by a first- or second-order accurate backward Euler scheme. The y-derivatives of

the PSE and APSE are approximated by Chebychev-polynomials and a second-order accurate finite-difference scheme for the BLE and ABLE. The L-BFGS-B package, which is based on the limited memory quasi-Newton method, is used in the optimization procedure (see Zhu *et al.* 1994; Byrd *et al.* 1995). Here we take $J^{k+1} - J^k = 10^{-15}$ as a converged solution. The gradient accuracy has been checked for the first and last iteration of the optimization process.

In all the results shown here, except for figure 9, the optimal suction distribution is computed for the whole streamwise computational domain. In figure 9 different control domains are investigated. In all computations, the suction is zero at the first streamwise point to assure that the original assumption of zero variation of disturbance at X_0 is met.

The relation between the regularization parameter, reduction of disturbance kinetic energy and control energy for all cases is found in the end of this section.

3.1. *Validation and accuracy of the gradient*

The optimization procedure depends on the accuracy of the gradient. If its accuracy is low, then it is less likely to find a minima and convergence problems will be encountered. Here, we check the accuracy of the gradient by a comparison of the adjoint based gradients (12) with those obtained from a finite-difference approach. The comparison is done considering a wall normal velocity perturbation δV_w at $y = 0$. The variation of the functional J with respect to this perturbation is

$$\delta J = \frac{\partial J}{\partial V_w} \delta V_w. \tag{27}$$

In the finite-difference approach $\partial J / \partial V_w$ is obtained by using the inhomogeneous wall boundary-condition $V_w = \pm \epsilon_w$ at $x = x_n$. The index n refers to the n-th streamwise position and ϵ_w is a small positive number. The derivative is then evaluated using a second-order accurate finite-difference scheme. The discretized expression for δJ in the adjoint approach is given by

$$\delta J = \int_{X_0}^{X_1} \left(\sum_{n=2}^{N-1} \nabla_{V_w} J_n \, \delta V_{w_n} \Delta_n \right) \mathrm{d}x \tag{28}$$

where $\Delta_n = (x_{n+1} - x_{n-1})/2$. In figure 3(*b*), the relative error between $\mathrm{d}J/\mathrm{d}V_w$ and $\nabla_{V_w} J_n \Delta_n$ is compared for different streamwise resolution ΔRe. The calculations are done for a streamwise range $Re = 250 - 760$ on a quasi three-dimensional boundary layer where $\mathrm{d}P_e/\mathrm{d}x = 0$ given a T-S wave as the initial disturbance at $x = X_0$. The inviscid flow at $Re = 250$ has an angle of 30°, the non-dimensional spanwise wavenumber $\beta = 0$ and the reduced frequency $F = 2\pi f^\star \nu_e^\star / U_e^{\star 2} = 10^{-4}$. As can be seen in figure 3(*b*), the relative error decreases as the ΔRe is decreased. Here, $\Delta Re = 6$ is the minimum streamwise step size for which the PSE calculations are stable. The values for $\Delta Re = 2$ are computed using the stabilization terms, explained in §2.4. In figure 3(*a*),
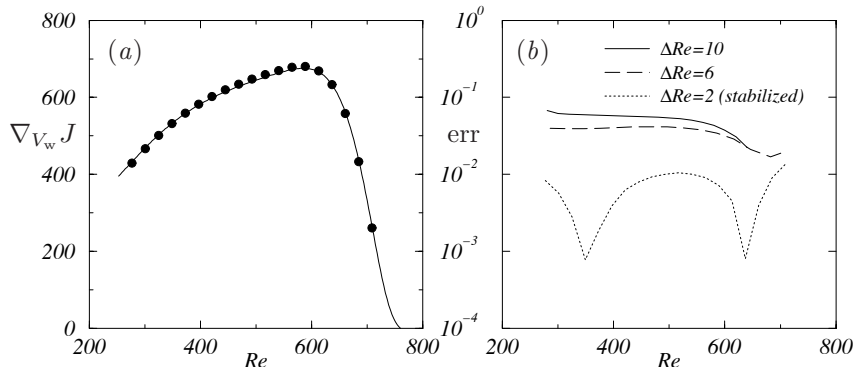
FIGURE 3. Comparison of the gradient from adjoint and central-difference calculations for different streamwise resolution ΔRe. (*a*) $\Delta Re = 2$, the continuous line is the gradient derived from adjoint equations, ● marks central-difference calculations. (*b*) The relative error (err) between adjoint and central-difference calculations of the gradient for different streamwise resolution ΔRe.

the gradient obtained from the adjoint equations is compared with central-differences when $\Delta Re = 2$ in order to visualize the agreement.

The results presented in §3, has a ΔRe chosen such that the relative error (err) was approximately 1%, which required the use of the stabilization procedure. A study was conducted on the influence of changing the streamwise resolution for control of T-S waves in the Blasius boundary layer. It was found that an increased resolution gives a faster convergence and a decrease of the objective function.

3.2. *Two-dimensional boundary layers*

In this section we investigate the disturbance control in a two-dimensional boundary layer with zero pressure gradient. The disturbances studied here are chosen to be a T-S wave and/or optimally growing steady streamwise streaks. The initial conditions for T-S waves are taken as the solutions of the local stability theory and the initial condition for the streaks has been calculated using the theory given in Andersson *et al.* (1999). For T-S waves, the streamwise range is chosen such that the unstable region is found between X_0 and X_1. In §3.2.1 the optimal suction distribution is calculated to control each of these disturbances individually. Here, we also investigate the effect of different domains along the streamwise axis for the control of T-S waves.

The results in this section on control of T-S waves are produced for a disturbance with a frequency of $F = 10^{-4}$. It is shown that the optimal suction distribution obtained to control the chosen T-S wave has a stabilizing effect on T-S waves with other frequencies. A study has also been performed to
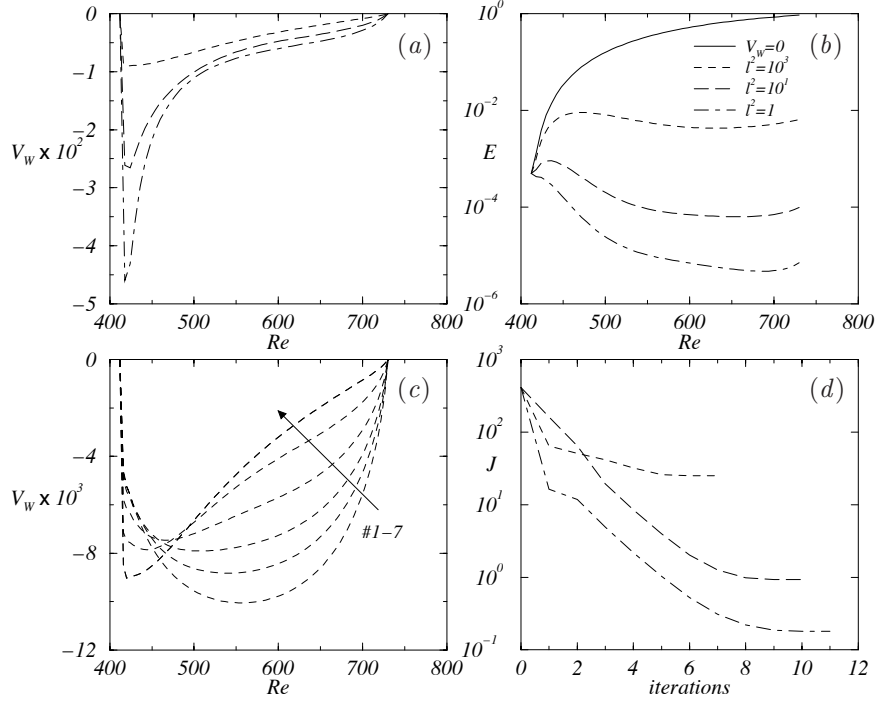
FIGURE 4. Disturbance control of optimally growing steady streamwise streaks in a two-dimensional boundary layer $(dP_e/dx = 0)$. The non-dimensional spanwise wavenumber $\beta = 0.292$ at $Re = 412$. Results are shown for $l^2 = 1, 10, 10^3$. (a) Optimal suction distributions. (b) The disturbance kinetic energy in a mean flow with zero and optimal suction distribution. (c) Suction profiles for the different steps in the optimization process, $l^2 = 10^3$. (d) The objective function as a function of the iteration step.

control T-S waves with both higher and lower frequencies than the one shown here. However, the effect of the optimization process on the growth rate of these disturbances, the corresponding optimal suction profiles and mean flow modifications all show the same behavior. Thus this choice of frequency give the general behavior of the optimization process given a T-S wave instability in a two-dimensional boundary layer.

3.2.1. *Control of single disturbances*

The optimal distribution of suction to control steady streamwise streaks is calculated for a streamwise range $Re = 412 - 730$. The initial condition which has the maximum energy at X_1, is computed using the optimization procedure
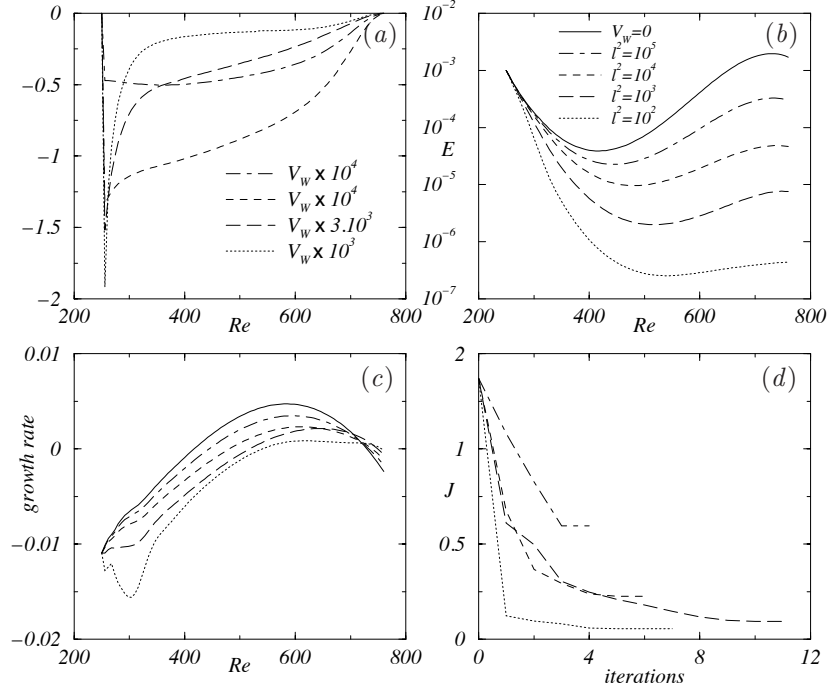
FIGURE 5. Disturbance control of a T-S wave with $F = 10^{-4}$ in a two-dimensional boundary layer $(\mathrm{d}P_e/\mathrm{d}x = 0)$. Results are shown for $l^2 = 10^2, 10^3, 10^4, 10^5$. (a) Optimal suction distributions (note the different scalings). (b) The disturbance kinetic energy in a mean flow with zero and optimal suction distribution. (c) The growth rate, -imag(α), in a mean flow with zero and optimal suction. (d) The objective function as a function of the iteration step.

given in Andersson *et al.* (1999). The non-dimensional spanwise wavenumber $\beta = 0.292$ and the frequency $\omega = 0$. Three test cases are analyzed for these parameters in which the regularization parameter l^2 was $1, 10$ and 10^3 and the control is applied at $Re = 418 - 724$. In figure $4(a)$ the optimal suction distributions for all cases are compared. A peak in the suction distribution is noticed upstream which becomes more pronounced as the regularization parameter is decreased. In figure $4(b)$ the disturbance kinetic energy of zero and optimal suction are compared. All three suction distributions result in a decrease of the disturbance kinetic energy. However, the main difference between the curves where control is applied is seen in the upstream region. The effect of the optimal suction distributions given in figure $4(a)$ is that the damping of the disturbance kinetic energy is increased in the upstream region as l^2 is
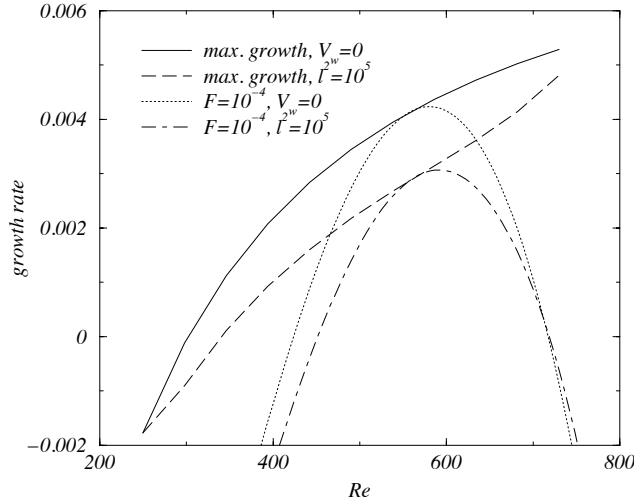
FIGURE 6. Maximum local growth rate compared with local growth rate of a T-S wave with $F = 10^{-4}$, for zero and optimal suction in a two-dimensional boundary layer $(\mathrm{d}P_e/\mathrm{d}x = 0)$. The optimal suction is computed for control of a T-S wave with $F = 10^{-4}$ given that $l^2 = 10^5$ for a streamwise range $Re = 250 - 760$. Calculations of maximum local growth rate are made with $\Delta F = 2.5 \times 10^{-6}$.

decreased. Figure $4(c)$ illustrates the changes in the suction distribution during the optimization procedure. Here, V_w is plotted for each iteration in the optimization loop for the case with $l^2 = 10^2$. The optimal distribution is found after 7 iterations. The difference between the sixth and seventh iteration can not be distinguished. In figure $4(d)$ the objective function is given as function of the iteration number for all cases to illustrate the convergence of the optimization procedure.

The optimal distribution of suction to control T-S wave instabilities is calculated for a streamwise range $Re = 250-760$. The first investigation is done by comparing different regularization parameters, here $l^2 = 10^2, 10^3, 10^4, 10^5$ while control is applied at $Re = 256 - 754$. The results can be seen in figure 5. In figure $5(a)$ the optimal suction distributions from all cases are compared. Here, it is noted that the optimal suction distribution tends to peak upstream as the penalty on the control is reduced, and this peak is upstream of the unstable region for all cases. Even though the magnitude of the suction rates are within the original assumptions, one should also note that a decreased penalty on the control produces suction distributions with large streamwise variations in the upstream domain. At the point where our results show a peak they are thus locally outside the range of validity of the parabolic theory employed, since the gradient of the control velocity at the initial control point
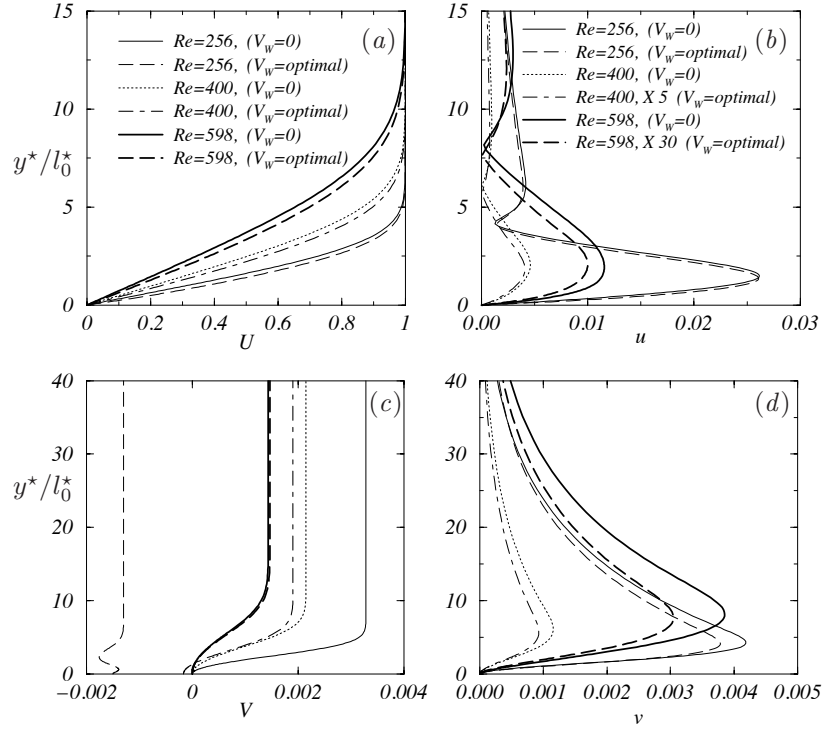
FIGURE 7. Modification of the two-dimensional mean flow ($\mathrm{d}P_e/\mathrm{d}x = 0$) and disturbance velocity due to optimal suction computed to control a T-S wave with $F = 10^{-4}$ when $l^2 = 10^2$ in a streamwise range $Re = 250 - 760$. Results are presented for $Re = 256, 400, 598$. (a) Streamwise and (c) wall normal velocity of the mean flow subject to zero and optimal suction. Absolute value of the (b) streamwise and (d) wall normal disturbance velocity (note the different scalings).

approaches infinity as the step size in the streamwise direction approaches zero. In figure 5(b) the disturbance kinetic energy is compared for zero and optimal suction distribution. A reduction of disturbance kinetic energy can be observed as the penalty of the control is reduced. The growth rate for all cases can are given in figure 5(c). In all cases the growth rate is decreased as l^2 is decreased and the reduction is more pronounced in the upstream region. Finally, in figure 5(d) the objective function is plotted as a function of the iteration number to show the convergence of the optimization procedure.

A question that arises is if the suction distribution which is optimal for one chosen T-S wave will damp or amplify other instability waves in the chosen streamwise domain. This is analyzed by computing the maximum local

growth rate, i. e. local growth rate over all possible frequencies, at a number
of streamwise positions both with zero and the optimal suction distribution.
The streamwise range and optimal suction distribution are taken from figure 5
with $l^2 = 10^5$. The results are shown in figure 6 where the maximum local
growth rate has been computed for $\Delta F = 2.5 \times 10^{-6}$ and $\Delta Re = 50$ as the
reduced frequency and streamwise resolution respectively. Here, it is shown
that the optimal suction distribution for one given frequency has a stabilizing
effect on all other frequencies in the given streamwise range. Further, the local
growth rate for the T-S wave with $F = 10^{-4}$ has been plotted both with zero
and optimal suction distribution. The result shows that the chosen disturbance
corresponds to the maximum growth rate both with zero and optimal suction
at a given streamwise position.

The effect of imposing suction at the wall is that the velocity profile of
the mean flow becomes fuller which is known to stabilize the viscous instabil-
ity waves. In figure 7 the effects on the streamwise and wall normal velocity
component of the mean flow are shown for three different streamwise positions.
There, the streamwise and wall normal disturbance velocity components are
also plotted. The suction distribution is that of figure 5 for $l^2 = 10^2$. The first
position, $Re = 256$, is close to X_0, the second position $Re = 400$ is close to
where the disturbance starts to grow and the last position $Re = 598$ is roughly
half way into the unstable region. In figure 7(a) the streamwise velocity pro-
file has been plotted for these three positions, when zero and optimal suction
are applied. In all three cases the mean flow profiles have become fuller (or
thickened). It should be noted that even though the optimal suction distribu-
tion shows a significant peak in the vicinity of $Re = 256$, see figure 5(a), the
effect on the streamwise mean velocity is not large. The effect of suction on
the mean flow is instead more pronounced for the wall normal component, see
figure 7(c), especially in the upstream region. The amplitude of the stream-
wise and wall normal disturbance velocities are shown for the cases of zero and
optimal suction in figure 7(b) and (d), respectively. The initial condition is
the same for zero and optimal suction and the effect of suction on both com-
ponents is similar. At the upstream position, the variation due to suction is
small. The results at the most downstream position show a larger reduction
of disturbance amplitude. Here, the results for the case of optimal suction at
$Re = 400$ and 598 are magnified to make the shape visible. In all cases the
disturbance shape is kept as the optimal suction distribution is applied but the
magnitude is decreased. Further, the peak velocity is moved somewhat closer
to the wall due to the decreased boundary layer thickness.

As pointed out in the introduction, the mean flow pressure distribution
is assumed to be unchanged due to the applied suction. If this would not
be the case, then an additional set of equations would be needed in order
to solve for the exterior pressure distribution in the optimization process. In
order to gain some insight into this, the shape factor H_{12} (displacement thick-
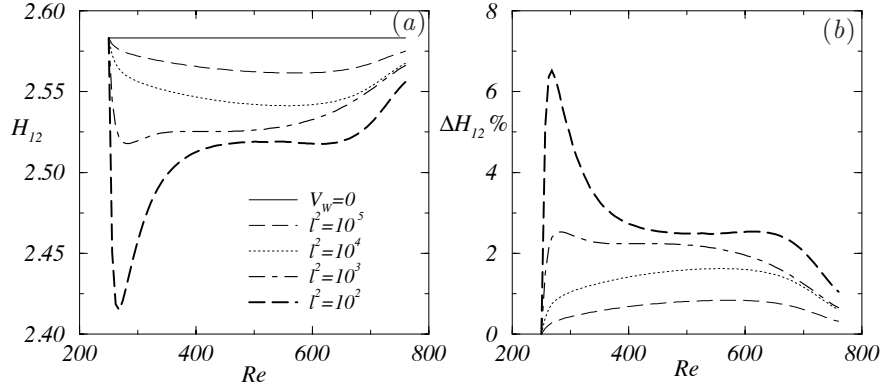ness/momentum thickness) is plotted in figure 8(a) for all cases in figure 5. In

FIGURE 8. Shape factor (H_{12}) for control of a T-S wave with
$F = 10^{-4}$ in a two-dimensional boundary layer ($\mathrm{d}P_e/\mathrm{d}x = 0$).
Results are shown for $l^2 = 10^2, 10^3, 10^4, 10^5$ (*a*) Shape factor.
(*b*) Relative change in the shape factor (ΔH_{12}) in percent,
between controlled and uncontrolled case.

figure 8(*b*) the relative change of H_{12} between the controlled and uncontrolled
case is plotted. For the three cases $l^2 = 10^3, 10^4, 10^5$, the difference in shape
factor ranges between $0.5 - 2\%$. However, for the case of $l^2 = 10^2$ a peak
of 6% in difference appears in the upstream region. Note, that all cases have
maximum suction velocities which are smaller than the original assumption of
$V_{\mathrm{w}} \sim O(1/Re)$.

Figure 9 illustrates the effects of changing the size and location of the
control domain. Here, the same case as in figure 5 with $l^2 = 10^3$ is used. Three
different control regions are compared. In the first case, the control is applied
to $Re = 412 - 554$ which is from the initial point of unstable region (branch I
of the neutral stability curve) to roughly halfway into the unstable region. The
second case, $Re = 412 - 718$ is the control domain extended over the whole
unstable region and in the last case, $Re = 256 - 754$, the control is applied
over the whole computational domain. The corresponding optimal suction
velocity profiles can be seen in figure 9(*a*). Results for all cases show a suction
peak in the upstream region of the control domain. In figure 9(*b*) the kinetic
disturbance energy is shown for all cases. The first case shows a significant
reduction of energy as the control is applied but continues to grow when the
control is turned off. The second and last case show that approximately the
same reduction of energy at the final streamwise position can be obtained either
by acting only in the unstable region or in the whole domain. The growth rate
is given in figure 9(*c*). In the first and second case, the growth rate follows the
curve of zero suction until the control is turned on. A large reduction in growth
rate can then be seen in the upstream region of the control domain. The first
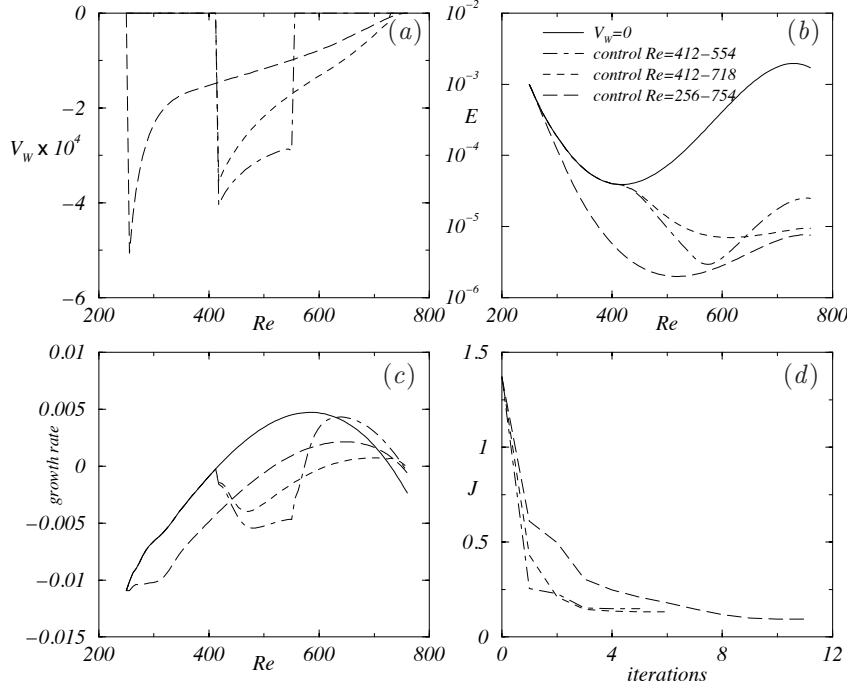case shows a significant increase as the control is turned off inside the unstable

FIGURE 9. Disturbance control of a T-S wave with $F = 10^{-4}$ in a two-dimensional boundary layer $(dP_e/dx = 0)$. Results are presented for different control domains given that $l^2 = 10^3$. (a) Optimal suction distributions. (b) The disturbance kinetic energy in a mean flow with zero and optimal suction. (c) The growth rate, -imag(α), in a mean flow with zero and optimal suction. (d) The objective function as a function of the iteration step.

region. In figure 9(d) the objective function is plotted as a function of the iteration number to visualize the convergence of the optimization procedure.

3.2.2. *Control of multiple disturbances*

The theory in § 2.3 was introduced to account for more than one disturbance in the domain. This will produce an optimal suction profile that reduces the disturbance kinetic energy for all disturbances accounted for. Here, we analyze two disturbances, a T-S wave and optimally growing streamwise steady streaks, with an initial energy such that they give the same maximum disturbance energy at the downstream position X_1. The domain is chosen so that X_0 and X_1 are at the first and second branch of the neutral stability curve for the T-S wave with $F = 10^{-4}$. The initial condition for the steady streaks is computed using the optimization technique given in Andersson *et al.* (1999) to provide
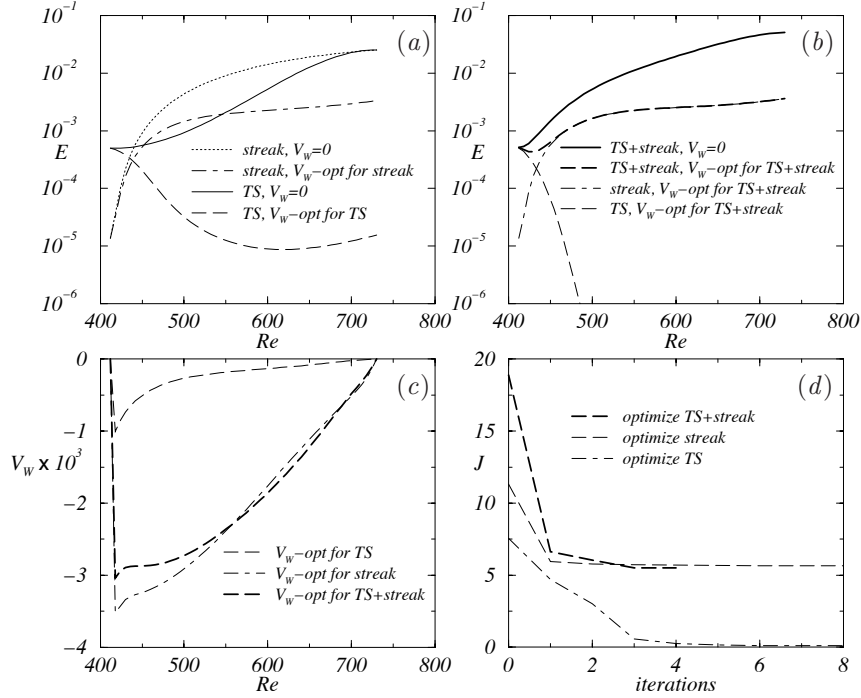
FIGURE 10. Control of two disturbances in a two-dimensional boundary layer $(\mathrm{d}P_e/\mathrm{d}x = 0)$. The disturbances are a T-S wave $(F = 10^{-4})$ and optimally growing streamwise streaks $(\beta = 0.292$ at $Re = 412)$ and $l^2 = 10^3$. Disturbance kinetic energy in a mean flow with zero and optimal suction (a) the suction distribution is computed for each disturbance separately, (b) the suction distribution is computed to account for both disturbances (see §2.3). (c) Optimal suction distributions. (d) The objective function as a function of the iteration step.

the maximum growth at X_1 for the chosen domain. In all calculations $l^2 = 10^3$ which means that the same weighting is given between the disturbance and control energy in all cases. The optimal suction profile was first computed for each of the disturbances individually. A comparison of the disturbance kinetic energy for zero and the corresponding optimal suction can be seen in figure $10(a)$. It is shown that the reduction of kinetic energy is more than two decades larger for the T-S wave as the optimal control is applied. Given the same l^2, it is therefore possible to say that optimally growing streamwise streaks demand a stronger control than T-S waves. The corresponding suction distributions can be seen in figure $10(c)$. It can be seen in this comparison that the magnitude of the control of steady streaks is larger compared to T-S waves.

This is however expected as the total disturbance kinetic energy of the streaks is larger than that of the T-S wave given that the energy is the same at X_1, see figure $10(a)$, and therefore should result in a larger control energy. Then, the optimal suction profile was calculated for the sum of both disturbances using (22) with $l^2 = 10^3$. In figure $10(b)$, the disturbance kinetic energy is shown when the optimal control for the sum of both disturbances is applied to each disturbance individually and the sum of both disturbances. The corresponding optimal suction distribution can be seen in figure $10(c)$. Here, the total kinetic energy for the streaks is larger than for the T-S wave, and the control will act primarily on the streaks. Therefore, the optimal suction distribution for the sum of the disturbances is similar to that of the streaks. When the optimal suction profile for the sum is used on the T-S wave then the energy decreases further and drops to 10^{-11}, out of range in figure $10(b)$, at the downstream position X_1. This is 5 decades lower than the optimal suction profile for control of just the T-S wave gives. In figure $10(d)$ the objective function is given as function of the iteration number to show the convergence of the optimization process.

3.3. *Three-dimensional boundary layers*

Here, we study the control of three-dimensional disturbances in quasi three-dimensional boundary layers subjected to a pressure gradient. In the first case, the flow is subject to an adverse pressure gradient and the disturbance parameters have been chosen such that it has the maximum growth rate (over all $F - \beta$) at some position in the computational domain. Further studies have been performed on control of oblique waves with other frequencies and spanwise wavenumbers than the one shown here. The behaviour of the optimal suction distributions, mean flow and disturbances are similar. Therefore, we find that the disturbance parameters chosen here represents the general behaviour of the optimization process and results. In the second case, control is presented for a steady cross-flow mode in a mean flow with a favorable pressure gradient where we have chosen the case from Högberg & Henningson (1998). Although the stationary cross-flow modes are not the most amplified ones, in the presence of surface roughness they are often the dominant disturbances.

3.3.1. *Control in a flow with an adverse pressure gradient*

The control of an oblique wave is analyzed in a quasi three-dimensional incompressible boundary layers with an adverse pressure gradient ($U_e = (x/x_0)^{-0.05}$). The streamwise range is $Re = 250-760$, the non-dimensional spanwise wavenumber $\beta = -0.02$ and the reduced frequency $F = 10^{-4}$. The inviscid flow at $Re = 250$ has an angle of 45° and the control has been applied at $Re = 256-754$. In this case l^2 has been altered to compare the impact of different regularization parameters on the control energy used. The results comparing various l^2 can be seen in figure 11. In figure $11(a)$ the optimal suction distribution V_w is plotted. A suction peak appears at an upstream position of the control domain
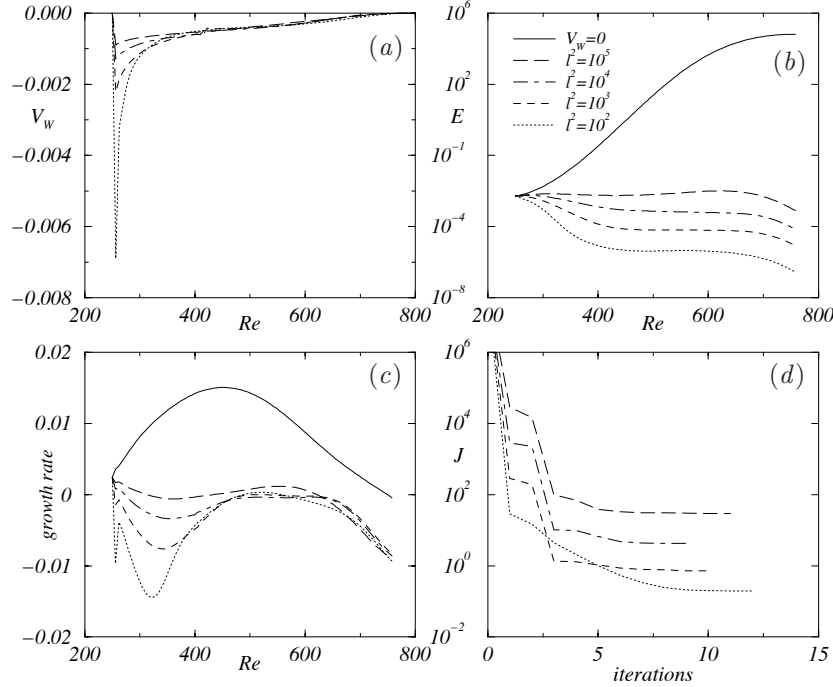
Figure 11. Control of an oblique wave in a three-dimensional boundary layer with an adverse pressure gradient ($U_e = (x/x_0)^{-0.05}$). The inviscid flow at $Re = 250$ has an angle of 45° and the non-dimensional spanwise wavenumber $\beta = -0.02$. Results are shown for $l^2 = 10^2, 10^3, 10^4, 10^5$. (a) Optimal suction distributions. (b) The disturbance energy in a mean flow with zero and optimal suction. (c) The growth rate, -imag(α), in a mean flow with zero and optimal suction. (d) The objective function as a function of the iteration step.

and is more pronounced as l^2 is decreased. Downstream of the suction peak the suction distribution is rather constant before it finally decreases to zero. It is evident from this figure that a decreased penalty on the control will concentrate the increased control effort in the upstream domain. This creates, as in figure 5, a strong streamwise variation of the suction distribution in this region. The disturbance kinetic energy is compared in figure 11(b) for the case of zero and optimal suction distribution. A reduction of kinetic energy is observed in all cases starting in the upstream region of the control domain. Further, the reduction is increased as l^2 is decreased. In figure 11(c) the growth rate is compared for zero and optimal suction distribution and it is shown that the growth rate is decreased as l^2 is decreased. Note that the growth rate for the
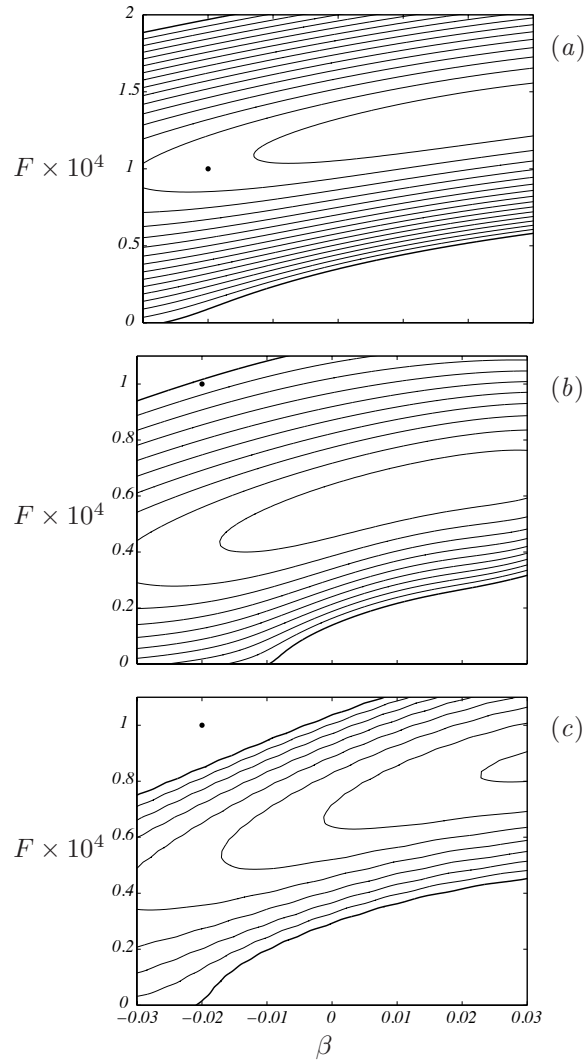
FIGURE 12. Contours of local growth rate at different stream-wise positions in a flow with an adverse pressure gradient $(U_e = (x/x_0)^{-0.05})$. The inviscid flow at $Re = 250$ has an angle of 45°. (*a*) At $Re = 418$ with zero suction. (all disturbances are damped using optimal suction at this position) (*b*) At $Re = 676$ with zero suction. (*c*) At $Re = 676$ with an optimal suction distribution given by the case in figure 11 where $l^2 = 10^2$. Here F, β and the local growth rate are scaled with reference values at X_0. The thick contours denote zero growth rate and the contour spacing is 0.0005. The • marks the disturbance initial condition used in figure 11.
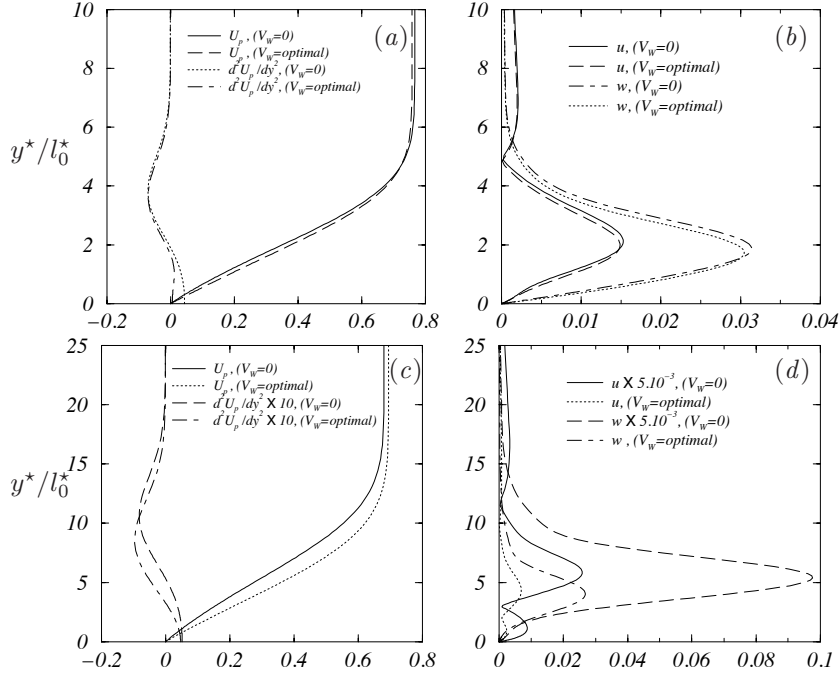
FIGURE 13. Modification of the three-dimensional mean flow with an adverse pressure gradient ($U_e = (x/x_0)^{-0.05}$) and disturbance velocity, due to optimal suction ($l^2 = 10^5$). The inviscid flow at $Re = 250$ has an angle of 45° and the control is computed for an oblique wave ($F = 10^{-4}, \beta = -0.02$ at $Re = 250$) between $Re = 250 - 760$. $U_p = (\alpha_r U + \beta W)/k$ and the absolute value of the streamwise and spanwise disturbance velocity are denoted u and w respectively. The streamwise positions are: $Re = 262$ in figures (a–b) and $Re = 694$ in figures (c–d)

case with $l^2 = 10^2$ shows a strong streamwise variation in the upstream domain. In figure 11(*d*) the objective function is plotted for each iteration in the optimization loop to demonstrate the convergence of the optimization process.

In this analysis only one oblique wave has been considered. The effects on the growth rate on other oblique waves are investigated using the suction distribution from the analysis above with $l^2 = 10^2$. This is done by computing the local growth rate in the $F - \beta$ plane at two different streamwise positions. Contours of the local growth rate can be seen in figure 12 where the thick contours mark zero growth rate and the ● marks the oblique wave analyzed in figure 11. Note here that the reduced frequency F, the non-dimensional spanwise wavenumber β and the growth rate are scaled with the reference values taken at X_0. Figure 12(*a*) shows the local growth rate for oblique waves

at $Re = 418$ with zero suction. Here it is shown that the disturbance analyzed in figure 11 is close to the maximum growth rate for all oblique waves at this streamwise position. No figure is shown for the case when optimal suction is applied as all waves are damped at this position. The result in figures 12(b–c) correspond to $Re = 676$ with the mean flow subjected to zero and optimal suction respectively. The optimal suction is shown to make all oblique waves more stable. However, the effect is less than in the upstream region.

It is also of interest to see how the inflection point due to the adverse pressure gradient is affected by the optimal suction. The suction distributions shown in figure 11(a) are similar except for the upstream region. Therefore, the case of figure 11 with $l^2 = 10^5$ is chosen to see if the smallest amount of suction still affects the inflection point of the mean flow. The results for two different streamwise positions are seen in figure 13. Here the mean flow has been projected in the direction of the wavenumber vector $\mathbf{k}$, with absolute value $k = (\alpha^2 + \beta^2)^{\frac{1}{2}}$, and is given as $U_p = (\alpha U + \beta W)/k$. In figure 13($a$) U_p and its corresponding second wall normal derivative are shown at $Re = 262$. The effect of the optimal suction is small but increases the velocity inside the boundary layer. The plot of the second wall normal derivative of U_p shows that the inflection point has almost disappeared. The effect on the disturbance velocities due to the mean flow modification at $Re = 262$ is shown in figure 13(b). Here, the absolute value of the streamwise and spanwise disturbance velocities are plotted. Both components have kept their shape but the maximum values are decreased and moved towards the wall. The quantities in figures 13(a–b) are plotted at $Re = 694$ in figures 13(c–d) respectively. At this streamwise position all suction distributions shown in figure 11(a) are similar and therefore are the mean flow modifications at this position similar for all cases shown in figure 11. The mean flow component shown in figure 13(c) have become fuller. However, the inflection point of the streamwise component does still exist but has moved towards the wall. The maximum value of the disturbance velocities shown in figure 13(d) have moved closer to the wall and decreased by a factor of 10^3. Further, it is noted that the disturbance shape has been kept also here.

3.3.2. *Control in a flow with a favorable pressure gradient*

The control of a steady cross-flow mode is analyzed in a quasi three-dimensional incompressible boundary layers with a favorable pressure gradient taken from Högberg & Henningson (1998) ($U_e = (x/x_0)^{0.34207}$). The streamwise range is $Re = 346 - 746$ and the inviscid flow at $Re = 346$ has an angle of 55.26^o. Here, the control has been applied at $Re = 351 - 741$. The initial condition of the disturbance is taken as the local solution at $Re = 346$ where the non-dimensional spanwise wavenumber is $\beta = -0.256$.

In figure 14 results are presented for the optimization with different values of the regularization parameter l^2. Here, $l^2 = 10^3$ gives a maximum suction velocity which is close to the maximum value for which the boundary layer equations are valid (see § 2.1.1). The optimal suction distributions due to the
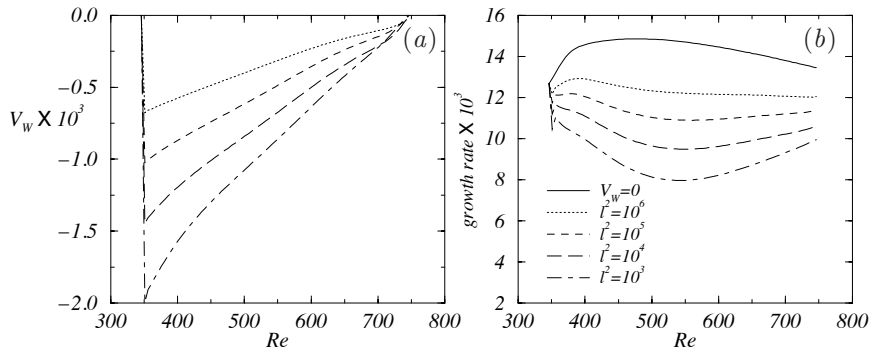
FIGURE 14. Control of a stationary cross-flow mode in a three-dimensional boundary layer with a favorable pressure gradient $(U_e = (x/x_0)^{0.34207})$. The inviscid flow at $Re = 346$ has an angle of 55.26^o and the non-dimensional spanwise wavenumber $\beta = -0.256$. Results are presented for $l^2 = 10^3, 10^4, 10^5, 10^6$. (*a*) Optimal suction distributions. (*b*) Growth rate -imag(α).

variation of l^2 are shown in figure 14(*a*). As l^2 is decreased the magnitude of the suction velocity is increased. The maximum of the suction velocity is found in the upstream region in all cases but does not appear as a pronounced peak as was shown in § 3.2 and § 3.3.1.

The corresponding growth rates for zero and optimal suction are presented in figure 14(*b*). The uncontrolled steady cross-flow mode studied here has a positive growth rate in the whole domain and it is shown here that the optimal suction manages to reduce the growth rate. However, not even the largest magnitude of steady optimal suction, i. e. the smallest l^2, can stabilize the cross-flow mode. The largest reduction of growth rate is found at approximately the same streamwise position regardless of l^2 and it should be noted that this is far downstream of the point where suction has its maximum.

The results shown in § 3 have not been computed given a certain amount of control energy. Instead has the regularization parameter l^2, given in (9), been used to balance the measured disturbance kinetic energy and the control energy. In practice this means that increasing l^2 will decrease the available control energy and vice verse in the optimization process. In an application of this theory it might be of interest to see how the benefit (reduction in disturbance kinetic energy) is related to a certain amount of control energy. This can be seen in figure 15(*a*) for all cases studied in § 3. Here, the benefit is given as the ratio between the disturbance kinetic energies for optimal and zero suction denoted as E_{opt} and E, respectively. The corresponding relation between l^2 and the benefit is given in figure 15(*b*).
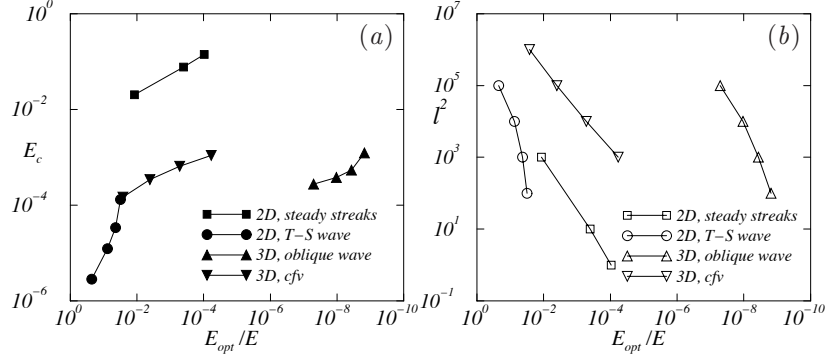
FIGURE 15. Relation between reduction in disturbance kinetic energy and (a) optimal control energy E_c, (b) the regularization parameter l^2. Here E_{opt} and E are the disturbance kinetic energies given optimal and zero suction respectively.

4. Discussion and conclusions

A procedure to control disturbances in quasi three-dimensional incompressible boundary layers on a flat plate has been derived and analyzed. Here, control of disturbances is done by modifying the mean flow using the wall normal velocity component of the mean flow on the wall. The optimization procedure is gradient based and the aim is to minimize an objective function balancing a measure of the state and the control energy. The gradient is derived using adjoint equations and here it is shown how the coupling is done between the adjoint of the PSE (APSE) and the adjoint of the boundary layer equations (ABLE). The measure of the state is the disturbance kinetic energy in the whole domain and here it has been generalized to account for more than one disturbance.

To increase the streamwise resolution, a stabilization procedure has been used for the PSE which modifies both the APSE and the ABLE. The gradients derived using the adjoint equations has been validated with a finite-difference approach and it has been shown that the gradient accuracy is increased as the streamwise resolution is increased. A finite-difference check has also been continuously done on the final gradients in the optimization indicating that the continuous approach used for the derivation of the adjoint equations has been adequate.

Numerical results have been presented for disturbance control in both two and quasi three-dimensional incompressible boundary layers. The results shown on suction distributions have a similar shape for control of T-S wave instabilities and steady optimally growing streamwise streaks in two-dimensional boundary layers and oblique waves in quasi three-dimensional boundary layers. The suction profiles tend to peak close to the first point of the computational domain but become significantly smaller and rather constant further downstream. This

tendency become more pronounced as the penalty of the control l^2 is reduced, i. e. the freedom of the control is increased. Although the magnitudes of the suction distributions are of order $V_\mathrm{w} \sim O(Re^{-1})$, care must be taken as a decrease in l^2 may result in large streamwise variations of both V_w and the growth rate. Caution must be taken so that this variation is small enough not to contradict the underlying hypothesis of a slow streamwise variation assumed in both the BLE and PSE.

If solutions without sharp peaks are desired then additional terms can be added to the objective function in which a penalty is put on e. g. the streamwise derivative of the control variable. This procedure has been used in e. g. shape optimization problems where the goal has been to create not only an optimal geometry but also with a certain degree of smoothness. Such constrains are not investigated here as they are more connected to user applications and an extension of the optimal control theory rather than the methodology itself.

In both two- and quasi three dimensional boundary layers it has been shown that the boundary layer velocity profiles have become fuller as the optimal suction distribution is applied. Both of these observations show that the stabilization obtained by the suction distribution is a modification of the mean flow similar to that of a flow with a favorable pressure gradient with zero suction. The relation between the suction velocity, pressure gradient and second wall normal derivative of the streamwise velocity on the wall is understood by looking at (2) for $y = 0$

$$V_\mathrm{w}\frac{\partial U}{\partial y} + \frac{\mathrm{d}P_e}{\mathrm{d}x} = \frac{1}{Re}\frac{\partial^2 U}{\partial y^2}. \tag{29}$$

In the case of a Blasius mean flow $(\mathrm{d}P_e/\mathrm{d}x = 0)$, the right hand side of (29) give the favorable pressure gradient which corresponds to a certain suction velocity. However, in the case of an adverse pressure gradient $(\mathrm{d}P_e/\mathrm{d}x > 0)$, the modification is dependent on the magnitude of the suction velocity as neither of the two terms on the left hand side of (29) is zero. Here, a favorable pressure gradient is only obtained if $V_\mathrm{w}\partial U/\partial y < \mathrm{d}P_e/\mathrm{d}x$. A stabilizing effect will still occur if $V_\mathrm{w}\partial U/\partial y > \mathrm{d}P_e/\mathrm{d}x$ but the location of the inflection point due to the adverse pressure gradient will be dependent of the magnitude of V_w.

As a result of the optimal suction distribution, the disturbance kinetic energy is decreased as the control energy is increased (here shown by decreasing l^2). For control of T-S waves in two-dimensional boundary layers and oblique waves in quasi three-dimensional boundary layers, the growth rate has the largest decrease in the upstream domain when l^2 is decreased. This corresponds to where the optimal suction has its peak. In the case control is applied to the steady cross-flow mode, the largest decrease in growth rate is positioned at the same streamwise location independent of l^2. Further, this is far downstream of the point where the suction has its maximum. For T-S wave instabilities in the Blasius flow it has been shown that essentially the same energy reduction at the last streamwise point is achieved when the control is applied in the whole

unstable region compared to control which starts just upstream and ends just downstream of the unstable region.

One of the assumptions made in this analysis is that the disturbances have homogeneous boundary conditions at the wall and therefore no coupling to the mean flow at the wall. This can be interpreted as uniform suction through a porous material. The validity of these boundary conditions should be analyzed if instead discrete holes are used.

Appendix A. Matrices of the PSE

The matrices A, B, C and D in the PSE are given as

$$
A = \begin{bmatrix} i\alpha & 0 & i\beta & 0 \\ \xi + \dfrac{\partial U}{\partial x} & \dfrac{\partial U}{\partial y} & 0 & i\alpha \\ 0 & \xi + \dfrac{\partial V}{\partial y} & 0 & 0 \\ \dfrac{\partial W}{\partial x} & \dfrac{\partial W}{\partial y} & \xi & i\beta \end{bmatrix}, \quad
B = \begin{bmatrix} 0 & 1 & 0 & 0 \\ V & 0 & 0 & 0 \\ 0 & V & 0 & 1 \\ 0 & 0 & V & 0 \end{bmatrix},
$$

$$
C = \begin{bmatrix} 0 & 0 & 0 & 0 \\ -\dfrac{1}{Re} & 0 & 0 & 0 \\ 0 & -\dfrac{1}{Re} & 0 & 0 \\ 0 & 0 & -\dfrac{1}{Re} & 0 \end{bmatrix}, \quad
D = \begin{bmatrix} 1 & 0 & 0 & 0 \\ U & 0 & 0 & 1 \\ 0 & U & 0 & 0 \\ 0 & 0 & U & 0 \end{bmatrix},
$$

where

$$
\xi = -i\omega + i\alpha U + i\beta W + \frac{1}{Re}(\alpha^2 + \beta^2).
$$

Appendix B. Derivation of adjoint equations

The gradient of the objective function, J, with respect to the wall normal velocity component of the mean flow on the wall, V_{w}, is derived using the APSE and the ABLE. The question is whether to use a 'discrete' or 'continuous' formulation. One of the conclusions in Högberg & Berggren (2000) was that a continuous formulation is a good enough approximation if control is performed on a problem with a dominating instability. Here, the analysis is done for dominating instabilities using the PSE why a continuous approach has been chosen for the derivation of the adjoint equations.

B.1. *Inner Product*

For a compact notation of the adjoint equations, we will use the *formal adjoint* L^* for the differential operator L defined by the relation

$$(\psi, L\phi) = (L^*\psi, \phi) + \text{ boundary terms}, \qquad (30)$$

where the inner product $(\cdot, \cdot)$ is defined as

$$(\phi, \psi) = \int_{Z_0}^{Z_1} \int_{X_0}^{X_1} \int_0^\infty \phi^H \psi \, dy \, dx \, dz, \qquad (31)$$

for $\mathbb{C}^n$-valued functions ϕ and ψ. Here, the superscript * denotes adjoint quantities and ψ is denoted the *co-state variable* which is chosen such that it satisfies the adjoint equations $L^*\psi = 0$.

B.2. *Derivation of the gradient*

The idea behind the derivation is to identify the gradient from the boundary terms in (30). There are earlier results on the derivation of the APSE (see Airiau 2000; Hill 1997a), however in this analysis, as in Pralits *et al.* (2000), the approach is somewhat different.

Here, we use a perturbation technique together with integration by parts in space. The APSE are derived directly from the PSE why also the auxiliary condition has to be taken into account. Further, there is no ansatz made on the co-state variables of the PSE such as (5). In this way a method has been introduced to derive the APSE which provides the corresponding adjoint auxiliary condition. The details of the derivation is given below. First, the objective function and the state equations are differentiated with respect to the control V_{w}. Differentiating (9) and (6)–(7) yields

$$\delta J = \mathrm{real}\Big\{ \int_{Z_0}^{Z_1} \int_{X_0}^{X_1} \int_0^\infty \delta \mathbf{u}^H \mathbf{u} \, dy \, dx \, dz + l^2 \int_{Z_0}^{Z_1} \int_{X_0}^{X_1} \delta V_{\mathrm{w}} V_{\mathrm{w}} \, dx \, dz \Big\}, \quad (32)$$

$$A\delta\hat{q} + B\frac{\partial \delta\hat{q}}{\partial y} + C\frac{\partial^2 \delta\hat{q}}{\partial y^2} + D\frac{\partial \delta\hat{q}}{\partial x} +$$
$$\Big(\frac{\partial A}{\partial Q}\delta Q + \frac{\partial A}{\partial \alpha}\delta\alpha + \frac{\partial B}{\partial Q}\delta Q + \frac{\partial D}{\partial Q}\delta Q \Big)\hat{q} = 0, \qquad (33)$$

$$\int_0^\infty (\delta\hat{\mathbf{u}}^H \frac{\partial \hat{\mathbf{u}}}{\partial x} + \hat{\mathbf{u}}^H \frac{\partial \delta\hat{\mathbf{u}}}{\partial x}) \, dy = 0. \qquad (34)$$

The variations, δq, δQ are the variations of q, Q caused by the variation of V_{w}. Note also that the variation of q results in a variation of both the amplitude function $\hat{q}$ and the streamwise wave-number α as

$$\delta q = \delta\hat{q}\,\Theta + \hat{q}\,\Theta \int_{X_0}^{x'} \delta\alpha \, dx', \qquad (35)$$

where

$$\Theta = \exp \mathrm{i}\Big(\int_{X_0}^{x'} \alpha \, dx' + \beta z - \omega t \Big).$$

Proceed by differentiating (1)–(3). This is given on a compact form as

$$\frac{\partial L_{BLE}}{\partial Q} \delta Q Q + L_{BLE}\, \delta Q = 0. \tag{36}$$

Now, introduce the complex functions $q^* = (p^*, u^*, v^*, w^*)^T$ and r^*, the so called co-state variables, which are multiplied with (33)–(34) respectively according to (31). Then (36) are multiplied with the co-state variables $Q^* = (V^*, U^*, W^*)^T$ in the same manner. The corresponding left hand side of (30) can now be written

$$
\int_{Z_0}^{Z_1} \int_{X_0}^{X_1} \int_0^\infty q^{*H}\Big(A\delta\hat{q} + B\frac{\partial \delta\hat{q}}{\partial y} + C\frac{\partial^2 \delta\hat{q}}{\partial y^2} + D\frac{\partial \delta\hat{q}}{\partial x} + \frac{\partial A}{\partial Q}\delta Q\hat{q} + \frac{\partial A}{\partial \alpha}\delta\alpha\hat{q} +
$$
$$
\frac{\partial B}{\partial Q}\delta Q\hat{q} + \frac{\partial D}{\partial Q}\delta Q\hat{q}\Big)\, \mathrm{d}y\, \mathrm{d}x\, \mathrm{d}z + \text{c.c.} +
$$
$$
\int_{Z_0}^{Z_1} \int_{X_0}^{X_1} \int_0^\infty \Big(\bar{r}^*\big(\delta\hat{\boldsymbol{u}}^H\frac{\partial\hat{\boldsymbol{u}}}{\partial x} + \hat{\boldsymbol{u}}^H\frac{\partial\delta\hat{\boldsymbol{u}}}{\partial x}\big) + r^*\big(\delta\hat{\boldsymbol{u}}^T\frac{\partial\bar{\hat{\boldsymbol{u}}}}{\partial x} + \hat{\boldsymbol{u}}^T\frac{\partial\delta\bar{\hat{\boldsymbol{u}}}}{\partial x}\big)\Big)\, \mathrm{d}y\, \mathrm{d}x\, \mathrm{d}z +
$$
$$
\int_{Z_0}^{Z_1} \int_{X_0}^{X_1} \int_0^\infty Q^{*T}\Big(\frac{\partial L_{BLE}}{\partial Q}\delta Q Q + L_{BLE}\delta Q\Big)\, \mathrm{d}y\, \mathrm{d}x\, \mathrm{d}z \tag{37}
$$

The right hand side of (30) is derived by removing the derivatives from the differentiated state equations using integration by parts in Ω. Note here that the co-state variable r^* has been introduced due to the additional equation, (7), of the PSE. Further, the complex conjugate has been added as the gradient by definition, (11), is a real-valued function. Here, the complex conjugate is written out explicitly for the auxiliary condition. Note here that terms in (37) of $\delta\alpha$ now must be integrated in the x-direction in order to obtain the same integral form as in (35).

After collecting terms of $\delta\hat{\mathbf{u}}, \delta\hat{q}, \delta Q$ and $\int_{X_0}^{x'} \delta\alpha \ dx'$, the right hand side including boundary terms is written

$$\int_{Z_0}^{Z_1} \int_{X_0}^{X_1} \int_0^\infty \left(A^H q^* - B^H \frac{\partial q^*}{\partial y} + C^H \frac{\partial^2 q^*}{\partial y^2} - D^H \frac{\partial q^*}{\partial x} \right) \delta\hat{q} \ dy \ dx \ dz + \text{c.c.} +$$

$$\int_{Z_0}^{Z_1} \int_{X_0}^{X_1} \int_0^\infty \left((r^* - \bar{r}^*) \frac{\partial\bar{\hat{\mathbf{u}}}}{\partial x} + \frac{\partial\bar{r}^*}{\partial x} \bar{\hat{\mathbf{u}}} \right) \delta\hat{\mathbf{u}} \ d\mathbf{y} \ d\mathbf{x} \ d\mathbf{z} + \text{c.c.} +$$

$$\int_{Z_0}^{Z_1} \int_{X_0}^{X_1} \int_0^\infty \left(L_{BLE}^*(Q) Q^* - f_{ABLE} \right) \delta Q \ dy \ dx \ dz -$$

$$\int_{Z_0}^{Z_1} \int_{X_0}^{X_1} \int_0^\infty \frac{\partial}{\partial x} \left(q^{*H} \frac{\partial A}{\partial\alpha} \hat{q} \right) \int_{X_0}^{x'} \delta\alpha \ dx' \ dy \ dx \ dz +$$

$$\int_{Z_0}^{Z_1} \int_{X_0}^{X_1} \int_0^\infty U_e \frac{\partial U^*}{\partial x} \delta U_e \ dy \ dx \ dz +$$

$$\int_{Z_0}^{Z_1} \int_0^\infty \left(\left[q^{*H} D\delta\hat{q} + \bar{r}^* \hat{\mathbf{u}}^H \delta\hat{\mathbf{u}} + q^{*H} \frac{\partial A}{\partial\alpha} \hat{q} \int_{X_0}^{x'} \delta\alpha \ dx' + \bar{u}^* \hat{u} \delta U + \bar{w}^* \hat{u} \delta W \right.\right.$$

$$\left.\left. + V^* \delta U + UU^* \delta U + U^* \delta P + W^* U \delta W - U^* U_e \delta U_e \right]_{X_0}^{X_1} \right) dy \ dz +$$

$$\int_{Z_0}^{Z_1} \int_{X_0}^{X_1} \left(\left[q^{*H} B\delta\hat{q} + q^{*H} C \frac{\partial\delta\hat{q}}{\partial y} - \frac{\partial(q^{*H}C)}{\partial y} \delta\hat{q} + \bar{u}^* \hat{v} \delta U + \bar{v}^* \hat{v} \delta V + \right.\right.$$

$$\bar{w}^* \hat{v} \delta W + V^* \delta V + VU^* \delta U + W^* V \delta W +$$

$$\left.\left. \frac{1}{Re} \left(U_y^* \delta U + W_y^* \delta W - W^* \delta W_y - U^* \delta U_y \right) \right]_0^\infty \right) dx \ dz \qquad (38)$$

Here, f_{ABLE} are the terms due the δQ in the PSE. In order to identify the objective function (32) in (38), we add and subtract the energy norm in (38). Using (35), this additional term can be written

$$\int_{Z_0}^{Z_1} \int_{X_0}^{X_1} \int_0^\infty (\delta\mathbf{u}^H \mathbf{u} - \delta\hat{\mathbf{u}}^H \hat{\mathbf{u}} |\Theta|^2 - \mathrm{i}|\hat{\mathbf{u}}|^2 \int_{X_0}^{x'} \delta\alpha \ dx' |\Theta|^2) \ dy \ dx \ dz + \text{c.c.} \quad (39)$$

Now impose the following boundary conditions on the state and co-state variables

$$
\begin{array}{lll}
\delta\hat{u} = \delta\hat{v} = \delta\hat{w} = 0 & \text{at} & y = 0 \\
\delta\hat{u}, \delta\hat{v}, \delta\hat{w}, \delta\hat{p} \to 0 & \text{as} & y \to \infty \\
\delta\hat{u} = \delta\hat{v} = \delta\hat{w} = \delta\hat{p} = 0 & \text{at} & x = X_0 \\
\delta\,U = \delta\,W = 0 & \text{at} & y = 0 \\
\delta\,U, \delta\,W \to 0 & \text{as} & y \to \infty \\
\delta U = \delta W = \delta U_e = 0 & \text{at} & x = X_0
\end{array}
$$

$$u^* = v^* = w^* = 0 \quad \text{at} \quad y = 0$$
$$u^*, v^*, w^*, p^* \to 0 \quad \text{as} \quad y \to \infty$$
$$U^* = W^* = 0 \quad \text{at} \quad y = 0$$
$$U^*, V^*, W^* \to 0 \quad \text{as} \quad y \to \infty$$

Let q^* and r^* satisfy the equations given by $\delta\mathbf{u}, \delta\hat{q}$ and $\int_{X_0}^{x'} \delta\alpha \, dx'$. Further, let Q^* satisfy the equations given by δQ. This is written explicitly as

$$\bar{p}^* i\alpha - \frac{\partial \bar{p}^*}{\partial x} + \frac{\partial \bar{u}^*}{\partial y} V - \frac{\partial \bar{u}^*}{\partial x} U + \bar{w}^* \frac{\partial W}{\partial x} - \frac{1}{Re} \frac{\partial^2 \bar{u}^*}{\partial y^2} +$$
$$\bar{u}^* \left[-i\omega + i\alpha U + \frac{\partial U}{\partial x} + i\beta W + \frac{1}{Re}(\alpha^2 + \beta^2) \right] =$$
$$-(r^* - \bar{r^*}) \frac{\partial \hat{\bar{u}}}{\partial x} + \frac{\partial \bar{r^*}}{\partial x} \hat{\bar{u}} + \hat{\bar{u}} |\Theta|^2, \tag{40}$$

$$\frac{\partial \bar{p}^*}{\partial y} + \bar{u}^* \frac{\partial U}{\partial y} - \frac{\partial \bar{v}^*}{\partial y} V - \frac{\partial \bar{v}^*}{\partial x} U + \bar{w}^* \frac{\partial W}{\partial y} - \frac{1}{Re} \frac{\partial^2 \bar{v}^*}{\partial y^2} +$$
$$\bar{v}^* \left[-i\omega + i\alpha U + \frac{\partial V}{\partial y} + i\beta W + \frac{1}{Re}(\alpha^2 + \beta^2) \right] =$$
$$-(r^* - \bar{r^*}) \frac{\partial \hat{\bar{v}}}{\partial x} + \frac{\partial \bar{r^*}}{\partial x} \hat{\bar{v}} + \hat{\bar{v}} |\Theta|^2, \tag{41}$$

$$\bar{p}^* i\beta - \frac{\partial \bar{w}^*}{\partial y} V - \frac{\partial \bar{w}^*}{\partial x} U - \frac{1}{Re} \frac{\partial^2 \bar{w}^*}{\partial y^2} +$$
$$\bar{w}^* \left[-i\omega + i\alpha U + i\beta W + \frac{1}{Re}(\alpha^2 + \beta^2) \right] =$$
$$-(r^* - \bar{r^*}) \frac{\partial \hat{\bar{w}}}{\partial x} + \frac{\partial \bar{r^*}}{\partial x} \hat{\bar{w}} + \hat{\bar{w}} |\Theta|^2, \tag{42}$$

$$-\frac{\partial \bar{u}^*}{\partial x} + \bar{u}^* i\alpha - \frac{\partial \bar{v}^*}{\partial y} + \bar{w}^* i\beta = 0, \tag{43}$$

$$\frac{\partial}{\partial x} \int_0^\infty \left(i(\bar{p}^* \hat{u} + \bar{u}^* \hat{p}) + (iU + \frac{2\alpha}{Re})(\bar{u}^* \hat{u} + \bar{v}^* \hat{v} + \bar{w}^* \hat{w}) \right) dy +$$
$$i|\Theta|^2 \int_0^\infty |\hat{\mathbf{u}}|^2 \, dy = 0, \tag{44}$$

$$\frac{\partial V^*}{\partial y} - \frac{\partial U}{\partial y} U^* - W^* \frac{\partial W}{\partial y} = \text{real}\left\{ \bar{u}^* \frac{\partial \hat{u}}{\partial y} - \frac{\partial \bar{v}^*}{\partial y} \hat{v} + \bar{w}^* \frac{\partial \hat{w}}{\partial y} \right\}, \tag{45}$$

$$\frac{\partial V^*}{\partial x} + U \frac{\partial U^*}{\partial x} + \frac{\partial V}{\partial y} U^* + V \frac{\partial U^*}{\partial y} - W^* \frac{\partial W}{\partial x} + \frac{1}{Re} \frac{\partial^2 U^*}{\partial y^2} =$$
$$\text{real}\left\{ i\alpha[\bar{u}^* \hat{u} + \bar{v}^* \hat{v} + \bar{w}^* \hat{w}] - \frac{\partial \bar{u}^*}{\partial x} \hat{u} - \frac{\partial \bar{u}^*}{\partial y} \hat{v} - \bar{u}^* \frac{\partial \hat{v}}{\partial y} + \bar{v}^* \frac{\partial \hat{v}}{\partial x} + \bar{w}^* \frac{\partial \hat{w}}{\partial x} \right\}, \tag{46}$$

$$\frac{\partial W^*}{\partial x}U + \frac{\partial W^*}{\partial y}V + \frac{1}{Re}\frac{\partial^2 W^*}{\partial y^2} =$$

$$\text{real}\Big\{\text{i}\beta[\bar{u}^*\hat{u} + \bar{v}^*\hat{v} + \bar{w}^*\hat{w}] - \frac{\partial \bar{w}^*}{\partial x}\hat{u} - \bar{w}^*\frac{\partial \hat{u}}{\partial x} - \frac{\partial \bar{w}^*}{\partial y}\hat{v} - \bar{w}^*\frac{\partial \hat{v}}{\partial y}\Big\}. \quad (47)$$

Equations (40)–(44) are the adjoint of the parabolized stability equation, APSE. The right hand side of (40)–(42), here denoted f_{APSE}, comes from the auxiliary condition (7) and the objective function (9). Equation (44) solves the additional unknown co-state variable r^* iteratively at each streamwise position. Equations (45)–(47) are the adjoint of the boundary layer equations, ABLE. The inhomogeneous right hand side, denoted f_{ABLE}, is calculated from the solution of the PSE and the APSE. However, only the real part is used as the left hand side consists of real-valued equations. The remaining boundary terms in (38) come from the boundary $x = X_1$ and the term of δV at $y = 0$. We impose the initial condition of both the ABLE and APSE to be zero at $x = X_1$. This does however not cause trivial solutions as both (40)–(44) and (45)–(47) have a non-zero right hand side in Ω. The remaining terms from (38) can now be written

$$\text{real}\Big\{\delta J - \int_{Z_0}^{Z_1}\int_{X_0}^{X_1}\Big((l^2 V_\text{w} + V_\text{w}^*)\delta V_\text{w}\Big)\,\text{d}x\,\text{d}z +$$

$$\int_{Z_0}^{Z_1}\int_{X_0}^{X_1}\int_0^\infty U_e\frac{\partial U^*}{\partial x}\delta U_e\,\text{d}y\,\text{d}x\,\text{d}z\Big\}= 0. \quad (48)$$

Index $_\text{w}$, here denotes the value at $y = 0$. Equation (48) can now be rewritten as

$$\delta J = \int_{Z_0}^{Z_1}\int_{X_0}^{X_1}\Big((l^2 V_\text{w} + V_\text{w}^*)\delta V_\text{w}\Big)\,\text{d}x\,\text{d}z -$$

$$\int_{Z_0}^{Z_1}\int_{X_0}^{X_1}\int_0^\infty U_e\frac{\partial U^*}{\partial x}\delta U_e\,\text{d}y\,\text{d}x\,\text{d}z. \quad (49)$$

If the first term on the right hand side of (49) is written, using (11) as

$$\delta J = \int_{Z_0}^{Z_1}\int_{X_0}^{X_1}\nabla_{V_\text{w}}J\,\delta V_\text{w}\,\text{d}x\,\text{d}z, \quad (50)$$

then the gradient of the objective function with respect to the wall normal velocity component of the mean flow at the wall can be identified as

$$\nabla_{V_\text{w}}J = l^2 V_\text{w} + V_\text{w}^* \quad \text{on} \quad y = 0. \quad (51)$$

The second term on the right hand side of (49) is the variation of the objective function due a variation of the free stream velocity. If a similar gradient definition as in (50) is used for U_e

$$\delta J = \int_{Z_0}^{Z_1}\int_{X_0}^{X_1}\int_0^\infty \nabla_{U_e}J\,\delta U_e\,\text{d}y\,\text{d}x\,\text{d}z, \quad (52)$$

then the gradient of the objective function with respect to the free stream velocity can be written

$$\nabla_{U_e} J = -U_e \int_0^\infty \frac{\partial U^*}{\partial x} \, \mathrm{d}y. \tag{53}$$

The variation U_e would be the consequence of e. g. a change in the geometry and consequently the free stream pressure, and is therefore not considered in this paper.

B.3. *Derivation of the gradient including stabilization*

The derivation of the gradient including the stabilization terms does not differ much from the derivation done in B.2. The same definition of the adjoint, (30), and inner product, (31), are used. The difference becomes clear if the stabilization terms are added to (37). This can be written

$$\int_{Z_0}^{Z_1} \int_{X_0}^{X_1} \int_0^\infty q^{*H} \Big(A\delta\hat{q} + B\frac{\partial\delta\hat{q}}{\partial y} + C\frac{\partial^2\delta\hat{q}}{\partial y^2} + D\frac{\partial\delta\hat{q}}{\partial x} + \frac{\partial A}{\partial Q}\delta Q\hat{q} + \frac{\partial A}{\partial\alpha}\delta\alpha\hat{q} +$$

$$\frac{\partial B}{\partial Q}\delta Q\hat{q} + \frac{\partial D}{\partial Q}\delta Q\hat{q} \Big) \, \mathrm{d}y \, \mathrm{d}x \, \mathrm{d}z + \text{c.c.} +$$

$$s\int_{Z_0}^{Z_1} \int_{X_0}^{X_1} \int_0^\infty q^{*H} \Big(A\frac{\partial\delta\hat{q}}{\partial x} + B\frac{\partial}{\partial x}\Big(\frac{\partial\delta\hat{q}}{\partial y}\Big) + C\frac{\partial}{\partial x}\Big(\frac{\partial^2\delta\hat{q}}{\partial y^2}\Big) + \frac{\partial A}{\partial Q}\delta Q\frac{\partial\delta\hat{q}}{\partial x} +$$

$$\frac{\partial A}{\partial\alpha}\delta\alpha\frac{\partial\delta\hat{q}}{\partial x} + \frac{\partial B}{\partial Q}\delta Q\frac{\partial\delta\hat{q}}{\partial x} \Big) \, \mathrm{d}y \, \mathrm{d}x \, \mathrm{d}z + \text{c.c.} +$$

$$\int_{Z_0}^{Z_1} \int_{X_0}^{X_1} \int_0^\infty \Big(\bar{r}^* \big(\delta\hat{\boldsymbol{u}}^H\frac{\partial\hat{\boldsymbol{u}}}{\partial x} + \hat{\boldsymbol{u}}^H\frac{\partial\delta\hat{\boldsymbol{u}}}{\partial x} \big) + r^* \big(\delta\hat{\boldsymbol{u}}^T\frac{\partial\bar{\hat{\boldsymbol{u}}}}{\partial x} + \hat{\boldsymbol{u}}^T\frac{\partial\delta\bar{\hat{\boldsymbol{u}}}}{\partial x} \big) \Big) \, \mathrm{d}y \, \mathrm{d}x \, \mathrm{d}z +$$

$$\int_{Z_0}^{Z_1} \int_{X_0}^{X_1} \int_0^\infty Q^{*T} \Big(\frac{\partial L_{BLE}}{\partial Q}\delta Q Q + L_{BLE}\delta Q \Big) \, \mathrm{d}y \, \mathrm{d}x \, \mathrm{d}z \tag{54}$$

The new terms only appear in the second integral expression in (54). However, this expression includes $\delta\hat{q}$, $\delta\alpha$ and δQ why (40)–(44) and (45)–(47) will all have additional terms due to s. The full derivation of the gradient using (54) is not necessary due to the resemblance between (37) and (54). Instead, it suffices to evaluate the additional terms associated with the stabilization. This is done following the steps in B.2 and yields

$$s\Big(\frac{\partial\bar{p}^*}{\partial x}\mathrm{i}\alpha - \frac{\partial^2\bar{u}^*}{\partial x\partial y}V + \frac{\partial\bar{w}^*}{\partial x}\frac{\partial W}{\partial x} - \frac{\partial\bar{u}^*}{\partial x}\frac{\partial V}{\partial y} - \frac{1}{Re}\frac{\partial^3\bar{u}^*}{\partial x\partial y^2} +$$

$$\frac{\partial\bar{u}^*}{\partial x}\Big[-\mathrm{i}\omega + \mathrm{i}\alpha U + \frac{\partial U}{\partial x} + \mathrm{i}\beta W + \frac{1}{Re}(\alpha^2 + \beta^2) \Big] \Big), \tag{55}$$

$$s\Big(-\frac{\partial^2\bar{p}^*}{\partial x\partial y} + \frac{\partial\bar{u}^*}{\partial x}\frac{\partial U}{\partial y} - \frac{\partial^2\bar{v}^*}{\partial x\partial y}V - \frac{\partial\bar{v}^*}{\partial x}\frac{\partial V}{\partial y} + \frac{\partial\bar{w}^*}{\partial x}\frac{\partial W}{\partial y} - \frac{1}{Re}\frac{\partial^3\bar{v}^*}{\partial x\partial y^2} +$$

$$\frac{\partial\bar{v}^*}{\partial x}\Big[-\mathrm{i}\omega + \mathrm{i}\alpha U + \frac{\partial V}{\partial y} + \mathrm{i}\beta W + \frac{1}{Re}(\alpha^2 + \beta^2) \Big] \Big), \tag{56}$$

$$s\Big(\frac{\partial \bar{p}^*}{\partial x}\mathrm{i}\beta - \frac{\partial^2 \bar{w}^*}{\partial x \partial y}V - \frac{\partial \bar{w}^*}{\partial x}\frac{\partial V}{\partial y} - \frac{1}{Re}\frac{\partial^3 \bar{w}^*}{\partial x \partial y^2} +$$
$$\frac{\partial \bar{w}^*}{\partial x}\Big[-\mathrm{i}\omega + \mathrm{i}\alpha U + \mathrm{i}\beta W + \frac{1}{Re}(\alpha^2 + \beta^2)\Big]\Big), \tag{57}$$

$$s\Big(\frac{\partial \bar{u}^*}{\partial x}\mathrm{i}\alpha - \frac{\partial^2 \bar{v}^*}{\partial x \partial y} + \frac{\partial \bar{w}^*}{\partial x}\mathrm{i}\beta\Big), \tag{58}$$

$$s\int_0^\infty \Big(\frac{\partial}{\partial x}\Big[\mathrm{i}(\bar{p}^*\frac{\partial \hat{u}}{\partial x} + \bar{u}^*\frac{\partial \hat{p}}{\partial x}) + (\mathrm{i}U + \frac{2\alpha}{Re})(\bar{u}^*\frac{\partial \hat{u}}{\partial x} + \bar{v}^*\frac{\partial \hat{v}}{\partial x} + \bar{w}^*\frac{\partial \hat{w}}{\partial x})\Big]\Big)\,\mathrm{d}y, \tag{59}$$

$$s\Big(\mathrm{real}\Big\{\bar{u}^*\frac{\partial^2 \hat{u}}{\partial x \partial y} - \frac{\partial \bar{v}^*}{\partial y}\frac{\partial \hat{v}}{\partial x} + \bar{w}^*\frac{\partial^2 \hat{w}}{\partial x \partial y}\Big\}\Big), \tag{60}$$

$$s\Big(\mathrm{real}\Big\{\mathrm{i}\alpha[\bar{u}^*\frac{\partial \hat{u}}{\partial x} + \bar{v}^*\frac{\partial \hat{v}}{\partial x} + \bar{w}^*\frac{\partial \hat{w}}{\partial x}] - \frac{\partial}{\partial x}\Big(\bar{u}^*\frac{\partial \hat{u}}{\partial x}\Big) - \frac{\partial}{\partial y}\Big(\bar{u}^*\frac{\partial \hat{v}}{\partial x}\Big)\Big\}\Big), \tag{61}$$

$$s\Big(\mathrm{real}\Big\{\mathrm{i}\beta[\bar{u}^*\frac{\partial \hat{u}}{\partial x} + \bar{v}^*\frac{\partial \hat{v}}{\partial x} + \bar{w}^*\frac{\partial \hat{w}}{\partial x}] - \frac{\partial}{\partial x}\Big(\bar{w}^*\frac{\partial \hat{u}}{\partial x}\Big) - \frac{\partial}{\partial y}\Big(\bar{w}^*\frac{\partial \hat{v}}{\partial x}\Big)\Big\}\Big). \tag{62}$$

Equations (55)–(58) are the additional terms in the (40)–(43) respectively. Equation (59) is the additional term in (44) and (60)–(62) are the additional terms in (45)–(47) respectively. It should be noted here that the boundary conditions do not change in any of the state or adjoint equations. Further, the gradient expression does not get any additional terms due to the stabilization parameter s.

References

AIRIAU, C. 2000 Non-parallel acoustic receptivity of a Blasius boundary layer using an adjoint approach. *Flow, Turbulence Combust* **65**, 347–367.

ANDERSSON, P., BERGGREN, M. & HENNINGSON, D. 1999 Optimal disturbances and bypass transition in boundary layers. *Phys. Fluids* **11**, 134–150.

ANDERSSON, P., HENNINGSON, D. S. & HANIFI, A. 1998 On a stabilization procedure for the parabolic stability equations. *J. Engng Maths* **33**, 311–332.

BALAKUMAR, P. & HALL, P. 1999 Optimum suction distribution for transition prediction. *Theor. Comput. Fluid Dyn.* **13**, 1–19.

BERTOLOTTI, F., HERBERT, T. & SPALART, S. 1992 Linear and nonlinear stability of the blasius boundary layer. *J. Fluid Mech.* **242**, 441–474.

BEWLEY, T. & LIU, S. 1998 Optimal and robust control and estimation of linear paths to transition. *J. Fluid Mech.* **365**, 305–349.

BEWLEY, T. & MOIN, P. 1997 Optimal and robust approaches for linear and nonlinear regulation problems in fluid mechanics. *AIAA Paper* 97-1872.

BYRD, R., LU, P., NOCEDAL, J. & ZHU, C. 1995 A limited memory algorithm for bound constrained optimization. *SIAM J. Sci. Comput.* **16**, 1190–1208.

DOBRINSKY, A. & COLLIS, S. S. 2000 Adjoint parabolized stability equations for receptivity prediction. *AIAA Paper* 2000-2651.

HAJ-HARIRI, H. 1994 Characteristics analysis of the parabolized stability equations. *Stud. Appl. Math.* **92**, 41–53.

HERBERT, T. 1997 Parabolized stability equations. *Annu. Rev. Fluid Mech.* **29**, 245–283.

HILL, D. C. 1997a Receptivity in non-parallel boundary layers. In *ASME Fluids Engineering Division Summer Meeting, FEDSM '97*.

HILL, D. C. 1997b Inverse design for laminar three-dimensional boundary layers. *Bull. Am. Phys. Soc.* **42**, 2120.

HÖGBERG, M. & BERGGREN, M. 2000 Numerical approaches to optimal control of a model equation for shear flow instabilities. *Flow, Turbulence Combust* **65**, 299–320.

HÖGBERG, M. & HENNINGSON, D. S. 1998 Secondary instability of cross-flow vortices in falkner-skan-cooke boundary layers. *J. Fluid Mech.* **368**, 339–357.

IGLISCH, R. 1949 Exakte berechnung der laminaren reibungsschicht an der längsangeströmten ebenen platte mit homogener absaugung. *NACA RM* **1205**.

JOSLIN, R. 1998 Overview of laminar flow control. *Tech. Rep.* 1998-208705. NASA, Langley Research Center, Hampton, Virginia.

LI, F. & MALIK, M. R. 1994 Mathematical nature of parabolized stability equations. In *4th IUTAM Symp. on Laminar-Turbulent Transition, Sendi, Japan* (ed. R. Kobayashi), pp. 205–212. Springer.

LI, F. & MALIK, M. R. 1996 On the nature of pse approximation. *Theor. Comput. Fluid Dyn.* **8**, 253–273.

MALIK, M. R. & BALAKUMAR, P. 1992 Nonparallel stability of rotating disk flow using pse. In *Instability, Transition and Turbulence* (eds. M. Hussaini, A. Kumar & C. Streett), pp. 168–180. Springer.

PRALITS, J. O., AIRIAU, C., HANIFI, A. & HENNINGSON, D. S. 2000a Sensitivity analysis using adjoint parabolized stability equations for compressible flows. *Flow, Turbulence Combust* **65**, 321–346.

PRALITS, J. O., HANIFI, A. & HENNINGSON, D. S. 2000b Adjoint-based suction optimization for 3d boundary layer flows. *Tech. Rep.* FFA TN 2000-58. Swedish Defence Research Agency, FOI, Aeronautics Division, FFA, SE-172 90 Stockholm, Sweden.

SCHLICHTING, H. 1979 *Boundary-Layer Theory*, 7th edn. McGRAW-HILL.

SIMEN, M. 1992 Local and non-local stability theory of spatially varying flows. In *Instability, Transition and Turbulence* (eds. M. Hussaini, A. Kumar & C. Streett), pp. 181–201. Springer.

ULRICH, A. 1944 Theoretishce untersuchungen über die widerstandsersparnis durch laminarhaltung mit absaugung. *Schriften dt. Adad. d. Luftfahrtforschung* **8 B** (2).

WALTHER, S., AIRIAU, C. & BOTTARO, A. 2001 Optimal control of tollmien-schlichting waves in a developing boundary layer. *Phys. Fluids* **13**, 2087–2096.

ZHU, C., BYRD, R., LU, P. & NOCEDAL, J. 1994 L-bfgs-b: Fortran subroutines for large scale bound constrained optimization. *Tech. Rep.* NAM-11. EECS Department, Northwestern University.

Paper 3

Optimization of Steady Suction for Disturbance Control on Infinite Swept Wings

By Jan O. Pralits[1,2] and Ardeshir Hanifi[2]

We present a theory for computing the optimal steady suction distribution to suppress convectively unstable disturbances in growing boundary layers on infinite swept wings. This work includes optimization based on minimizing the disturbance kinetic energy and the integral of the shape factor. Further, a suction distribution in a continuous control domain is compared to an approach using a number of discrete pressure chambers. In the latter case, the internal static pressures of these chambers are optimized. Optimality systems are derived using Lagrange multipliers. The corresponding optimality conditions are evaluated using the adjoint of the parabolized stability equations and the adjoint of the boundary layer equations. Results are presented for an airfoil designed for medium range commercial aircraft. We show that an optimal suction distribution based on a minimization of the integral of the shape factor is not always successful in the sense of delaying laminar-turbulent transition. It is also demonstrated that including different types of disturbances, e. g. Tollmien-Schlichting and cross-flow types, in the analysis may be crucial.

---

1. Introduction

Reducing the viscous drag on a wing while maintaining operational properties such as lift for example, is of great interest and the research in this area is vast (see Joslin 1998). It is known that the viscous drag increases dramatically as the boundary layer flow changes from a laminar to a turbulent state. Therefore, a decrease in drag can be seen as increasing the laminar portion of the wing, or moving the point of laminar-turbulent transition downstream. Transition in the boundary layer on aircraft wings is usually caused by breakdown of small disturbances which grow as they propagate downstream. The growth of these disturbances can be analyzed using linear stability theory in which it is assumed that perturbations with infinitely small amplitude are superposed on the laminar mean flow. The growth rate can then be used to predict the transition location using the so called e^N method (see van Ingen 1956; Smith & Gamberoni 1956). Here it is assumed that transition will occur at the location where the total amplification of the disturbance, with respect

---

[1]Department of Mechanics, KTH, SE-100 44 Stockholm, Sweden.
[2]Swedish Defence Research Agency, FOI, Aeronautics Division, FFA, SE-172 90 Stockholm, Sweden.

to the first streamwise position where the disturbance starts to grow, attains an empirically determined value, whose logarithm is generally denoted by N.

The stabilization effect of steady boundary layer suction on disturbance growth is well known (see Schlichting 1943/44) and has been utilized for laminar flow control, for an extensive review see Joslin (1998). However, in most cases the design of suction distributions relies on the experience of the engineer which may not always give the optimal solution, i. e. to give the largest delay of laminar-turbulence transition at a given suction power. In the last ten years, the development of optimal control theory and its application to fluid mechanics problems has been rapid and a number of attempts have been made to optimize the steady suction distribution in order to control the growth of disturbances, e. g. Hill (1997b); Balakumar & Hall (1999); Cathalifaud & Luchini (2000); Pralits *et al.* (2002); Airiau *et al.* (2003). In all of these works the optimization methods are gradient based and utilize the potential of adjoint methods to obtain the gradients of interest. Other investigations including those by Mughal (1998); Walther *et al.* (2001); Högberg & Henningson (2001) consider unsteady suction/blowing. This approach may not be suitable for flow control on aircraft wings at the present time (see Bewley 2001) due to the complexity of its implementation. A common approach in the works by Balakumar & Hall (1999); Cathalifaud & Luchini (2000); Pralits *et al.* (2002); Airiau *et al.* (2003) is to minimize some measure of the disturbance growth, either the disturbance kinetic energy (see Cathalifaud & Luchini 2000; Pralits *et al.* 2002; Airiau *et al.* 2003) or the N-factor (see Balakumar & Hall 1999). The work by Airiau *et al.* (2003), in contrast to the others, did also try to minimize the shape factor which for 2D disturbances in a 2D boundary layer should result in a suppression of disturbance amplification. Minimizing the shape factor is a more heuristic approach based on the knowledge that in such flows the two-dimensional disturbances are stabilized by any thinning of the boundary layer. Their results showed that an optimal suction distribution based on minimizing the shape factor does have a damping effect on the disturbance growth. The advantage of this approach is that only one state equation has to be solved which saves computational time. A negative aspect of not explicitly minimizing a measure of the disturbances is that one cannot know if the computed suction distribution will have a damping effect on the disturbances. This has to be calculated afterwards, once the optimal suction distribution is obtained.

In Pralits *et al.* (2002) the idea of multi-disturbance control was introduced. The reason behind it is that, for certain types of flows, it is not clear which types of disturbances will be dominant in terms of amplification. An example is the Blasius flow in which, depending on the initial amplitudes, either two-dimensional Tollmien-Schlichting (TS) waves or streamwise streaks grow the most. In three-dimensional boundary layers on wings there is usually a streamwise region close to the leading edge with a strong negative pressure gradient, where cross-flow waves are the most amplified disturbances. Further downstream, where the pressure gradient is zero or positive, TS waves are the

most amplified ones. When computing an optimal suction distribution it is also necessary to make sure that the mean flow modification due to a computed suction distribution for a specific disturbance does not trigger the growth of other disturbances.

In real applications, steady boundary layer suction is usually done using a number of discrete pressure chambers (see Reneaux & Blanchard 1992; Ellis & Poll 1996; Preist & Paluch 1996; Bieler & Preist 1992; Joslin 1998). In such cases, the suction velocity is a function of the surface porosity, hole geometry and the pressure difference between the pressure distribution on the wing and static pressure in the chambers (see Bieler & Preist 1992; Preist & Paluch 1996). This means that the size, position and the internal static pressure of each chamber are the design variables. The suction distribution is then given by the specific choice of these parameters. Atkin (2000) used an engineering approach to design of the suction system in which he utilized the stability characteristics of the flow. Here, the static pressure in the pressure chambers, based on an automatized trial and error technique, were chosen such that the amplification of disturbances stayed under a specified value.

Most of the previous works such as Balakumar & Hall (1999); Cathalifaud & Luchini (2000); Pralits *et al.* (2002); Airiau *et al.* (2003) on optimal steady suction deal with incompressible boundary layer flows on flat plates. Hill (1997b) analyzed an infinite swept wing for inverse design of laminar boundary layers but no details were given of how this was done. The considered suction distributions have been applied in a continuous (see Balakumar & Hall 1999; Cathalifaud & Luchini 2000; Pralits *et al.* 2002; Airiau *et al.* 2003) or a number of discrete control domains (see Airiau *et al.* 2003). However, so far no study has shown how to incorporate the use of pressure chambers in order to approach a real application.

In this paper we extend the work by Pralits *et al.* (2002), to compressible boundary flows on infinite swept wings. Here we compare the case of minimizing the disturbance kinetic energy with the simplified approach by Airiau *et al.* (2003) of minimizing the integral of the shape factor. The feasibility of the control is addressed by comparing two different ways of computing the suction distribution: a continuous distribution of mass flux on the wall in a control domain, and a number of discrete pressure chambers, which constitutes a more realistic approach to obtaining a suction distribution on the wall. The evolution of disturbances is analyzed using the Parabolized Stability Equations (PSE) (see Bertolotti *et al.* 1992; Malik & Balakumar 1992; Simen 1992; Herbert 1997), and the laminar mean flow is computed using the two-dimensional three-component boundary layer equations (BLE). We use optimal control theory, in which the aim is to minimize a given objective function with state equations and the control energy as constraints. The problem is solved using a Lagrange multiplier technique, which yields an optimality system consisting of state and corresponding adjoint equations from which an optimality condition is evaluated. Here, we couple the adjoint of the PSE with the adjoint of the
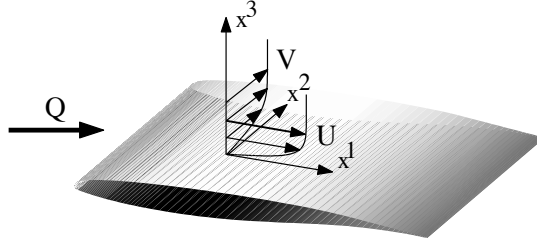
FIGURE 1. Definition of the coordinates for the infinite swept wing.

boundary-layer equations in order to find the optimality condition. The derivation of the optimality system is similar to that presented in Pralits *et al.* (2002) and is therefore presented here in a more compact form. Results are presented for control of disturbance growth in a boundary layer on a wing designed for commercial aircraft.

2. Problem formulation

The flow field considered here is the boundary layer on a swept wing with infinite span which is obtained by solving the mass, momentum and energy conservation equations for a viscous compressible fluid. The equations are written in an orthogonal curvilinear coordinate system with streamwise, spanwise and wall-normal coordinates denoted as x^1, x^2 and x^3 respectively, see Fig. 1. A length element is defined as $ds^2 = (h_1 dx^1)^2 + (h_2 dx^2)^2 + (h_3 dx^3)^2$ where h_i is the scale factor. The total flow field, q_{tot} is decomposed into a mean, $\bar{q}$, and a perturbation part, $\tilde{q}$, as

$$q_{tot}(x^1, x^2, x^3, t) = \bar{q}(x^1, x^3) + \tilde{q}(x^1, x^2, x^3, t)$$

where $\bar{q} \in [U, V, W, P, T, \rho]$ and $\tilde{q} \in [\tilde{u}, \tilde{v}, \tilde{w}, \tilde{p}, \tilde{T}, \tilde{\rho}]$. Here U, V, W are the streamwise, spanwise and wall-normal velocity components of the mean flow respectively, T is the temperature, ρ the density and P the pressure. The respective lower case variables correspond to the disturbance quantities. The equations are derived for a quasi three-dimensional mean flow with zero variation in the spanwise direction. The evolution of convectively unstable disturbances is analyzed in the framework of the nonlocal stability theory. The mean flow and disturbance equations in the following sections are given in dimensionless form. All flow and material quantities are made dimensionless with the corresponding reference flow quantities at a fixed streamwise position $x_0^\star$, except the pressure, which is referred to twice the corresponding dynamic pressure. Here, dimensional quantities are denoted by the superscript $\star$.

The reference length scale is taken as $l_0^\star = (\nu_0^\star x_0^\star / U_0^\star)^{\frac{1}{2}}$. The Reynolds and Mach number are defined as $Re = l_0^\star U_0^\star / \nu_0^\star$ and $M = U_0^\star / (\mathcal{R}\gamma T_0^\star)^{\frac{1}{2}}$ respectively where $\mathcal{R}$ is the specific gas constant, ν the kinematic viscosity and γ the ratio

of the specific heats. In the proceeding sections the scale factors $h_2, h_3 = 1$ are due to the infinite swept wing assumption.

2.1. *Mean-Flow equations*

The dimensionless boundary layer equations (BLE) written in primitive variable form can be seen in Appendix A and are here written in symbolic form as

$$L_B \mathbf{Q} = 0 \tag{1}$$

where $\mathbf{Q} = (U, V, W, T)^T$. The suction distribution is imposed using the wall normal velocity component at the wall $W_{\mathrm{w}}(x^1) = W(x^1, x^3)$. Non slip conditions are applied to the other velocity components and we assume an adiabatic wall condition for the temperature. Equation (1) is integrated from the stagnation point in the downstream direction normal to the leading edge. Note that for the boundary layer approximation to be valid, the wall normal velocity at the wall, W_{w}, should be of $O(Re^{-1})$. Here, it is assumed that the pressure distribution on the airfoil does not change as the suction distribution is applied. If the suction distribution would result in a large change in the boundary layer thickness, then it might be necessary to update the pressure distribution in the optimization process.

2.2. *Disturbance equations*

The perturbations are assumed to be time and spanwise periodic waves as

$$\tilde{\mathbf{q}}(x^i, t) = \hat{\mathbf{q}}(x^1, x^3)\Theta, \quad \text{where} \quad \Theta = \exp\left(\mathrm{i}\int_{X_0}^{x^1} \alpha(x')dx' + \mathrm{i}\beta x^2 - \mathrm{i}\omega t\right). \tag{2}$$

Here α is the complex streamwise wavenumber, β the real spanwise wavenumber and ω the real disturbance angular frequency. X_0 is the initial streamwise position where the disturbances are superimposed on the mean flow. We assume a scale separation Re^{-1} between the weak variation in the x^1-direction and the strong variation in the x^3-direction. Further, it is assumed that $\partial/\partial x^1 \sim O(Re^{-1})$ and $W \sim O(Re^{-1})$. Introducing the ansatz given by Eq. (2) and the assumptions above in the linearized governing equations, yields a set of nearly parabolic partial differential equations (see Bertolotti *et al.* 1992; Malik & Balakumar 1992; Simen 1992; Herbert 1997). The system of equations, denoted parabolized stability equations (PSE), can be seen in Appendix A and are here written in symbolic form as

$$L_P \hat{\mathbf{q}} = 0, \tag{3}$$

where $\hat{\mathbf{q}} = (\hat{\rho}, \hat{u}, \hat{v}, \hat{w}, \hat{T})^T$. Here $\hat{u}, \hat{v}, \hat{w}$ and $\hat{T}$ are subject to Dirichlet boundary conditions. To remove the ambiguity of having x^1-dependence of both the amplitude and wave function in the ansatz, and to maintain a slow streamwise variation of the amplitude function $\hat{\mathbf{q}}$, a so called 'auxiliary condition' is

introduced

$$\int_0^{+\infty} \hat{\mathbf{q}}^H \frac{\partial \hat{\mathbf{q}}}{\partial x^1} dx^3 = 0, \tag{4}$$

where superscript H denotes the complex conjugate transpose. Equation (3) is integrated in the downstream direction normal to the leading edge with an initial condition given by local stability theory. At each x^1-position the streamwise wavenumber α is iterated such that the condition given by Eq. (4) is satisfied. After a converged streamwise wavenumber has been obtained, the growth rate of the disturbance kinetic energy can be calculated from the following relation

$$\sigma = -\alpha_i + \frac{\partial}{\partial x^1}(\ln \sqrt{E}),$$

where

$$E = \int_0^{+\infty} \rho \left(|\hat{u}|^2 + |\hat{v}|^2 + |\hat{w}|^2 \right) dx^3.$$

The growth rate can then be used to predict the transition location using the so called e^N-method (see van Ingen 1956; Smith & Gamberoni 1956). The N-factor based on the disturbance kinetic energy is given as

$$N_E = \int_{X_{n1}}^X \sigma \, dx^1,$$

where X_{n1} is the lower branch of the neutral curve. A complete description of Eq. (3) is found in Pralits *et al.* (2000), and corresponding numerical schemes used here are given in Hanifi *et al.* (1994).

3. Optimal control

The approach of the current work is to use optimal control theory to find the optimal mean flow suction distribution in order to suppress the growth of convectively unstable disturbances. In this paper we investigate different control variables and objective functions. First, a general introduction is given in this section. Then follows a concise description of the Lagrange multiplier technique applied to the problem of minimizing a measure of the disturbances using the mass flux on the wall ($\dot{m}_{\mathrm{w}} = W_{\mathrm{w}}\rho_{\mathrm{w}}$) as control variable.

The problem consists of the state variables $\mathbf{Q}$ and $\tilde{\mathbf{q}}$; a control variable given by the mass flux on the wall; constraints on the state variables given by the BLE and PSE; and an objective function, a measure of the state, to be minimized.

The final goal of boundary-layer suction is to increase the laminar portion of the wing i. e. to move the location of laminar-turbulent transition further downstream, and thus decrease the viscous drag. It is therefore important that the chosen objective function can be related to the transition process. One choice is to measure the kinetic energy of a certain disturbance at a downstream

position, say X_f. This can be written as

$$E_f = \frac{1}{2} \int_{Z_0}^{Z_1} \int_0^{+\infty} \tilde{\mathbf{q}}^H M \tilde{\mathbf{q}} \, h_1 dx^2 dx^3 \bigg|_{x^1 = X_f} , \tag{5}$$

where $M = \mathrm{diag}(0,1,1,1,0)$ which means that the disturbance kinetic energy is calculated from the disturbance velocity components. Hanifi *et al.* (1996) used a measure which also included $\hat{\rho}$ and $\hat{T}$. If the position X_f is chosen as the upper branch of the neutral curve, then the measure can be related to the maximum value of the N-factor (see Airiau *et al.* 2003). If in addition, the value of the N-factor of the measured disturbance is the one which first (with zero control) reaches the transition N-factor, then the position can be related to the onset of laminar-turbulent transition. It is however not clear, a priori, that such a measure will damp the chosen disturbance or other ones in the whole unstable region, especially if different types of disturbances are present, such as TS and cross-flow waves. For Blasius flow, it has been shown that an objective function based on a single TS wave is sufficient to successfully damp the growth of other TS waves (see Pralits *et al.* 2002; Airiau *et al.* 2003). On a wing however, it is common that both TS and cross-flow waves are present. An alternative is therefore to measure the kinetic energy as the streamwise integral over a defined domain. Using such an approach several different disturbances, with respective maximum growth rate at different positions, can be accounted for in the same domain. Here, the size of K disturbances superimposed on the mean flow at an upstream position X_0, is measured by their total kinetic energy as

$$E_\Omega = \sum_{k=1}^{K} \frac{1}{2} \int_{X_{ms}}^{X_{me}} \int_{Z_0}^{Z_1} \int_0^{+\infty} \tilde{\mathbf{q}}_k^H M \tilde{\mathbf{q}}_k h_1 dx^1 dx^2 dx^3 . \tag{6}$$

We now define the objective function based on the disturbance growth as

$$\mathcal{J}_0 = \xi E_\Omega + (1 - \xi) E_f, \tag{7}$$

where the parameter ξ can be chosen between zero and one, depending on the quantity one wants to minimize. In order to have a well-posed problem, the control needs to be bounded. This is done by quantifying the control effort as

$$E_C = \int_{X_{cs}}^{X_{ce}} \dot{m}_{\mathrm{w}}^2 h_1 dx^1 . \tag{8}$$

This measure has a physical meaning and also enables comparison of efficiency of different objective functions. Taking the square of $\dot{m}_{\mathrm{w}}$ means that both blowing and suction will be accounted for in E_C.

A concise description of the objective can now be made: find the control $\dot{m}_{\mathrm{w}}$, and corresponding states $\mathbf{Q}$ and $\tilde{\mathbf{q}}$ which minimizes the objective function $\mathcal{J}_0$ with the constraints given by Eqs. (1), (3), (4) and (8). We now use a Lagrange multiplier technique to replace the original constrained problem with an unconstrained one, see e. g. Gunzburger (1997). In order to enforce

the constraints we introduce the adjoint variables $\mathbf{Q}^*, \mathbf{q}^*, r^*, \lambda^*, \chi^*$ and the Lagrangian functional

$$\mathcal{L} = \mathcal{J}_0 - \mathcal{J}_1 \tag{9}$$

where

$$
\begin{aligned}
\mathcal{J}_1 &= \langle \mathbf{Q}^*, L_B \, \mathbf{Q} \rangle + \int_{X_{cs}}^{X_{ce}} \lambda^* \left[\dot{m}(x^1, 0) - \dot{m}_{\mathrm{w}} \right] h_1 dx^1 \\
&+ \chi^* (E_C - \int_{X_{cs}}^{X_{ce}} \dot{m}_{\mathrm{w}}^2 h_1 dx^1) + \langle \mathbf{q}^*, L_P \, \hat{\mathbf{q}} \rangle + \langle r^* \hat{\mathbf{q}}, \frac{1}{h_1} \frac{\partial \hat{\mathbf{q}}}{\partial x^1} \rangle + \text{c.c.}
\end{aligned}
$$

where c.c. denotes the complex conjugate. The inner products $\langle \cdot, \cdot \rangle$ appearing above are defined as

$$\langle \psi, \phi \rangle = \int_{X_0}^{X_1} \int_{Z_0}^{Z_1} \int_0^{+\infty} \psi^H \phi \, h_1 dx^1 dx^2 dx^3, \tag{10}$$

for complex valued vectors ψ and ϕ. We can now define the problem as: find the control $\dot{m}_{\mathrm{w}}$, states $\mathbf{Q}, \tilde{\mathbf{q}}$ and adjoint variables $\lambda^*, \chi^*, \mathbf{Q}^*, \mathbf{q}^*$ and r^* such that $\mathcal{L}$ is rendered stationary according to the first-order necessary condition for an extremal point. This is done by setting the first variation of $\mathcal{L}$ with respect to the variables considered here to zero, while each of $\mathcal{L}$'s arguments are considered to be independent variables. This requirement comes from the fact that at an extremal point the first variation of $\mathcal{L}$ with respect to each variable vanishes. We start by setting the first variation of $\mathcal{L}$ with respect to each adjoint variable to zero, which gives the state equations (1), (3) and (4), and the constraint on the control effort, Eq. (8). We continue by setting the first variation of the state variables $\hat{\mathbf{q}}$, α and $\mathbf{Q}$ to zero. After a procedure which involves successive integrations by parts (see Pralits *et al.* 2002), this yields the adjoint equations

$$L_P^* \, \mathbf{q}^* = S_P^*, \tag{11}$$

$$\frac{\partial}{\partial x^1} \int_0^{+\infty} \mathbf{q}^{*H} \frac{\partial L_P}{\partial \alpha} \hat{\mathbf{q}} h_1 dx^3 = \begin{cases} 0 & \forall x^1 \notin [X_{ms}, X_{me}] \\ -\mathrm{i} |\Theta|^2 \int_0^{+\infty} \hat{\mathbf{q}}^H M \hat{\mathbf{q}} h_1 dx^3 & \forall x^1 \in [X_{ms}, X_{me}], \end{cases} \tag{12}$$

$$L_B^* \, \mathbf{Q}^* = S_B^*, \tag{13}$$

where $\mathbf{q}^* = (\rho^*, u^*, v^*, w^*, \theta^*)^T$ and $\mathbf{Q}^* = (U^*, V^*, W^*, T^*)^T$. Equation (11) is the adjoint of the PSE (APSE) where u^*, v^*, w^* and θ^* are subject to Dirichlet boundary conditions. The right hand side S_P^* is due to the auxiliary condition of the PSE and the objective function. Equation (12) is a closure relation obtained by setting the first variation of $\mathcal{L}$ with respect to the streamwise wavenumber α to zero. At each streamwise position, r^* is solved iteratively such that Eq. (12) is satisfied. Equation (13) is the adjoint of the BLE (ABLE) and the right hand side S_B^* is the sensitivity of the PSE with respect to the mean flow. Both the APSE and ABLE are parabolic equations which are solved

by backward integration in the streamwise direction. The above equations are found in A.1, and the complete derivations are found in Pralits *et al.* (2000) and Pralits (2001). Finally, we set the first variation of $\mathcal{L}$ with respect to $\dot{m}_{\mathrm{w}}$ to zero which gives the so called optimality condition as

$$W_{\mathrm{w}}^* + 2\chi^* \dot{m}_{\mathrm{w}} = 0. \tag{14}$$

The left hand side of the above expression is the gradient of the Lagrangian functional with respect to the mass flux at the wall. As shown in Eq. (9), χ^* is the adjoint variable used to enforce the control effort and can be solved iteratively in the optimization by substituting Eq. (14) into Eq. (8) as

$$\chi^* = \left(\frac{1}{4E_C} \int_{X_{cs}}^{X_{ce}} W_{\mathrm{w}}^{*2} h_1 dx^1 \right)^{\frac{1}{2}}. \tag{15}$$

The complete optimality system contains Eqs. (1), (3), (4) and (11)–(15) which can be found in Appendix A.

3.1. *Solution procedure*

The procedure of solving the optimization problem derived in Sec. 3 is described here. We start by considering the case of minimizing a single disturbance, i. e. $K = 1$ in Eq. (6).

The optimal distribution of the mass flow is found through an iterative procedure. During each iteration step, we perform successive calculations of boundary-layer and stability equations from X_0 to X_1; and adjoint boundary-layer and stability equations from X_1 to X_0. Then, a new mass-flow distribution is computed using the gradient information given by solution of the adjoint equations. Here we use the L-BFGS-B optimization routine, see Zhu *et al.* (1994) and Byrd *et al.* (1995). The calculations are repeated until the relative change in the objective function is less than a prescribed value.

If $K > 1$ in Eq. (6) then instead of solving both state and adjoint equations K times, we can utilize the fact that the ABLE are linear equations. In this case the optimality condition is evaluated as follows: the BLE is solved once; the PSE and APSE are solved K times; the forcing of the ABLE, S_B^*, is calculated as

$$S_B^* = \sum_{k=1}^{K} S_{B_k}^*.$$

Finally, the optimality condition is evaluated from a single calculation of the ABLE.

The results presented here are obtained by numerically integrating the discretized state and adjoint equations. The x^1-derivatives are approximated by a first- or second-order accurate backward Euler scheme. The x^3-derivatives of the PSE and APSE are approximated by a fourth-order accurate compact finite-difference scheme and a second-order accurate finite-difference scheme for the BLE and ABLE. The convergence criteria is $(\mathcal{J}^{k+1} - \mathcal{J}^k)/\mathcal{J}^k < 10^{-4}$,
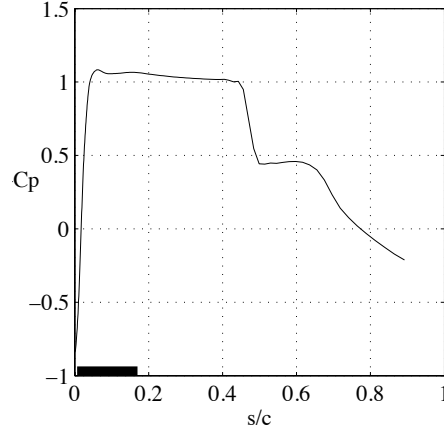
FIGURE 2. The pressure distribution, C_p, as a function of the arc-length normal to the leading edge, s/c. The black box shows the available control domain, Γ_c.

where k denotes the iteration number in the optimization procedure. Further, in all calculations the initial guess on the suction profile, $\dot{m}_w^{in}$, has been varied to make sure that the optimal solution does not depend on the initial state.

3.2. *Case studied*

The flow studied here is the boundary layer on the upper side of a wing designed for commercial aircraft. The flow conditions are characterized by a free stream Mach number $M_\infty = 0.8$, temperature $T_\infty = 230$ K, Reynolds number $Re_\infty = 3.04 \times 10^7$ and leading edge sweep angle $\phi_{le} = 30.2°$. The control domain, $\Gamma_c = [X_{cs}, X_{ce}]$, available for mounting the suction-system has been specified by the manufacturer. The control domain is limited in the upstream direction, $0 < s/c < 0.006$, by a suction strip used to control the stagnation line and in the downstream direction by the front spar (s/c=0.17). Here s is the arc-length normal to the leading edge measured from the stagnation point and c is the chord length. The suction strip at the stagnation line is case specific and will be held unchanged. However, this does not create any difficulties in the optimization procedure. In Fig. 2 the pressure coefficient C_p is plotted as a function of s/c. The available control domain $0.006 \leq s/c \leq 0.17$ is also indicated in this figure as a black box.

Parameters for the disturbances analyzed here are given in Table 1. At the initial streamwise position ($s/c = 0.0075$), the flow has a strong favorable pressure gradient and the mean flow velocity component perpendicular to the outer streamline has an inflection point. There, waves with the wavenumber vector **k** approximately perpendicular to the outer streamline have positive growth rate. These are the so called cross-flow (CF) waves. Further downstream ($s/c = 0.05$) where the pressure gradient is weaker and adverse, Tollmien-Schlichting (TS)

X_0	f^*	Δf^*	β^*	$\Delta\beta^*$	Type
0.0075	$[1000, 8500]$	500	$[1000, 6000]$	500	CF
0.0075	0	0	$[500, 6500]$	500	CF
0.05	$[2250, 9500]$	250	0	0	TS
0.05	$[2250, 7000]$	250	$[25, 225]$	50	TS

TABLE 1. Initial position ($s/c = X_0$), dimensional frequency (f^*), dimensional spanwise wave number (β^*) and type of disturbances analyzed (CF = cross-flow wave, TS = Tollmien-Schlichting wave). Δf^* and $\Delta\beta^*$ denote respective dimensional step-length.
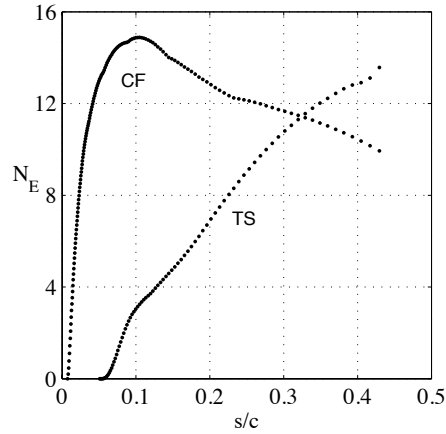
FIGURE 3. Envelope of envelopes of N_E-factor curves for the two disturbance types given in table 1 for the case of zero suction.

waves are amplified. The angles between the wavenumber vectors of the TS waves analyzed here and the outer streamline are $0 - 60$ degrees. In Fig. 3, the envelope of envelopes (EoE) of the N_E-factor curves are plotted for the CF and TS disturbances given in Table 1 and for zero suction rate.

The control effort which is quantified by Eq. (8) depends on the specific suction system chosen, i. e. compressors and tubing. We have therefore chosen a number of different magnitudes of E_C to examine the dependency of the achieved stabilization on the amplitude of the control energy. Here we introduce a new parameter $Q_C = E_C Re_\infty$. In our calculations the values of Q_C are chosen so that a noticeable control effect is achieved and to avoid the magnitude of mean wall-normal velocity (at the wall) W_w exceeding $O(Re^{-1})$. This was checked after each calculation.
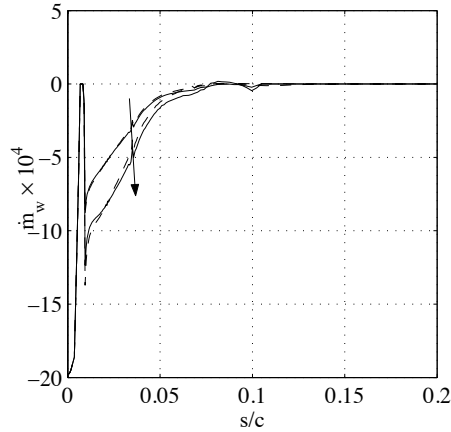
FIGURE 4. Optimal suction distributions, $\dot{m}_w$, minimizing the disturbance kinetic energy of a CF wave ($f^* = 5500\ s^{-1}$, $\beta^* = 2500\ m^{-1}$) measured as E_Ω (dashed), E_f (solid). $Q_C = 0.35$ and 0.58, and the arrow marks increasing Q_C.

3.3. *Results*

Results are shown here for minimization of the disturbance kinetic energy, Eq. (5.17), in which ξ has been chosen depending on the desired objective function. In the latter, the measure is given as the sum of the kinetic energy of K disturbances. Before the optimization is performed, it has to be decided if one or several disturbances should be included. One of the conclusions from Pralits *et al.* (2002) and Airiau *et al.* (2003) was that the optimal suction distribution for a given disturbance will also have a damping effect on other disturbances of the same type. The reason for including more than one disturbance in the measure (see Pralits *et al.* 2002) is that in some cases it is not clear which type of disturbance will cause laminar-turbulent transition first. Another reason is that if different types of disturbances are present in the flow, then the mean flow modification that minimizes some measure of one type of disturbance may amplify rather than damp disturbances of another type. One should keep in mind that the larger number of disturbances considered, the more costly the optimization procedure will be. As a first investigation, a comparison is made between minimizing the kinetic energy of a single disturbance integrated in a streamwise domain ($\xi = 1$), with the case of minimizing the same disturbance at a final streamwise position ($\xi = 0$). Eq. (5.16) is integrated between X_0 and the end of the control domain which means that the aim is to delay transition at least up to this position. X_f in Eq. (5.14) is chosen as the position where the maximum disturbance kinetic energy is found over all disturbances in Table 1, here $X_f = 0.105$. The corresponding disturbance, which also has the largest E_Ω over all disturbances in Table 1, is chosen as the one to minimize in both cases. This disturbance is a CF wave with dimensional frequency and
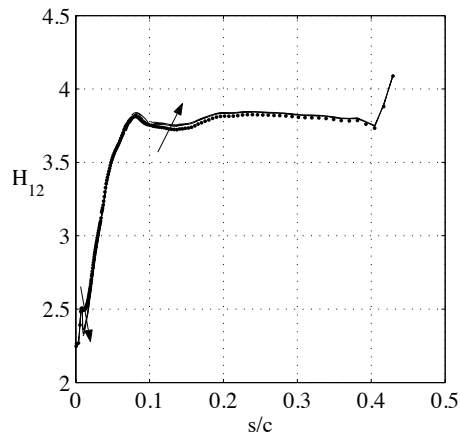
FIGURE 5. Shape factor, H_{12}, given zero (dotted) and optimal suction distribution from Fig. 4 minimizing the disturbance kinetic energy of a CF wave ($f^* = 5500\ s^{-1}$, $\beta^* = 2500\ m^{-1}$) measured as E_Ω (dashed), E_f (solid). $Q_C = 0$, 0.35 and 0.58, and the arrow marks increasing Q_C.

spanwise wave number of 5500 s^{-1} and 2500 m^{-1}, respectively. The calculations are performed for $Q_C = 0.25$, 0.35, 0.45 and 0.58. The optimal suction distributions given by the two different objective functions can be seen in Fig. 4. Here, results are only shown for two different values of the control energy to make the plot more clear. The arrow indicates the direction of increasing Q_C and the uppermost streamwise suction distribution is the fixed stagnation line control. It is interesting to note the similarity between the results when comparing the two objective functions as opposed to a similar comparison for control of TS waves reported by Airiau *et al.* (2003). The reason for this may be that the growth and decay of CF waves in the case analyzed here occurs over a short streamwise interval, and as a consequence the growth measured by E_Ω approach that for E_f. In all cases, the optimal control acts primarily in the region where a strong favorable pressure gradient exists and then decays further downstream. As the control effort is increased, the additional control energy is concentrated to the beginning of the control domain. The effect of the control on the shape factor is however small, which can be seen in Fig. 5. The magnitudes of the suction distributions presented in this paper are all within the range of validity for the boundary layer equations, i. e. of order $O(Re^{-1})$. This was investigated by Airiau *et al.* (2003), where suction distributions with magnitudes within the limits experienced locally rapid streamwise variations. They compared solutions from the Navier-Stokes equations with those using the boundary layer equations. They found that the pressure gradient from the Navier-Stokes solution varies rapidly close to the suction peak but relaxes very rapidly downstream where it becomes small, in accordance
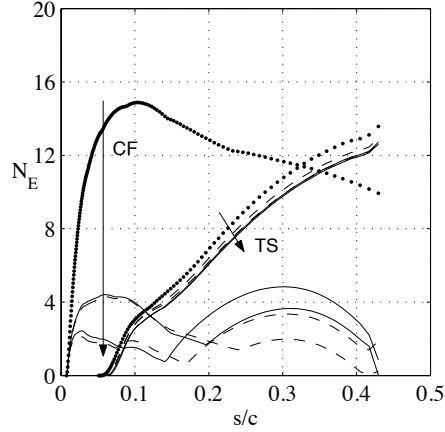
FIGURE 6. Envelope of envelopes of N_E-factor curves for the disturbances given in table 1 given zero (dotted) and optimal suction distribution from Fig. 4 minimizing the disturbance kinetic energy of a CF wave ($f^* = 5500\ s^{-1}$, $\beta^* = 2500\ m^{-1}$) measured as E_Ω (dashed), E_f (solid). $Q_C = 0$, 0.35 and 0.58, and the arrows mark increasing Q_C.

with the parabolic assumption of the boundary layer equations. They further showed that shape factors from the boundary layer and Navier-Stokes solutions agree well and conclude that there is a weak dependence of the shape factor on the mean pressure gradient and that the solutions of the boundary-layer equations are valid. In Fig. 6, the EoE of the N_E-factor curves of CF and TS waves are plotted for the cases of zero and optimal suction distributions shown in Fig. 4. In the control domain, the CF waves are more damped as Q_C is increased. However, downstream of the control region the CF waves are increasingly amplified as Q_C is increased. As expected the TS waves are less affected by the controls since we know that the control acts upstream of the region where the TS waves are amplified. In the results shown here, the optimal suction distributions are based on minimizing a single disturbance only. The damping effect of such a control on other disturbances of the same type can be seen from EoE curves given in Fig. 6. In Figs. 7 and 8, this has been emphasized by plotting contours of E_Ω for CF and TS waves in the (f^*, β^*)-plane comparing zero and optimal suction distributions for all values of Q_C. In all cases the kinetic energy of all disturbances has been reduced. It is clear from the ratio between the maximum value of E_Ω for the zero and optimal control, that the CF waves are mostly affected. This is true for all values of Q_C studied here. From these results, as discussed in Pralits *et al.* (2002) and Airiau *et al.* (2003), one can conclude that minimizing the disturbance kinetic energy of one disturbance (in this case CF waves) does have a damping effect on other disturbances of the same type. To confirm this, computations were
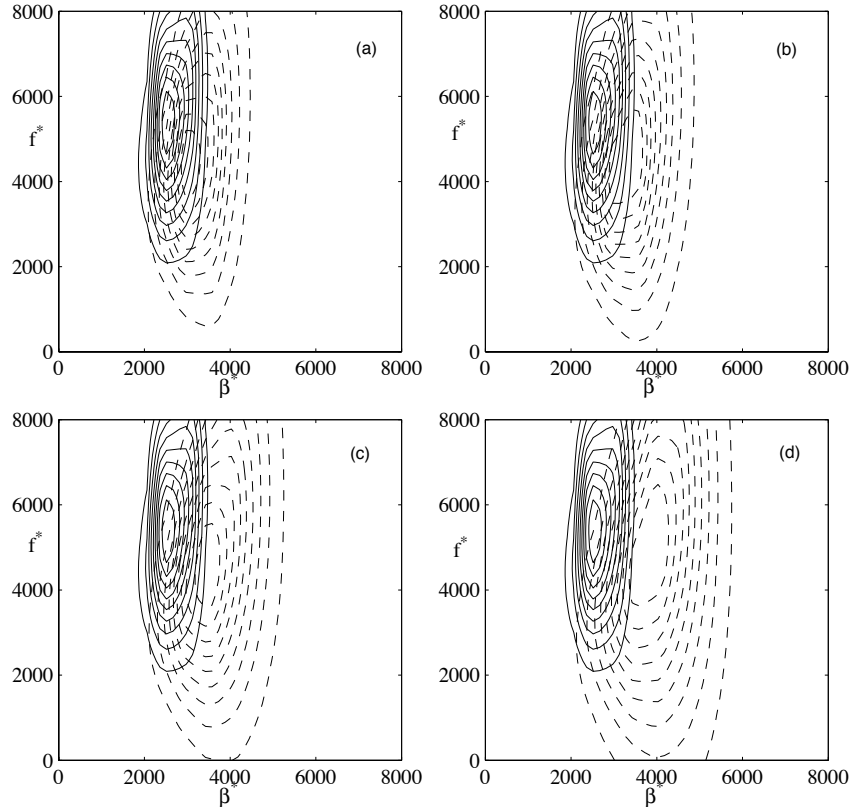
FIGURE 7. Contours of E_Ω for CF waves comparing zero (solid) and optimal suction distribution (dashed) minimizing the disturbance kinetic energy of a CF wave ($f^* = 5500\ s^{-1}$, $\beta^* = 2500\ m^{-1}$). Both cases are normalized with their respective maximum value and the contour spacing $= 0.1$. The control effort Q_C and the ratio between the maximum values are respectively (a) 0.25, 1.4×10^{-8}; (b) 0.35, 6.7×10^{-10}; (c) 0.45, 6.4×10^{-11}; (d) 0.58, 5.5×10^{-12}.

also performed in which the TS wave with the largest total disturbance kinetic energy was controlled. The suction distribution from these calculations had a damping effect on all other TS waves. These results are not shown here. The absence of control in the region where the TS waves are amplified can be overcome by adding a disturbance of TS type in the objective function when $\xi = 1$. Therefore, as a next step both the CF and TS wave with the largest E_Ω over all respective disturbances in Table 1 are considered. The dimensional frequency and spanwise wave number for the TS wave are 5750 s^{-1} and 225 m^{-1}, respectively, and the calculations are performed with the same values of
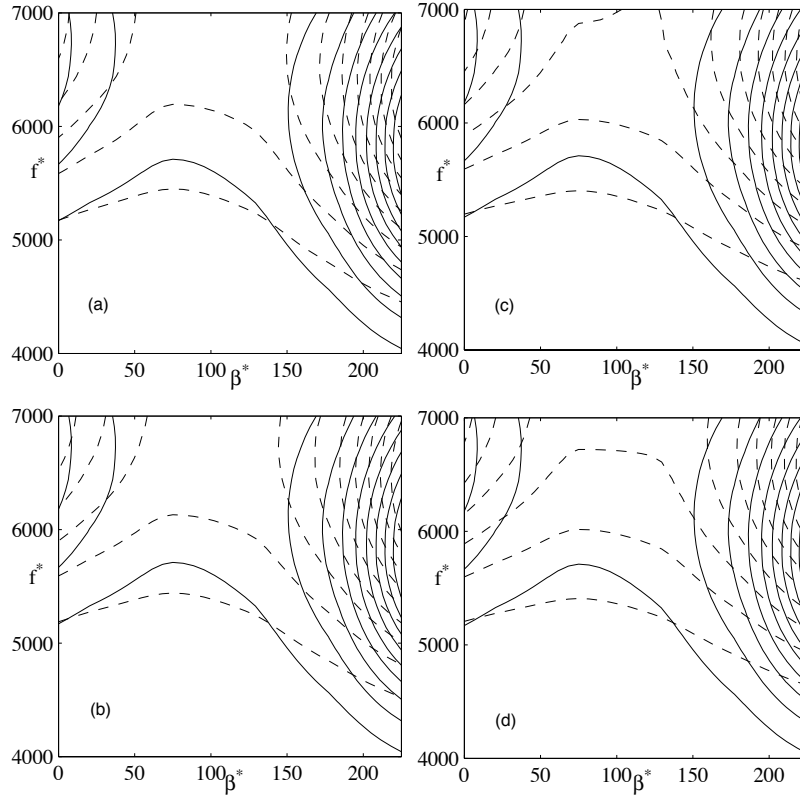
FIGURE 8. Contours of E_Ω for TS waves comparing zero (solid) and optimal suction distribution (dashed) minimizing the disturbance kinetic energy of a CF wave ($f^* = 5500 \ s^{-1}$, $\beta^* = 2500 \ m^{-1}$). Both cases are normalized with their respective maximum value and the contour spacing $= 0.1$. The control effort Q_C and the ratio between the maximum values are respectively (a) 0.25, 0.21; (b) 0.35, 0.16; (c) 0.45, 0.1; (d) 0.58, 0.092.

Q_C used for control of a single CF wave. In Table 2 the ratio between the maximum values of E_Ω for CF waves using optimal and zero suction are given. Here, we compare the case of optimal suction based on minimizing a CF wave with the case of minimizing the sum of a CF and a TS wave. It is seen that the change of the ratio is small between the cases, even when Q_C is increased. In Table 3 the same comparison is done for the ratio of the maximum values of E_Ω for TS waves. Here, it is clear that the ratio has decreased when both CF and TS disturbances are considered. As the same amount of control effort is used, this means that Q_C is redistributed in the streamwise direction to control

Disturbance	$Q_C = 0.25$	$Q_C = 0.35$	$Q_C = 0.45$	$Q_C = 0.58$
CF	1.4×10^{-8}	6.7×10^{-10}	6.4×10^{-11}	5.5×10^{-12}
CF+TS	2.2×10^{-8}	1.4×10^{-9}	5.7×10^{-11}	1.1×10^{-11}

TABLE 2. Ratio between maximum values of E_Ω for CF waves when zero and optimal suction distribution minimizing the disturbance kinetic energy is applied. The ratio is calculated when equation (5.16) includes CF and CF+TS for different values of Q_C.

Disturbance	$Q_C = 0.25$	$Q_C = 0.35$	$Q_C = 0.45$	$Q_C = 0.58$
CF	2.1×10^{-1}	1.6×10^{-1}	1.0×10^{-1}	9.2×10^{-2}
CF+TS	6.1×10^{-3}	8.6×10^{-3}	1.1×10^{-3}	6.6×10^{-5}

TABLE 3. Ratio between maximum values of E_Ω for TS waves when zero and suction distribution control minimizing the disturbance kinetic energy is applied. The ratio is calculated when equation (5.16) includes CF and CF+TS for different values of Q_C.

the TS wave. The corresponding optimal suction distributions are plotted in Fig. 9 for the cases when E_C=0.35 and 0.58. The suction distributions in the upstream part of the control domain are similar to the ones in Fig. 4, but the magnitudes are smaller. Further downstream, the suction distribution is rather constant before it goes to zero at the end of the control domain. The latter is similar to what is shown in Pralits *et al.* (2002) for control of two-dimensional TS waves in two-dimensional boundary layer flows when a small control effort is used. The effect of the control on the shape factor is plotted in Fig. 10. Compared to the results given in Fig. 5, a larger decrease of H_{12} occurs in the downstream portion of the control domain. The corresponding thinning of the boundary layer is favorable in terms of damping the TS waves. The EoE of the N_E-factor curves are plotted in Fig. 11. Here, the CF waves are less damped compared to the previous case, see Fig. 6. However, the TS waves are now more damped.

It is of interest to know if a larger reduction of the disturbance kinetic energy can be obtained for a given control effort if additional modes, apart from the two discussed here, are included in the calculations. Such a parameter study has been performed and the results show that the additional decrease in disturbance kinetic energy is small when more modes are included. The reason is that the control mainly acts on the modes with the largest energy. Since the control affects all other disturbances (shown here), it will continue to act on the mode with the initially largest energy even if additional modes are included.
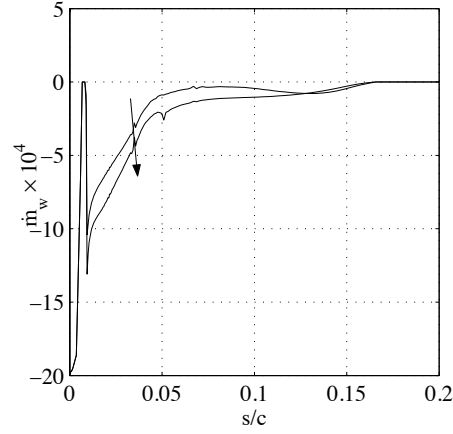
FIGURE 9. Optimal suction distributions, $\dot{m}_{\mathrm{w}}$, minimizing the disturbance kinetic energy E_Ω of a CF ($f_1^* = 5500\ s^{-1}$, $\beta_1^* = 2500\ m^{-1}$) and TS wave ($f_2^* = 5750\ s^{-1}$, $\beta_2^* = 225\ m^{-1}$). Q_C = 0.35 and 0.58, and the arrow marks increasing Q_C.
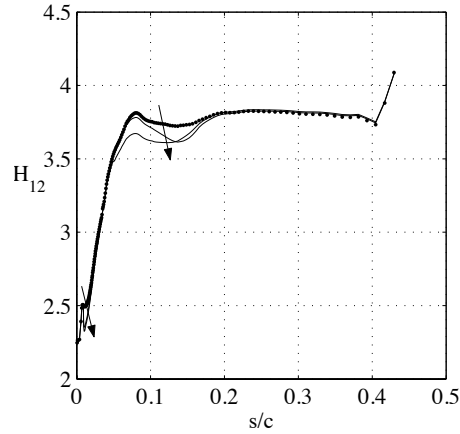

FIGURE 10. Shape factor, H_{12}, given zero (dotted) and optimal suction distribution (solid) from Fig. 9 minimizing the disturbance kinetic energy E_Ω of a CF ($f_1^* = 5500\ s^{-1}$, $\beta_1^* = 2500\ m^{-1}$) and TS wave ($f_2^* = 5750\ s^{-1}$, $\beta_2^* = 225\ m^{-1}$). $Q_C = 0$, 0.35 and 0.58, and the arrow marks increasing Q_C.

4. Simplified approach

In design of suction distributions for the purpose of delaying laminar-turbulent transition, it is important that the procedure is not computationally expensive. The same argument can be made when designing on-line control systems, where
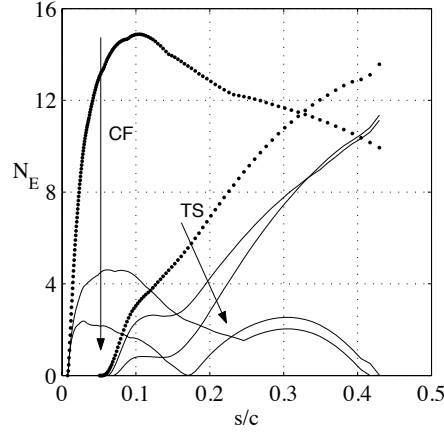
FIGURE 11. Envelope of envelopes of N_E-factor curves for the disturbances given in table 1 given zero (dotted) and optimal suction distribution from Fig. 9 minimizing the disturbance kinetic energy E_Ω of a CF ($f_1^* = 5500\ s^{-1}$, $\beta_1^* = 2500\ m^{-1}$) and TS wave ($f_2^* = 5750\ s^{-1}$, $\beta_2^* = 225\ m^{-1}$). $Q_C = 0$, 0.35 and, 0.58 and the arrows mark increasing Q_C.

fast feed back is needed. For this purpose, an alternative approach was analyzed in Airiau *et al.* (2003) for the control of TS waves in incompressible flat-plate boundary layers. In their study the optimal suction distribution is computed by minimizing the streamwise integral of the shape factor. This means that only the boundary layer and corresponding adjoint equations are involved in the optimization process which is computationally more efficient. However, the effect of the optimal suction distribution on the disturbance growth is analyzed afterwards. This choice of objective function is based on the knowledge that any thinning of the boundary layer has a stabilizing effect on the boundary layer. Successful results are shown for control of TS waves. The positive features of this approach motivates an investigation here.

4.1. *Optimality system*

The objective function is now given as

$$\mathcal{J}_0 = \int_{X_{ms}}^{X_{me}} H_{12} h_1 dx^1, \text{where} H_{12} = \frac{\delta_1}{\delta_2} = \frac{\displaystyle\int_0^{+\infty} \left(1 - \frac{\rho U_{SL}}{\rho_e Q_e}\right) dx^3}{\displaystyle\int_0^{+\infty} \frac{\rho U_{SL}}{\rho_e Q_e} \left(1 - \frac{U_{SL}}{Q_e}\right) dx^3}. \quad (16)$$

Both the displacement δ_1 and momentum thickness δ_2 are based on the velocity component $U_{SL} = U\cos(\phi) + V\sin(\phi)$ which is in the direction of the outer streamline. Here $\phi = \tan^{-1}(V_e/U_e)$ and $Q_e = (U_e^{\ 2} + V_e^{\ 2})^{\frac{1}{2}}$. Now, only one state equation is considered and the problem consists of finding the control $\dot{m}_w$,
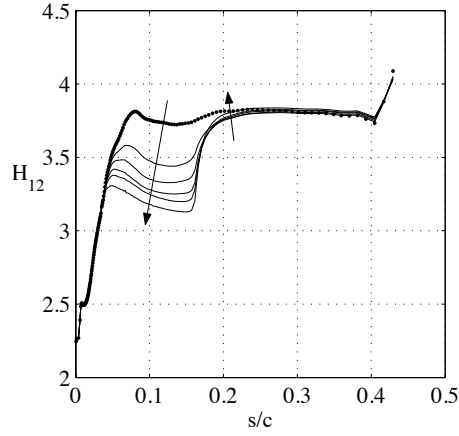
FIGURE 12. Shape factor, H_{12} for zero (dotted) and optimal suction distributions (solid) minimizing the shape factor. Q_C = 0, 0.1, 0.3, 0.58, 0.81 and 1.43 and the arrows mark increasing Q_C.

and corresponding state $\mathbf{Q}$ which minimizes $\mathcal{J}_0$ given the constraints shown in Eqs. (1) and (8). The technique using Lagrange multipliers is also used here to enforce the constraints. The adjoint variables $\mathbf{Q}^*, \lambda^*, \chi^*$ are introduced and the new Lagrangian functional is given as

$$\mathcal{L} = \mathcal{J}_0 - \mathcal{J}_1 \qquad (17)$$

where $\mathcal{J}_1$ is now written

$$\mathcal{J}_1 = \langle \mathbf{Q}^*, L_B \, \mathbf{Q} \rangle + \int_{X_{cs}}^{X_{ce}} \lambda^* \left[\dot{m}(x^1, 0) - \dot{m}_{\mathrm{w}} \right] \, h_1 dx^1 +$$

$$\chi^*(E_C - \int_{X_{cs}}^{X_{ce}} \dot{m}_{\mathrm{w}}^2 h_1 dx^1).$$

The derivation is performed as previously described which yields an optimality system which contains the BLE, Eq. (1), corresponding adjoint equation and optimality condition. Compared to the previously derived ABLE, differences occur in the boundary conditions and forcing term S_B^*. These differences are due to the objective function, Eq. (16). Details of the optimality system can be seen in Appendix B.

4.2. Results

Results are shown here on minimizing the shape factor. First we consider control in the whole available domain Γ_c, and the objective function is integrated in the same streamwise region used for Eq. (5.16) in Sec. 3.3. The control efforts in these calculations are Q_C = 0.1, 0.3, 0.58, 0.81 and 1.43. In Fig. 12 the shape factors for these cases are compared to that of the uncontrolled
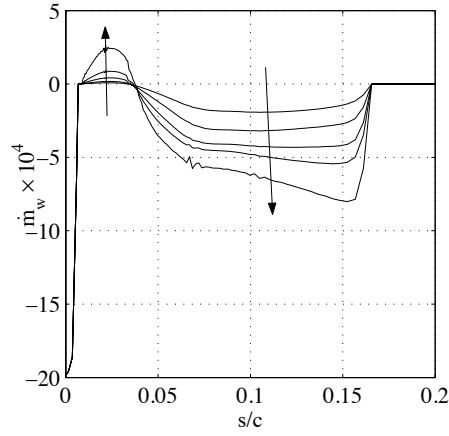
FIGURE 13. Optimal suction distributions, $\dot{m}_w$, minimizing the shape factor, H_{12}. $Q_C = 0.1$, 0.3, 0.58, 0.81, 1.43 and the arrows mark increasing Q_C.
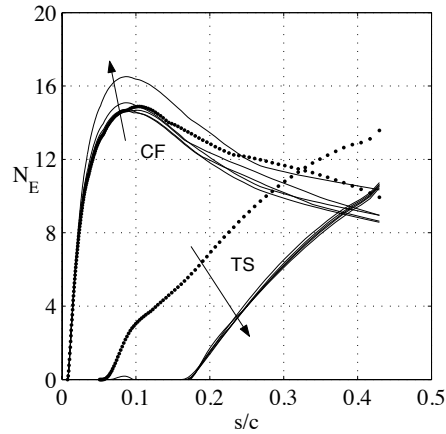

FIGURE 14. Envelope of envelopes of N_E-factor curves for the two disturbance types given in table 1 given zero (dotted) and optimal suction distribution minimizing (solid) the shape factor. $Q_C = 0$, 0.1, 0.3, 0.58, 0.81, 1.43 and the arrows mark increasing Q_C.

case. As the control effort is increased, the shape factor is decreased within the major part of the control domain. Downstream of the control domain a small increase of the shape factor is observed.

The corresponding suction profiles are plotted in Fig. 13. Note that the uppermost streamwise suction distribution is due to the stagnation line control which is taken to be fixed. In all cases, the optimal control is divided roughly at
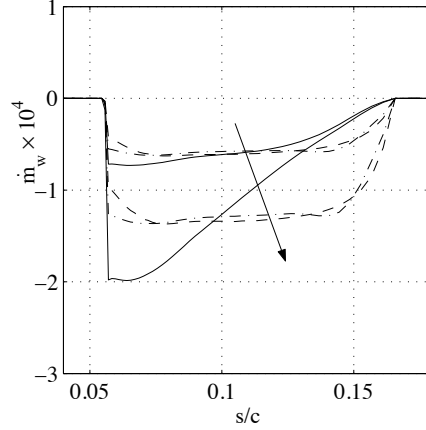
FIGURE 15. Comparison of optimal suction distributions for
the cases of: minimizing the disturbance kinetic energy of a
TS wave measured as E_Ω (solid), E_f (dashed-dotted), and the
case of minimizing the shape factor (dashed). $Q_C =$0.01, 0.05,
and the arrow indicates increasing Q_C.

$s/c = 0.04$ into blowing upstream and suction downstream, and the magnitude
of the control is increased in both regions as Q_C is increased. At this position
the flow goes from a strongly accelerating one to a weakly decelerating one.

Compared to Fig. 3, one can see that the region of blowing is where the
CF waves are amplified and the region of suction is where the TS waves are
amplified. In Fig. 14 the EoE of the N_E-factor curves for CF and TS waves
are plotted for zero and optimal suction distributions ($Q_C = 0$, 0.1, 0.3, 0.58,
0.81, 1.43). When control is applied, the TS waves are completely stabilized
in the control domain and are then amplified downstream, except for $Q_C =$
0.1. The CF waves are instead amplified in the region where blowing occurs
and this becomes more pronounced as Q_C is increased. For the airfoil analyzed
here, this means that applying an optimal control based on minimizing the
streamwise integral of the shape factor will not delay but rather precipitate
laminar-turbulent transition.

In the results shown so far, the most efficient way to control CF waves is
a suction distribution based on minimizing the most amplified CF wave. The
TS waves, on the other hand, have so far shown to be more efficiently con-
trolled using the suction distribution based on minimizing the shape factor.
In order to further investigate the control of TS waves, the case of minimiz-
ing the shape factor is compared with the cases of minimizing the integrated
disturbance kinetic energy of a TS wave and its value at a given streamwise
position X_f. The latter two objective functions are obtained by setting ξ equal
to one and zero respectively in Eq. (5.17). In this comparison, a smaller control
domain, $\Gamma_C = [0.05, 0.17]$, is used, as the TS waves are amplified downstream
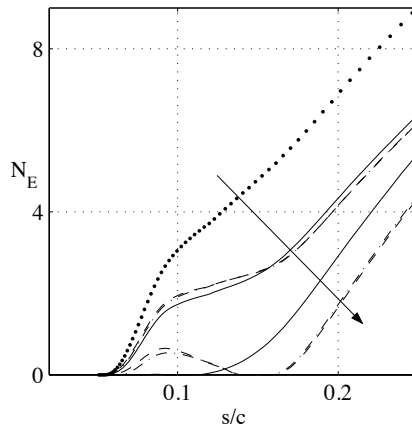
FIGURE 16. Comparison of envelope of envelopes of N_E-factor curves for the cases of: minimizing the disturbance kinetic energy of a TS wave measured as E_Ω (solid), E_f (dashed-dotted), the case of minimizing the shape factor (dashed), and zero control (dotted). $Q_C =$ 0, 0.01, 0.05, and the arrow indicates increasing Q_C.

of the region with negative pressure gradient. The disturbances are measured at $X_f = X_{ce}$ and in the control domain for ξ equals zero and one respectively. For the comparison, a noticeable reduction in the disturbance growth is obtained choosing the control effort as $Q_C = 0.01$ and 0.05. The corresponding suction distributions can be seen in Fig. 15. For the cases of minimizing the shape factor, and the disturbance kinetic energy at X_f evenly distributed suction distributions are obtained for both values of Q_C. The suction distributions based on minimizing the total disturbance kinetic energy, on the other hand, concentrates the control effort close to the lower branch of the neutral curve. The corresponding EoE of the N_E-factor curves for TS waves are shown in Fig. 16 and are compared with the uncontrolled case. In all cases when control is applied a reduction of the disturbance growth is obtained. When the lower value of the control effort is used, the difference between the three approaches is small, see also Fig. 15. As the control effort is increased, the suction distribution based on minimizing the E_Ω completely stabilizes the disturbances upstream of $s/c \approx 0.12$. The other two approaches, due to the evenly distributed suction, produce a continuous thinning of the boundary layer and consequently larger damping of disturbances downstream.

5. Control using pressure chambers

The most common approach for computing optimal suction distributions is to use the wall mass flux as the control variable (see Balakumar & Hall 1999;

Airiau *et al.* 2003; Pralits *et al.* 2002). In a realistic setting, such as an experiment or suction systems used on wings, the suction velocity is a function of the surface porosity, hole geometry and the pressure difference between the pressure distribution on the surface and static pressure in a number of discrete chambers (see Reneaux & Blanchard 1992; Ellis & Poll 1996; Preist & Paluch 1996; Bieler & Preist 1992; Joslin 1998). The aim here is to derive the optimal control problem of Sec. 3 using the static pressures of a number of discrete chambers, with fixed size and position, as control variables. We will then compare the results with the previously computed continuous suction distribution to assess the feasibility of the latter approach.

If a porous surface is used, then at least for flows with low free-stream velocity, the relation between the pressure difference and the suction velocity is linear, in accordance with Darcy's law. The relation between the pressure difference and suction velocity used here is taken from Bieler & Preist (1992). It is based on measurements carried out in the framework of the ELFIN (European Laminar Flow INvestigation) program. In dimensionless form this formula is given as

$$\Delta P_j = \frac{C_1}{\rho_{\mathrm{w}}}\dot{m}_{\mathrm{w}}^2 + C_2\frac{\mu_{\mathrm{w}}}{\rho_{\mathrm{w}}}\dot{m}_{\mathrm{w}} \quad \forall x^1 \in [X_{cs_j}, X_{ce_j}], \quad j = 1, \cdots, K \qquad (18)$$

where $\Delta P_j = P_e - P_{c_j}$, in which P_e is the pressure distribution on the wing and P_{c_j} is the static pressure in chamber j. The first term on the right hand side of Eq. (18) is due to the dynamic pressure loss, and the second term is the pressure loss due to skin friction. The coefficients C_1 and C_2 together with a brief description of Eq. (18) are given in Appendix C. The choice of static pressure in the chambers is not without restrictions. The Mach number of the flow through the holes of the porous plate should be limited. If ΔP_j is too small then blowing instead of suction might occur. Disturbances might be introduced as an effect of strong suction through discrete holes, which can accelerate instead of delay laminar-turbulent transition (see Reneaux & Blanchard 1992; Ellis & Poll 1996). These restrictions are related to the design of the perforated plate and therefore not considered as constraints in the theory presented here.

5.1. *Optimality system*

Here a concise description of the derivation of the optimality system including pressure chambers is given for the case of minimizing the disturbance kinetic energy. The optimal control problem is now defined as: find controls P_{c_j}, and states $\mathbf{Q}$ and $\tilde{\mathbf{q}}$ which minimize the objective function $\mathcal{J}_0$ given by Eq. (7) with the constraints given by Eqs. (1), (3), (4) and (8). The Lagrange multiplier technique is also used here to enforce the constraints. The adjoint variables $\mathbf{Q}^*, \mathbf{q}^*, r^*, \chi^*$ and λ_j^* where $j = 1, \cdots, K$, are introduced and the new Lagrangian functional is given as

$$\mathcal{L} = \mathcal{J}_0 - \mathcal{J}_1, \qquad (19)$$

where

$$
\begin{aligned}
\mathcal{J}_1 &= \langle \mathbf{Q}^*, L_B\, \mathbf{Q} \rangle + \sum_{j=1}^{K} \int_{X_{cs_j}}^{X_{ce_j}} \lambda_j^* \left[\dot{m}(x^1,0) - \dot{m}_{\mathrm{w}} \right] h_1 dx^1 \\
&+ \chi^*(E_C - \sum_{j=1}^{K} \int_{X_{cs_j}}^{X_{ce_j}} \dot{m}_{\mathrm{w}}^2 h_1 dx^1) + \langle \mathbf{q}^*, L_P\, \hat{\mathbf{q}} \rangle + \langle r^* \hat{\mathbf{q}}, \frac{1}{h_1} \frac{\partial \hat{\mathbf{q}}}{\partial x^1} \rangle + \mathrm{c.c.}
\end{aligned}
$$

Compared to the previously described Lagrangian functionals, the wall boundary condition has now been divided into K discrete domains, and the mass flux at the wall is given by Eq. (18). No additional difficulties appear in the derivation compared to the one in Sec. 3. The optimality condition is now obtained by setting the functional derivative with respect to the static pressure of each chamber to zero. The resulting optimality system can be seen in detail in Appendix C.

5.2. *Results*

Here results are given for the case of minimizing the disturbance kinetic energy using pressure chambers. The parameters in Eq. (18) which specify the porous surface are taken from Bieler & Preist (1992). The plate thickness L and hole diameter at the surface d are 0.9 mm and 0.046 mm, respectively. The porosity $\pi/(4\epsilon^2)$ is calculated given a hole pitch to diameter ratio $\epsilon = 13.8$. The coefficients of inertial and viscous pressure loss are $A = 1.6$ and $B = 0.092$, respectively.

Before the calculations are performed, the size, position and number of pressure chambers must be set. The different sizes are chosen such that the chambers are smaller where the pressure gradient of the wing is large and vice verse. This is done to avoid large pressure drops which result in large suction peaks. The whole control domain $\Gamma_c = [X_{cs}, X_{ce}]$ is used such that the pressure chamber closest to the leading edge starts at $X_{cs_1} = X_{cs}$ and the last pressure chamber ends at $X_{ce_K} = X_{ce}$.

The results in Sec. 4.2 show that minimizing the shape factor does not always give an optimal suction distribution which reduces the disturbance growth. Further, it is seen in Sec. 3.3 that both CF and TS type disturbances should be included in the calculations when the disturbance kinetic energy is minimized. Therefore, we choose to minimize the total disturbance kinetic energy, $\xi = 1$ in Eq. (7), including both the CF and TS waves given in Sec. 3.3. The control effort $Q_C = 0.35$ and the calculations are done for the cases of 5, 6 and 7 pressure chambers.

Results of the optimal static pressures P_{c_j} of each case are plotted (thick lines) in Fig. 17. The pressure distribution on the wing P_e is also plotted (thin lines) for comparison. The region s/c=[0.05,0.175] has been magnified to enhance the details. As shown, the pressure difference $\Delta P_j = P_e - P_{c_j}$ is larger close to the leading edge and decreases downstream.
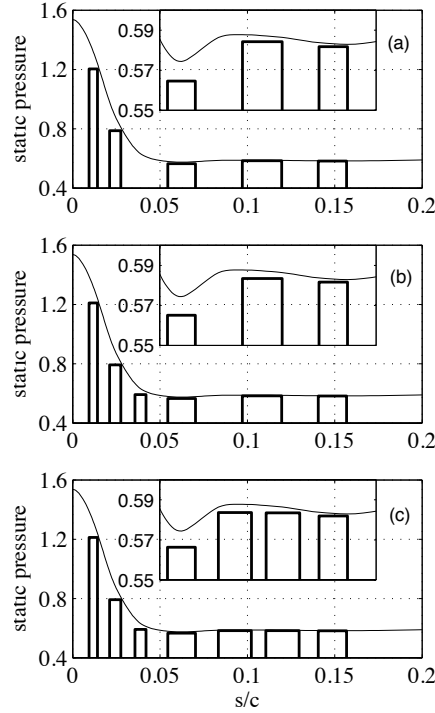
FIGURE 17. Pressure distribution on the wing (thin lines) and optimal static pressure in the chambers (thick lines) for the cases of (a) 5; (b) 6; and (c) 7 pressure chambers minimizing the disturbance kinetic energy E_Ω of a CF ($f_1^* = 5500 \; s^{-1}$, $\beta_1^* = 2500 \; m^{-1}$) and TS wave ($f_2^* = 5750 \; s^{-1}$, $\beta_2^* = 225 \; m^{-1}$) when $Q_C = 0.35$.

The suction distributions corresponding to the optimal static pressures in Fig. 17 are plotted in Fig. 18. Note that the uppermost streamwise suction distribution in each case is due to the stagnation line control and is taken be fixed. In each case the suction distribution downstream of $s/c = 0.05$ is rather constant. Upstream of this streamwise position the suction distributions have more of a saw-tooth shape. The latter is an effect of the strong pressure gradient in this region.

For each case in Fig. 17, a comparison is made with the optimal suction distribution from Fig. 9 (thin lines) for the case when $Q_C = 0.35$. As the same control effort is used in these calculations, it is interesting to compare the optimal suction distribution in a continuous control domain with the cases using pressure chambers. It is seen that the magnitude of both the suction distribution from Fig. 9 and the suction distributions using pressure chambers is rather constant downstream of $s/c = 0.05$ and increases upstream of this
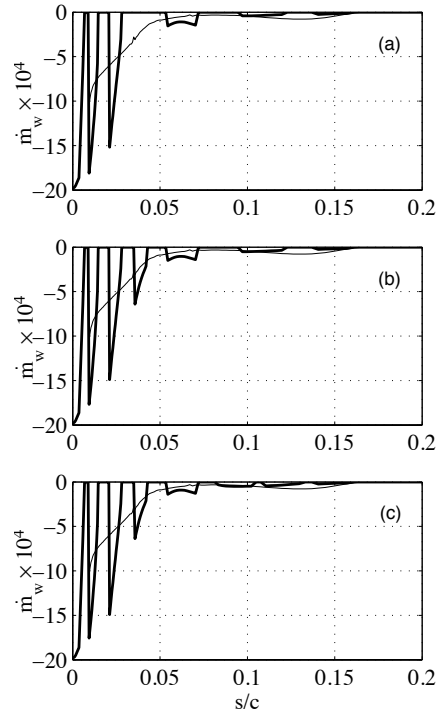
FIGURE 18. Suction distributions (thick lines) corresponding
to the optimal pressure drop for the cases of (a) 5; (b) 6; and
(c) 7 pressure chambers in figure 17. A comparison is done
with the optimal suction distribution (thin lines) from figure
9 when $Q_C = 0.35$.

position. Further, the distribution using pressure chambers approaches the
continuous one when the number of chambers is increased. This is most evident
downstream of $s/c = 0.05$.

The effect on the disturbance growth using the optimal pressure differences
for the cases of 5, 6 and 7 pressure chambers is shown in Fig. 19. Here the EoE
of the N_E-factor curves for CF and TS waves are plotted for zero and optimal
pressure differences of all cases (solid lines). The arrows mark the direction
of increasing number of pressure chambers. A decrease in the growth of both
CF and TS waves is obtained for all optimal pressure differences calculated
here compared to the case of zero suction. The CF waves are more damped
in the control domain when the number of pressure chambers is increased.
However, the difference between the cases of having 6 and 7 pressure chambers
is small as the additional chamber is placed where the CF waves begin to
decay. The results for the TS waves show that upstream of $s/c = 0.1$, the EoE
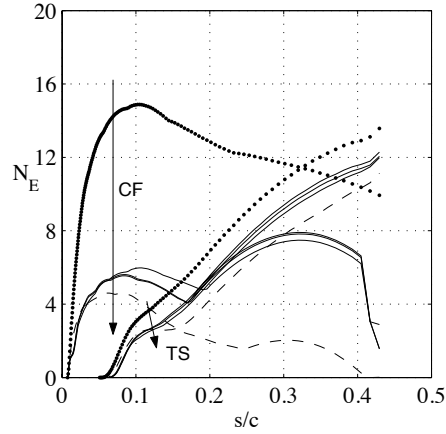curves increase in magnitude as the number of pressure chambers increases.

FIGURE 19. Envelope of envelopes (EoE) of N_E-factor curves for the disturbances given in table 1 for the cases of zero control (dotted) and the optimal pressure chambers in figure 17 (solid). The arrows mark increasing number of pressure chambers. A comparison is done with the EoE of N_E-factor curves (dashed) from figure 11 with $Q_C = 0.35$.

Downstream of this position EoE curves decrease in magnitude. A comparison is made with the EoE of the N_E-factor curves in Fig. 11 which are calculated using the suction distribution from Fig. 9 with $Q_C = 0.35$ (dashed lines). It is seen that as the number of pressure chambers are increased, the results within the control domain using pressure chambers approach those using a suction distribution in a continuous control domain. This is true for the results of both the CF and TS waves.

6. Discussion and conclusions

A method to control convectively unstable disturbances in boundary layers on infinite swept wings for compressible fluids has been derived and analyzed. The method has been developed in the framework of optimal control theory. The mean of disturbance control is a modification of the mean flow by the mass flow through a porous surface. The optimization problem is derived using Lagrange multipliers from which optimality systems are obtained containing the adjoint of the parabolized stability equations (APSE) and the adjoint of the boundary layer equations (ABLE).

Two different control variables are considered. The first control variable is the mass flow at the wall. Here, it is assumed that given a certain control domain, the suction distribution is not constrained by how it will be implemented on the wing and thus has the optimal distribution with respect to a certain objective function. The second control variable is the static pressure in a number of pressure chambers. Here, the suction velocity is a function of the

surface porosity, hole geometry and the pressure difference between the pressure distribution on the wing and the internal static pressure of the pressure chambers. In this case, the internal static pressure of each box is optimized. In both cases, the control effort has not been regularized, but instead enforced as a constraint.

Different measures of the state (objective functions) have been analyzed. The first objective function is a measure of the disturbance kinetic energy. A comparison has been made between minimizing the kinetic energy of a single disturbance at a fixed streamwise position, and minimizing the streamwise integral of the kinetic energy of an arbitrary number of disturbances. For control of a single CF wave, the difference between the two objective functions is small. The advantage of the latter is that more than one disturbance can be included in the measure. On the wing studied here, both cross flow and TS waves are amplified on the upstream part. Results show that both disturbance types need to be accounted for in the objective function in order for the control to decrease their growth. Further, it is sufficient to account for one of each disturbance type in order to control all other disturbances of the same type.

The second measure of the state used here is the streamwise integral of the shape factor, H_{12}. Airiau *et al.* (2003) showed that this quantity is successful for control of two-dimensional disturbances in Blasius flow. In terms of computational effort, the approach of minimizing the shape factor is efficient. The optimality condition for each iteration in the optimization process is obtained after solving the boundary layer and corresponding adjoint equation once. The disadvantage lies in the fact that one does not take into account the disturbance growth in the optimization process, and consequently the effect of the control on the disturbance growth needs to be analyzed afterwards. Results here show that a control based on this objective function amplify instead of damp crossflow modes in the region close to the leading edge of the wing. In this region, the optimal mass-flow distribution has a positive sign i. e. blowing occurs. The amplification of disturbances mean that the point of laminar-turbulent transition will move upstream and the laminar portion of the wing will decrease. Further, as the current way of implementing suction systems relies on pressure chambers, a region of blowing is not realizable.

Results are also presented for the optimal static pressure in a number of pressure chambers. These results depend on the choice of size, position and number of the chambers. However, it can be shown that the corresponding suction distributions are similar in magnitude compared to the result of the optimal suction distribution in a continuous control domain. This similarity increases as the number of pressure chambers is increased.

The magnitudes of the suction distributions presented in this paper are all of order $O(Re^{-1})$, which is within the range of validity of the boundary-layer equations. As Airiau *et al.* (2003) showed, for the suction rate of this order, the boundary-layer and Navier-Stokes calculations agreed well though the optimal mass flux experiences locally large streamwise variation.

7. Acknowledgment

Appendix A. Optimal control using the wall mass flux to minimize the disturbance kinetic energy

A.1. *State equations*

The boundary-layer equations for a viscous compressible flow over a swept wing with an infinite span are

$$\frac{1}{h_1}\frac{\partial(\rho U)}{\partial x^1} + \frac{\partial(\rho W)}{\partial x^3} = 0, \tag{20}$$

$$\frac{\rho U}{h_1}\frac{\partial U}{\partial x^1} + \rho W\frac{\partial U}{\partial x^3} = -\frac{1}{h_1}\frac{dP_e}{dx^1} + \frac{1}{Re}\frac{\partial}{\partial x^3}\left(\mu\frac{\partial U}{\partial x^3}\right), \tag{21}$$

$$\frac{\rho U}{h_1}\frac{\partial V}{\partial x^1} + \rho W\frac{\partial V}{\partial x^3} = \frac{1}{Re}\frac{\partial}{\partial x^3}\left(\mu\frac{\partial V}{\partial x^3}\right), \tag{22}$$

$$c_p\frac{\rho U}{h_1}\frac{\partial T}{\partial x^1} + c_p\rho W\frac{\partial T}{\partial x^3} = \frac{1}{RePr}\frac{\partial}{\partial x^3}\left(\kappa\frac{\partial T}{\partial x^3}\right) +$$

$$(\gamma-1)\frac{UM^2}{h_1}\frac{dP_e}{dx^1} + (\gamma-1)\frac{\mu M^2}{Re}\left[\left(\frac{\partial U}{\partial x^3}\right)^2 + \left(\frac{\partial V}{\partial x^3}\right)^2\right]. \tag{23}$$

The parabolized stability equations are lengthy and here are given in a symbolic form

$$\mathcal{A}\hat{\mathbf{q}} + \mathcal{B}\frac{\partial\hat{\mathbf{q}}}{\partial x^3} + \mathcal{C}\frac{\partial^2\hat{\mathbf{q}}}{(\partial x^3)^2} + \mathcal{D}\frac{1}{h_1}\frac{\partial\hat{\mathbf{q}}}{\partial x^1} = 0, \tag{24}$$

$$\int_0^{+\infty}\hat{\mathbf{q}}^H\frac{\partial\hat{\mathbf{q}}}{\partial x^1}dx^3 = 0, \quad \forall x^1 \in [X_0, X_1], \tag{25}$$

where $\hat{\mathbf{q}} = (\hat{\rho}, \hat{u}, \hat{v}, \hat{w}, \hat{T})^T$. The coefficients of the 5×5 matrices $\mathcal{A}, \mathcal{B}, \mathcal{C}$ and $\mathcal{D}$ are found in Pralits *et al.* (2000). The corresponding boundary conditions are

$$W(x^1, 0) = W_{\mathrm{w}}(x^1) \qquad \forall x^1 \in \Gamma_c,$$
$$W(x^1, 0) = 0 \qquad \forall x^1 \notin \Gamma_c,$$
$$\left[U, V, \frac{\partial T}{\partial x^3}\right](x^1, 0) = [0, 0, 0] \qquad \forall x^1 \in [X_S, X_1],$$
$$\lim_{x^3\to+\infty}[U, V, T](x^1, x^3) = [U_e, V_e, T_e](x^1) \quad \forall x^1 \in [X_S, X_1],$$
$$\left[\hat{u}, \hat{v}, \hat{w}, \hat{T}\right](x^1, 0) = [0, 0, 0, 0] \qquad \forall x^1 \in [X_0, X_1],$$
$$\lim_{x^3\to+\infty}\left[\hat{u}, \hat{v}, \hat{w}, \hat{T}\right](x^1, x^3) = [0, 0, 0, 0] \qquad \forall x^1 \in [X_0, X_1],$$

where variables with subscript w are evaluated at the wall, and subscript e at the boundary layer edge. The initial conditions are

$$
\begin{aligned}
\mathbf{Q}(X_S, x^3) &= \mathbf{Q}_S(x^3) \quad \forall x^3 \in [0, +\infty), \\
\hat{\mathbf{q}}(X_0, x^3) &= \hat{\mathbf{q}}_0(x^3) \quad \forall x^3 \in [0, +\infty),
\end{aligned}
$$

where the solution of variables with subscript 0 is given by the local stability analysis, and subscript S by the solution at the stagnation line.

A.2. *Adjoint equations*

The adjoint of the boundary-layer equations are

$$
\rho \frac{\partial(h_1 W^*)}{\partial x^3} - h_1 \rho \left(\frac{\partial U}{\partial x^3} U^* + \frac{\partial V}{\partial x^3} V^* + c_p \frac{\partial T}{\partial x^3} T^* \right) = F_W \ h_1, \tag{26}
$$

$$
\frac{\partial(\rho U U^*)}{\partial x^1} + \frac{\partial(h_1 \rho W U^*)}{\partial x^3} - \rho \left(\frac{\partial U}{\partial x^1} U^* + \frac{\partial V}{\partial x^1} V^* - \frac{\partial W^*}{\partial x^1} + c_p \frac{\partial T}{\partial x^1} T^* \right) +
$$

$$
(\gamma - 1) M^2 \frac{dP_e}{dx^1} T^* - \frac{2(\gamma - 1)}{Re} M^2 \frac{\partial}{\partial x^3} \left(h_1 \mu \frac{\partial U}{\partial x^3} T^* \right) +
$$

$$
\frac{1}{Re} \frac{\partial}{\partial x^3} \left(\mu \frac{\partial(h_1 U^*)}{\partial x^3} \right) = F_U \ h_1, \tag{27}
$$

$$
\frac{\partial(\rho U V^*)}{\partial x^1} + \frac{\partial(h_1 \rho W V^*)}{\partial x^3} - \frac{2(\gamma - 1)}{Re} M^2 \frac{\partial}{\partial x^3} \left(h_1 \mu \frac{\partial V}{\partial x^3} T^* \right) +
$$

$$
\frac{1}{Re} \frac{\partial}{\partial x^3} \left(\mu \frac{\partial(h_1 V^*)}{\partial x^3} \right) = F_V \ h_1, \tag{28}
$$

$$
c_p \frac{\partial(\rho U T^*)}{\partial x^1} + c_p \frac{\partial(h_1 \rho W T^*)}{\partial x^3} + \frac{\rho U}{T} \left(\frac{\partial U}{\partial x^1} U^* + \frac{\partial V}{\partial x^1} V^* - \frac{\partial W^*}{\partial x^1} \right) +
$$

$$
\frac{\rho U}{T} c_p \frac{\partial T}{\partial x^1} T^* + \frac{\kappa}{RePr} \frac{\partial^2(h_1 T^*)}{(\partial x^3)^2} \frac{(\gamma - 1)}{Re} M^2 \frac{d\mu}{dT} \left[\left(\frac{\partial U}{\partial x^3} \right)^2 + \left(\frac{\partial V}{\partial x^3} \right)^2 \right] T^* -
$$

$$
\frac{1}{Re} \frac{d\mu}{dT} \left[\frac{\partial U}{\partial x^3} \frac{\partial(h_1 U^*)}{\partial x^3} + \frac{\partial V}{\partial x^3} \frac{\partial(h_1 V^*)}{\partial x^3} \right] = F_E h_1, \tag{29}
$$

where $F_E = (F_T + F_W \ W/T) h_1$, and F_W, F_U, F_V, F_T are found in Pralits (2001). The adjoint of the parabolized stability equations can be written as

$$
\tilde{\mathcal{A}} \mathbf{q}^* + \tilde{\mathcal{B}} \frac{\partial \mathbf{q}^*}{\partial x^3} + \tilde{\mathcal{C}} \frac{\partial^2 \mathbf{q}^*}{(\partial x^3)^2} + \tilde{\mathcal{D}} \frac{1}{h_1} \frac{\partial \mathbf{q}^*}{\partial x^1} = S_P^*, \tag{30}
$$

$$
\frac{\partial}{\partial x^1} \int_0^{+\infty} \mathbf{q}^{*H} \left(\frac{\partial \mathcal{A}}{\partial \alpha} + \frac{\partial \mathcal{B}}{\partial \alpha} \right) \hat{\mathbf{q}} \ h_1 dx^3 =
$$

$$
\begin{cases}
0 & \forall x^1 \notin [X_{ms}, X_{me}], \\
-\mathrm{i}|\Theta|^2 \int_0^{+\infty} \hat{\mathbf{q}}^H M \hat{\mathbf{q}} \ h_1 dx^3 & \forall x^1 \in [X_{ms}, X_{me}],
\end{cases} \tag{31}
$$

where

$$S_P^* = \begin{cases} -\bar{r}^* \dfrac{\partial \hat{\mathbf{q}}}{\partial x^1} - \dfrac{\partial (r^* \hat{\mathbf{q}})}{\partial x^1} & \forall x^1 \notin [X_{ms}, X_{me}], \\[3mm] -\bar{r}^* \dfrac{\partial \hat{\mathbf{q}}}{\partial x^1} - \dfrac{\partial (r^* \hat{\mathbf{q}})}{\partial x^1} + \xi M^H \hat{\mathbf{q}} |\Theta|^2 & \forall x^1 \in [X_{ms}, X_{me}], \end{cases}$$

and

$$\tilde{\mathcal{A}} = \mathcal{A}^H - \frac{\partial \mathcal{B}^H}{\partial x^3} - m_{13}\, \mathcal{B}^H + \frac{\partial^2 \mathcal{C}^H}{(\partial x^3)^2} + 2\, m_{13} \frac{\partial \mathcal{C}^H}{\partial x^3} - \frac{\partial \mathcal{D}^H}{\partial x^1},$$

$$\tilde{\mathcal{B}} = -\mathcal{B}^H + 2\frac{\partial \mathcal{C}^H}{\partial x^3} + 2\, m_{13}\, \mathcal{C}^H,$$

$$\tilde{\mathcal{C}} = \mathcal{C}^H,$$

$$\tilde{\mathcal{D}} = -\mathcal{D}^H.$$

The vector $\mathbf{q}^* = (\rho^*, u^*, v^*, w^*, \theta^*)^T$, and the complete derivation of these equations is found in Pralits *et al.* (2000). The above equations are subjected to the following boundary conditions

$$[u^*, v^*, w^*, \theta^*]\,(x^1, 0) = [0, 0, 0, 0] \quad \forall x^1 \in [X_0, X_1],$$

$$\lim_{x^3 \to +\infty} [u^*, v^*, w^*, \theta^*]\,(x^1, x^3) = [0, 0, 0, 0] \quad \forall x^1 \in [X_0, X_1],$$

$$[U^*, V^*]\,(x^1, 0) = [0, 0] \quad \forall x^1 \in [X_0, X_1],$$

$$\left[\frac{\kappa}{RePr} \frac{\partial (h_1 T^*)}{\partial x^3} + h_1 \rho c_p W T^* \right] (x^1, 0) = 0 \quad \forall x^1 \in [X_0, X_1],$$

$$\lim_{x^3 \to +\infty} [U^*, V^*, W^*, T^*]\,(x^1, x^3) = [0, 0, 0, 0] \quad \forall x^1 \in [X_0, X_1].$$

The initial conditions are

$$\mathbf{q}^*(X_1, x^3) = (1 - \xi)\mathbf{q}_1^*(x^3) \quad \forall x^3 \in [0, +\infty),$$
$$r^*(X_1) = (1 - \xi)r_1^* \quad \forall x^3 \in [0, +\infty),$$
$$\mathbf{Q}^*(X_1, x^3) = \mathbf{0} \quad \forall x^3 \in [0, +\infty),$$

with $\mathbf{q}_1^*$ and r_1^* evaluated at $x^1 = X_1$ as

$$\mathbf{q}_1^* = |\Theta|^2 \mathcal{D}^+ (M - c_1 \mathcal{I}) \hat{\mathbf{q}}, \qquad r_1^* = |\Theta|^2\, c_1,$$

$$\bar{c}_1 = \frac{\displaystyle\int_0^\infty (h_1 \hat{\mathbf{q}}^H M\, \mathcal{D}^{+H} \left(\frac{\partial \mathcal{A}}{\partial \alpha} + \frac{\partial \mathcal{B}}{\partial \alpha} \right) \hat{\mathbf{q}} - i\hat{\mathbf{q}}^H M \hat{\mathbf{q}})\, dx^3}{\displaystyle\int_0^\infty \hat{\mathbf{q}}^H \mathcal{D}^{+H} \left(\frac{\partial \mathcal{A}}{\partial \alpha} + \frac{\partial \mathcal{B}}{\partial \alpha} \right) \hat{\mathbf{q}}\, h_1\, dx^3}, \tag{32}$$

where $\mathcal{D}^+ = (\mathcal{D}^H)^{-1}$.

A.3. *Optimality condition*

The optimality condition is

$$W_{\text{w}}^* = \begin{cases} -2\chi^* \dot{m}_{\text{w}} & \forall x^1 \in \Gamma_c, \\ 0 & \forall x^1 \notin \Gamma_c, \end{cases} \tag{33}$$

where

$$\chi^* = \left(\frac{1}{4E_C} \int_{X_{cs}}^{X_{ce}} W_{\rm w}^{*2} h_1 dx^1 \right)^{\frac{1}{2}}.$$

Appendix B. Optimal control using the wall mass flux to minimize the shape factor

B.1. *State equations*

The boundary layer equations are given by Eqs. (20), (21), (22) and (23) with corresponding boundary and initial conditions as given in A.1.

B.2. *Adjoint equations*

The adjoint boundary layer equations are given by Eqs. (26), (27), (28) and (29) where the component of the forcing $S_B^* = (F_W, F_U, F_V, F_E)$ are now

$$F_W = 0, \qquad F_U = \frac{1}{\delta_2} \rho \cos(\phi)(1 + H_{12}(1 - 2U_{SL})) \frac{U_{e_0}}{Q_e},$$

$$F_V = \frac{1}{\delta_2} \rho \sin(\phi)(1 + H_{12}(1 - 2U_{SL})) \frac{U_{e_0}}{Q_e}, \quad F_E = -\frac{1}{\delta_2} \frac{\rho}{T} U_{SL}(1 + H_{12}(1 - U_{SL})) \frac{T_{e_0}}{T_e},$$

The initial and boundary conditions are the ones given in A.2, except for freestream boundary conditions which are now given as

$$\lim_{x^3 \to +\infty} \left[\frac{\partial U^*}{\partial x^3}, \frac{\partial V^*}{\partial x^3}, W^*, \frac{\partial T^*}{\partial x^3} \right] (x^1, x^3) = [0, 0, 0, 0] \quad \forall x^1 \in [X_0, X_1].$$

B.3. *Optimality condition*

The optimality condition is given by Eq. (33).

Appendix C. Optimal control using pressure chambers to minimize the disturbance kinetic energy

C.1. *Relation between internal static pressure and mass flux*

The relation between the pressure difference and suction velocity used here is taken from Bieler & Preist (1992). It is based on measurements carried out in the framework of the ELFIN (European Laminar Flow INvestigation) program. In dimensionless form this formula is given as

$$\Delta P_j = P_e - P_{c_j} = \frac{C_1}{\rho_{\rm w}} \dot{m}_{\rm w}^2 + C_2 \frac{\mu_{\rm w}}{\rho_{\rm w}} \dot{m}_{\rm w}$$

where

$$C_1 = \frac{A}{2} \left(\frac{4\epsilon^2}{\pi} \right)^2, \qquad C_2 = \frac{32B}{Re} \frac{4\epsilon^2}{\pi} \frac{L}{d^2}.$$

The porous plate has a thickness L and a hole diameter d at the surface. Due to manufacturing reasons the holes were slightly conical with an inner

diameter D. The porosity is given as $\pi/(4\epsilon^2)$, where ϵ is the ratio between the hole diameter on the surface and the distance between the holes.

It was found in experiments that the relationship between the suction velocity and pressure difference was non-linear and that adding a term due to dynamic pressure loss with an empirically obtained coefficient A gave a good agreement with experiments (see Bieler & Preist 1992). The second term on the right hand side of the formula is based on the Hagen-Poiseuille equation for pressure loss due to skin friction in a hole with parallel walls. The coefficient B is a function of the inner and outer hole diameters and serves as a correction due to the conical shape of the holes.

C.2. *State equations*

The boundary-layer equations are given by Eqs. (20), (21), (22) and (23) with corresponding initial conditions as given in A.1. All boundary conditions are the same as given in A.1, except for the wall normal mean velocity at the wall, which is now given by

$$
W(x^1,0) = \begin{cases} 0 & \forall x^1 \notin [X_{cs_j}, X_{ce_j}], \\ -\dfrac{1}{2}\dfrac{C_2}{C_1}\dfrac{\mu_{\mathrm{w}}}{\rho_{\mathrm{w}}} + \sqrt{\left(\dfrac{1}{2}\dfrac{C_2}{C_1}\dfrac{\mu_{\mathrm{w}}}{\rho_{\mathrm{w}}}\right)^2 + \Delta P_j \dfrac{\rho_{\mathrm{w}}}{C_1}} & \forall x^1 \in [X_{cs_j}, X_{ce_j}]. \end{cases}
$$

The values used here for A, B, L, d and ϵ are taken from Bieler & Preist (1992). The parabolized stability equations are given by Eqs. (24) and (25) with corresponding boundary and initial conditions as given in A.1.

C.3. *Adjoint equations*

The adjoint parabolized stability equations are given by Eqs. (30) and (31) with corresponding boundary and initial conditions as given in A.1. The adjoint boundary layer equations are given by Eqs. (26), (27), (28) and (29) with corresponding initial conditions as given in A.2. All boundary conditions are the same as given in A.2, except for T^* at the wall, which is now given by

$$
\left[\frac{\kappa}{RePr}\frac{\partial(h_1 T^*)}{\partial x^3} + h_1 \rho c_p W T^*\right](x^1,0) = \begin{cases} 0 & \forall x^1 \notin [X_{cs_j}, X_{ce_j}], \\ K_j(W^* + 2\chi^* \dot{m}_{\mathrm{w}}) & \forall x^1 \in [X_{cs_j}, X_{ce_j}], \end{cases}
$$

where

$$
K_j = \frac{\partial P_{c_j}}{\partial T_{\mathrm{w}}} \Big/ \frac{\partial P_{c_j}}{\partial \dot{m}_{\mathrm{w}}},
$$

and

$$
\left.\begin{aligned}
\frac{\partial P_{c_j}}{\partial T_{\mathrm{w}}} &= \frac{1}{\rho_{\mathrm{w}} T_{\mathrm{w}}} C_1 \dot{m}_{\mathrm{w}}^2 + C_2 \frac{1}{\rho_{\mathrm{w}}}\left(\frac{\mu_{\mathrm{w}}}{T_{\mathrm{w}}} + \frac{d\mu_{\mathrm{w}}}{dT_{\mathrm{w}}}\right)\dot{m}_{\mathrm{w}} \\
\frac{\partial P_{c_j}}{\partial \dot{m}_{\mathrm{w}}} &= \frac{2C_1}{\rho_{\mathrm{w}}}\dot{m}_{\mathrm{w}} + C_2 \frac{\mu_{\mathrm{w}}}{\rho_{\mathrm{w}}}
\end{aligned}\right\} \quad \forall x^1 \in [X_{cs_j}, X_{ce_j}].
$$

C.4. *Optimality condition*

$$-\int_{X_{cs_j}}^{X_{ce_j}} (W_{\mathrm{w}}^* + 2\chi^* \dot{m}_{\mathrm{w}}) \left(\frac{\partial P_{c_j}}{\partial \dot{m}_{\mathrm{w}}}\right)^{-1} h_1 dx^1 = 0, \qquad j = 1, \cdots, K.$$

where

$$\chi^* = \left(\frac{1}{4E_C}\sum_{j=1}^{K}\int_{X_{cs_j}}^{X_{ce_j}} W_{\mathrm{w}}^{*2} h_1 dx^1\right)^{\frac{1}{2}}.$$

References

AIRIAU, C., BOTTARO, A., WALTHER, S. & LEGENDRE, D. 2003 A methodology for optimal laminar flow control: Application to the damping of tollmien-schlichting waves in a boundary layer. *Phys. Fluids* **15**, 1131–1145.

ATKIN, C. 2000 New aerodynamic approach to suction system design. In *CEAS/DragNet European Drag Reduction Conference* (ed. P. Thiede). Potsdam, Germany: Springer.

BALAKUMAR, P. & HALL, P. 1999 Optimum suction distribution for transition prediction. *Theor. Comput. Fluid Dyn.* **13**, 1–19.

BERTOLOTTI, F., HERBERT, T. & SPALART, S. 1992 Linear and nonlinear stability of the blasius boundary layer. *J. Fluid Mech.* **242**, 441–474.

BEWLEY, T. 2001 Flow control: new challenges for a new renaissance. *Progess in Aerospace Sciences* **37**, 21–58.

BIELER, H. & PREIST, J. 1992 Hlfc for commercial aircraft. In *First european forum on laminar flow technology*, pp. 193–199. Hamburg.

BYRD, R., LU, P., NOCEDAL, J. & ZHU, C. 1995 A limited memory algorithm for bound constrained optimization. *SIAM J. Sci. Comput.* **16**, 1190–1208.

CATHALIFAUD, P. & LUCHINI, P. 2000 Algebraic growth in a boundary layer: optimal control by blowing and suction at the wall. *Eur. J. Mech. B/Fluids* **19** (4), 469–490.

ELLIS, J. & POLL, D. 1996 Laminar and laminarizing boundary layers by suction through perforated plates. In *Second european forum on laminar flow technology*, pp. 8.17–8.26. Bordeaux.

GUNZBURGER, M. D. 1997 Introduction into mathematical aspects of flow control and optimization, von karman institute for fluid dynamics, lecture series 1997-05. *Inverse Design and Optimization Methods* .

HANIFI, A., HENNINGSON, D. S., HEIN, S. & BERTOLOTTI, F. P.AND SIMEN, M. 1994 Linear non-local instability analysis - the linear nolot code. *FFA TN* **1994-54**.

HANIFI, A., SCHMID, P. J. & HENNINGSON, D. S. 1996 Transient growth in compressible boundary layer flow. *Phys. Fluids* **8 (3)**, 826–837.

HERBERT, T. 1997 Parabolized stability equations. *Annu. Rev. Fluid Mech.* **29**, 245–283.

HILL, D. C. 1997b Inverse design for laminar three-dimensional boundary layers. *Bull. Am. Phys. Soc.* **42**, 2120.

HÖGBERG, M. & HENNINGSON, D. S. 2001 Linear optimal control applied to instabilities in spatial boundary layers. *J. Fluid Mech.* Submitted.

VAN INGEN, J. L. 1956 A suggested semiempirical method for the calculation of the boundary layer transition region. *Tech. Rep.* VTH-74. Department of Aeronautical Engineering, University of Delft.

JOSLIN, R. 1998 Overview of laminar flow control. *Tech. Rep.* 1998-208705. NASA, Langley Research Center, Hampton, Virginia.

MALIK, M. R. & BALAKUMAR, P. 1992 Nonparallel stability of rotating disk flow using pse. In *Instability, Transition and Turbulence* (eds. M. Hussaini, A. Kumar & C. Streett), pp. 168–180. Springer.

MUGHAL, M. 1998 Active control of instabilities in three-dimensional compressible flows. *Theor. Comput. Fluid Dyn.* **12**, 195–217.

PRALITS, J. O. 2001 Towards optimal design of vehicles with low drag: Applications to sensitivity analysis and optimal control. Licentiate thesis KTH/MEK/TR-01/07. Royal Institute of Technology, SE-172 90 Stockholm, Sweden.

PRALITS, J. O., AIRIAU, C., HANIFI, A. & HENNINGSON, D. S. 2000 Sensitivity analysis using adjoint parabolized stability equations for compressible flows. *Flow, Turbulence and Combustion* **65**, 321–346.

PRALITS, J. O., HANIFI, A. & HENNINGSON, D. S. 2002 Adjoint-based optimization of steady suction for disturbance control in incompressible flows. *J. Fluid Mech.* **467**, 129–161.

PREIST, K. & PALUCH, B. 1996 Design specification and inspection of perforated panels for hlf suction systems. In *Second european forum on laminar flow technology*, pp. 6.20–6.34. Bordeaux.

RENEAUX, J. & BLANCHARD, A. 1992 The design and testing of an airfoil with hybrid laminar flow control. In *First european forum on laminar flow technology*, pp. 164–174. Hamburg.

SCHLICHTING, H. 1943/44 Die beeinflussung der grenzschicht durch absaugung und ausblasen. *Jb. dt. Adad. d. Luftfahrtforschung* **90-108**.

SIMEN, M. 1992 Local and non-local stability theory of spatially varying flows. In *Instability, Transition and Turbulence* (eds. M. Hussaini, A. Kumar & C. Streett), pp. 181–201. Springer.

SMITH, A. M. O. & GAMBERONI, N. 1956 Transition, pressure gradient and stability theory. *Tech. Rep.* ES 26388. Douglas Aircraft Co.

WALTHER, S., AIRIAU, C. & BOTTARO, A. 2001 Optimal control of tollmien-schlichting waves in a developing boundary layer. *Phys. Fluids* **13**, 2087–2096.

ZHU, C., BYRD, R., LU, P. & NOCEDAL, J. 1994 L-bfgs-b: Fortran subroutines for large scale bound constrained optimization. *Tech. Rep.* NAM-11. EECS Department, Northwestern University.

Paper 4

4

Optimization of Steady Wall Temperature for Disturbance Control

By Jan O. Pralits[1,2] and Ardeshir Hanifi[2]

We present a theory for computing the optimal steady wall temperature distribution to suppress the growth of convectively unstable disturbances in compressible boundary layer flows on flat plates. A gradient based iterative procedure is used to minimize an objective function measuring the disturbance kinetic energy. The gradient of interest is obtained from the solution of the adjoint of the boundary layer and parabolized stability equations, which are derived using a Lagrange multiplier technique. The study includes a comparison between the cases of minimizing the terminal, and an integrated value of the disturbance kinetic energy for different freestream Mach numbers and control magnitudes. A comparison is also made for the cases of zero and non-zero wall heat transfer outside the control domain.

1. Introduction

Delay of laminar-turbulent transition is desired in a number of applications. It was early recognized that uniformly distributed cooling has a damping effect on viscous instabilities for various Mach number flows, see e. g. experiments by Diaconis *et al.* (1957) and Jack *et al.* (1957). Liepmann & Fila (1947), showed that at low subsonic speeds the transition location moves upstream on a heated flat plate. The destabilizing effect of heating is due to the increase of the viscosity of air close to the wall, which creates inflectional velocity profiles there. Cooling the wall on the other hand, decreases the viscosity near the wall which results in a thicker velocity profile and thus a more stable flow. Lees & Lin (1946) using inviscid theory and Mack (1984) using viscous theory found that subsonic air boundary layers can be completely stabilized by uniformly distributed wall-cooling. Mack also showed that uniformly distributed wall-cooling has a destabilizing effect on the higher modes (also known as the Mack modes) which appear at high Mach numbers. His results for supersonic flows have been experimentally verified by Lysenko & Maslov (1984). Masad *et al.* (1992) reported similar results using the spatial stability equations for compressible flows.

[1]Department of Mechanics, KTH, SE-100 44 Stockholm, Sweden.
[2]Swedish Defence Research Agency, FOI, Aeronautics Division, FFA, SE-172 90 Stockholm, Sweden.

More recent studies by Masad & Nayfeh (1992) and Lo *et al.* (1995), have shown that discrete heating strips located upstream of the first neutral point decreases the maximum amplification of disturbances in subsonic boundary layers. As the heating strip is moved downstream, into the unstable region, the maximum amplification is increased. The opposite was found for discrete cooling strips which was explained to be due to the fact that the flow which leaves the cooled domain experiences a relatively hotter surface downstream. Massad & Nayfeh used also the interactive boundary-layer theory to account for the pressure gradient induced by thickening/thinning of boundary layer due to heating/cooling strips. However, they concluded that the differences between the N-factors using the mean flow obtained from interactive, and non-similar boundary layer equations are small.

In the most of the works found in the literature, the effects of wall-cooling or -heating on disturbance growth are studied using a predefined temperature distribution in either a continuous or discrete domain (strips). However, in some earlier works by other researchers, the problem of temperature optimization has been addressed. In Masad & Nayfeh (1992), a parameter study was performed in order to find the best location for a heating strip with a given length and a constant ratio between the wall and adiabatic temperature. In Gunzburger *et al.* (1993) an optimal control problem using boundary controls for the incompressible Navier-Stokes equations was derived. An application of control by heating and cooling was given with the wall heat flux as the control parameter and a target wall temperature as the objective. However, in none of these works an optimal temperature distribution in terms of minimizing a measure of disturbance amplitude has been derived. In Hill (1997b), an inverse method to compute the optimal cooling/heating distributions was mentioned but no details were given there.

In this paper, we present the theory and examples of optimal distribution of temperature in discrete domains which minimize the growth of connectively unstable disturbances in a growing boundary layer. The evolution of these disturbances in a quasi three-dimensional boundary layer is here analyzed using the Parabolized Stability Equations (PSE) (see Bertolotti *et al.* 1992; Simen 1992; Malik & Balakumar 1992; Herbert 1997) derived for compressible flows, see section 2. The control problem is defined in section 3 using optimal control theory in which a Lagrange multiplier technique is used. The aim is to minimize some measure of the disturbance amplitude for a given cooling/heating energy. The optimality systems consists of solving state and corresponding adjoint equations from which an optimality condition is evaluated. Here, we couple the adjoint of the PSE with the adjoint of the boundary-layer equations in order to find the optimality condition.

In section 5 results are presented for optimal temperature distribution to control disturbance growth in flat plate boundary-layer flows. Here, the effects of the control magnitude, objective function, Mach number and heat transfer

outside the control domain are investigated. The summary and conclusions are given in section 6.

2. State equations

The flow field is given by the solution of the mass, momentum and energy conservation equations for a viscous compressible flow. The equations are written for Cartesian coordinates with streamwise, spanwise and wall-normal coordinates denoted as x^1, x^2 and x^3 respectively. The total flow field, q_{tot} is decomposed into a mean, $\bar{q}$, and a perturbation part, $\tilde{q}$, as

$$q_{tot}(x^1, x^2, x^3, t) = \bar{q}(x^1, x^3) + \tilde{q}(x^1, x^2, x^3, t)$$

where $\bar{q} \in [U, V, W, P, T, \rho]$ and $\tilde{q} \in [\tilde{u}, \tilde{v}, \tilde{w}, \tilde{p}, \tilde{T}, \tilde{\rho}]$. Here U, V, W are the streamwise, spanwise and wall-normal velocity components of the mean flow respectively, T is the temperature, ρ the density and P the pressure. The respective lower case variables correspond to the disturbance quantities. The mean flow has zero variation in the spanwise direction and the evolution of convectively unstable disturbances is analyzed in the frame-work of the nonlocal stability theory. The mean flow and disturbance equations in the following sections are given in dimensionless form. All flow and material quantities are made dimensionless with the corresponding reference flow quantities at a fixed streamwise position $x_0^\star$, except the pressure, which is referred to twice the corresponding dynamic pressure. Here, dimensional quantities are denoted by the superscript $\star$.

The reference length scale is taken as $l_0^\star = (\nu_0^\star x_0^\star / U_0^\star)^{\frac{1}{2}}$. The Reynolds and Mach number are defined as $Re_0 = l_0^\star U_0^\star / \nu_0^\star$ and $M = U_0^\star / (\mathcal{R}\gamma T_0^\star)^{\frac{1}{2}}$ respectively where $\mathcal{R}$ is the specific gas constant, ν the kinematic viscosity and γ the ratio of specific heats. The dynamic viscosity is calculated using the Sutherland law. The coefficient of the specific heat c_p and the thermal conductivity κ are both functions of temperature as 4th order polynomials fitted to a set of experimental data. The bulk viscosity is calculated using the formula given by Bertolotti (1998) and the Prandtl number is calculated based on the reference temperature, see Appendix B.

2.1. *Mean Flow equations and control variable*

The dimensionless boundary layer equations (BLE) written in the primitive variables form can be found in Appendix A. These are here written in symbolic form as

$$L_B \, \mathbf{Q} = 0 \tag{1}$$

where $\mathbf{Q} = (U, V, W, T)^T$. The velocity components are zero at the wall and the heated or cooled plate is defined by $T(x^1, 0) = T_w(x^1)$ in a streamwise domain $\Gamma_C = [X_{cs}, X_{ce}]$. Here, subscripts cs and ce refers to the start and end of the control domain, respectively. As the control $T_w(x^1)$ is not applied along the whole plate, it is necessary to define the boundary condition of the temperature upstream and downstream of Γ_C. Here, two different choices of boundary

conditions are considered outside of the control domain. In the first, denoted TW1, the wall temperature is prescribed as $T(x^1,0) = T_{w_0}$. Here T_{w_0} can be for instance the adiabatic wall temperature for the uncontrolled case. The second choice for boundary condition, denoted TW2, is to set $\partial T(x^1,0)/\partial x^3 = 0$ outside of the control domain. The effects on the mean flow due to the choice of boundary condition will appear as cooling or heating is applied. However, due to the parabolic nature of the BLE, only the mean flow in the domain downstream of Γ_C will change. If TW1 is chosen then as the control is applied, the flow downstream of Γ_C will no longer satisfy $\partial T(x^1,0)/\partial x^3 = 0$, i. e. the wall is no longer considered to be adiabatic. If TW2 is chosen then as the control is applied, the wall temperature will change in order to satisfy the adiabatic wall boundary condition. Note that we here assume that the freestream velocity does not change as the control is applied. If the temperature distribution would result in a large change in the boundary layer thickness, then it may be necessary to update the freestream velocity in the optimization process.

2.2. *Disturbance equations*

The perturbations are assumed to be time and spanwise periodic disturbances as

$$\tilde{\mathbf{q}}(x^i, t) = \hat{\mathbf{q}}(x^1, x^3)\Theta \quad \text{where} \quad \Theta = \exp\left(\mathrm{i}\int_{X_0}^{x^1} \alpha(x')dx' + \mathrm{i}\beta x^2 - \mathrm{i}\omega t\right), \quad (2)$$

where α is the complex streamwise wavenumber, β the real spanwise wavenumber and ω the real disturbance angular frequency. The initial streamwise position where the disturbances are superimposed on the mean flow is denoted X_0. We assume a scale separation Re^{-1} between the weak variation in the x^1-direction and the strong variation in the x^3-direction. Further, it is assumed that $\partial/\partial x^1 \sim O(Re^{-1})$ and $W \sim O(Re^{-1})$. Introducing Eq. (2) and the assumptions above in the linearized governing equations, keeping terms up to order $O(Re^{-1})$, yield a set of nearly parabolic partial differential equations (see Bertolotti *et al.* 1992; Malik & Balakumar 1992; Simen 1992; Herbert 1997). A complete description of the equations and corresponding numerical schemes used here are given in Hanifi *et al.* (1994) and Hein *et al.* (1994). The system of equations, denoted parabolized stability equations (PSE) are given in Appendix A and are here written in symbolic form as

$$L_P \, \hat{\mathbf{q}} \quad = \quad 0 \tag{3}$$

where $\hat{\mathbf{q}} = (\hat{\rho}, \hat{u}, \hat{v}, \hat{w}, \hat{T})^T$. The variables $\hat{u}, \hat{v}, \hat{w}$ and $\hat{T}$ are subject to Dirichlet boundary conditions. To remove the ambiguity of having x^1-dependence of both the amplitude and the wave function in Eq. (2) and to maintain a slow streamwise variation of the amplitude function $\hat{\mathbf{q}}$, a so called 'auxiliary condition' is introduced

$$\int_0^{+\infty} \hat{\mathbf{q}}^H \frac{\partial \hat{\mathbf{q}}}{\partial x^1} \, dx^3 = 0, \tag{4}$$

where superscript H refers to the complex conjugate transpose. Equation (3) is integrated in the downstream direction with an initial condition given by the local stability theory at $x^1 = X_0$. At each x^1-position the streamwise wavenumber α is iterated such that Eq. (4) is satisfied. When a converged streamwise wavenumber has been obtained, the growth rate can be calculated from the following relation

$$\sigma_E = -\alpha_i + \frac{\partial}{\partial x^1}(\ln \sqrt{E})$$

where

$$E = \int_0^{+\infty} \rho\,(|\hat{u}|^2 + |\hat{v}|^2 + |\hat{w}|^2)\,dx^3,$$

is the kinetic energy based on the amplitude functions of the disturbance velocity components. The growth rate can then be used to predict the transition location using the so called e^N-method (see van Ingen 1956; Smith & Gamberoni 1956). The N-factor based on the disturbance kinetic energy N_E is here defined as

$$N_E = \int_{X_{n1}}^{x^1} \sigma_E\,dx^1,$$

where X_{n1} is the first neutral point ($\sigma_E = 0$).

3. Disturbance control

The approach of the current work is to use optimal control theory to find the optimal mean wall-temperature distribution in order to suppress the growth of convectively unstable disturbances. The problem consists of the state variables $\mathbf{Q}$ and $\tilde{\mathbf{q}}$; a control variable given by the temperature at the wall; constraints on the state variables given by the BLE and PSE; and a cost function, a measure of the state, to be minimized.

The final goal of cooling or heating the plate is to increase the laminar portion i. e. to move the location of the laminar-turbulent transition further downstream, and thus decrease the viscous drag. It is therefore important that the chosen cost function can be related to the transition process. One choice is to measure the kinetic energy of a certain disturbance at a given downstream position, say X_f. This can be written as

$$E_f = \frac{1}{2}\int_{Z_0}^{Z_1}\int_0^{+\infty} \tilde{\mathbf{q}}^H M \tilde{\mathbf{q}}\,dx^2 dx^3 \bigg|_{x^1 = X_f}, \tag{5}$$

where $M = \mathrm{diag}(0, 1, 1, 1, 0)$ which means that the disturbance kinetic energy is calculated from the disturbance velocity components. If the position X_f is chosen as the upper branch of the neutral curve, then the measure can be

related to the maximum value of the N-factor of a given disturbance as

$$N_{max} = \ln \sqrt{\frac{E_f}{E_0}}, \tag{6}$$

where E_0 is the disturbance kinetic energy at the first neutral point. If in addition the measured disturbance is the one which first (with zero control) reaches the transition N-factor, then X_f can be related to the onset of the laminar-turbulent transition. It is however not clear, a priori, that minimizing such a measure will damp the chosen disturbance in the whole unstable region. If the optimal control only acts close to the position of the measurement then a situation might occur where the amplification of the disturbance upstream of this position is still large enough to cause transition. We also have to consider that many different instability waves simultaneously exist inside the boundary layer. Even though the one which first causes transition in the uncontrolled case is chosen to compute E_f, it is not certain that the resulting optimal temperature distribution will have a damping effect also on other waves. For computation of optimal suction distributions in Blasius flow, it has been shown that a cost function based on a single TS wave is sufficient to successfully damp the growth of other TS waves (see Pralits *et al.* 2002; Airiau *et al.* 2003). There are however other situations, such as the boundary layer flow on infinite swept wings, where it is common that both TS and cross-flow waves are present. As these waves are amplified in different streamwise regions due to the streamwise variation of the mean flow pressure gradient, an optimal control based on minimizing e. g. a TS wave does not necessarily have a damping effect on the cross flow waves. See Pralits & Hanifi (2003) for such results regarding optimization of mean flow suction distributions. An alternative is therefore to measure the kinetic energy as the streamwise integral over a defined domain. Using such an approach, several different disturbances having their maximum growth rate at different positions, can be accounted for in one and the same optimization. Here, the size of K disturbances superimposed on the mean flow at an upstream position X_0, is measured by their total kinetic energy as

$$E_\Omega = \sum_{k=1}^{K} \frac{1}{2} \int_{X_{ms}}^{X_{me}} \int_{Z_0}^{Z_1} \int_0^{+\infty} \tilde{\mathbf{q}}_k^H M \tilde{\mathbf{q}}_k \; dx^1 dx^2 dx^3, \tag{7}$$

where X_{ms} and X_{me} refer to start and end positions of the measuring domain. We now define the objective function based on the disturbance growth as

$$\mathcal{J}_0 = \xi E_\Omega + (1 - \xi) E_f, \tag{8}$$

where the parameter ξ can have values between zero or one, depending on the quantity one wants to minimize.

If no restriction is given on the magnitude of the wall temperature then the cooling level is bounded by $T(x^1, 0) = 0$ and in terms of heating, the wall temperature is unbounded. We therefore define a dimensionless measure of the

control effort as

$$E_C = \frac{E_C^*}{T_0^{*2}} = \int_{X_{cs}}^{X_{ce}} \left(T_{\mathrm{w}} - T_{ad_0}(x^1,0)\right)^2 dx^1, \tag{9}$$

where E_C^* is the dimensional value of the control effort. With expression (9) we can compare control at different Mach numbers for a fixed value of E_C^*. Equation (9) expresses the deviation of the control from the zero control state. Here, the zero control case corresponds to adiabatic wall temperature, $T_{ad_0}(x^1,0)$, i. e. the wall temperature satisfying $\partial T/\partial x^3(x^1,0) = 0$ when no cooling or heating is applied. At each streamwise position, the amplitude of the control can be expressed as $\Delta T = T_{\mathrm{w}} - T_{ad_0}(x^1,0)$. In order to account for both cooling and heating, we take the square of ΔT.

A concise description of the objective can now be made: find the control T_{w}, and corresponding states $\mathbf{Q}$ and $\tilde{\mathbf{q}}$ which minimizes the objective function $\mathcal{J}_0$ with the constraints given by Eqs. (1), (3), (4) and (9). We now use a Lagrange multiplier technique to replace the original constrained problem with an unconstrained one, see e. g. Gunzburger (1997). In order to enforce the constraints we introduce the adjoint variables $\mathbf{Q}^*, \mathbf{q}^*, r^*, \lambda^*, \chi^*$ and the Lagrangian functional

$$\mathcal{L} = \mathcal{J}_0 - \mathcal{J}_1 \tag{10}$$

where

$$\begin{aligned}
\mathcal{J}_1 &= \langle \mathbf{Q}^*, L_B\,\mathbf{Q}\rangle + \int_{X_{cs}}^{X_{ce}} \lambda^* \left[T(x^1,0) - T_{\mathrm{w}}\right] dx^1 \\
&+ \chi^*(E_C - \int_{X_{cs}}^{X_{ce}} \left(T_{\mathrm{w}} - T_{ad_0}(x^1,0)\right)^2 dx^1) \\
&+ \langle \mathbf{q}^*, L_P\,\hat{\mathbf{q}}\rangle + \langle r^*\hat{\mathbf{q}}, \frac{\partial \hat{\mathbf{q}}}{\partial x^1}\rangle + \text{c.c.}
\end{aligned}$$

and c.c. denotes the complex conjugate. The inner products $\langle \cdot, \cdot\rangle$ appearing above are defined as

$$\langle \psi, \phi\rangle = \int_{X_0}^{X_1} \int_{Z_0}^{Z_1} \int_0^{+\infty} \psi^H \phi\,dx^1 dx^2 dx^3, \tag{11}$$

for complex valued vectors ψ and ϕ. We can now define the problem as: find the control T_{w}, state variables $\mathbf{Q}, \tilde{\mathbf{q}}$ and adjoint variables $\lambda^*, \chi^*, \mathbf{Q}^*, \mathbf{q}^*$ and r^* such that $\mathcal{L}$ is rendered stationary according to the first-order necessary condition for an extremal point. This is done by setting the first variation of $\mathcal{L}$ with respect to the variables considered here to zero, while each of $\mathcal{L}$'s arguments are considered to be independent variables. This requirement comes from the fact that at an extremal point the first variation of $\mathcal{L}$ with respect to each variable vanishes. We start by setting the first variation of $\mathcal{L}$ with respect to each of the adjoint variables to zero, which gives the state equations (1), (3) and (4), and the constraint on the control effort, Eq. (9). We continue by setting the first variation of $\mathcal{L}$ with respect to the state variables $\hat{\mathbf{q}}$, α and $\mathbf{Q}$

to zero. After a procedure which involves successive integrations by parts (see Pralits *et al.* 2002), this yields the adjoint equations

$$L_P^* \, \mathbf{q}^* = S_P^*, \tag{12}$$

$$\frac{\partial}{\partial x^1} \int_0^{+\infty} \mathbf{q}^{*H} \frac{\partial L_P}{\partial \alpha} \hat{\mathbf{q}} h_1 dx^3 = \begin{cases} 0 & \forall x^1 \notin [X_{ms}, X_{me}] \\ -\mathrm{i}|\Theta|^2 \int_0^{+\infty} \hat{\mathbf{q}}^H M \hat{\mathbf{q}} h_1 dx^3 & \forall x^1 \in [X_{ms}, X_{me}], \end{cases} \tag{13}$$

$$L_B^* \, \mathbf{Q}^* = S_B^*, \tag{14}$$

where $\mathbf{q}^* = (\rho^*, u^*, v^*, w^*, \theta^*)^T$ and $\mathbf{Q}^* = (U^*, V^*, W^*, T^*)^T$. Equation (12) is the adjoint of the PSE (APSE) where u^*, v^*, w^* and θ^* are subject to Dirichlet boundary conditions. The right hand side S_P^* is due to the auxiliary condition of the PSE and the objective function. Equation (13) is a closure relation obtained by setting the first variation of $\mathcal{L}$ with respect to the streamwise wavenumber α to zero. At each streamwise position, r^* is solved iteratively such that Eq. (13) is satisfied. Equation (14) is the adjoint of the BLE (ABLE) and the right hand side S_B^* is the sensitivity of the PSE with respect to the mean flow. Both the APSE and ABLE are parabolic equations which are solved by backward integration in the streamwise direction. Finally, we set the first variation of $\mathcal{L}$ with respect to T_w to zero which gives the so called optimality condition as

$$\frac{\kappa}{RePr} \frac{\partial T^*(x^1, 0)}{\partial x^3} + 2\chi^* \left(T_w - T_{ad_0}(x^1, 0) \right) = 0 \tag{15}$$

The left hand side of the above expression is the gradient of the Lagrangian functional with respect to the mean flow temperature at the wall. As shown in Eq. (10), χ^* is the adjoint variable used to enforce the constraint on the control effort and can be solved iteratively in the optimization by substituting Eq. (15) into Eq. (9) as

$$\chi^* = \left(\frac{1}{4E_C} \int_{X_{cs}}^{X_{ce}} \left(\frac{\kappa}{RePr} \frac{\partial T^*(x^1, 0)}{\partial x^3} \right)^2 dx^1 \right)^{\frac{1}{2}}. \tag{16}$$

The complete optimality system, Eqs. (1), (3), (4) and (12)–(16), is found in Appendix A.

4. Numerical implementation

The results presented here are obtained by numerically integrating the discretized state and adjoint equations. The x^1-derivatives of both state and corresponding adjoint equations are approximated by a second order accurate backward Euler scheme. The x^3-derivatives of the PSE and APSE are approximated by a fourth order accurate compact finite difference scheme (see Hanifi *et al.* 1994), and a second order accurate finite difference scheme for the BLE and ABLE.

The procedure of solving the optimization problem derived in Sec. 3 is described here. We first consider the problem of minimizing a single disturbance, $K = 1$ in (7). The optimal temperature distribution is found through an iterative procedure. During each iteration step, we perform successive calculations of boundary-layer and stability equations from X_0 to X_1; and adjoint boundary-layer and stability equations from X_1 to X_0. Then, a new temperature distribution is computed using the gradient information given by $\partial \mathcal{L}/\partial T_{\rm w}$ which is evaluated from the solution of the adjoint equations. Here we use the L-BFGS-B optimization routine, see Zhu *et al.* (1994); Byrd *et al.* (1995). The calculations are repeated until the relative change in the objective function is less than a prescribed value. If $K > 1$ then instead of solving both state and adjoint equations K times, we can utilize the fact that the ABLE are linear equations. In this case the optimality condition is evaluated as follows: the BLE is solved once; the PSE and APSE are solved K times; the forcing of the ABLE, S_B^*, is calculated as

$$S_B^* = \sum_{k=1}^{K} S_{B_k}^*.$$

Finally, the optimality condition is evaluated from a single calculation of the ABLE.

The convergence criteria is $(\mathcal{J}_0^{j+1} - \mathcal{J}_0^j)/\mathcal{J}_0^j < 10^{-4}$, where j denotes the iteration number in the optimization procedure. Further, in all calculations the initial guess on the temperature profile, $T_{\rm w}$, has been varied to make sure that the optimal solution does not depend on the initial state.

5. Results

In the problem formulation presented in the previous section we considered two different measures of the disturbance growth, cost functions, to be minimized when disturbances are superimposed on a given boundary layer flow. It was also discussed that the boundary layer flow outside of the control domain will depend on whether the wall is considered to be adiabatic or not. In order to investigate the latter, the optimal control problem has been formulated both for the case of having a fixed temperature outside the control domain, and for the case of using an adiabatic wall condition. Obviously keeping the wall at a specified temperature downstream of the control domain requires extra energy. However, we have chosen to investigate this case in order to explain the stabilizing effect of the heating strip upstream of the first neutral point reported by Masad & Nayfeh (1992). Our investigations showed that this stabilizing effect is found only when the wall-temperature downstream of the strip is set to the adiabatic temperature in the uncontrolled case, T_{ad_0}. If the wall is insulated also downstream of the heating strip, the wall-temperature will be larger than T_{ad_0}. That is due to the fact that extra heat has been added to the flow as it passes the heating strip. This higher wall-temperature will increase the instability of the flow.
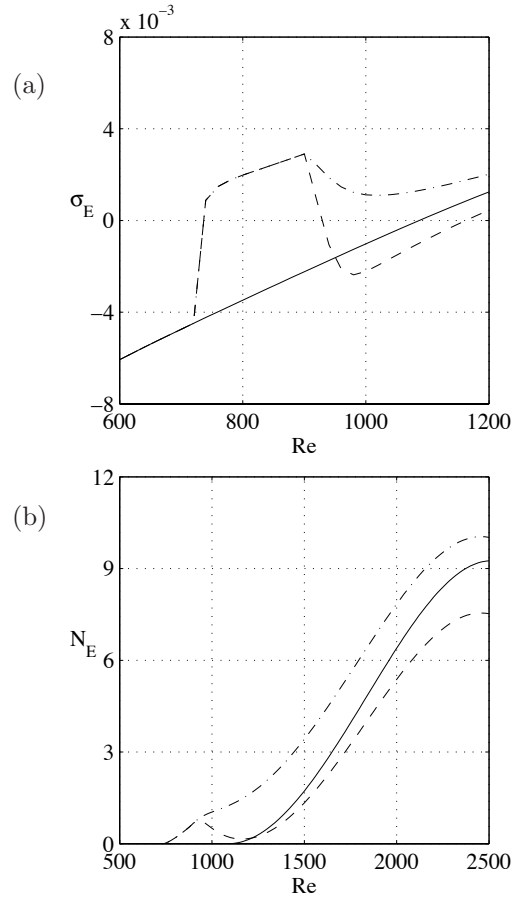
FIGURE 1. Disturbance control on a flat plate boundary layer using a heating strip with a temperature of 1.5 times the adiabatic temperature when no control is applied, located at $720 \leq Re \leq 900$. (a) Streamwise variation of the local growth rate of a 2D disturbance with $F = 15 \times 10^{-6}$, for the cases of zero control (solid), compared to the cases when the heating strip is used and the plate downstream of the heating strip is assumed insulated (dash-dot), and heat transfer occurs (dash), $M = 0.8$, $T_\infty = 300$ K, Pr $= 0.72$. (b) corresponding N-factors.

Here we have reproduced Masad & Nayfeh (1992)'s results based on the non-similar boundary-layer profiles shown in Fig. 16 of their article. The case is a flat plate boundary layer with a free stream Mach number of 0.8. A two-dimensional wave with reduced frequency $F = 2\pi f^\star \nu_e^\star / U_e^{\star 2} = 15 \times 10^{-6}$ is
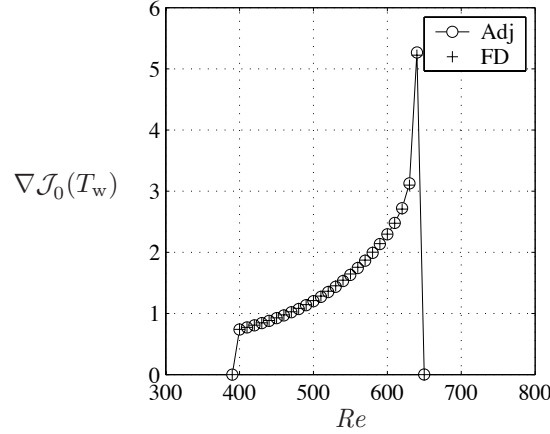
FIGURE 2. comparison between the gradient obtained from solution of the adjoint equations (o) and the finite-difference method (+). $\mathcal{J}_0 = E_\Omega$ for a two-dimensional wave with $F = 90 \times 10^{-6}$.

superimposed on the boundary layer. Here, $f^\star$, is the dimensional frequency and the subscript e denotes values evaluated at the edge of the boundary layer. The heating strip, which has a temperature of 1.5 times the temperature corresponding to an adiabatic wall when no control is applied, is placed upstream of the first neutral point. For the comparison, the stability analysis is computed using linear local theory. The results for thermal boundary conditions TW1 and TW2 are given in Fig. 1. The growth rates for both cases are given in Fig. 1a which are compared with the uncontrolled case. When the plate is not insulated downstream of the heating strip, the heated fluid at the strip encounters relatively cooler fluid downstream which is stabilizing the boundary layer. The magnitude of the growth rate downstream of the strip is lower compared to the case of no control. If on the other hand, the wall downstream of the heating strip is assumed to be insulated, the decay of growth rate is less and the magnitude of the growth rate is larger than that of uncontrolled case. The corresponding N-factors are plotted in Fig. 1b. It is clear that the heating strip which is stabilizing when the wall-temperature downstream of the control domain is kept fixed to T_{ad_0}, is in fact destabilizing when the wall is assumed adiabatic.

Before we proceed with presentation of optimization results, we demonstrate the accuracy of the gradient obtained from the solutions of the adjoint equations. In Fig. 2 the adjoint-based gradient, $\nabla \mathcal{J}_0(T_\mathrm{w})$, is compared to that given by the finite-difference calculations. Here, the objective function is $\mathcal{J}_0 = E_\Omega$ (integrated between $Re = 370$ and $Re = 760$). The disturbance is a two-dimensional wave with $F = 90 \times 10^{-6}$. The control domain is between
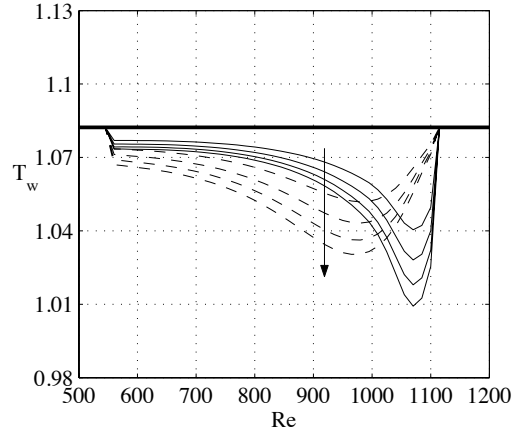
FIGURE 3. Optimal temperature distributions obtained by minimizing $\mathcal{J}_0 = E_f$ (solid), $\mathcal{J}_0 = E_\Omega$ (dashed) for a two-dimensional disturbance with $F = 2\pi f^* \nu_e^* / U_e^{*2} = 50 \times 10^{-6}$ in a flat plate boundary layer where $M = 0.7$. The control magnitudes are $E_c^* \times 10^{-4} = 6$, 10, 14 and 18, the arrow shows the direction of increasing E_c^*. A comparison is made with case of zero control (thick solid).

$Re = 370$ and $Re = 650$. The wall downstream of the control domain is assumed to be adiabatic. As can be seen there, the agreement is very good. Note that the computation costs are much higher for the finite-difference method (two calculations of BLE and PSE for each streamwise position).

Below, we present results for a comparison between the two cost functions discussed in Sec. 3. We consider a two-dimensional flat plate boundary layer with free stream Mach number $M = 0.7$ and zero pressure gradient. The mean flow in the results presented here is calculated using a stagnation temperature of 311 K if not stated otherwise. This temperature is chosen as the one used by Mack (1984), if comparisons are desired. A two-dimensional disturbance with reduced frequency $F = 2\pi f^* \nu_e^* / U_e^{*2} = 50 \times 10^{-6}$ is superimposed on the mean flow at $Re = 500$. When $\mathcal{J}_0 = E_f$, then the energy is measured at the second neutral point, $Re = 1130$, of the considered disturbance. This position is the natural choice for the considered cost function as it corresponds to the position where the N-factor has its maximum value. The disturbance kinetic energy in the second cost function $\mathcal{J}_0 = E_\Omega$ is integrated between $Re = 500$ and the second neutral point. We assume having a control domain available between the first and second neutral point and the temperature outside the control domain corresponds to $\partial T(x^1, 0)/\partial x^3 = 0$ when no control is applied (TW1). Calculations are performed for minimization of respective cost function for a number of different magnitudes of the control effort E_c^*. The control
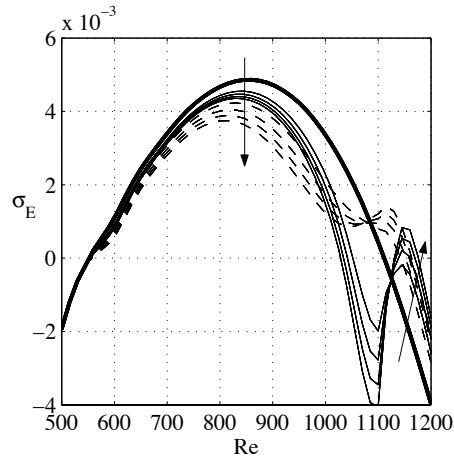
FIGURE 4. Growth rates corresponding to the temperature distributions in Fig. 3. The arrow shows the direction of increasing E_c^*.
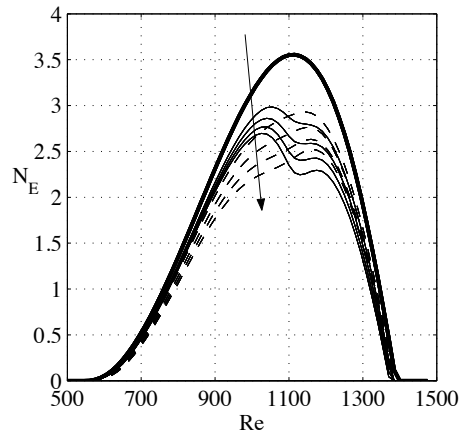

FIGURE 5. N-factor curves corresponding to the temperature distributions in Fig. 3. The arrow shows the direction of increasing E_c^*.

magnitudes are chosen such that a noticeable effect is obtained on the reduction of the disturbance growth.

In Fig. 3 the optimal temperature distributions computed by minimizing respective cost functions are shown for different values of E_c^* in comparison with the case of zero control. In all cases of control, the wall temperature is decreased with respect to the uncontrolled case. This is in accordance with previous studies for control of viscous instabilities when cooling is applied along
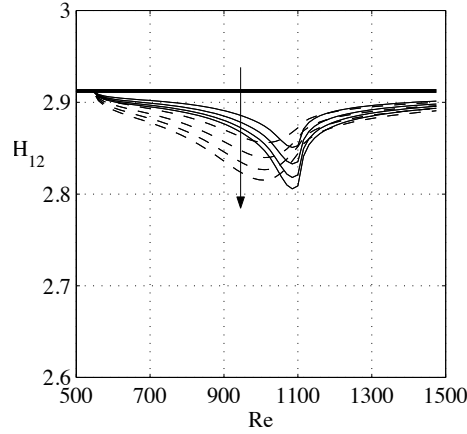
FIGURE 6. Shape factor H_{12}, ratio between displacement and momentum thickness, for the cases presented in Fig. 3.

the whole plate (see Mack 1984). The temperature distributions are however different depending on the cost function used in the optimization. Minimization of $\mathcal{J}_0 = E_f$ clearly results in a cooling peak close to the second neutral point and this is more pronounced as E_c^* is increased. Minimization of $\mathcal{J}_0 = E_\Omega$ on the other hand produces temperature distributions which are more equally distributed in the control domain. The corresponding growth rates are shown in Fig. 4. The effect of the cooling peak in the results obtained by minimizing $\mathcal{J}_0 = E_f$, gives a significant damping close to the second neutral point and less in the rest of the unstable domain. As a consequence of the more equally distributed cooling obtained by minimizing $\mathcal{J}_0 = E_\Omega$, also the damping of the growth rate is distributed over the whole unstable domain. Downstream of the control domain, i. e. where the control is turned off, the growth rates for all optimized cases increase above the value of the uncontrolled case. The reason is that as the flow leaves the cooling domain it experiences a relatively hotter surface which is destabilizing. A similar effect is seen for the growth rates just upstream of the second neutral point for the cases of minimizing $\mathcal{J}_0 = E_\Omega$. Here the effect is weaker but nevertheless due to the decrease in cooling magnitude downstream of $Re \approx 950$. The differences in damping of the growth rate seen in Fig. 4 is also seen in the corresponding N-factors found in Fig. 5. For the cases of minimizing $\mathcal{J}_0 = E_f$ the value of the N-factors are larger upstream of the second neutral point, i. e. where E_f is evaluated. Minimizing $\mathcal{J}_0 = E_\Omega$ on the other hand gives a more evenly distributed stabilizing effect on the disturbances in the unstable domain. In comparison with zero control, the peak N-factors using the optimal temperature distributions move upstream when $\mathcal{J}_0 = E_f$ is minimized, and downstream for the case of minimizing $\mathcal{J}_0 = E_\Omega$. An assumption made in the analysis here, is that the control does not have a large effect on the flow at the boundary layer edge. A comparison is
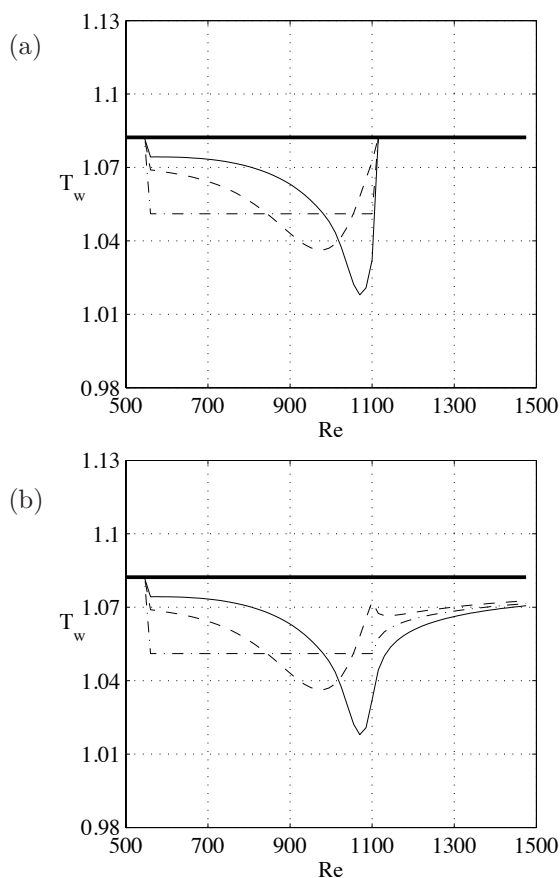
FIGURE 7. Effects of temperature boundary conditions for $x^1 > X_{ce}$: (a) $T(x^1,0) = T_{w_0}$ (b) $\partial T(x^1,0)/\partial x^3 = 0$. The wall temperature distributions are: zero control (thick solid) , optimal for $\mathcal{J}_0 = E_f$ (solid), optimal for $\mathcal{J}_0 = E_\Omega$ (dash), T_w/T_{w_0}=constant (dash-dot). In all cases $E_c^* \times 10^{-4} = 14$.

therefore made between the shape factors (displacement/momentum thickness) computed for the cases of optimized suction distribution, and zero control. In Fig. 6 it is shown that the maximum difference is about 3.5%.

The development of the mean flow downstream of the control domain and consequently the disturbance amplification, varies depending on the assumptions made regarding the heat transfer at the wall. The results shown so far are computed assuming that the flow which is cooled at the wall in the control domain does not change the wall temperature downstream of the control domain. If on the other hand the wall is assumed to be insulated, then the wall downstream of the control domain will change in temperature, satisfying the
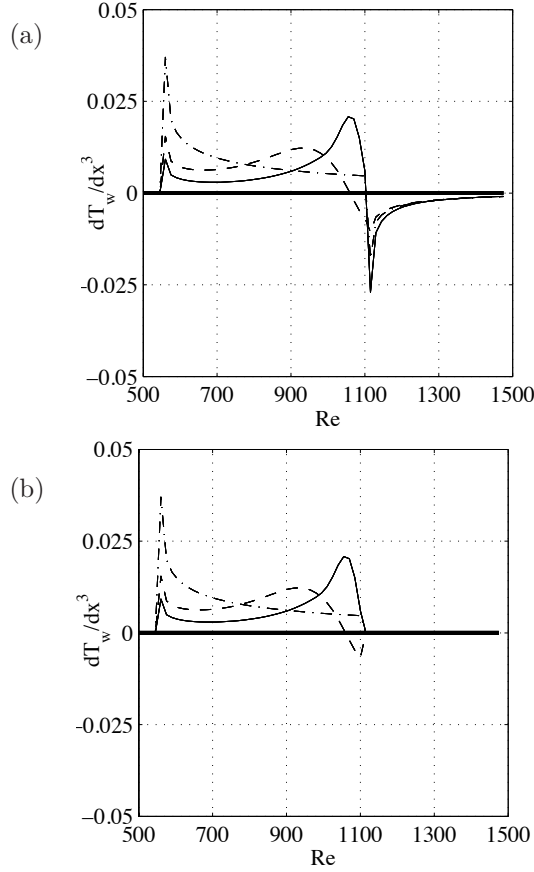
FIGURE 8. $\partial T(x^1,0)/\partial x^3$ as a function of the Reynolds number corresponding to the cases in Fig 7.

adiabatic wall condition. In the calculations this is accomplished using wall boundary condition TW2. As the cost functions used to compute the optimal temperature distributions shown in Fig. 3 are not evaluated downstream of the control domain, we can directly change the temperature boundary condition, from TW1 to TW2, in that region and recompute the mean flow. This is made for a given value of E_c^* and temperature distributions obtained by minimizing respective cost function. A comparison is also made with a constant cooling distribution which has the same value of E_c^* as the optimal ones. The temperature distribution subject to different temperature boundary conditions outside of the control domain are plotted in Fig. 7. The cooling of the plate downstream of the control domain when the plate is assumed to be insulated can be seen in Fig. 7b. As the flow moves downstream, the cooling decreases in all cases. However, for the optimal distribution for $\mathcal{J}_0 = E_\Omega$, a short region
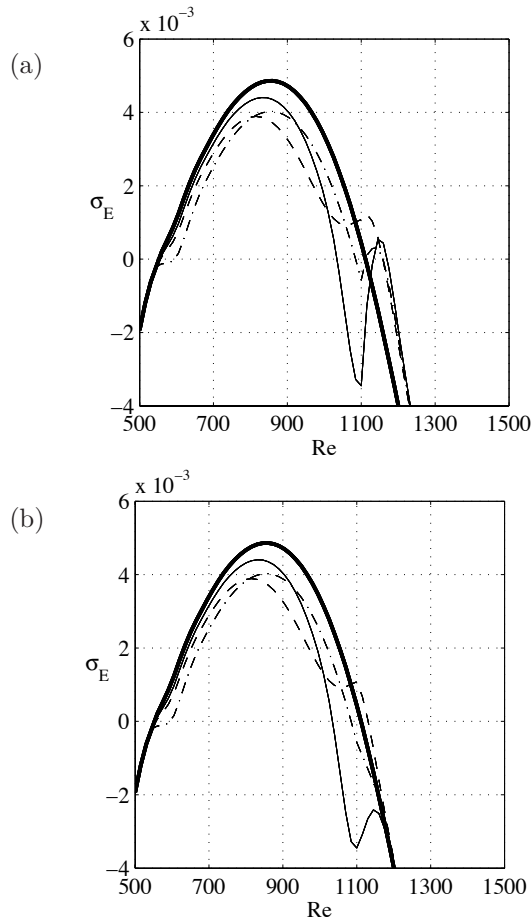
FIGURE 9. Growth rate as a function of the Reynolds number corresponding the cases in Fig 7.

of increased cooling first occurs immediately after the control domain. This appears as the temperature gradient at the wall in the end of the control domain actually is negative. This can be seen in Fig. 8 where $\partial T(x^1, 0)/\partial x^3$, which is proportional to the wall heat transfer, has been plotted for all cases corresponding to Fig. 7. We can note that inside the control domain, the constant temperature control has a decrease in wall heat transfer downstream, while the optimal controls have an increase. In Fig. 8a, the effect of the cold fluid from the control domain entering a region of relatively hotter surface is seen in the rapid change of sign of $\partial T(x^1, 0)/\partial x^3$. This is most pronounced for the temperature distribution based on minimizing $\mathcal{J}_0 = E_f$. The effect on the growth rate of the disturbance is shown in Fig. 9. The increase in growth above the value corresponding to zero control almost disappear as adiabatic
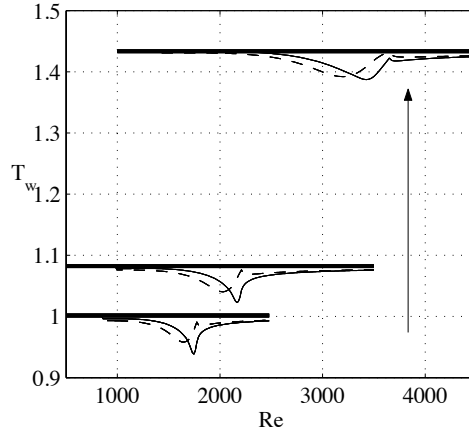
FIGURE 10. Comparison of optimal temperature distributions when $E_c^* \times 10^{-4} = 18$ for different Mach numbers. M=0.1, 0.7 and 1.6 and the arrow shows the direction of increasing M. The wall temperature distributions are: zero control (thick solid) , optimal based on minimizing: $\mathcal{J}_0 = E_f$ (solid), $\mathcal{J}_0 = E_\Omega$ (dash). The disturbances used in the cost functions are two-dimensional with $F = 28.5 \times 10^{-6}$ and $F = 18.5 \times 10^{-6}$ for $M = 0.1$ and $M = 0.7$, respectively, and three-dimensional with a reduced frequency of $F = 5.7 \times 10^{-6}$ and wave angle of $\psi = 64°$ at $Re = 1275$ for $M = 1.6$.

wall conditions (TW2) is applied. As a result the N-factors downstream of the control domain will have a lower magnitude when the plate is assumed to be insulated.

It has been shown in earlier studies by e. g. Masad & Nayfeh (1991), that the cooling is much less effective in stabilizing first-mode disturbances at high Mach number flows. We investigate this by comparing the disturbance growth for optimal temperature distributions at different Mach numbers for a given value of E_c^*. The temperature distributions are computed by minimizing the two different cost functions, $\mathcal{J}_0 = E_f$ and $\mathcal{J}_0 = E_\Omega$, respectively. The disturbance used to compute respective cost function is chosen as the one which first reach an N-factor value of 9, as this is commonly used as a transition prediction criterion. They are sometimes denoted as the most dangerous disturbances. Computations are performed for two-dimensional flat plate boundary layers with free stream Mach numbers of $M = 0.1$, 0.7 and 1.6. At the lower Mach numbers, the most dangerous disturbances are two-dimensional and the reduced frequencies are $F = 28.5 \times 10^{-6}$ and $F = 18.5 \times 10^{-6}$ for $M = 0.1$ and $M = 0.7$, respectively. At $M = 1.6$, the most dangerous disturbance is three-dimensional with a reduced frequency of about $F = 5.7 \times 10^{-6}$ and a wave angle ψ of about $64°$ at $Re = 1275$. The wall temperature is optimized
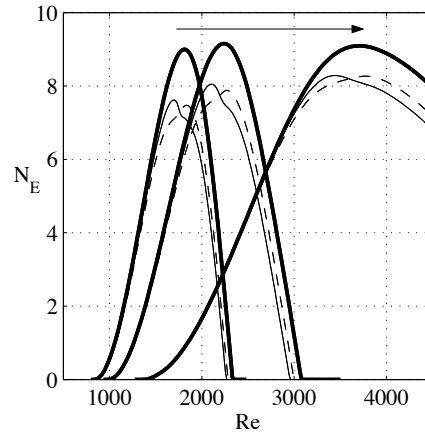
FIGURE 11. *N*-factors corresponding to the optimal temper-
ature distributions in Fig. 10. The arrow shows the direction
of increasing Mach number.

in a streamwise domain corresponding to the unstable region of respective dis-
turbance. Outside of the control domain the plate is assumed to be insulated
(TW2). The disturbances are superimposed on the mean flow upstream of the
first neutral point at X_0 corresponding to Re=800, 935 and 1275 for $M = 0.1$,
0.7 and 1.6, respectively. For $\mathcal{J}_0 = E_\Omega$, the disturbance kinetic energy is inte-
grated from X_0 to the second neutral point, and $\mathcal{J}_0 = E_f$ is evaluated at the
second neutral point. Results of the optimal temperature distributions com-
pared to the case of zero control for all Mach numbers are shown in Fig. 10.
As the Mach number is increased, the wall temperature increases too. In all
optimal temperature distributions, the magnitude of temperature is lower com-
pared to the uncontrolled case, i. e. cooling occurs. For all Mach numbers the
optimal temperature distributions for $\mathcal{J}_0 = E_f$ has its minimum located close
to the second neutral point. This is more pronounced as the Mach number is
decreased. As shown before, the optimal temperature distributions computed
by minimizing the streamwise integral of the disturbance kinetic energy gives a
more even cooling distribution in the control domain. The stabilizing effect on
the disturbances for different Mach numbers and cost functions are shown in
Fig. 11 comparing the *N*-factors for the uncontrolled and optimal temperature
distributions. As the Mach number is increased the stabilizing effect of the op-
timal temperature distributions is decreased. This is independent of the choice
of the cost functions used here. We further note that for all Mach numbers, the
streamwise position of the maximum *N*-factor for $\mathcal{J}_0 = E_f$ moves upstream
compared to the uncontrolled case. The opposite occurs in the cases where
$\mathcal{J}_0 = E_\Omega$ is minimized.

6. Discussion and conclusions

A theory has been presented for computation of the optimal steady wall temperature distribution to suppress the growth of convectively unstable disturbances in compressible boundary layer flows on flat plates. A gradient based iterative procedure is used to minimize an objective function measuring the disturbance kinetic energy. The gradient of interest are obtained from the solution of the adjoint of the boundary layer and parabolized stability equations. These adjoint equations are derived using a Lagrange multiplier technique. The optimizations are performed for a given magnitude of the control effort, which is evaluated from the deviation of the control temperature from the adiabatic wall temperature in the case of zero control. Two different cost functions based on the disturbance kinetic energy are compared. The first is evaluated at a given streamwise position, here corresponding to the position of maximum kinetic energy of a given unstable wave. The second is a streamwise integral of the kinetic energy of a given wave. In addition, both the cases of zero and non-zero heat transfer outside of the control domain have been included in the formulation of the optimization problem. Results have been presented for the optimal temperature distributions obtained by minimizing the different cost functions, for different freestream Mach numbers and control magnitudes. A comparison has also been made for the cases of zero and non-zero heat transfer downstream of the control domain. In all cases, the wall temperature has been optimized in a streamwise region corresponding to that of the unstable domain of the disturbance considered in the cost function. The results show that an optimal temperature distribution obtained by minimizing the kinetic energy at the second neutral point, concentrates most of its effort close to where the energy is measured. As a result, the growth rate, and resulting N-factors are locally larger upstream of this position. Minimizing the integrated disturbance kinetic energy on the other hand produces more evenly distributed temperature distributions. The resulting maximum value of the N-factors move downstream with respect to the uncontrolled case. Even though the temperature distributions obtained from both of these cases result in a damping of the disturbance growth, the latter appears favorable in terms of transition delay. An attempt has been made to compare the effect of optimal temperature distributions on the disturbance growth for different Mach numbers. Here, a dimensional value of the control effort has been kept fixed for a given cost function, and the disturbance considered in each case correspond to that which first reaches an N-factor value of 9. The results show that independent of the choice of cost function, the stabilizing effect on the disturbance growth decreases with increasing Mach number. We have also demonstrated that the stabilizing effect of a heating strip located upstream of the first neutral point (see Masad & Nayfeh 1992) diminishes if the wall downstream of the strip is assumed to be insulated. For a given Mach number and control effort, results have been shown for a comparison between different thermal wall boundary conditions downstream of the control domain. In case of non-insulated wall, the cooler

flow from the control domain is destabilized as it enters a region of relatively hotter surface. The destabilizing effect is seen by an increase in growth rate of the disturbances above the value obtained without control. This is more pronounced for the case of minimizing the terminal kinetic energy. If the wall is assumed to be insulated, the wall temperature downstream of the control domain adjusts itself to the adiabatic wall condition. In the cases shown here, this means that the wall downstream of the control domain, relative to uncontrolled case, is cooled. As the flow is convected downstream, further away from the control domain, the cooling decreases.

Appendix A. Optimality system

A.1. *State equations*

The boundary-layer equations for a quasi three dimensional viscous compressible flow are

$$\frac{\partial(\rho U)}{\partial x^1} + \frac{\partial(\rho W)}{\partial x^3} = 0,$$

$$\rho U \frac{\partial U}{\partial x^1} + \rho W \frac{\partial U}{\partial x^3} = -\frac{dP_e}{dx^1} + \frac{1}{Re}\frac{\partial}{\partial x^3}\left(\mu \frac{\partial U}{\partial x^3}\right),$$

$$\rho U \frac{\partial V}{\partial x^1} + \rho W \frac{\partial V}{\partial x^3} = \frac{1}{Re}\frac{\partial}{\partial x^3}\left(\mu \frac{\partial V}{\partial x^3}\right),$$

$$c_p\rho U \frac{\partial T}{\partial x^1} + c_p\rho W \frac{\partial T}{\partial x^3} = \frac{1}{RePr}\frac{\partial}{\partial x^3}\left(\kappa \frac{\partial T}{\partial x^3}\right) +$$

$$(\gamma-1)UM^2\frac{dP_e}{dx^1} + (\gamma-1)\frac{\mu M^2}{Re}\left[\left(\frac{\partial U}{\partial x^3}\right)^2 + \left(\frac{\partial V}{\partial x^3}\right)^2\right].$$

The parabolized stability equations are lengthy and here are given in a symbolic form

$$\mathcal{A}\hat{\mathbf{q}} + \mathcal{B}\frac{\partial \hat{\mathbf{q}}}{\partial x^3} + \mathcal{C}\frac{\partial^2 \hat{\mathbf{q}}}{(\partial x^3)^2} + \mathcal{D}\frac{\partial \hat{\mathbf{q}}}{\partial x^1} = 0,$$

$$\int_0^{+\infty} \hat{\mathbf{q}}^H \frac{\partial \hat{\mathbf{q}}}{\partial x^1} dx^3 = 0, \quad \forall x^1 \in [X_0, X_1],$$

where $\hat{\mathbf{q}} = (\hat{\rho}, \hat{u}, \hat{v}, \hat{w}, \hat{T})^T$. The above parabolized stability equations are found in Pralits *et al.* (2000) derived for orthogonal curvlinear coordinates. The coefficients of the 5×5 matrices $\mathcal{A}, \mathcal{B}, \mathcal{C}$ and $\mathcal{D}$ are the ones found in Pralits *et al.* (2000) when the scale factors are $h_1 = h_2 = h_3 = 1$. The corresponding boundary conditions are at the wall

$$T(x^1, 0) = T_{\mathrm{w}}(x^1) \quad \forall x^1 \in [X_{cs}, X_{ce}],$$

$$T(x^1, 0) = T_{\mathrm{w}_0}(x^1) \quad \forall x^1 \in [X_0, X_{cs}) \text{ and } \forall x^1 \in (X_{ce}, X_1] \quad \text{TW1},$$

$$\frac{\partial T}{\partial x^3}(x^1, 0) = 0 \quad \forall x^1 \in [X_0, X_{cs}) \text{ and } \forall x^1 \in (X_{ce}, X_1] \quad \text{TW2},$$

$$[U, V, W](x^1, 0) = [0, 0, 0] \quad \forall x^1 \in [X_0, X_1],$$

$$\left[\hat{u}, \hat{v}, \hat{w}, \hat{T}\right](x^1, 0) = [0, 0, 0, 0] \quad \forall x^1 \in [X_0, X_1],$$

and in the free stream

$$\lim_{x^3 \to +\infty} [U, V, T](x^1, x^3) = [U_e, V_e, T_e](x^1) \quad \forall x^1 \in [X_0, X_1],$$

$$\lim_{x^3 \to +\infty} \left[\hat{u}, \hat{v}, \hat{w}, \hat{T}\right](x^1, x^3) = [0, 0, 0, 0] \quad \forall x^1 \in [X_0, X_1],$$

where variables with subscript w are evaluated at the wall, and subscript e at the boundary layer edge. TW1 and TW2 denote two choices of boundary

conditions outside the control domain. The initial conditions are

$$\mathbf{Q}(X_0, x^3) = \mathbf{Q}_0(x^3) \quad \forall x^3 \in [0, +\infty),$$
$$\hat{\mathbf{q}}(X_0, x^3) = \hat{\mathbf{q}}_0(x^3) \quad \forall x^3 \in [0, +\infty),$$

A.2. *Adjoint equations*

The adjoint of the boundary-layer equations are

$$\rho \frac{\partial(h_1 W^*)}{\partial x^3} - h_1 \rho \left(\frac{\partial U}{\partial x^3} U^* + \frac{\partial V}{\partial x^3} V^* + c_p \frac{\partial T}{\partial x^3} T^* \right) = F_W,$$

$$\frac{\partial(\rho U U^*)}{\partial x^1} + \frac{\partial(h_1 \rho W U^*)}{\partial x^3} - \rho \left(\frac{\partial U}{\partial x^1} U^* + \frac{\partial V}{\partial x^1} V^* - \frac{\partial W^*}{\partial x^1} + c_p \frac{\partial T}{\partial x^1} T^* \right) +$$

$$(\gamma - 1) M^2 \frac{dP_e}{dx^1} T^* - \frac{2(\gamma - 1)}{Re} M^2 \frac{\partial}{\partial x^3} \left(h_1 \mu \frac{\partial U}{\partial x^3} T^* \right) +$$

$$\frac{1}{Re} \frac{\partial}{\partial x^3} \left(\mu \frac{\partial(h_1 U^*)}{\partial x^3} \right) = F_U,$$

$$\frac{\partial(\rho U V^*)}{\partial x^1} + \frac{\partial(h_1 \rho W V^*)}{\partial x^3} - \frac{2(\gamma - 1)}{Re} M^2 \frac{\partial}{\partial x^3} \left(h_1 \mu \frac{\partial V}{\partial x^3} T^* \right) +$$

$$\frac{1}{Re} \frac{\partial}{\partial x^3} \left(\mu \frac{\partial(h_1 V^*)}{\partial x^3} \right) = F_V,$$

$$c_p \frac{\partial(\rho U T^*)}{\partial x^1} + c_p \frac{\partial(h_1 \rho W T^*)}{\partial x^3} + \frac{\rho U}{T} \left(\frac{\partial U}{\partial x^1} U^* + \frac{\partial V}{\partial x^1} V^* - \frac{\partial W^*}{\partial x^1} \right) +$$

$$\frac{\rho U}{T} c_p \frac{\partial T}{\partial x^1} T^* + \frac{\kappa}{Re Pr} \frac{\partial^2(h_1 T^*)}{(\partial x^3)^2} \frac{(\gamma - 1)}{Re} M^2 \frac{d\mu}{dT} \left[\left(\frac{\partial U}{\partial x^3} \right)^2 + \left(\frac{\partial V}{\partial x^3} \right)^2 \right] T^* -$$

$$\frac{1}{Re} \frac{d\mu}{dT} \left[\frac{\partial U}{\partial x^3} \frac{\partial(h_1 U^*)}{\partial x^3} + \frac{\partial V}{\partial x^3} \frac{\partial(h_1 V^*)}{\partial x^3} \right] = F_E,$$

where $F_E = (F_T + F_W W/T)$, and F_W, F_U, F_V, F_T are found in Pralits (2001). The adjoint of the parabolized stability equations can be written as

$$\tilde{\mathcal{A}} \mathbf{q}^* + \tilde{\mathcal{B}} \frac{\partial \mathbf{q}^*}{\partial x^3} + \tilde{\mathcal{C}} \frac{\partial^2 \mathbf{q}^*}{(\partial x^3)^2} + \tilde{\mathcal{D}} \frac{\partial \mathbf{q}^*}{\partial x^1} = S_P^*,$$

$$\frac{\partial}{\partial x^1} \int_0^{+\infty} \mathbf{q}^{*H} \left(\frac{\partial \mathcal{A}}{\partial \alpha} + \frac{\partial \mathcal{B}}{\partial \alpha} \right) \hat{\mathbf{q}} \, dx^3 =$$

$$\begin{cases} 0 & \forall x^1 \notin [X_{ms}, X_{me}], \\ -\mathrm{i} |\Theta|^2 \int_0^{+\infty} \hat{\mathbf{q}}^H M \hat{\mathbf{q}} \, dx^3 & \forall x^1 \in [X_{ms}, X_{me}], \end{cases}$$

where

$$S_P^* = \begin{cases} -\bar{r}^* \dfrac{\partial \hat{\mathbf{q}}}{\partial x^1} - \dfrac{\partial(r^* \hat{\mathbf{q}})}{\partial x^1} & \forall x^1 \notin [X_{ms}, X_{me}], \\ -\bar{r}^* \dfrac{\partial \hat{\mathbf{q}}}{\partial x^1} - \dfrac{\partial(r^* \hat{\mathbf{q}})}{\partial x^1} + \xi M^H \hat{\mathbf{q}} |\Theta|^2 & \forall x^1 \in [X_{ms}, X_{me}], \end{cases}$$

and

$$\tilde{\mathcal{A}} = \mathcal{A}^H - \frac{\partial \mathcal{B}^H}{\partial x^3} + \frac{\partial^2 \mathcal{C}^H}{(\partial x^3)^2} - \frac{\partial \mathcal{D}^H}{\partial x^1},$$

$$\tilde{\mathcal{B}} = -\mathcal{B}^H + 2\frac{\partial \mathcal{C}^H}{\partial x^3},$$

$$\tilde{\mathcal{C}} = \mathcal{C}^H,$$

$$\tilde{\mathcal{D}} = -\mathcal{D}^H.$$

and the vector $\mathbf{q}^* = (\rho^*, u^*, v^*, w^*, \theta^*)^T$. The complete derivation of these equations is found in Pralits *et al.* (2000). The above equations are subjected to the following boundary conditions at the wall

$$[u^*, v^*, w^*, \theta^*](x^1, 0) = [0, 0, 0, 0] \quad \forall x^1 \in [X_0, X_1],$$
$$[U^*, V^*](x^1, 0) = [0, 0] \qquad \forall x^1 \in [X_0, X_1],$$
$$T^*(x^1, 0) = 0 \qquad \forall x^1 \in [X_{cs}, X_{ce}],$$

$$T^*(x^1, 0) = 0 \quad \forall x^1 \in [X_0, X_{cs}) \text{ and } \forall x^1 \in (X_{ce}, X_1] \quad \text{TW1},$$

$$\frac{\partial T^*}{\partial x^3}(x^1, 0) = 0 \quad \forall x^1 \in [X_0, X_{cs}) \text{ and } \forall x^1 \in (X_{ce}, X_1] \quad \text{TW2},$$

and in the free stream

$$\lim_{x^3 \to +\infty} [u^*, v^*, w^*, \theta^*](x^1, x^3) = [0, 0, 0, 0] \quad \forall x^1 \in [X_0, X_1],$$
$$\lim_{x^3 \to +\infty} [U^*, V^*, W^*, T^*](x^1, x^3) = [0, 0, 0, 0] \quad \forall x^1 \in [X_0, X_1].$$

The initial conditions are

$$\mathbf{q}^*(X_1, x^3) = (1 - \xi)\mathbf{q}_1^*(x^3) \quad \forall x^3 \in [0, +\infty),$$
$$r^*(X_1) = (1 - \xi)r_1^* \qquad \forall x^3 \in [0, +\infty),$$
$$\mathbf{Q}^*(X_1, x^3) = \mathbf{0} \qquad \forall x^3 \in [0, +\infty),$$

with $\mathbf{q}_1^*$ and r_1^* evaluated at $x^1 = X_1$ as

$$\mathbf{q}_1^* = |\Theta|^2 \mathcal{D}^+(M - c_1 \mathcal{I})\hat{\mathbf{q}}, \qquad r_1^* = |\Theta|^2 \, c_1,$$

$$\bar{c}_1 = \frac{\int_0^\infty \left(\hat{\mathbf{q}}^H M \, \mathcal{D}^{+H} \left(\frac{\partial \mathcal{A}}{\partial \alpha} + \frac{\partial \mathcal{B}}{\partial \alpha}\right) \hat{\mathbf{q}} - i\hat{\mathbf{q}}^H M \hat{\mathbf{q}}\right) dx^3}{\int_0^\infty \hat{\mathbf{q}}^H \mathcal{D}^{+H} \left(\frac{\partial \mathcal{A}}{\partial \alpha} + \frac{\partial \mathcal{B}}{\partial \alpha}\right) \hat{\mathbf{q}} \, dx^3},$$

where $\mathcal{D}^+ = (\mathcal{D}^H)^{-1}$.

A.3. *Optimality condition*

The optimality condition is

$$\frac{\kappa}{RePr} \frac{\partial T^*(x^1, 0)}{\partial x^3} = \begin{cases} -2\chi^* \left(T_{\mathrm{w}} - T_{ad_0}(x^1, 0)\right) & \forall x^1 \in \Gamma_c, \\ 0 & \forall x^1 \notin \Gamma_c, \end{cases}$$

where

$$\chi^* = \left(\frac{1}{4E_C} \int_{X_{cs}}^{X_{ce}} \left(\frac{\kappa}{RePr} \frac{\partial T^*(x^1, 0)}{\partial x^3} \right)^2 dx^1 \right)^{\frac{1}{2}}.$$

Appendix B. Thermodynamic properties

The thermodynamic properties are calculated assuming that the fluid is a thermally ideal gas. The dynamic viscosity μ, heat conductivity κ, and specific heat c_p are therefore given as functions of temperature only.

- Dynamic viscosity μ:
  (a) Two part Sutherland law
    for $T > 110.4$ K

    $$\mu(T) = 1.458 \cdot 10^{-6} \frac{T^{3/2}}{T + 110.4} \quad [kg/(m \cdot s)]$$

    for $T \leq 110.4$ K

    $$\mu(T) = 0.0693873 \cdot 10^{-6} \, T \quad [kg/(m \cdot s)]$$

  (b) A 4th degree polynomial fit to experimental data, see table 1.
- Heat conductivity κ:
  (a) Keye's formula
    for $T > 80$ K

    $$\kappa(T) = 2.648151 \cdot 10^{-3} \frac{T^{1/2}}{1 + \frac{245.4}{T} 10^{-12/T}} \quad [W/(m \cdot K)]$$

    for $T \leq 80$ K

    $$\kappa(T) = 9.335056752 \cdot 10^{-5} \, T \quad [W/(m \cdot K)]$$

  (b) A 4th degree polynomial fit to experimental data, see table 1.

- Specific heat c_p:
  A 4th degree polynomial fit to experimental data, see table 1.
- Bulk viscosity μ_v:
  Formula from Bertolotti (1998)

  $$\frac{\mu_v(T)}{\mu(T)} = \left(\frac{\mu_v}{\mu} \right)_{T=293.3K} \exp \left[\frac{T - 293.3}{1940} \right],$$

  with $\mu_v/\mu = 0.8$ at 1000 K. Valid within the temperature range of 200 to 1400 K.

$\text{expr} = a_0 + a_1\,T + a_2\,T^2 + a_3\,T^3 + a_4\,T^4$		
μ $[kg/(m \cdot s)]$	c_p $[J/(kg \cdot K)]$	κ $[W/(m \cdot K)]$
a_i		
0	$-1.561632014 \cdot 10^{-7}$	$1.058183878 \cdot 10^{3}$	$-1.305884703 \cdot 10^{-3}$
1	$7.957989891 \cdot 10^{-8}$	$-4.52457049 \cdot 10^{-1}$	$1.099134492 \cdot 10^{-4}$
2	$-6.930149679 \cdot 10^{-11}$	$1.141345135 \cdot 10^{-3}$	$-6.84697087 \cdot 10^{-8}$
3	$4.068157752 \cdot 10^{-14}$	$-7.957390422 \cdot 10^{-7}$	$3.327083322 \cdot 10^{-11}$
4	$-9.182486030 \cdot 10^{-18}$	$1.910858151 \cdot 10^{-10}$	$-5.397866355 \cdot 10^{-15}$

TABLE 1. Values of the coefficients used in the polynomial fit
to the experimental data, see Bertolotti (1991).

References

AIRIAU, C., BOTTARO, A., WALTHER, S. & LEGENDRE, D. 2003 A methodology
for optimal laminar flow control: Application to the damping of Tollmien-
Schlichting waves in a boundary layer. *Phys. Fluids* **15**, 1131–1145.

BERTOLOTTI, F. P. 1998 The influence of rotational and vibrational energy relaxation
on boundary-layer stability. *J. Fluid Mech.* **372**, 93–118.

BERTOLOTTI, F. P., HERBERT, T. & SPALART, S. 1992 Linear and nonlinear stability
of the Blasius boundary layer. *J. Fluid Mech.* **242**, 441–474.

BYRD, R., LU, P., NOCEDAL, J. & ZHU, C. 1995 A limited memory algorithm for
bound constrained optimization. *SIAM J. Sci. Comput.* **16**, 1190–1208.

DIACONIS, N. S., JACK, J. R. & WISNIEWSKI, R. J. 1957 Boundary-layer transition
at mach 3.12 as affected by cooling and nose blunting. *NACA Tech. Note No.
3928* .

GUNZBURGER, M. D. 1997 Introduction into mathematical aspects of flow control
and optimization, von karman institute for fluid dynamics, lecture series 1997-
05. *Inverse Design and Optimization Methods* .

GUNZBURGER, M. D., HOU, L. S. & SVOBODNY, T. P. 1993 The approximation
of boundary control problems for fluid flows with an application to control by
heating and cooling. *Comp. Fluids* **22** (2/3), 239–251.

HANIFI, A., HENNINGSON, D. S., HEIN, S. & BERTOLOTTI, F. P.AND SIMEN, M.
1994 Linear non-local instability analysis - the linear NOLOT code. *FFA TN*
1994-54.

HEIN, S., BERTOLOTTI, F. P., SIMEN, M., HANIFI, A. & HENNINGSON, D. S. 1994
Linear non-local instability analysis - the linear NOLOT code. *DLR-IB* **223-94
A 43**.

HERBERT, T. 1997 Parabolized stability equations. *Annu. Rev. Fluid Mech.* **29**, 245–
283.

HILL, D. C. 1997b Inverse design for laminar three-dimensional boundary layers.
Bull. Am. Phys. Soc. **42**, 2120.

VAN INGEN, J. L. 1956 A suggested semiempirical method for the calculation of the

boundary layer transition region. *Tech. Rep.* VTH-74. Department of Aeronautical Engineering, University of Delft.

JACK, J. R., WISNIEWSKI, R. J. & DIACONIS, N. S. 1957 Effects of extreme surface cooling on boundary-layer transition. *NACA Tech. Note No. 4094* .

LEES, L. & LIN, C. C. 1946 Investigation of the stability of the laminar boundary layer in a compressible fluid. *NACA Tech. Note No. 1115* .

LIEPMANN, H. W. & FILA, G. H. 1947 Investigations of effects of surface temperature and single roughness elements on boundary-layer transition. *NACA Tech. Report No. 890* .

LO, C. F., LAFRANCE, R., MEREDITH, W. S. & WIBERG, C. G. 1995 Laminar flow control with wall temperature distribution for quiet supersonic wind tunnels. *AIAA Paper* (95-2296).

LYSENKO, V. I. & MASLOV, A. A. 1984 The effect of cooling on supersonic boundary-layer stability. *J. Fluid Mech.* **147**, 39–52.

MACK, L. M. 1984 Boundary-layer linear stability theory. *AGARD Report No. 709* .

MALIK, M. R. & BALAKUMAR, P. 1992 Nonparallel stability of rotating disk flow using PSE. In *Instability, Transition and Turbulence* (eds. M. Hussaini, A. Kumar & C. Streett), pp. 168–180. Springer.

MASAD, J. A. & NAYFEH, A. H. 1991 Effect of heat transfer on the subharmonic instability of compressible boundary layers. *Phys. Fluids A* **3**, 2148–2163.

MASAD, J. A. & NAYFEH, A. H. 1992 Laminar flow control of subsonic boundary layers by suction and heat-transfer strips. *Phys. Fluids A* **4** (6), 1259–1272.

MASAD, J. A., NAYFEH, A. H. & AL-MAAITAH, A. A. 1992 Effect of heat transfer on the stability of compressible boundary layers. *Comp. Fluids* **21** (1), 43–61.

PRALITS, J. O. 2001 Towards optimal design of vehicles with low drag: Applications to sensitivity analysis and optimal control. Licentiate thesis KTH/MEK/TR-01/07. Royal Institute of Technology, SE-172 90 Stockholm, Sweden.

PRALITS, J. O., AIRIAU, C., HANIFI, A. & HENNINGSON, D. S. 2000 Sensitivity analysis using adjoint parabolized stability equations for compressible flows. *Flow, Turbulence and Combustion* **65** (3), 321–346.

PRALITS, J. O. & HANIFI, A. 2003 Optimization of steady suction for disturbance control on infinite swept wings. *Phys. Fluids* **15** (9), 2756–2772.

PRALITS, J. O., HANIFI, A. & HENNINGSON, D. S. 2002 Adjoint-based optimization of steady suction for disturbance control in incompressible flows. *J. Fluid Mech.* **467**, 129–161.

SIMEN, M. 1992 Local and non-local stability theory of spatially varying flows. In *Instability, Transition and Turbulence* (eds. M. Hussaini, A. Kumar & C. Streett), pp. 181–201. Springer.

SMITH, A. M. O. & GAMBERONI, N. 1956 Transition, pressure gradient and stability theory. *Tech. Rep.* ES 26388. Douglas Aircraft Co.

ZHU, C., BYRD, R., LU, P. & NOCEDAL, J. 1994 L-BFGS-B: Fortran subroutines for large scale bound constrained optimization. *Tech. Rep.* NAM-11. EECS Department, Northwestern University.

Paper 5

5

Shape optimization for delay of laminar-turbulent transition

By Olivier Amoignon[3], Jan O. Pralits[1,2], Ardeshir Hanifi[2], Martin Berggren[2,3], and Dan S. Henningson[1,2]

Theory and results are presented for an approach to perform aerodynamic shape optimization with the aim of transition delay, and thus a decrease of the viscous drag. Linear stability theory is used to calculate the growth rate of perturbations with infinitely small amplitude, superimposed on the laminar mean flow. The location of laminar-turbulent transition is assumed to occur at the location where the total amplification of disturbances, with respect to the first streamwise position where the disturbance starts to grow, attains an empirically determined value, whose logarithm is generally denoted N. In the present approach, an iterative gradient-based optimization procedure is used with the aim of minimizing an objective function based on the disturbance kinetic energy. Here, the gradients of interest are efficiently evaluated using adjoint equations. The inviscid flow is obtained by solving the Euler equations for compressible flows, and the viscous mean flow is obtained from the solution of the boundary layer equations for compressible flows on infinite swept wings. The evolution of convectively unstable disturbances is analyzed using the linear parabolized stability equations (PSE). Large effort is used here to explain the state and adjoint equations involved, gradient evaluation, and validity tests of the gradient computed using the solution of the adjoint equations. Some first results are presented of shape optimization for transition delay. Numerical tests are carried out on the RAE 2822 airfoil and are formulated to reduce the disturbance kinetic energy while maintaining a fixed volume, angle of attack, leading edge radius and trailing edge position. Tests are also carried out to simultaneously reduce the wave drag and the disturbance kinetic energy while maintaining lift and pitch moment coefficients near their values at initial design.

1. Introduction

In the aeronautics industry, reducing the viscous drag on a wing while maintaining operational properties such as lift is of great interest, and the research

[1]Department of Mechanics, KTH, SE-100 44 Stockholm, Sweden.
[2]Swedish Defence Research Agency, FOI, Aeronautics Division, FFA, SE-172 90 Stockholm, Sweden.
[3]Department of Scientific Computing, Uppsala University, SE-751 05 Uppsala, Sweden

in this area regarding active flow control is vast, see Joslin (1998) for a thorough review on the topic of Laminar Flow Control (LFC). It is known that the viscous drag increases dramatically as the boundary layer flow changes from a laminar to a turbulent state. Therefore, an increase of the laminar portion of the wing, that is, moving downstream the point of laminar-turbulent transition, may decrease the viscous drag. Design of a geometry such that the laminar portion is increased or maximized is commonly denoted Natural Laminar Flow (NLF) design, which is a simpler and more robust technique than the ones devised in the area of active flow control. Once a feasible geometry is found, no additional devices such as suction systems, sensors, or actuators need to be mounted.

Transition in the boundary layer on aircraft wings is usually caused by breakdown of small disturbances that grow as they propagate downstream. The growth of these disturbances can be analyzed using linear stability theory, in which it is assumed that perturbations with infinitely small amplitude are superimposed on the laminar mean flow. The growth rate can then be used to predict the transition location using the so called e^N method, see van Ingen (1956); Smith & Gamberoni (1956); Arnal (1993). In this method it is assumed that transition will occur at the location where the total amplification of the disturbance, with respect to the first streamwise position where the disturbance starts to grow, attains an empirically determined value, whose logarithm is generally denoted by N.

A distinctive feature of any flow design process is its computational cost. Despite that the complete flow field can in principle be obtained by solving the complete Navier-Stokes equations numerically, the computation is often very costly, or even totally out of reach for any existing computer when transitional and turbulent flow in complex geometries are involved. It is therefore common practice to introduce approximations. One approach, appropriate for flow over slender bodies, is to divide the flow into an inviscid outer flow field, and a viscous part describing the boundary layer at the surface. In this way, the growth rate of a disturbance superimposed on the boundary layer of a given geometry can be calculated as follows:

  1 the solution of the equations describing the inviscid flow provides a pressure distribution on the surface of a given body,
  2 the viscous mean flow is obtained by solving the boundary layer equations given the pressure distribution on the surface of the body and the geometry,
  3 the linear stability equations are solved for a given mean flow and geometry, providing the growth rate.

Using this approach, three state equations must be solved (inviscid, boundary layer, linear stability), for any variation of the geometry in order to accurately predict the growth rate. However, if we consider the inviscid flow being the solution of the Euler equations, such a computation might be completed in minutes.

Independently from the strategy that enables to predict the growth rate of propagating disturbances for given geometry and flight data (Mach number, angle of attack, and Reynolds number), there are several approaches to the NLF design problem. Based on the knowledge how the growth rate of convectively unstable disturbances change due to variations of the pressure distribution, see for instance Schubauer & Skramstad (1948); Malik (1989); Zurigat *et al.* (1990), an existing pressure distribution for a given wing can be altered manually followed by an analysis of the growth rate. Other approaches exist, where approximative relations have been derived between variations in the pressure distribution and N-factors, see Green & Whitesides (1996). Once a pressure distribution has been obtained that meets a given criteria regarding transition delay, a geometry must be designed which meets this "target" pressure distribution. Such an analysis is sometimes denoted *inverse design*, and was first studied by Lighthill (1945) who solved it for the case of incompressible two-dimensional flow by conformal mapping. A review of different techniques to perform inverse design can be found in Jameson (1988).

In this presentation, we investigate an optimal-control approach of a shape optimization problem that is formulated to perform NLF design. Optimal control theory concerns optimization problems 'constrained' by ordinary or partial differential equations (PDEs). The inverse design problem, mentioned above, may be attacked using an optimal-control approach: Given a flow model to compute the pressure distribution p on a surface Γ, that is, a system of PDEs with boundary conditions on Γ, find the shape $\hat{\Gamma}$ that minimizes a measure of the difference between the target pressure p^t and p. A relevant measure, called objective function in the context of optimization, is

$$J\left(p, \Gamma\right) = \frac{1}{2} \int_{\Gamma} |p\left(\boldsymbol{x}\right) - p^t\left(\boldsymbol{x}\right)|^2 \mathrm{d}\boldsymbol{x}\,. \tag{1}$$

The target pressure could, for example, be such that it damps the growth of disturbances as mentioned above. Let us denote

$$\mathcal{A}\left(p, \Gamma\right) = \boldsymbol{0} \tag{2}$$

the relation between the shape Γ, the system of PDEs with boundary conditions (on Γ), and its solution p. The optimization problem is summarized as

$$\min_{\Gamma \,\in\, \mathcal{F}} \, J\left(p, \Gamma\right) \quad \text{subject to } \mathcal{A}\left(p, \Gamma\right) = \boldsymbol{0}\,, \tag{3}$$

where $\mathcal{F}$ is a set of admissible shapes. The system of PDEs, denoted $\mathcal{A}$, imposes constraints between the pressure distribution and the subject of optimization, the shape Γ. The objective function J depends on the shape Γ as well as on the solution p of a PDE. Moreover, the pressure p is a function of Γ if it is the unique solution of the system (2). We denote by $\tilde{J}\left(\Gamma\right)$ the function defined by

$$\tilde{J}\left(\Gamma\right) = J\left(p\left(\Gamma\right), \Gamma\right)\,, \tag{4}$$

where $p(\Gamma)$ is solution of the PDE (2). The problem (3) may then be reformulated in the *nested form*

$$\min_{\Gamma \in \mathcal{F}} \tilde{J}(\Gamma) \, . \tag{5}$$

Gradient-based methods prove to be the most efficient for solving problems like (5), assumed that $\tilde{J}$ (4) is continuous and differentiable. These methods are explained in details in text books on optimization, for example Nocedal & Wright (1999). Meanwhile, the computation of the gradient of an objective function like $\tilde{J}$ (4) is not trivial as J (1) depends explicitly on the design variable, here the shape Γ, as well as implicitly through the pressure, which is uniquely defined by the shape through the state equation (2). This is often a major difficulty in optimal-control problems. However, a practical method consists in approximating each component of the gradient $\nabla \tilde{J}$ by finite difference (each is a partial derivative). The cost is prohibitive for large scale problems, that is, for a large number of design parameters, due to expensive solutions of the PDEs (a 3D RANS solution may take days of computation). The cure is the solution of an additional PDE, called the adjoint problem, as it provides a means to calculate $\nabla \tilde{J}$ at a cost that is independent of the number of parameters. The use of adjoint equations in design optimization may be viewed as an off-spring of the theory of optimal control for PDE developed by Lions (1971) in the 60's. Based on this approach, the optimal shape of a body in viscous flow at very low Reynolds number, called Stokes flows, could be derived by Pironneau (1973) in 1973. In 1988, Jameson (1988) formulated the adjoints of the full potential flow equations and of the Euler equations in order to solve inverse problems. Thereafter, research teams have developed adjoint codes for industrial applications to improve the design of aircrafts in which CFD codes are used for the flow computation (see Anderson & Bonhaus 1999; Baysal & Ghayour 2001; Burgreen 1994; Elliot 1998; Enoksson 2000; Jameson 1997; Mohammadi 1997; Reuther 1999; Soemarwoto 1996; Sung & Kwon 2000). The reader will find an introduction to the method of adjoints, applied to aerodynamic design, in Giles & Pierce (2000). In our approach of NLF design, three systems of PDEs are solved sequentially, in order to calculate the objective function J, which is a function of the disturbance kinetic energy. The present work emphasizes the relation between the three adjoint problems that need to be solved for the calculation of the gradient ∇J.

Linear stability analysis has been used in the context of optimal NLF design in a number of investigations. In Green & Whitesides (1996), an iterative approach uses a target pressure-N-factor relationship to compute the desired pressure distribution, and an inverse method to find the geometry which satisfies the computed pressure distribution. The N-factor method has also been used in multidisciplinary optimization problems of whole aircraft configurations, where aerodynamics is considered as one discipline. In Lee *et al.* (1998), it was used to predict the onset of transition in order to determine where to turn on a chosen turbulence model in the Reynolds-Averaged-Navier-Stokes equations, enabling calculation of the friction drag. In Manning & Kroo (1999), a

surface panel method was coupled with an approximative boundary layer calculation, and stability analysis. Note however, that none of these investigations explicitly calculated the sensitivities of a quantity obtained from the linear stability analysis such as the N-factor or disturbance kinetic energy, with respect to the geometry.

In the approach taken here, we use an iterative gradient-based optimization procedure (see Byrd 1994) with the aim of minimizing an objective function, based on the disturbance kinetic energy, by changing the geometry of an airfoil. The inviscid flow is obtained by solving the Euler equations for compressible flows, and the viscous mean flow is obtained from the solution of the boundary layer equations for compressible flows on infinite swept wings. The evolution of convectively unstable disturbances is analyzed in the framework of nonlocal stability theory, which means that the growth of the boundary layer is taken into account, as opposed to the commonly used linear local stability theory. Indirectly, through minimization of the quadratic form associated with the Poisson equation, the design variables control the displacements of the nodes that are situated on the airfoil. Linear constraints on the displacements are accounted for in this parameterization so that they are fulfilled independently from the design variable. In this way we fix the volume, or cross section area, a limited region of the airfoil (around the leading edge) and the position of the trailing edge. The resulting quadratic programming formulation of the displacements is comparable to the formulation of the obstacle problems in mechanics. This technique generates smooth shapes at each optimization step without reducing the set of possible shapes, within the limit of the constraints and the size of the discretization. A simple mesh movement algorithm is used to propagate the nodal displacements from the airfoil to the rest of the computation domain of the inviscid flow. The gradient of the objective function is obtained from the solution of adjoint state equations, mesh sensitivities, and sensitivities of the parameterization.

The current report is an introduction and gives the status of an ongoing project on shape optimization for transition delay. Therefore a large effort is made to present the state and adjoint equations involved, gradient evaluation, and validity tests of the gradient computed using the solution of the adjoint equations. As this work is a joint project between one regarding shape optimization using the Euler equations, and another using the boundary layer and parabolized stability equations (PSE) for disturbance control, differences occur in the numerical schemes and methods used to derive the adjoint equations. Issues related to the latter is also discussed herein. Finally, some first results are presented of shape optimization for transition delay.

2. Theory

The aim of the current work is to perform gradient-based shape optimization in order to delay transition, and thus decrease the viscous drag, possibly in conjunction with wave-drag minimization. The objective function to be minimized

is a measure of the disturbance growth. Its value is obtained by computing consecutively the inviscid flow for a given geometry, the viscous mean flow given the pressure distribution from the inviscid solution, and finally the linear growth rate for a given mean flow. In this section a concise description is given of the state equations involved, objective function based on the disturbance growth, gradient derivation, and resulting adjoint equations.

2.1. *State equation for the inviscid flow*

The system of Euler equations governs the flow of an inviscid compressible fluid and expresses the conservation of mass, momentum and energy. In steady state, the following integral form holds for any fixed region V with boundary ∂V

$$\int_{\partial V} \mathbf{f} \cdot \hat{\boldsymbol{n}} \mathrm{dS} = \mathbf{0} \,, \tag{6}$$

where $\hat{\boldsymbol{n}}$ is the unit normal, outward oriented, of the control volume V, and $\mathbf{f}$ is the 3-by-1 matrix of tensors

$$\mathbf{f} = \begin{pmatrix} \rho \boldsymbol{u} \\ \rho \, \boldsymbol{u} \otimes \boldsymbol{u} + \boldsymbol{I} p \\ \boldsymbol{u} \, (E + p) \end{pmatrix} \,, \tag{7}$$

where E, the total energy per unit volume, is related to the pressure p, the density ρ and the velocity $\boldsymbol{u}$. In the framework of ideal fluids, assuming the law of perfect gas applies, E is given by

$$E = \frac{p}{\gamma - 1} + \frac{1}{2} \rho \boldsymbol{u}^2 \,. \tag{8}$$

In the case of an inviscid fluid, the condition

$$\boldsymbol{u} \cdot \hat{\boldsymbol{n}} = 0 \tag{9}$$

applies at the walls. The fluid state in conservative variables is denoted $\mathbf{w}$ and is the 3-by-1 matrix

$$\mathbf{w} = \begin{pmatrix} \rho \\ \boldsymbol{m} \\ E \end{pmatrix} \,, \tag{10}$$

where $\boldsymbol{m} = \rho \boldsymbol{u}$. Primitive variables are also used at some parts of the implementation and are denoted $\mathbf{v}$, the 3-by-1 matrix

$$\mathbf{v} = \begin{pmatrix} \rho \\ \boldsymbol{u} \\ p \end{pmatrix} \,. \tag{11}$$

In order to solve (6)-(9) for the flow around an airfoil, a finite sub-domain Ω is defined. Artificial boundary conditions are thus needed, and in the case of an airfoil, these are usually farfield conditions. We use the program Edge (see Eliasson 2001), a node-centered and edge-based finite-volume solver for Euler and the Reynolds Averaged Navier–Stokes equations (RANS). It is used here to solve equations (6)-(9) plus boundary conditions at the farfield.
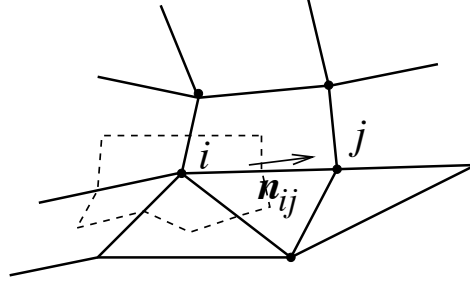
FIGURE 1. Dual grid (dashed lines) for inviscid flow computation.

Given a triangulation $\mathcal{T}_h$ of the discrete domain Ω, we will denote by $\mathcal{V}(\overline{\Omega})$ the set of all node indexes, V_i the dual control volume at node i, and $\boldsymbol{n}_{ij}$ the surface normal vector associated with edge ij (see Figure 1). For an introduction to this type of discretization, we refer to Barth (1991). The set of edges is denoted $\mathcal{E}(\overline{\Omega})$. The steady state equations are solved by explicit time integration of the system

$$V_i \frac{\mathrm{d}\mathbf{w}_i}{\mathrm{d}t} + \mathbf{R}_i = 0, \qquad \forall i \in \mathcal{V}(\overline{\Omega}), \tag{12}$$

until the residuals $\mathbf{R}_i$ vanish within some tolerance. Convergence is accelerated by local time stepping, multigrid, and implicit residual smoothing. The residuals $\mathbf{R}_i$ are

$$\begin{aligned}
\mathbf{R}_i &= \sum_{j \in \mathcal{N}_i} \left(\boldsymbol{n}_{ij} \cdot \mathbf{f}_{ij} + \mathbf{d}_{ij} \right) \qquad \forall i \in \mathcal{V}(\Omega), \\
\mathbf{R}_i &= \sum_{j \in \mathcal{N}_i} \left(\boldsymbol{n}_{ij} \cdot \mathbf{f}_{ij} + \mathbf{d}_{ij} + \boldsymbol{n}_i \cdot \mathbf{f}_i^{\mathrm{bc}} \right) \qquad \forall i \in \mathcal{V}(\partial\Omega).
\end{aligned} \tag{13}$$

where $\mathcal{N}_i$ is the set of indexes of nodes that are connected to node i with an edge. The residuals may be assembled by a single loop over all edges and all boundary nodes (see Eliasson 2001). The fluxes $\mathbf{f}$ on a control surface associated with $\boldsymbol{n}_{ij}$ is approximated by $\mathbf{f}_{ij}$ which in this study is

$$\mathbf{f}_{ij} = \frac{1}{2} \left(\mathbf{f}_i + \mathbf{f}_j \right) \qquad \text{with} \qquad \mathbf{f}_i = \mathbf{f}\left(\mathbf{w}_i \right), \tag{14}$$

which gives a central scheme. An artificial dissipation flux $\mathbf{d}_{ij}$, a blend of second and fourth-order differences of Jameson type is used,

$$\mathbf{d}_{ij} = \epsilon_2^{ij} (\mathbf{w}_i - \mathbf{w}_j) + (\epsilon_4^i \nabla^2 \mathbf{w}_i - \epsilon_4^j \nabla^2 \mathbf{w}_j), \tag{15}$$

with

$$\nabla^2 \mathbf{w}_i = \sum_{k \in \mathcal{N}_i} (\mathbf{w}_k - \mathbf{w}_i) \qquad \forall i \in \mathcal{V}(\overline{\Omega}). \tag{16}$$

The second-order dissipation is active where pressure gradients are large to prevent oscillations in the vicinity of shocks. The fourth-order dissipation is

meant to remove oscillating solutions from grid point to grid point while preserving the second-order accuracy of the central scheme away from the shocks. The fluxes $\mathbf{f}$ at the boundary are computed using a weak formulation of the boundary conditions (see Eliasson 2001) here denoted $\mathbf{f}^{\mathrm{bc}}$. At node i on a wall, applying (9) for computing $\mathbf{f}_i \cdot \boldsymbol{n}_i$ amounts to taking

$$\mathbf{f}_i^{\mathrm{bc}} = \begin{pmatrix} \mathbf{0} \\ \boldsymbol{I} p_i \\ \mathbf{0} \end{pmatrix}. \tag{17}$$

At node i on a farfield boundary the fluxes (7) are computed using either the primitive farfield data $\mathbf{v}_\infty$, for incoming characteristics, or an extrapolation of the primitive variables $\mathbf{v}_i$ for characteristics leaving the domain of computation:

$$\mathbf{f}_i^{\mathrm{bc}} = \mathbf{f}\left(\mathbf{v}_i^c\left(\hat{\boldsymbol{n}}_i\right)\right),$$
$$\mathbf{v}_i^c\left(\hat{\boldsymbol{n}}_i\right) = \mathbf{L}\left(\hat{\boldsymbol{n}}_i, \mathbf{v}_\infty\right) \mathbf{H}\left(\lambda_i\right) \mathbf{L}^{-1}\left(\hat{\boldsymbol{n}}_i, \mathbf{v}_\infty\right) \mathbf{v}_i \tag{18}$$
$$+ \mathbf{L}\left(\hat{\boldsymbol{n}}_i, \mathbf{v}_\infty\right)\left(\mathbf{I} - \mathbf{H}\left(\lambda_i\right)\right) \mathbf{L}^{-1}\left(\hat{\boldsymbol{n}}_i, \mathbf{v}_\infty\right) \mathbf{v}_\infty,$$

where $\mathbf{L}\left(\hat{\boldsymbol{n}}_i, \mathbf{v}_\infty\right)$ is a matrix of left eigenvectors that diagonalizes the Jacobian matrix of the flux in primitive variables along the outward-directed unit normal $\hat{\boldsymbol{n}}_i$, $\mathbf{H}\left(\lambda_i\right)$ is a diagonal matrix whose diagonal is 0 for negative eigenvalues and 1 for positive ones, and $\mathbf{I}$ is the identity matrix.

2.2. *State equations for the viscous flow*

The flow field considered here is the boundary layer on a swept wing with infinite span, which is obtained by solving the mass, momentum, and energy conservation equations for a viscous compressible fluid. The equations are written in an orthogonal curvilinear coordinate system with streamwise, spanwise, and wall-normal coordinates denoted as x^1, x^2 and x^3 respectively. A length element is defined as $ds^2 = \left(h_1 dx^1\right)^2 + \left(h_2 dx^2\right)^2 + \left(h_3 dx^3\right)^2$ where h_i is the scale factor. The total flow field, q_{tot} is decomposed into a mean, $\bar{q}$, and a perturbation part, $\tilde{q}$, as

$$q_{tot}(x^1, x^2, x^3, t) = \bar{q}(x^1, x^3) + \tilde{q}(x^1, x^2, x^3, t)$$

where $\bar{q} \in [U, V, W, P, T, \rho]$ and $\tilde{q} \in [\tilde{u}, \tilde{v}, \tilde{w}, \tilde{p}, \tilde{T}, \tilde{\rho}]$. Here U, V, W are the streamwise, spanwise and wall-normal velocity components of the mean flow, respectively, T is the temperature, ρ the density, and P the pressure. The lower case variables correspond to the disturbance quantities. The equations are derived for a quasi three-dimensional mean flow with zero variation in the spanwise direction. The evolution of convectively unstable disturbances is analyzed in the framework of the nonlocal stability theory. All flow and material quantities are made dimensionless with the corresponding reference flow quantities at a fixed streamwise position $x_0^\star$, except the pressure, which is made dimensionless with twice the corresponding dynamic pressure. Here, dimensional quantities are indicated by the superscript $\star$. The reference length scale is taken as $l_0^\star = (\nu_0^\star x_0^\star / U_0^\star)^{\frac{1}{2}}$. The Reynolds and Mach number are defined

as $Re = l_0^\star U_0^\star / \nu_0^\star$ and $M = U_0^\star / (\mathcal{R} \gamma T_0^\star)^{\frac{1}{2}}$ respectively where $\mathcal{R}$ is the specific gas constant, ν the kinematic viscosity and γ the ratio of the specific heats. In the proceeding sections the scale factors $h_2 = h_3 = 1$ are due to the infinite swept wing assumption.

2.2.1. *Mean-flow equations*

The dimensionless boundary-layer equations describing the steady viscous compressible mean flow on a swept wing with infinite span written on primitive variable form are given as

$$\frac{1}{h_1} \frac{\partial(\rho U)}{\partial x^1} + \frac{\partial(\rho W)}{\partial x^3} = 0, \quad (19)$$

$$\frac{\rho U}{h_1} \frac{\partial U}{\partial x^1} + \rho W \frac{\partial U}{\partial x^3} - \frac{1}{h_1} \frac{dP_e}{dx^1} + \frac{1}{Re} \frac{\partial}{\partial x^3} \left(\mu \frac{\partial U}{\partial x^3} \right) = 0, \quad (20)$$

$$\frac{\rho U}{h_1} \frac{\partial V}{\partial x^1} + \rho W \frac{\partial V}{\partial x^3} \frac{1}{Re} \frac{\partial}{\partial x^3} \left(\mu \frac{\partial V}{\partial x^3} \right) = 0, \quad (21)$$

$$c_p \frac{\rho U}{h_1} \frac{\partial T}{\partial x^1} + c_p \rho W \frac{\partial T}{\partial x^3} + \frac{1}{Re Pr} \frac{\partial}{\partial x^3} \left(\kappa \frac{\partial T}{\partial x^3} \right) +$$

$$(\gamma - 1) \frac{U M^2}{h_1} \frac{dP_e}{dx^1} + (\gamma - 1) \frac{\mu M^2}{Re} \left[\left(\frac{\partial U}{\partial x^3} \right)^2 + \left(\frac{\partial V}{\partial x^3} \right)^2 \right] = 0, \quad (22)$$

where the dynamic viscosity is given by μ, specific heat at constant pressure c_p, and heat conductivity by κ. Under the boundary layer assumptions, the pressure is constant in the direction normal to the boundary layer, i. e. $P = P_e(x^1)$. The equation of state can then be expressed as

$$\gamma M^2 P_e = \rho T,$$

and the streamwise derivative of the pressure is given as

$$\frac{dP_e}{dx^1} = -\rho_e U_e \frac{dU_e}{dx^1}$$

Here variables with subscript e are evaluated at the boundary layer edge. For a given pressure distribution given by the pressure coefficient

$$C_p = \frac{P^\star - P_\infty^\star}{\frac{1}{2} \rho_\infty^\star Q_\infty^\star},$$

where $Q_\infty^\star$ is the dimensional free stream velocity, and the sweep angle given by ψ, the values at the boundary layer edge are given as

$$P_e = \frac{P}{P_\infty} \frac{1}{\gamma M^2}, \quad T_e = \left(\frac{P}{P_\infty} \right)^{\frac{\gamma - 1}{\gamma}}, \quad \rho_e = \left(\frac{P}{P_\infty} \right)^{\frac{1}{\gamma}}, \quad U_e = \sqrt{Q_e^2 - V_e^2},$$

where

$$\frac{P}{P_\infty} = 1 + \frac{1}{2} C_p \gamma M^2, \quad Q_e^2 = 1 + \frac{1 - T_e c_{p_\infty}}{(\gamma - 1) \frac{1}{2} M^2}, \quad \text{and} \quad V_e = \sin \psi.$$

Here, we have used the assumptions that for an inviscid, steady, and adiabatic flow the total enthalpy is constant along a streamline, and the isentropic relations are used to obtain the relation between total and static quantities. A domain Ω_B is defined for equations (19)–(22) such that $x^1 \in [X_S, X_1]$, $x^2 \in [Z_0, Z_1]$ and $x^3 \in [0, \infty)$. The no-slip condition is used for the velocity components and the adiabatic wall condition for the temperature. In the free stream, the streamwise and spanwise velocity components, and the temperature takes the corresponding values at the boundary layer edge. This can be written as

$$
\begin{aligned}
\left[U, V, W, \frac{\partial T}{\partial x^3} \right] (x^1, 0) &= [0, 0, 0, 0] & \forall x^1 \in [X_S, X_1], \\
\lim_{x^3 \to +\infty} [U, V, T] (x^1, x^3) &= [U_e, V_e, T_e] (x^1) & \forall x^1 \in [X_S, X_1],
\end{aligned}
\tag{23}
$$

These non-linear equations are solved in an iterative way. From (20)–(22) we obtain the solution of $\tilde{\mathbf{Q}} = (U, V, T)$ using the boundary condition above for a given value of W. Equation (19) is then integrated in the wall normal direction to obtain W. The solution is considered converged when the relative change in the wall-normal derivative of the streamwise velocity component at the wall is below a specified value. In the proceeding sections we consider $\mathbf{Q} = (U, V, W, T)$ to be the solution of the boundary layer state. This is made to simplify the presentation.

2.2.2. *Disturbance equations*

The perturbations are assumed to be time- and spanwise periodic waves as

$$
\tilde{\mathbf{q}}(x^i, t) = \hat{\mathbf{q}}(x^1, x^3)\Theta, \quad \text{where} \quad \Theta = \exp\left(i \int_{X_0}^{x^1} \alpha(x')dx' + i\beta x^2 - i\omega t \right).
\tag{24}
$$

Here α is the complex streamwise wavenumber, β the real spanwise wavenumber, and ω the real disturbance angular frequency. Disturbances are superimposed on the mean flow at a streamwise position denoted X_0. We assume a scale separation Re^{-1} between the weak variation in the x^1-direction and the strong variation in the x^3-direction. Further, it is assumed that $\partial/\partial x^1 \sim O(Re^{-1})$ and $W \sim O(Re^{-1})$. Introducing the ansatz given by equation (24) and the assumptions above in the linearized governing equations, keeping terms up to order $O(Re^{-1})$, yields a set of nearly parabolic partial differential equations (see Bertolotti *et al.* 1992; Malik & Balakumar 1992; Simen 1992; Herbert 1997). The system of equations, called Parabolized Stability Equations (PSE), are lengthy and therefore written here as

$$
\mathcal{A}\hat{\mathbf{q}} + \mathcal{B}\frac{\partial \hat{\mathbf{q}}}{\partial x^3} + \mathcal{C}\frac{\partial^2 \hat{\mathbf{q}}}{(\partial x^3)^2} + \mathcal{D}\frac{1}{h_1}\frac{\partial \hat{\mathbf{q}}}{\partial x^1} = 0,
\tag{25}
$$

where $\hat{\mathbf{q}} = (\hat{\rho}, \hat{u}, \hat{v}, \hat{w}, \hat{T})^T$. The coefficients of the 5×5 matrices $\mathcal{A}, \mathcal{B}, \mathcal{C}$ and $\mathcal{D}$ are found in Pralits *et al.* (2000). A domain Ω_P for equation (25) is defined such

that $x^1 \in [X_0, X_1]$, $x^2 \in [Z_0, Z_1]$ and $x^3 \in [0, \infty)$. The boundary conditions corresponding to equation (25) are given as

$$\left[\hat{u}, \hat{v}, \hat{w}, \hat{T}\right](x^1, 0) = [0, 0, 0, 0] \quad \forall x^1 \in [X_0, X_1],$$

$$\lim_{x^3 \to +\infty} \left[\hat{u}, \hat{v}, \hat{w}, \hat{T}\right](x^1, x^3) = [0, 0, 0, 0] \quad \forall x^1 \in [X_0, X_1],$$

To remove the ambiguity of having x^1-dependence of both the amplitude and wave function in the ansatz, and to maintain a slow streamwise variation of the amplitude function $\hat{\mathbf{q}}$, a so called 'auxiliary condition' is introduced

$$\int_0^{+\infty} \hat{\mathbf{q}}^H \frac{\partial \hat{\mathbf{q}}}{\partial x^1} dx^3 = 0, \tag{26}$$

where superscript H denotes the complex conjugate transpose. Equation (25) is integrated in the downstream direction normal to the leading edge with an initial condition given by local stability theory. At each x^1-position the streamwise wavenumber α is iterated such that the condition given by equation (26) is satisfied. After a converged streamwise wavenumber has been obtained, the growth rate of the disturbance kinetic energy can be calculated from the relation

$$\sigma = -\alpha_i + \frac{\partial}{\partial x^1}(\ln \sqrt{E}),$$

where

$$E = \int_0^{+\infty} \rho \left(|\hat{u}|^2 + |\hat{v}|^2 + |\hat{w}|^2\right) dx^3.$$

The growth rate can then be used to predict the transition location using the so called e^N-method. The N-factor based on the disturbance kinetic energy is given as

$$N_E = \int_{X_{n1}}^X \sigma \, dx^1,$$

where X_{n1} is the lower branch of the neutral curve. A complete description of equation (25) is found in Pralits *et al.* (2000), and the numerical schemes used here are given in Hanifi *et al.* (1994).

2.3. *Objective function related to viscous drag*

The objective here is to use shape optimization to reduce the viscous drag on a wing. A reduction of the viscous drag can be seen as an increase of the laminar portion of the wing, that is, to move the location of laminar-turbulent transition further downstream. It is therefore important that the chosen objective function can be related to the transition process. One choice is to measure the kinetic energy of a certain disturbance at a downstream position, say X_f. This can be written as

$$E_f = \frac{1}{2} \int_{Z_0}^{Z_1} \int_0^{+\infty} \tilde{\mathbf{q}}^H M \tilde{\mathbf{q}} \, h_1 dx^2 dx^3 \bigg|_{x^1 = X_f}, \tag{27}$$

where $M = \text{diag}(0, 1, 1, 1, 0)$ which means that the disturbance kinetic energy is calculated from the disturbance velocity components. If the position X_f is chosen as the upper branch of the neutral curve, then the measure can be related to the maximum value of the N-factor of a given disturbance as

$$N_{max} = \ln \sqrt{\frac{E_f}{E_0}}, \tag{28}$$

where E_0 is the disturbance kinetic energy at the first neutral point. If in addition, the value of the N-factor of the measured disturbance is the one which first reaches the transition N-factor, then the position can be related to the onset of laminar-turbulent transition. It is however not clear, a priori, that minimizing such a measure will damp the chosen or other disturbances in the whole unstable region, especially if different types of disturbances are present, such as TS and cross-flow waves. For Blasius flow, it has been shown that an objective function based on a single TS wave is sufficient to successfully damp the growth of other TS waves (see Pralits *et al.* 2002; Airiau *et al.* 2003). On a wing however, it is common that both TS and cross-flow waves are present simultaneously. An alternative is therefore to measure the kinetic energy as the streamwise integral over a defined domain. Using such an approach, several different disturbances can be accounted for, with respective maximum growth rate at different positions. Here, the size of K disturbances superimposed on the mean flow at an upstream position X_0, is measured by their total kinetic energy as

$$E_K = \frac{1}{2} \sum_{k=1}^{K} \int_{X_{ms}}^{X_{me}} \int_{Z_0}^{Z_1} \int_0^{+\infty} \tilde{\mathbf{q}}_k^H M \tilde{\mathbf{q}}_k h_1 dx^1 dx^2 dx^3. \tag{29}$$

Here X_{ms} and X_{me} are the first and last streamwise position between which the disturbance kinetic energy is integrated, and adds the possibility to evaluate E_K in a streamwise domain within $[X_0, X_1]$. For a measure of a single disturbance, expression (29) is denoted E_1.

2.4. Derivation of the gradient

The objective function evaluated for a single disturbance $J \equiv E_1$, expression (29), depends explicitly on $\tilde{\mathbf{q}}$ and on the (Euler) mesh[1], here defined by the vector of nodal coordinates $\mathbf{X}$, that is

$$J \equiv J(\tilde{\mathbf{q}}, \mathbf{X}). \tag{30}$$

The aim of our investigation is to minimize J (30), where $\tilde{\mathbf{q}}$ is the solution of the PSE (25). The latter is here given as

$$\mathcal{A}_q(\tilde{\mathbf{q}}, \mathbf{Q}, \mathbf{X}) = \mathbf{0}, \tag{31}$$

---

[1]The nodes on the airfoil are common to the three discretized equations: Euler, BLE and PSE.

Objective function:
$$\begin{array}{ccc} V_q \times V_X & \longrightarrow & \mathbb{R} \\ \{\tilde{\mathbf{q}}, \mathbf{X}\} & & J\left(\tilde{\mathbf{q}}, \mathbf{X}\right) \end{array}$$

subject to (31):
$$\begin{array}{ccc} V_Q \times V_X & \longrightarrow & \mathbb{R} \\ \{\mathbf{Q}, \mathbf{X}\} & & J_Q\left(\mathbf{Q}, \mathbf{X}\right) \quad \equiv J\left(\tilde{\mathbf{q}}\left(\mathbf{Q}, \mathbf{X}\right), \mathbf{X}\right) \end{array}$$

subject to (31)-(32):
$$\begin{array}{ccc} V_w \times V_X & \longrightarrow & \mathbb{R} \\ \{\mathbf{w}, \mathbf{X}\} & & J_w\left(\mathbf{w}, \mathbf{X}\right) \quad \equiv J_Q\left(\mathbf{Q}\left(\mathbf{w}, \mathbf{X}\right), \mathbf{X}\right) \end{array}$$

subject to (31)-(33):
$$\begin{array}{ccc} V_X & \longrightarrow & \mathbb{R} \\ \mathbf{X} & & J_X\left(\mathbf{X}\right) \quad \equiv J_w\left(\mathbf{w}\left(\mathbf{X}\right), \mathbf{X}\right) \end{array}$$

TABLE 1. Functionals defined by the objective function J and the state equations (31)-(33).

where (31) is defined for given $\mathbf{X}$ and $\mathbf{Q}$. The mean flow $\mathbf{Q}$ is solution of the BLE (19)-(22), here denoted

$$\mathcal{A}_Q\left(\mathbf{Q}, \mathbf{w}, \mathbf{X}\right) = \mathbf{0}, \tag{32}$$

which is defined for a given $\mathbf{X}$ and $\mathbf{w}$. Finally, the inviscid flow $\mathbf{w}$ is solution of the Euler equations (6)-(9), denoted

$$\mathcal{A}_w\left(\mathbf{w}, \mathbf{X}\right) = \mathbf{0}. \tag{33}$$

In the presentation of the adjoint problems it will be convenient to introduce the functions J_X, J_Q and J_w, defined in Table 1. These are just objective function (30) in which various intermediate quantities are regarded as independent variables.

The mesh nodes $\mathbf{X}$ are calculated from the displacements $\mathbf{y}$ of the nodes on the airfoil, by a mesh movement algorithm. This can be written $\mathbf{X} \equiv \mathbf{X}\left(\mathbf{y}\right)$, and is described in §3. The displacements are controlled by the parameters $\mathbf{a}$, that is $\mathbf{y} \equiv \mathbf{y}\left(\mathbf{a}\right)$, see §3. Given a function J_X of the variable $\mathbf{X}$, for example defined as in Table 1, it will also be convenient to define J_y and J_a, as

$$\begin{aligned} J_y\left(\mathbf{y}\right) &= J_X\left(\mathbf{X}\left(\mathbf{y}\right)\right), \\ J_a\left(\mathbf{a}\right) &= J_y\left(\mathbf{y}\left(\mathbf{a}\right)\right). \end{aligned} \tag{34}$$

To summarize our approach, the aim is to minimize J, subject to (31)-(33) with respect to the design parameters $\mathbf{a}$, using a gradient-based method. This requires the computation of the gradient ∇J_a which is computed from ∇J_X in §3. The aim of this section is to show that ∇J_X can be computed at an efficient cost using an optimal control approach.

In the following it is assumed that $\tilde{\mathbf{q}} \in V_q$, $\mathbf{Q} \in V_Q$, $\mathbf{w} \in V_w$, and $\mathbf{X} \in V_X$, and that V_q, V_Q, V_w and V_X are vector spaces equipped with the inner products $\langle \cdot, \cdot \rangle_q$, $\langle \cdot, \cdot \rangle_Q$, $\langle \cdot, \cdot \rangle_w$ and $\langle \cdot, \cdot \rangle_X$, respectively. Furthermore, it is assumed that all mappings are differentiable and, for example, $\partial \mathcal{A}_q / \partial \tilde{\mathbf{q}}$ denotes linearization

with respect to variable $\tilde{\mathbf{q}}$ of the mapping $\mathcal{A}_q$, at the given state $\{\tilde{\mathbf{q}}, \mathbf{Q}, \mathbf{w}, \mathbf{X}\}$. The notations $(\partial \mathcal{A}_q / \partial \tilde{\mathbf{q}})^{-1}$, and $(\partial \mathcal{A}_q / \partial \tilde{\mathbf{q}})^*$, denote the inverse, and the adjoint of the linearized mapping $\partial \mathcal{A}_q / \partial \tilde{\mathbf{q}}$, respectively. Finally, the notation $(\partial \mathcal{A}_q / \partial \tilde{\mathbf{q}}) \, \delta \tilde{\mathbf{q}}$ denotes the application of $\partial \mathcal{A}_q / \partial \tilde{\mathbf{q}}$ on $\delta \tilde{\mathbf{q}}$.

2.4.1. *Sensitivity of the PSE*

For arbitrary variations $\{\delta \mathbf{Q}, \delta \mathbf{X}\} \in V_Q \times V_X$, of $\{\mathbf{Q}, \mathbf{X}\}$ in the PSE (31), the first variation of the solution of the PSE is denoted $\delta \tilde{\mathbf{q}} \in V_q$, and is defined by the *sensitivity equations*

$$\frac{\partial \mathcal{A}_q}{\partial \tilde{\mathbf{q}}} \delta \tilde{\mathbf{q}} = -\frac{\partial \mathcal{A}_q}{\partial \mathbf{Q}} \delta \mathbf{Q} - \frac{\partial \mathcal{A}_q}{\partial \mathbf{X}} \delta \mathbf{X} \,. \tag{35}$$

Furthermore, for any variations $\{\delta \tilde{\mathbf{q}}, \delta \mathbf{X}\}$ in $V_q \times V_X$ we define the first variation of the objective function J as

$$\delta J = \left\langle \frac{\partial J}{\partial \tilde{\mathbf{q}}}, \delta \tilde{\mathbf{q}} \right\rangle_q + \left\langle \frac{\partial J}{\partial \mathbf{X}}, \delta \mathbf{X} \right\rangle_X \tag{36}$$

In the remaining, $\delta \tilde{\mathbf{q}}$ is solution of the sensitivity equations (35), which yields a new expression for (36)

$$\delta J = \left\langle \frac{\partial J}{\partial \tilde{\mathbf{q}}}, \left(\frac{\partial \mathcal{A}_q}{\partial \tilde{\mathbf{q}}} \right)^{-1} \left(-\frac{\partial \mathcal{A}_q}{\partial \mathbf{Q}} \delta \mathbf{Q} - \frac{\partial \mathcal{A}_q}{\partial \mathbf{X}} \delta \mathbf{X} \right) \right\rangle_q + \left\langle \frac{\partial J}{\partial \mathbf{X}}, \delta \mathbf{X} \right\rangle_X , \tag{37}$$

and, for $\tilde{\mathbf{q}}$ solution of (31) and $\delta \tilde{\mathbf{q}}$ solution of (35) , the definition of J_Q (Table 1) yields

$$\delta J_Q = \delta J \,. \tag{38}$$

The gradient of the functional J_Q is $\nabla J_Q = \{\partial J_Q / \partial \mathbf{Q}, \partial J_Q / \partial \mathbf{X}\}$ and is a vector of the product space $V_Q \times V_X$ such that for all $\{\delta \mathbf{Q}, \delta \mathbf{X}\}$ in $V_Q \times V_X$ we have

$$\delta J_Q = \left\langle \frac{\partial J_Q}{\partial \mathbf{Q}}, \delta \mathbf{Q} \right\rangle_Q + \left\langle \frac{\partial J_Q}{\partial \mathbf{X}}, \delta \mathbf{X} \right\rangle_X \,. \tag{39}$$

Using the definition of the adjoint of the operator $\partial \mathcal{A}_q / \partial \tilde{\mathbf{q}}$ in expression (37) and using (38), we obtain

$$
\begin{aligned}
\delta J_Q = {} & \left\langle \left(\left(\frac{\partial \mathcal{A}_q}{\partial \tilde{\mathbf{q}}} \right)^{-1} \right)^* \frac{\partial J}{\partial \tilde{\mathbf{q}}}, -\frac{\partial \mathcal{A}_q}{\partial \mathbf{Q}} \delta \mathbf{Q} - \frac{\partial \mathcal{A}_q}{\partial \mathbf{X}} \delta \mathbf{X} \right\rangle_q \\
& + \left\langle \frac{\partial J}{\partial \mathbf{X}}, \delta \mathbf{X} \right\rangle_X ,
\end{aligned}
\tag{40}
$$

which is in turn rewritten using the definition of the adjoint of $\partial \mathcal{A}_q / \partial \mathbf{Q}$, and $\partial \mathcal{A}_q / \partial \mathbf{X}$, respectively, as

$$
\delta J_Q = - \left\langle \left(\frac{\partial \mathcal{A}_q}{\partial \mathbf{Q}} \right)^* \left(\left(\frac{\partial \mathcal{A}_q}{\partial \tilde{\mathbf{q}}} \right)^{-1} \right)^* \frac{\partial J}{\partial \tilde{\mathbf{q}}}, \delta \mathbf{Q} \right\rangle_Q
$$
$$
- \left\langle \left(\frac{\partial \mathcal{A}_q}{\partial \mathbf{X}} \right)^* \left(\left(\frac{\partial \mathcal{A}_q}{\partial \tilde{\mathbf{q}}} \right)^{-1} \right)^* \frac{\partial J}{\partial \tilde{\mathbf{q}}}, \delta \mathbf{X} \right\rangle_X + \left\langle \frac{\partial J}{\partial \mathbf{X}}, \delta \mathbf{X} \right\rangle_X .
$$

(41)

Therefore, by introducing the adjoint state $\mathbf{q}^*$, solution of the system

$$
\left(\frac{\partial \mathcal{A}_q}{\partial \tilde{\mathbf{q}}} \right)^* \mathbf{q}^* = \frac{\partial J}{\partial \tilde{\mathbf{q}}} ,
$$

(42)

we obtain that

$$
\frac{\partial J_Q}{\partial \mathbf{Q}} = - \left(\frac{\partial \mathcal{A}_q}{\partial \mathbf{Q}} \right)^* \mathbf{q}^* \quad \text{and} \quad \frac{\partial J_Q}{\partial \mathbf{X}} = \frac{\partial J}{\partial \mathbf{X}} - \left(\frac{\partial \mathcal{A}_q}{\partial \mathbf{X}} \right)^* \mathbf{q}^* .
$$

(43)

The cost for obtaining gradient of J_Q is reduced to one solution of the system (42) and two matrix–vector products as shown in (43).

2.4.2. *Sensitivity of the BLE*

For arbitrary variations $\{\delta \mathbf{w}, \delta \mathbf{X}\} \in V_w \times V_X$, of $\{\mathbf{w}, \mathbf{X}\}$ in the BLE (32), the first variation of the solution of the BLE is denoted $\delta \mathbf{Q} \in V_Q$, and is defined by the sensitivity equations

$$
\frac{\partial \mathcal{A}_Q}{\partial \mathbf{Q}} \delta \mathbf{Q} = -\frac{\partial \mathcal{A}_Q}{\partial \mathbf{w}} \delta \mathbf{w} - \frac{\partial \mathcal{A}_Q}{\partial \mathbf{X}} \delta \mathbf{X} .
$$

(44)

Furthermore, from the definition (39) and the expression of the gradient (43), for arbitrary variations $\{\delta \mathbf{Q}, \delta \mathbf{X}\}$ in $V_Q \times V_X$, the variation δJ_Q is

$$
\delta J_Q = \left\langle - \left(\frac{\partial \mathcal{A}_q}{\partial \mathbf{Q}} \right)^* \mathbf{q}^*, \delta \mathbf{Q} \right\rangle_Q + \left\langle \frac{\partial J}{\partial \mathbf{X}} - \left(\frac{\partial \mathcal{A}_q}{\partial \mathbf{X}} \right)^* \mathbf{q}^*, \delta \mathbf{X} \right\rangle_X .
$$

(45)

In the following, $\delta \mathbf{Q}$ is solution of the sensitivity equation (44). The variation δJ_Q is expressed, making use of (45) and (44), as

$$
\delta J_Q = \left\langle - \left(\frac{\partial \mathcal{A}_q}{\partial \mathbf{Q}} \right)^* \mathbf{q}^*, \left(\frac{\partial \mathcal{A}_Q}{\partial \mathbf{Q}} \right)^{-1} \left(-\frac{\partial \mathcal{A}_Q}{\partial \mathbf{w}} \delta \mathbf{w} - \frac{\partial \mathcal{A}_Q}{\partial \mathbf{X}} \delta \mathbf{X} \right) \right\rangle_Q
$$
$$
+ \left\langle \frac{\partial J}{\partial \mathbf{X}} - \left(\frac{\partial \mathcal{A}_q}{\partial \mathbf{X}} \right)^* \mathbf{q}^*, \delta \mathbf{X} \right\rangle_X ,
$$

(46)

and, for $\mathbf{Q}$ solution of (32) and $\delta \mathbf{Q}$ solution of (44), the definition of J_w (Table 1) yields

$$
\delta J_w = \delta J_Q .
$$

(47)

The gradient of J_w is the vector $\{\partial J_w/\partial \mathbf{w}, \partial J_w/\partial \mathbf{X}\}$ in the product space $V_w \times V_X$ such that for all $\{\delta \mathbf{w}, \delta \mathbf{X}\}$ in $V_w \times V_X$ we have

$$\delta J_w = \left\langle \frac{\partial J_w}{\partial \mathbf{w}}, \delta \mathbf{w} \right\rangle_w + \left\langle \frac{\partial J_w}{\partial \mathbf{X}}, \delta \mathbf{X} \right\rangle_X . \tag{48}$$

Using the adjoint of the inverse linearized BLE operator $(\partial \mathcal{A}_Q/\partial \mathbf{Q})^{-1}$ in (46), δJ_w (47) is expressed as

$$\delta J_w = \left\langle -\left(\left(\frac{\partial \mathcal{A}_Q}{\partial \mathbf{Q}}\right)^{-1}\right)^* \left(\frac{\partial \mathcal{A}_q}{\partial \mathbf{Q}}\right)^* \mathbf{q}^*, -\frac{\partial \mathcal{A}_Q}{\partial \mathbf{w}}\delta \mathbf{w} - \frac{\partial \mathcal{A}_Q}{\partial \mathbf{X}}\delta \mathbf{X} \right\rangle_Q$$
$$+ \left\langle \frac{\partial J}{\partial \mathbf{X}} - \left(\frac{\partial \mathcal{A}_q}{\partial \mathbf{X}}\right)^* \mathbf{q}^*, \delta \mathbf{X} \right\rangle_X . \tag{49}$$

Using the adjoints of $\partial \mathcal{A}_Q/\partial \mathbf{w}$ and $\partial \mathcal{A}_Q/\partial \mathbf{X}$ enables us to rewrite relation (49) as

$$\delta J_w = \left\langle \left(\frac{\partial \mathcal{A}_Q}{\partial \mathbf{w}}\right)^* \left(\left(\frac{\partial \mathcal{A}_Q}{\partial \mathbf{Q}}\right)^{-1}\right)^* \left(\frac{\partial \mathcal{A}_q}{\partial \mathbf{Q}}\right)^* \mathbf{q}^*, \delta \mathbf{w} \right\rangle_w$$
$$+ \left\langle \left(\frac{\partial \mathcal{A}_Q}{\partial \mathbf{X}}\right)^* \left(\left(\frac{\partial \mathcal{A}_Q}{\partial \mathbf{Q}}\right)^{-1}\right)^* \left(\frac{\partial \mathcal{A}_q}{\partial \mathbf{Q}}\right)^* \mathbf{q}^*, \delta \mathbf{X} \right\rangle_X \tag{50}$$
$$+ \left\langle \frac{\partial J}{\partial \mathbf{X}} - \left(\frac{\partial \mathcal{A}_q}{\partial \mathbf{X}}\right)^* \mathbf{q}^*, \delta \mathbf{X} \right\rangle_X .$$

It suggests, as previously, to define an adjoint state $\mathbf{Q}^*$ as

$$\left(\frac{\partial \mathcal{A}_Q}{\partial \mathbf{Q}}\right)^* \mathbf{Q}^* = \left(\frac{\partial \mathcal{A}_q}{\partial \mathbf{Q}}\right)^* \mathbf{q}^* . \tag{51}$$

Setting $\mathbf{Q}^*$ in (50) and identifying the new expression with (48) we obtain

$$\frac{\partial J_w}{\partial \mathbf{w}} = \left(\frac{\partial \mathcal{A}_Q}{\partial \mathbf{w}}\right)^* \mathbf{Q}^* \quad \text{and} \quad \frac{\partial J_w}{\partial \mathbf{X}} = \frac{\partial J}{\partial \mathbf{X}} - \left(\frac{\partial \mathcal{A}_q}{\partial \mathbf{X}}\right)^* \mathbf{q}^* + \left(\frac{\partial \mathcal{A}_Q}{\partial \mathbf{X}}\right)^* \mathbf{Q}^* . \tag{52}$$

The use of adjoint equations limits cost for obtaining the gradient of J_w to solving the systems (42) and (51), as well as four matrix–vector products: one to 'assemble' the right-hand side of the adjoint system (51) and three to obtain the final expression (52).

2.4.3. *Sensitivity of the Euler equations*

For arbitrary variations $\delta \mathbf{X} \in V_X$, of $\mathbf{X}$ in the Euler equation (33), the first variation of solution of the Euler equation is denoted $\delta \mathbf{w} \in V_w$, and is defined by the sensitivity equation

$$\frac{\partial \mathcal{A}_w}{\partial \mathbf{w}}\delta \mathbf{w} = -\frac{\partial \mathcal{A}_w}{\partial \mathbf{X}}\delta \mathbf{X} . \tag{53}$$

Furthermore, for arbitrary variations $\{\delta\mathbf{w}, \delta\mathbf{X}\}$ in $V_w \times V_X$ the first variation of the functional J_w is expressed, from the gradient (52)

$$
\begin{aligned}
\delta J_w &= \left\langle \left(\frac{\partial \mathcal{A}_Q}{\partial \mathbf{w}}\right)^* \mathbf{Q}^*, \delta\mathbf{w} \right\rangle_w \\
&+ \left\langle \frac{\partial J}{\partial \mathbf{X}} - \left(\frac{\partial \mathcal{A}_q}{\partial \mathbf{X}}\right)^* \mathbf{q}^* + \left(\frac{\partial \mathcal{A}_Q}{\partial \mathbf{X}}\right)^* \mathbf{Q}^*, \delta\mathbf{X} \right\rangle_X
\end{aligned}
\tag{54}
$$

In the following, $\delta\mathbf{w}$ is the solution of the sensitivity equation (53), which enables us to rewrite expression (54) as

$$
\begin{aligned}
\delta J_w &= \left\langle \left(\frac{\partial \mathcal{A}_Q}{\partial \mathbf{w}}\right)^* \mathbf{Q}^*, -\left(\frac{\partial \mathcal{A}_w}{\partial \mathbf{w}}\right)^{-1} \frac{\partial \mathcal{A}_w}{\partial \mathbf{X}} \delta\mathbf{X} \right\rangle_w \\
&+ \left\langle \frac{\partial J}{\partial \mathbf{X}} - \left(\frac{\partial \mathcal{A}_q}{\partial \mathbf{X}}\right)^* \mathbf{q}^* + \left(\frac{\partial \mathcal{A}_Q}{\partial \mathbf{X}}\right)^* \mathbf{Q}^*, \delta\mathbf{X} \right\rangle_X,
\end{aligned}
\tag{55}
$$

and, for $\mathbf{w}$ solution of (33) and $\delta\mathbf{w}$ solution of (53), the definition of J_X (Table 1) yields

$$
\delta J_X = \delta J_w.
\tag{56}
$$

The gradient of J_X is the vector ∇J_X in the space V_X such that for all $\delta\mathbf{X}$ in V_X we have

$$
\delta J_X = \langle \nabla J_X, \delta\mathbf{X} \rangle_X.
\tag{57}
$$

The adjoint of the linearized Euler operator is used in (55) to express δJ_X (56) as

$$
\begin{aligned}
\delta J_X &= \left\langle \left(\left(\frac{\partial \mathcal{A}_w}{\partial \mathbf{w}}\right)^{-1}\right)^* \left(\frac{\partial \mathcal{A}_Q}{\partial \mathbf{w}}\right)^* \mathbf{Q}^*, -\frac{\partial \mathcal{A}_w}{\partial \mathbf{X}} \delta\mathbf{X} \right\rangle_w \\
&+ \left\langle \frac{\partial J}{\partial \mathbf{X}} - \left(\frac{\partial \mathcal{A}_q}{\partial \mathbf{X}}\right)^* \mathbf{q}^* + \left(\frac{\partial \mathcal{A}_Q}{\partial \mathbf{X}}\right)^* \mathbf{Q}^*, \delta\mathbf{X} \right\rangle_X.
\end{aligned}
\tag{58}
$$

The adjoint instead of the linear operator $\partial \mathcal{A}_w / \partial \mathbf{X}$ is used in (58) and leads to

$$
\begin{aligned}
\delta J_X &= \left\langle \frac{\partial J}{\partial \mathbf{X}} - \left(\frac{\partial \mathcal{A}_q}{\partial \mathbf{X}}\right)^* \mathbf{q}^* + \left(\frac{\partial \mathcal{A}_Q}{\partial \mathbf{X}}\right)^* \mathbf{Q}^*, \delta\mathbf{X} \right\rangle_X \\
&- \left\langle \left(\frac{\partial \mathcal{A}_w}{\partial \mathbf{X}}\right)^* \left(\left(\frac{\partial \mathcal{A}_w}{\partial \mathbf{w}}\right)^{-1}\right)^* \left(\frac{\partial \mathcal{A}_Q}{\partial \mathbf{w}}\right)^* \mathbf{Q}^*, \delta\mathbf{X} \right\rangle_X,
\end{aligned}
\tag{59}
$$

The method of adjoint is again applied as we define an adjoint state $\mathbf{w}^*$, here solution of the system

$$
\left(\frac{\partial \mathcal{A}_w}{\partial \mathbf{w}}\right)^* \mathbf{w}^* = \left(\frac{\partial \mathcal{A}_Q}{\partial \mathbf{w}}\right)^* \mathbf{Q}^*,
\tag{60}
$$

which enables us to give expression for the gradient (57)

$$
\nabla J_X = \frac{\partial J}{\partial \mathbf{X}} - \left(\frac{\partial \mathcal{A}_q}{\partial \mathbf{X}}\right)^* \mathbf{q}^* + \left(\frac{\partial \mathcal{A}_Q}{\partial \mathbf{X}}\right)^* \mathbf{Q}^* - \left(\frac{\partial \mathcal{A}_w}{\partial \mathbf{X}}\right)^* \mathbf{w}^*.
\tag{61}
$$

The total cost of this gradient evaluation is three adjoint systems (42), (51) and (60), and five matrix–vector products: two for the assembly of the right-hand-sides of the systems (51) and (60), and three for the final expression (61).

2.5. *Adjoint equations*

The concise description given in §2.4 gives an expression of the gradient ∇J_X (61), which is a function of three adjoint states $\mathbf{q}^*$, $\mathbf{Q}^*$ and $\mathbf{w}^*$. These states are the solutions of the adjoint of the parabolized stability equations (42), adjoint of the boundary layer equations (51) and adjoint of the Euler equations (60), respectively. There are in principle two different approaches on how to derive these adjoint equations. In the first, sometimes denoted the "discrete approach" or "discretize-then-differentiate", the adjoint equations are derived from the discretized set of state equations. In the second approach, sometimes denoted the "continuous approach" or "differentiate-then-discretize", the adjoint equations are derived from the continuous state equations. The continuous adjoint equations are then discretized, commonly in a similar way as the corresponding state equations, in which the original code written for solving the state is reused with some modifications.

2.5.1. *Adjoint of the Parabolized Stability Equations*

The adjoint of the parabolized stability equations (42) are derived using a continuous approach. The complete derivation is found in Pralits *et al.* (2000) and they are here given as

$$\tilde{\mathcal{A}}\mathbf{q}^* \;+\; \tilde{\mathcal{B}}\frac{\partial \mathbf{q}^*}{\partial x^3} \;+\; \tilde{\mathcal{C}}\frac{\partial^2 \mathbf{q}^*}{(\partial x^3)^2} \;+\; \tilde{\mathcal{D}}\frac{1}{h_1}\frac{\partial \mathbf{q}^*}{\partial x^1} \;=\; \mathbf{S}_P^*, \tag{62}$$

$$\frac{\partial}{\partial x^1} \int_0^{+\infty} \mathbf{q}^{*H}\left(\frac{\partial \mathcal{A}}{\partial \alpha} + \frac{\partial \mathcal{B}}{\partial \alpha}\right) \hat{\mathbf{q}}\, h_1 dx^3 =$$
$$\begin{cases} \qquad\qquad 0 & \forall x^1 \notin [X_{ms}, X_{me}], \\[2mm] -\mathrm{i}|\Theta|^2 \displaystyle\int_0^{+\infty} \hat{\mathbf{q}}^H M \hat{\mathbf{q}}\, h_1 dx^3 & \forall x^1 \in [X_{ms}, X_{me}], \end{cases} \tag{63}$$

where

$$\mathbf{S}_P^* = \begin{cases} -\bar{r}^*\dfrac{\partial \hat{\mathbf{q}}}{\partial x^1} - \dfrac{\partial (r^*\hat{\mathbf{q}})}{\partial x^1} & \forall x^1 \notin [X_{ms}, X_{me}], \\[3mm] -\bar{r}^*\dfrac{\partial \hat{\mathbf{q}}}{\partial x^1} - \dfrac{\partial (r^*\hat{\mathbf{q}})}{\partial x^1} + \xi M^H\hat{\mathbf{q}}|\Theta|^2 & \forall x^1 \in [X_{ms}, X_{me}], \end{cases}$$

and

$$
\tilde{\mathcal{A}} = \mathcal{A}^H - \frac{\partial \mathcal{B}^H}{\partial x^3} - m_{13} \, \mathcal{B}^H + \frac{\partial^2 \mathcal{C}^H}{(\partial x^3)^2} + 2 \, m_{13} \frac{\partial \mathcal{C}^H}{\partial x^3} - \frac{\partial \mathcal{D}^H}{\partial x^1},
$$

$$
\tilde{\mathcal{B}} = -\mathcal{B}^H + 2\frac{\partial \mathcal{C}^H}{\partial x^3} + 2 \, m_{13} \, \mathcal{C}^H,
$$

$$
\tilde{\mathcal{C}} = \mathcal{C}^H,
$$

$$
\tilde{\mathcal{D}} = -\mathcal{D}^H.
$$

Here, $\mathbf{q}^* = (\rho^*, u^*, v^*, w^*, \theta^*)^T$, and the above equations are subject to the following boundary conditions

$$
[u^*, v^*, w^*, \theta^*] \, (x^1, 0) = [0, 0, 0, 0] \quad \forall x^1 \in [X_0, X_1],
$$

$$
\lim_{x^3 \to +\infty} [u^*, v^*, w^*, \theta^*] \, (x^1, x^3) = [0, 0, 0, 0] \quad \forall x^1 \in [X_0, X_1].
$$

The initial conditions are

$$
\mathbf{q}^*(X_1, x^3) = (1 - \xi)\mathbf{q}_1^*(x^3) \quad \forall x^3 \in [0, +\infty),
$$

$$
r^*(X_1) = (1 - \xi)r_1^* \quad \forall x^3 \in [0, +\infty),
$$

with $\mathbf{q}_1^*$ and r_1^* evaluated at $x^1 = X_1$ as

$$
\mathbf{q}_1^* = |\Theta|^2 \mathcal{D}^+(M - c_1 \mathcal{I})\hat{\mathbf{q}}, \qquad r_1^* = |\Theta|^2 \, c_1,
$$

$$
\bar{c}_1 = \frac{\displaystyle\int_0^\infty (h_1 \hat{\mathbf{q}}^H M \, \mathcal{D}^{+H} \left(\frac{\partial \mathcal{A}}{\partial \alpha} + \frac{\partial \mathcal{B}}{\partial \alpha} \right) \hat{\mathbf{q}} - i\hat{\mathbf{q}}^H M\hat{\mathbf{q}}) \, dx^3}{\displaystyle\int_0^\infty \hat{\mathbf{q}}^H \mathcal{D}^{+H} \left(\frac{\partial \mathcal{A}}{\partial \alpha} + \frac{\partial \mathcal{B}}{\partial \alpha} \right) \hat{\mathbf{q}} \, h_1 \, dx^3}, \tag{64}
$$

where $\mathcal{D}^+ = (\mathcal{D}^H)^{-1}$. Equation (62) is solved by backward integration in space. Even though it is a linear equation, in order to reuse the code developed to solve the PSE iteratively to satisfy the auxiliary condition, at each streamwise position r^* is solved iteratively such that expression (63) is satisfied. The right hand side of equation (62) and the initial condition depend on the choice of objective function, i. e. the value of ξ.

2.5.2. *Adjoint of the Boundary Layer Equations*

The adjoint of the boundary-layer equations are derived using a continuous approach. Details regarding the derivation is found in Pralits (2001) and Pralits

& Hanifi (2003) and they are here given as

$$\rho\frac{\partial(h_1 W^*)}{\partial x^3} - h_1\rho\left(\frac{\partial U}{\partial x^3}U^* + \frac{\partial V}{\partial x^3}V^* + c_p\frac{\partial T}{\partial x^3}T^*\right) = S_W^*, \tag{65}$$

$$\frac{\partial(\rho U U^*)}{\partial x^1} + \frac{\partial(h_1\rho W U^*)}{\partial x^3} - \rho\left(\frac{\partial U}{\partial x^1}U^* + \frac{\partial V}{\partial x^1}V^* - \frac{\partial W^*}{\partial x^1} + c_p\frac{\partial T}{\partial x^1}T^*\right) +$$
$$(\gamma-1)M^2\frac{dP_e}{dx^1}T^* - \frac{2(\gamma-1)}{Re}M^2\frac{\partial}{\partial x^3}\left(h_1\mu\frac{\partial U}{\partial x^3}T^*\right) +$$
$$\frac{1}{Re}\frac{\partial}{\partial x^3}\left(\mu\frac{\partial(h_1 U^*)}{\partial x^3}\right) = S_U^*, \tag{66}$$

$$\frac{\partial(\rho U V^*)}{\partial x^1} + \frac{\partial(h_1\rho W V^*)}{\partial x^3} - \frac{2(\gamma-1)}{Re}M^2\frac{\partial}{\partial x^3}\left(h_1\mu\frac{\partial V}{\partial x^3}T^*\right) +$$
$$\frac{1}{Re}\frac{\partial}{\partial x^3}\left(\mu\frac{\partial(h_1 V^*)}{\partial x^3}\right) = S_V^*, \tag{67}$$

$$c_p\frac{\partial(\rho U T^*)}{\partial x^1} + c_p\frac{\partial(h_1\rho W T^*)}{\partial x^3} + \frac{\rho U}{T}\left(\frac{\partial U}{\partial x^1}U^* + \frac{\partial V}{\partial x^1}V^* - \frac{\partial W^*}{\partial x^1}\right) +$$
$$\frac{\rho U}{T}c_p\frac{\partial T}{\partial x^1}T^* + \frac{\kappa}{RePr}\frac{\partial^2(h_1 T^*)}{(\partial x^3)^2}\frac{(\gamma-1)}{Re}M^2\frac{d\mu}{dT}\left[\left(\frac{\partial U}{\partial x^3}\right)^2 + \left(\frac{\partial V}{\partial x^3}\right)^2\right]T^* -$$
$$\frac{1}{Re}\frac{d\mu}{dT}\left[\frac{\partial U}{\partial x^3}\frac{\partial(h_1 U^*)}{\partial x^3} + \frac{\partial V}{\partial x^3}\frac{\partial(h_1 V^*)}{\partial x^3}\right] = S_E^*, \tag{68}$$

where the right hand side $\mathbf{S}_B^* = (S_W^*,\ S_U^*,\ S_V^*,\ S_E^*)^T$ is given as

$$\mathbf{S}_B^* = \begin{cases} (F_W,\ F_U,\ F_V,\ F_T + F_W\,W/T)^T\,h_1 & \forall x^1 \in (X_0, X_1), \\ \mathbf{0} & \forall x^1 \in (X_S, X_0], \end{cases} \tag{69}$$

The non-zero right hand side is the coupling between the APSE and the ABLE and express the sensitivity of the PSE with respect the variations in W, U, V and T respectively. A detailed description is found in Pralits (2001). The above equations are subjected to the following boundary conditions

$$\left[U^*, V^*, \frac{\partial(h_1 T^*)}{\partial x^3}\right](x^1, 0) = [0, 0, 0] \qquad \forall x^1 \in [X_0, X_1],$$

$$\lim_{x^3 \to +\infty}[U^*, V^*, W^*, T^*](x^1, x^3) = [0, 0, 0, 0] \quad \forall x^1 \in [X_0, X_1].$$

The initial condition at $x^1 = X_1$ is given as

$$\mathbf{Q}^*(X_1, x^3) = \mathbf{0}. \quad \forall x^3 \in [0, +\infty),$$

These equations are linear oppose to the BLE but are however solved in a similar iterative way as was outlined in §2.2.1 in order to reuse the existing solver for the boundary layer equations. The ABLE are solved by backward integration in the streamwise direction. At each streamwise position we obtain the solution of $\tilde{\mathbf{Q}}^* = (U^*, V,^* T^*)$ from equations (66)–(68) using the boundary conditions above for a given value of W^*. Equation (65) is integrated in the wall-normal direction in order to obtain W^*. The solution at each streamwise position is considered converged when the relative variation of W^* is below a specified value.

The coupling between the Euler and the boundary-layer equations is the pressure distribution P_e and the mesh given by the nodal coordinates $\mathbf{X}$. A variation of the geometry which affects the Euler solution, will therefore appear as variations of the pressure distribution in the boundary layer equations, which consequently will affect the solution of the stability equations. In Pralits *et al.* (2002), the possibility of an optimal control problem using the pressure distribution as control variables and the total disturbance kinetic energy as the objective function, was considered. From the coupled APSE and ABLE for incompressible flows, an expression was derived for the gradient of the objective function with respect to the pressure distribution. From the present APSE and ABLE a similar expression can be evaluated and is here given as

$$\nabla J_P = \int_0^{+\infty} \left(-\frac{\partial U^*}{\partial x^1} + (\gamma - 1)M^2 \frac{\partial(T^* U)}{\partial x^1} \right) dx^3 \qquad \forall x^1 \in (X_S, X_1). \quad (70)$$

Setting the Mach number equal to zero in expression (70), we find exactly the same expression as the one derived in Pralits *et al.* (2002). Note that a variation of $\mathbf{X}$ will also affect the nodal coordinates of the BLE and PSE. This can be seen in expression (61).

2.5.3. *Adjoint of the Euler equations*

The adjoint equations (60) are solved following the same technique used for solving the Euler equations (§2.1), by explicit time integration of the system

$$V_i \frac{\mathrm{d}\mathbf{w}_i^*}{\mathrm{d}t} + \mathbf{R}_i^* = \mathbf{0}, \qquad \forall i \in \mathcal{V}(\overline{\Omega}) \tag{71}$$

until the residuals $\mathbf{R}_i^*$ vanish within some tolerance. Derivation of the adjoint of the Euler equations can be found in Amoignon (2003). The following gives expression for the adjoint residuals

$$\mathbf{R}_i^* = \sum_{j \in \mathcal{N}_i} \left[\frac{\partial (\mathbf{f}_i \cdot \boldsymbol{n}_{ij})}{\partial \mathbf{w}_i} \right]^T \frac{(\mathbf{w}_i^* - \mathbf{w}_j^*)}{2} + \sum_{j \in \mathcal{N}_i} \mathbf{d}_{ij}^* \qquad \forall i \in \mathcal{V}(\Omega) \,,$$

$$\mathbf{R}_i^* = \sum_{j \in \mathcal{N}_i} \left[\frac{\partial (\mathbf{f}_i \cdot \boldsymbol{n}_{ij})}{\partial \mathbf{w}_i} \right]^T \frac{(\mathbf{w}_i^* - \mathbf{w}_j^*)}{2}$$

$$+ \sum_{j \in \mathcal{N}_i} \mathbf{d}_{ij}^* + \sum_{j \in \mathcal{N}_i} \left[\frac{\partial (\mathbf{f}_i^{\mathrm{bc}} \cdot \boldsymbol{n}_i)}{\partial \mathbf{w}_i} \right]^T \mathbf{w}_i^* \qquad \forall i \in \mathcal{V}(\partial\Omega) \,, \tag{72}$$

$$\mathbf{R}_i^* = \sum_{j \in \mathcal{N}_i} \left[\frac{\partial (\mathbf{f}_i \cdot \boldsymbol{n}_{ij})}{\partial \mathbf{w}_i} \right]^T \frac{(\mathbf{w}_i^* - \mathbf{w}_j^*)}{2}$$

$$+ \sum_{j \in \mathcal{N}_i} \mathbf{d}_{ij}^* + \sum_{j \in \mathcal{N}_i} \left[\frac{\partial (\mathbf{f}_i^{\mathrm{bc}} \cdot \boldsymbol{n}_i)}{\partial \mathbf{w}_i} \right]^T \mathbf{w}_i^* - \mathbf{g}_i^* \qquad \forall i \in \mathcal{V}(\partial\Omega^o) \,,$$

where $\mathcal{V}(\partial\Omega^o)$ is the set of nodes at which the pressure P_e is measured, according to the definition of the BLE (19)–(22). The right-hand-side of equation (60), is included in the residuals

$$\mathbf{g}_i^* = \left(\left(\frac{\partial \mathcal{A}_Q}{\partial \mathbf{w}} \right)^* \mathbf{Q}^* \right)_i \tag{73}$$

The adjoint $\mathbf{d}^*$ of the artificial dissipation fluxes $\mathbf{d}$ (15) are obtained by freezing the artificial viscosities (see Amoignon 2003), that is, the differentiation of ϵ_2^{ij} and ϵ_4^i with respect to $\mathbf{w}_h$ is assumed to give terms which can be neglected. This assumption yields that

$$\mathbf{d}_{ij}^* = \epsilon_2^{ij}(\mathbf{w}_i^* - \mathbf{w}_j^*) + (\epsilon_i \nabla^2 \mathbf{w}_i^* - \epsilon_j \nabla^2 \mathbf{w}_j^*) \,. \tag{74}$$

However, the resulting truncation error may not be negligible in the computation of the gradient ∇J. This is studied later in this report through numerical tests. A similar freezing of the coefficients in the farfield boundary conditions yields the following expression for the Jacobian of the farfield flux:

$$\frac{\partial (\mathbf{f}_i^{\mathrm{bc}} \cdot \boldsymbol{n}_i)}{\partial \mathbf{w}_i} = \frac{\partial (\mathbf{f} \cdot \boldsymbol{n}_i)}{\partial \mathbf{v}_i} \mathbf{L}(\hat{\boldsymbol{n}}_i, \mathbf{v}_\infty) \mathbf{H}(\lambda_\mathbf{i}) \mathbf{L}^{-1}(\hat{\boldsymbol{n}}_i, \mathbf{v}_\infty) \frac{\mathrm{d}\mathbf{v}_i}{\mathrm{d}\mathbf{w}_i} \,. \tag{75}$$

The Jacobian of the Euler wall flux function is expressed as follows

$$\frac{\partial \left(\mathbf{f}_i^{\mathrm{bc}} \cdot \boldsymbol{n}_i \right)}{\partial \mathbf{w}_i} = (\gamma - 1) \begin{pmatrix} \frac{1}{2} |\boldsymbol{u}_i|^2 \\ -\boldsymbol{u}_i \\ 1 \end{pmatrix} \,. \tag{76}$$

3. Implementation issues

3.1. *Mesh displacements*

In the current study an explicit affine mapping is used to smoothly propagate changes in the geometry to the entire mesh. It is formulated as

$$\mathbf{X}^k = \mathbf{X}^0 + \mathbf{L}\mathbf{y}^k \,. \tag{77}$$

where $\mathbf{y}^k \in \mathbb{R}^n$ is the vector of node displacements on the airfoil, for the design number k, $\mathbf{X}^k \in \mathbb{R}^{2N}$ is the vector of all nodal coordinates (N is the total number of nodes in the grid), $\mathrm{L} \in \mathbb{R}^{2N \times n}$ is a constant coefficients matrix, and, $\mathbf{X}^0$ is the reference mesh, defined by its vector of nodal coordinates. Given the gradient ∇J_X, of a functional J_X such as defined in Table 1, the gradient of the functional $J_y(\mathbf{y}) \equiv J_X(\mathbf{X}(\mathbf{y}))$ is obtained by a matrix–vector product

$$\nabla J_y = \mathrm{L}^T \nabla J_X. \tag{78}$$

The definition of L was possible because the meshes we used here are issued from structured grids. More general schemes are needed when using general unstructured meshes (see Berggren 2003).

3.2. *Parameterization of displacements and constraints*

In shape optimization, the combination of gradient-methods and piecewise polynomial interpolations, such as B-splines, may induce oscillations in the shapes, as investigated in Frank & Shubin (1992). In the current approach, smooth shapes are obtained, together with geometric constraints, by taking the vectors of displacements $\mathbf{y}$ that are solution of a minimization problem (see Amoignon 2003) of the form

$$\mathbf{y} = \left\{ \begin{array}{l} \min_{\mathbf{v} \in \mathbb{R}^n} \dfrac{1}{2}\mathbf{v}^T \mathrm{A}_s \mathbf{v} - \mathbf{v}^T \mathrm{M}_s \mathbf{a}, \\ \mathrm{C}^T \mathbf{y} = \mathbf{b} \end{array} \right. , \tag{79}$$

where A_s is the stiffness matrix associated with the Laplace operator, M_s is a mass matrix, C is a matrix whose rows are the gradients of constraints imposed on the displacements (in $\mathbb{R}^{n \times m}$) and $\mathbf{b}$ is the vector of values imposed to the constraints (in $\mathbb{R}^m$). The solution $\mathbf{y}$ to the above system is the vector of displacements, which, according to the norm defined by the stiffness matrix A_s, is the closest to the solution of the discretized Laplace equation defined by

$$\mathrm{A}_s \tilde{\mathbf{y}} = \mathrm{M}_s \mathbf{a}, \tag{80}$$

and that fulfills exactly the constraints

$$\mathrm{C}^T \mathbf{y} = \mathbf{b}. \tag{81}$$

Such a parameterization implies that the controls are the vector $\mathbf{a}$, right side of the Laplace equation (80), and the vector $\mathbf{b}$, right side of the constraints relations (81). Therefore, from the gradient with respect to the displacements ∇J_y, that is eventually obtained by (78) it is needed to calculate a gradient with respect to $\{\mathbf{a}, \mathbf{b}\}$, the control variables in our method. This can be achieved by solving an adjoint problem of the form (see Amoignon 2003)

$$\begin{pmatrix} A_s^T & -C \\ -C^T & 0 \end{pmatrix} \begin{pmatrix} \mathbf{y}^* \\ \lambda^* \end{pmatrix} = \begin{pmatrix} \nabla J_y \\ \mathbf{0} \end{pmatrix}, \tag{82}$$

from which it holds that

$$\nabla J_a = M_s^T \mathbf{y}^* \quad \text{and} \quad \nabla J_b = -\lambda^*. \tag{83}$$

3.3. *Optimization algorithm*

All numerical tests carried out here are formulated so that aerodynamic constraints (lift and pitch) are integrated to the objective function via a simple penalization technique. Geometrical constraints (volume and fixed domain) can be treated as simple bounds constraints via the parameterization previously discussed (see §3.2). However, the geometrical constraints are equality constraints, so that the the right hand side, **b** in (79), will be a constant vector. The only control parameter used in our applications is therefore the vector **a**, expression (79).

The optimization algorithm is the limited memory quasi-Newton method developed by Byrd *et al.* (1995). It is based on a limited memory BFGS approximation of the Hessian matrix of the functional f, and a gradient projection method is used to account for bounds on the data which makes it suitable for large scale problems where only the gradient of f is available.

3.4. *Solution procedure*

A simple chart of the order in which the state and adjoint equations are solved and gradients are evaluated in order to perform optimal NLF is given in figure 2. There, k denotes the iteration number and the procedure is as follows:

1. For $k = 1$, we start with an initial Euler mesh $\mathbf{X}^0$
2. The Euler, BLE and PSE are solved in the given order
3. The objective function J^k is evaluated
4. The adjoint equations, APSE, ABLE and AEuler are solved
5. The gradients ∇J_X^k, ∇J_y^k and ∇J_a^k are evaluated in the given order
6. A new control parameter $\mathbf{a}^{k+1}$ is calculated[2] using the gradient ∇J_a^k
7. If $k > 1$, check convergence: If $|(J^{k+1} - J^k)/J^k| < \epsilon$, else[3] continue
8. A new mesh $\mathbf{X}^{k+1}$ is calculated from the new control parameter $\mathbf{a}^{k+1}$
9. Goto 2.

4. Numerical tests

The accuracy of the gradient ∇J_a (83) of the objective function is a critical issue in optimization. The first order necessary optimality condition is that the gradient of the objective function or, of the Lagrangian, is zero at an optimal design. Difficulties related to low accuracy, such as difficulty to find descent directions even far from the optimal design, are quite common. There are two possible causes of inaccuracies in our calculation of the gradient. As mentioned previously, the derivation of the adjoint of the discretized Euler equations makes use of an approximation as it does not linearize the coefficients of the 2nd order artificial dissipation. Effects of this approximation are investigated in §4.1. The adjoint equations of the BLE and PSE are derived from the continuous

---

[2]In the computations shown here, the L-BFGS-B routine was used, normally requiring several functional and gradient evaluations in order to build up the approximative Hessian matrix.
[3]Several convergence criteria exist in the L-BFGS-B routine, (see Zhu *et al.* 1994)
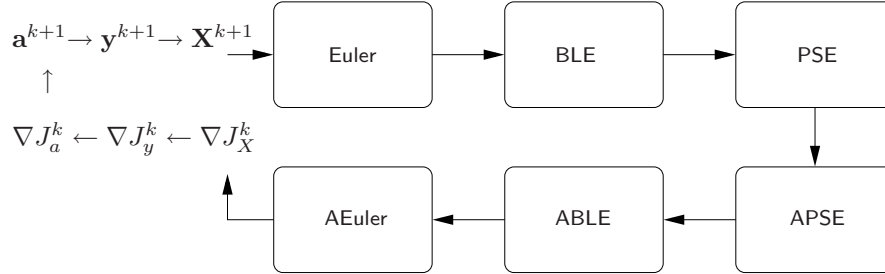
FIGURE 2. Flow chart for the case of minimizing the disturbance kinetic energy using the parameter **a** to control the shape of geometry.

state equations. The effects of this method on the accuracy of the gradients of the type ∇J_w (for J_X defined as in Table 1) is investigated in §4.2.1. The calculation of ∇J_a is obtained by coupling the three systems of adjoint equations, and the accuracy is investigated in §4.2.2.

The accuracy of the gradient at a design point **a** can be analyzed, comparing the value obtained from the solution of the adjoint equations, with the one estimated by finite differences as

$$(\nabla J_a)_k \approx \frac{J_a(\mathbf{a} + \epsilon_a \mathbf{e}_k) - J_a(\mathbf{a} - \epsilon_a \mathbf{e}_k)}{2\epsilon_a}, \tag{84}$$

where $\mathbf{e}_k$ is the vector having component k equal to 1 and all other components being 0. Several calculations of $(\nabla J_a)_k$ is commonly performed, using different values of ϵ_a in order to find the best compromise between accuracy and rounding errors, the last being inherent to the finite difference method. The relative error between the gradient obtained by adjoint method $\nabla_{\mathrm{AD}} J_a$ and the one approximated by finite-differences ∇J_a can be calculated as

$$\mathrm{err}_{\nabla J_a} = \frac{\|\nabla_{\mathrm{AD}} J_a - \nabla J_a\|}{\|\nabla J_a\|}, \tag{85}$$

where $\|.\|$ denotes the norm in $\mathbb{R}^n$ defined by the dot product.

These tests are performed on different C-type meshes of the RAE 2822. They are here denoted coarse, medium and fine, and the sizes are:

- Coarse: 3412 nodes with 112 nodes on the airfoil.
- Medium: 13352 nodes with 224 nodes on the airfoil.
- Fine: 52816 nodes with 448 nodes on the airfoil.

4.1. *The inviscid case*

Possible inaccuracies, due to the approximation made in the Euler adjoint equations, are expected to be independent from the forcing of the these equations. In our investigation the right-hand-side of the adjoint equation (60) is

M_∞	$\mathrm{err}_{\nabla C_L}$	$\mathrm{err}_{\nabla C_D}$	$\mathrm{err}_{\nabla C_M}$
0.754	1.9×10^{-2}	2.6×10^{-2}	1.6×10^{-2}
0.734	2.8×10^{-2}	3.8×10^{-2}	2.2×10^{-2}
0.68	5.5×10^{-3}	4.9×10^{-2}	4.6×10^{-3}

TABLE 2. Effect of the Mach number on the relative errors between the gradients calculated based on the adjoint equations and the ones calculated by finite differences, defined by (85), of the drag, lift and pitch moment coefficients.

M_∞	$\|\nabla C_L\|$	$\|\nabla C_D\|$	$\|\nabla C_M\|$
0.754	3.3×10^{-1}	3.0×10^{-2}	2.2×10^{-1}
0.734	3.2×10^{-1}	2.3×10^{-2}	2.0×10^{-1}
0.68	3.0×10^{-1}	2.4×10^{-3}	1.5×10^{-1}

TABLE 3. Effect of the Mach number on the norm of the gradient of the coefficients of lift (C_L), drag (C_D) and pitch (C_M). The gradients are calculated from the adjoint equations.

$(\partial \mathcal{A}_Q / \partial \mathbf{w}^*) \mathbf{Q}^*$ (see §2.4), identically equal to $\partial J_w / \partial \mathbf{w}$, according to the definition of J_w given in Table 1. It is therefore the same as usual aerodynamic optimization problems based on Euler flow analysis where J_w is usually one the functions defined by the wave drag, the lift or the moments coefficients. In order to avoid influences of possible errors when solving the BLE, the PSE and their adjoint equations, we investigate here the accuracy of the gradient of the wave drag (C_D), the lift (C_L) and the pitch moment coefficients (C_M).

The tests are carried out on the coarse grid, at three different design points (different Mach number and angle of attack). In the results shown here, the value of ϵ_a in the finite difference approximation of the gradient $(\nabla J)_k$, is equal to 10^{-6}. However, various values in the interval $\left[10^{-4}, 10^{-8}\right]$ were tested without significant influence on the relative error. A summary of the results is given in Table 2. The relative error varies between 0.5% and 5% and clearly depends on the design point. Quite unexpected is that the error associated with the gradient of the drag coefficient (C_D) increases when reducing the Mach number whereas the influence of the 2nd order artificial dissipation would be expected to decrease as the influence of the shock decreases. Indeed, the influence of the shock on the flow solution is measured by the sensitivity of the wave drag and given in Table 3. Additional tests were carried out at Mach number 0.68 without the second artificial dissipation showing that the approximation in the derivation of the adjoint of these fluxes are causing the errors as, seen in Table 4.

VIS2	$\mathrm{err}_{\nabla C_L}$	$\mathrm{err}_{\nabla C_D}$	$\mathrm{err}_{\nabla C_M}$
1.	5.5×10^{-3}	4.9×10^{-2}	4.6×10^{-3}
0.	4.5×10^{-4}	3.4×10^{-3}	3.8×10^{-4}

TABLE 4. Effect of the 2nd order artificial viscosity fluxes on the relative errors between the gradients calculated from the adjoint equations and the ones calculated by finite differences for the drag, lift and pitch moment coefficients. The 2nd order artificial viscosity is active for $VIS2 = 1$ and inactive for $VIS2 = 0$.

4.2. *The coupled inviscid-viscous case*

The solutions of the adjoint of the stability and boundary layer equations are used as input to the adjoint of the Euler equations as well as the gradient assembly. From the adjoint of the boundary layer equations an expression for the gradient of the objective function with respect to the pressure distribution is obtained, expression (70). This is the coupling between the adjoint of the boundary layer equations and the adjoint of the Euler equations and is used to evaluate expression (73). The variation of the boundary layer and stability equations with respect to the node coordinates are additional terms in the assembly of the gradient, 61.

4.2.1. *Gradient of objective function w.r.t. the pressure distribution*

In the coupling between the inviscid and viscous solution, there are two issues which make a large impact on the accuracy of the gradients. The first is that a grid resolution commonly used to obtain results with the Euler equations, is too coarse to obtain converged results using the stability equations. A second issue is how the adjoint equations are derived. The adjoint Euler equations are derived from the discretized Euler equations, and its solution should not depend on the grid resolution. The adjoint of the boundary layer and stability equations on the other hand, are derived using the continuous approach, and the solution might therefore depend more on the grid resolution. As a consequence difficulties appear when increasing the accuracy.

Tests have been performed using the coarse, medium and fine grid when the free stream Mach number $M_\infty = 0.73$, Reynolds number $Re = 6.7 \times 10^6$, temperature $T_\infty = 300$ K and zero sweep angle. From the Euler solutions, the pressure distributions and coordinates of the upper side starting from the stagnation point have been used as input to the boundary layer and stability equations. The disturbance used in the stability calculations is a two dimensional wave with dimensional frequency $f^\star = 15.5$ kHz. The objective function is evaluated as the disturbance kinetic energy, E_1, integrated in a streamwise domain which is kept the same for the different grids used here.
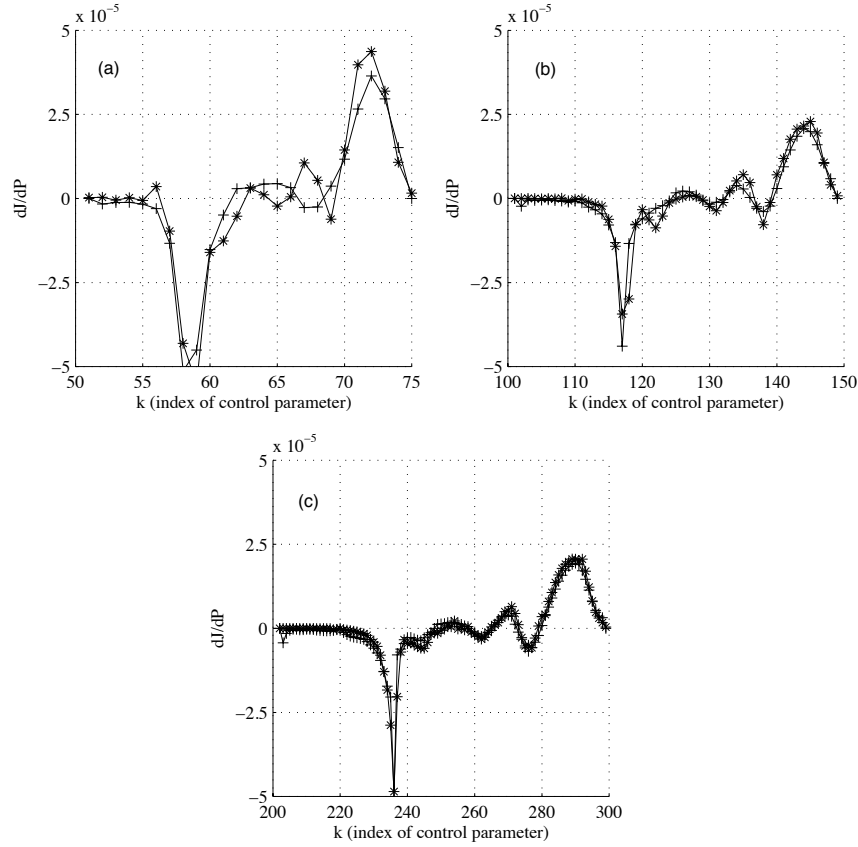
FIGURE 3. Gradient of objective function with respect to pressure distribution. Comparison between finite-difference approximation (solid-stars) and adjoint solution (solid-plus) computed on (a) coarse, (b) medium, and (c) fine grid.

In figure 3 results are shown for a comparison between expression (70) and a finite difference approximation of the gradient of the objective function with respect to the pressure distribution. The latter is evaluated in the same way as expression (84), where the design $\mathbf{a}$ has been replaced by the pressure P. Computations have been performed for different values of the finite-difference step ϵ_p, and these values are 10^{-4}, 10^{-5}, 10^{-6}, 10^{-7}. Only the results for $\epsilon_p = 10^{-5}$ are shown. A first thing to note is that the gradient evaluated using the finite-difference approximation appears to converge as the grid resolution increases. This is due both to the solution of the pressure distribution converging in the Euler computation, and the solution of the stability equations converging as the grid is refined. Secondly it can be seen that the difference
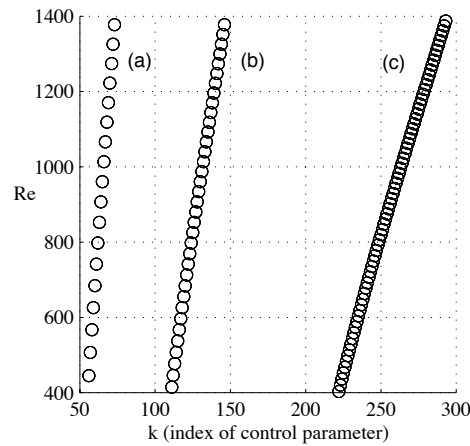
FIGURE 4. Local Reynolds number as a function of the control parameter k (a) coarse grid, (b), medium grid, (c) fine grid.

between gradients obtained from the finite-difference approximation and those obtained from the solution of the adjoint equations, decreases as the grid is refined. This is due to the continuous approach used to derive the adjoint equations.

The adjoint of the boundary layer and stability equations used here have been used in other problems concerning gradient evaluations for the purpose of optimal control problems (see Pralits *et al.* 2000; Pralits & Hanifi 2003; Pralits *et al.* 2002). There, different grid resolutions expressed as a step length in the local Reynolds number ΔRe, where $Re = \sqrt{U_e x/\nu_e}$, were tested to see the effect on the gradient accuracy. In Pralits *et al.* (2000), it was shown that a step length of $\Delta Re = 20$ was needed to converge the physical result for a flat plate boundary layer with zero pressure gradient. Further, it was shown that a value of $\Delta Re = 10$ was needed to obtain a relative difference of 10^{-3} between the approximative finite difference calculation and the adjoint calculation, in the major part of the computational domain. In figure 4, the step length expressed as local Reynolds number has been plotted for the different grids used here. It can be seen that the step length is almost constant through out respective domain and the values are $\Delta Re = 50$, 25 and 13 for the coarse, medium and fine grids, respectively. Due to the variation of the pressure gradient along wing profiles, the step lengths found in the previous study of flat-plate boundary layers, might not be small enough to obtain the same convergence in the results and accuracy of the gradients in the case studied here. It should further be noted that the finest grid shown in figures 3 and 4, is computationally heavy for the Euler solver, and might not be reasonable to use in the case of optimization.

One option to increase the accuracy of the gradients is to use some interpolation technique for the calculation of the boundary layer, stability and
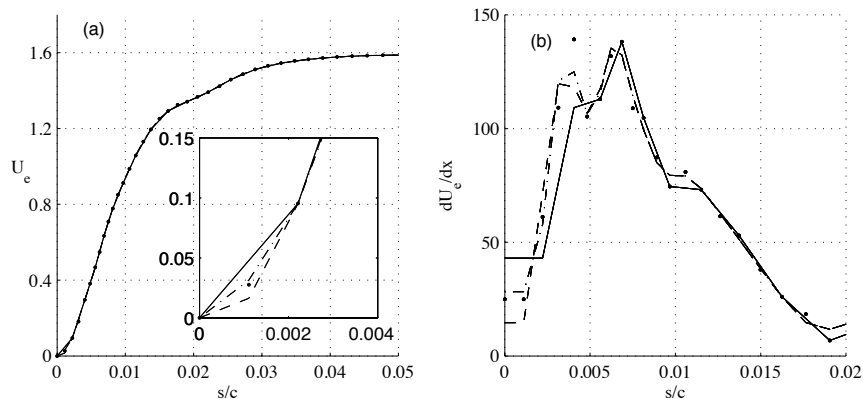
FIGURE 5. Comparison of U_e and $\partial U_e/\partial x^1$ between original medium grid (solid), and interpolated values using quadratic polynomial on half grid (dot), cubic splines on half grid (dash), and cubic splines on whole grid (dash-dot). The refined grids are obtained by inserting one additional point in between old grid points.

corresponding adjoint equations, given the solution of the pressure distribution computed on a 'coarse' grid. Such an approach could also be favorable when three-dimensional flows are considered, and thus the computational effort increase considerably for the Euler equations. The outline of an interpolation approach can be made as follows: the pressure distribution from the Euler solution is interpolated on a grid with higher resolution, the boundary layer, stability and corresponding adjoint equations are solved on the new grid, the gradient ∇J_P is evaluated and then interpolated back on the original grid. Here, decisions need to be made on how to produce the new grid distribution, i. e. the distribution of the coordinate x/c describing the geometry, and further which interpolation scheme to use, in order to obtain y/c and P_e. One approach to refine the grid is to insert additional node points in between the old ones. An advantage of inserting additional nodes in between the old ones, is that the function values of the original nodes can be used in the chosen interpolation scheme. Here, we have chosen to interpolate U_e instead of P_e. In figure 5, results of U_e and $\partial U_e/\partial x^1$ can be seen using different interpolation schemes. We have used the medium grid shown earlier and the new grid is obtained by inserting an additional point in between the old grid points, i. e. the new grid has twice as many points as the original one. Two calculations have been performed when interpolation has been made using only the upper part of the wing, i. e. from the stagnation point to the trailing edge. The interpolation schemes are a piecewise quadratic polynomial and cubic splines. In addition a cubic spline interpolation has been made when the whole grid was used. In figure 5a, results are shown of U_e close to the leading edge. A
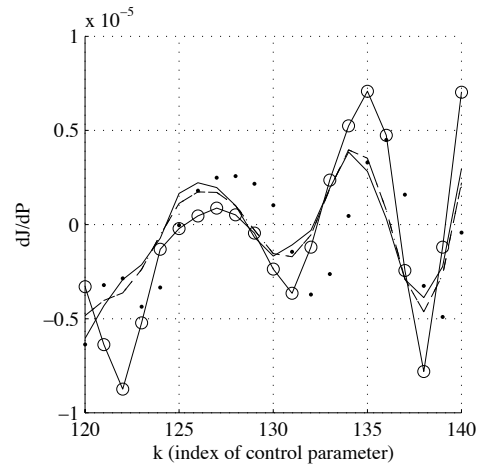
FIGURE 6. Comparison of the gradient $\partial J / \partial P_e$ computed from the solution of the adjoint equations using the mean flows corresponding to the cases in figure 5. A comparison is made with the finite difference approximation of the gradient (solid-circle).

close up around the leading edge show that the magnitude of U_e of both cases where only the upper part of the wing was used in the interpolation, is larger at the first interpolation point. The streamwise derivative of the free stream velocity corresponding to the cases in figure 5a are shown in figure 5b. The respective interpolated mean flows were then used to compute gradient ∇J_P by solving the PSE, APSE and ABLE. In figure 6 a comparison is made between gradient computed using the finite difference approximation, and those obtained using the adjoint solutions. The gradient computed by solving the adjoint equations on the original grid is included for comparison. There, it is seen that the gradient computed using the piecewise quadratic polynomial interpolation technique oscillates and deviates most from the finite difference approximation. The cases of using the cubic splines cannot be distinguished from one another, and in comparison with the gradient computed on the original grid using the adjoint equations, a small improvement has been obtained. In the results of shape optimization for transition delay shown in this report, no interpolation technique has been used.

4.2.2. *Gradient of objective function w.r.t. the shape parameterization*

In the previous sections, tests have been performed to assess the accuracies of the inviscid (§4.1), and viscous parts (§4.2.1) separately. In this section, we investigate the accuracy of the gradient ∇J_a (83) which will be used in the optimization procedure, when the objective function is based on a measure of the disturbance kinetic energy. The reference case, denoted FD, is computed using
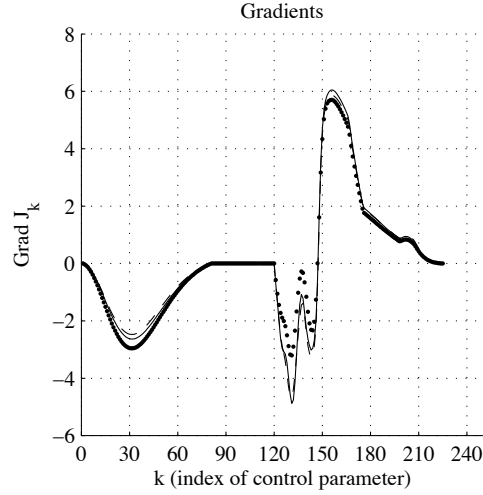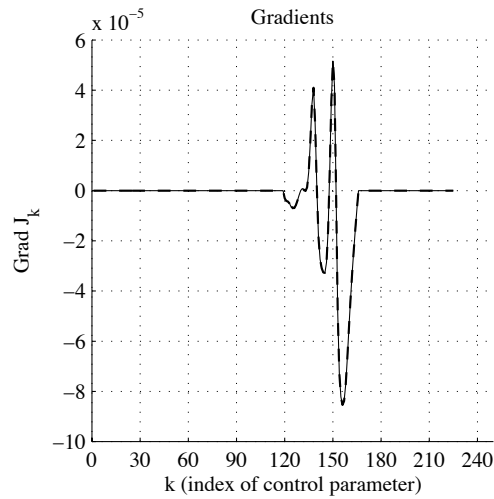
FIGURE 7. $M_\infty = 0.734$ - Gradients of the objective function (Disturbance kinetic energy) with respect to the optimization parameters (parameters that control the shape of the airfoil). The curves show FD (solid), ADJ1 (dot), ADJ2 (dash). The error between the FD and respective adjoint solution are: FD–ADJ1 (17.2%), FD–ADJ2 (4.95%), and FD–ADJ3 (4.85%, not shown).

the finite difference approximation of the gradient given by expression (84), which is evaluated solving consecutively the Euler, BLE and PSE. The objective function in all tests performed here is given as the disturbance kinetic energy of a single disturbance integrated in a defined streamwise region, expression (29) with K=1. The gradient ∇J_a is calculated from the gradient ∇J_X (61) by variables transformations, from the nodal coordinates $\mathbf{X}$ to the displacements of the shape $\mathbf{y}$, according to (78), and, from the displacements of the shape $\mathbf{y}$ to the right side of the Laplace equation $\mathbf{a}$, which requires to solve (82) and to apply (83). The gradient ∇J_X is given by expression (61)

$$\nabla J_X = \underbrace{\frac{\partial J_q}{\partial \mathbf{X}} - \left(\frac{\partial \mathcal{A}_q}{\partial \mathbf{X}}\right)^* \mathbf{q}^* + \left(\frac{\partial \mathcal{A}_Q}{\partial \mathbf{X}}\right)^* \mathbf{Q}^*}_{cont.} - \underbrace{\left(\frac{\partial \mathcal{A}_w}{\partial \mathbf{X}}\right)^* \mathbf{w}^*}_{discr.}.$$

As outlined in §3, it is evaluated from three systems of adjoint equations which are solved in the following order

$$\underbrace{\text{APSE} \quad \rightarrow \quad \text{ABLE}}_{cont.} \quad \rightarrow \quad \underbrace{\text{adjoint Euler,}}_{discr.}$$

where each calculation depends on the solution of the previous one. The APSE and ABLE are derived using the continuous approach, while the adjoint Euler

FIGURE 8. $M = 0.68$ - Gradients of the objective function (Disturbance kinetic energy) with respect to the optimization parameters (parameters that control the shape of the airfoil). The curves show FD (solid), ADJ2 (dash). The error is: FD–ADJ2 (0.02%)

is derived using the discrete approach. This is above denoted *cont.*, and *discr.*, respectively. The latter has in the previous sections shown to be more accurate on the grids used here. In this section we therefore investigate the influence of the solution of the adjoint Euler, and the solution of the APSE and ABLE, on the accuracy of the gradient which will be used in the optimization. This is made by comparing the accuracy of the gradient computed from the solution of all adjoint equations with the one evaluated from the solution of the adjoint Euler in which the right hand side, see expression (60), is approximated by finite differences. The right hand side is evaluated from expression (70) ($\partial J/\partial P$) when the solution of the APSE and ABLE are used. The finite difference approximation used here is the same that was used in §4.2.1. In addition, the influence of including the geometrical terms in the gradient evaluation from the solution of the PSE, APSE and ABLE (denoted *cont.*) is investigated.

The different cases are summarized below:

- FD: finite difference approximation of the gradient given by expression (84), computed solving the Euler, BLE and PSE.
- ADJ1: gradient evaluated from the solution of the adjoint Euler, ABLE, and APSE
- ADJ2: gradient evaluated from the solution of the adjoint Euler. The right hand side of the adjoint Euler, evaluated from $\partial J/\partial P$, is approximated by finite differences computed by BLE and PSE.

- ADJ3: gradient evaluated from the solution of the adjoint Euler, and by a finite difference approximation of the terms from the BLE and PSE. The right hand side of the adjoint Euler, evaluated from $\partial J/\partial P$, is approximated by finite differences computed by BLE and PSE.

The relative difference between the FD and respective gradient evaluated from the solution of the adjoint equations, is calculated using expression (85). In the first test we consider the medium grid when the Mach number $M_\infty = 0.734$. A part of the geometry around the leading edge is kept fixed, and a comparison is made between the FD and respective adjoint solution outlined in the summary above. The gradients are plotted as functions of the index of the surface nodes, where index 224 denote the trailing edge. The fixed region around the leading edge is given between indexes 80 and 119. The largest error, 17.2%, is found in the comparison between the FD and the complete adjoint solution, ADJ1. When the right hand side of the adjoint Euler equations is approximated by finite differences, the error is reduced to 4.95%. Including the geometrical terms obtained from the BLE and PSE in the gradient evaluation (ADJ3) only reduces the error by 0.1% compared to the previous case (ADJ2).

The influence of including the second artificial viscosity on the gradient accuracy was shown in (§4.1) for the inviscid flow equations. As the influence is expected to decrease in the absence of a shock, a test was performed also here. We consider the flow at Mach number 0.68, and the surface is kept fixed everywhere, except for the region where the objective function is evaluated. In figure 8, a comparison is made between the FD and ADJ2. The error in this case is 0.02%.

5. Optimization results

5.1. *Description of the cases*

Following the study performed on the accuracy of the sensitivities obtained using the continuous adjoint, §4.2, we chose to perform the optimization on the medium grid. Viscous calculations (RANS) are also carried out with EDGE[4] by Eliasson (2001) prior to and after some of the optimization tests in order to compare the N-factors based on the pressure distribution obtained from the viscous calculation with those that are computed using the Euler pressure distribution. These calculations are also used to compare the viscous drag between the initial and the final optimized design. The C-type grid for RANS calculations has the size:

- Medium 'RANS' mesh: 22088 nodes with 224 nodes on the airfoil.

In a first series of tests the objective is to reduce the disturbances kinetic energy. The only constraints are geometrical and imposed using the parameterization given in §3.2. The objective function to minimize is the total disturbance kinetic energy of a single disturbance, E_1 from expression (29). There are

---

[4]The turbulence model used is the EARSM by Wallin & Johansson (2000) and the $k - \omega$ model.

several reasons for imposing geometrical constraints. A constant volume is intuitively a way to account for other industrial constraints such as having a minimum fuel tank capacity in the wings or a maximum weight of the material structure. The displacements of the nodes should not be allowed to be constant over all nodes, which would mean a translation of the wing. To remove this singularity one point should remain fixed, and our choice is the trailing edge. In addition, we chose to fix a region of the airfoil around the leading edge in order to prevent changes in the position of the stagnation point.

To summarize, the geometrical constraints are:

- Constant volume,
- Constant position of the trailing edge,
- Fixed region around the leading edge (between 0 of the chord length and X_{ms} given in Table 5).

In order to test if the optimization can account for the usual aerodynamic requirements, two additional tests are carried out with a modified objective function, denoted J_C. The aim is to simultaneously reduce the disturbance kinetic energy and the wave drag, and in addition penalize changes in the coefficients of lift, and pitch-moment. The geometrical constraints are identical to the first type of optimization which is described above. The modified objective function is given as

$$
J_C = \lambda_U E_1 + \lambda_D C_D + \frac{1}{2}\lambda_L \left(C_L - C_L^0\right)^2 + \frac{1}{2}\lambda_M \left(C_M - C_M^0\right)^2 , \qquad (86)
$$

where E_1 is the functional from expression (29), C_D, C_L and C_M are the drag, lift, and pitch moment coefficients, respectively

$$
\begin{aligned}
C_D &= \sum_{i \in \mathcal{V}(\partial\Omega_w)} \frac{p_i \boldsymbol{n}_i \cdot \boldsymbol{d}_D}{\frac{1}{2}\rho_\infty \boldsymbol{v}_\infty^2 S_{\text{ref}}} , \\
C_L &= \sum_{i \in \mathcal{V}(\partial\Omega_w)} \frac{p_i \boldsymbol{n}_i \cdot \boldsymbol{d}_L}{\frac{1}{2}\rho_\infty \boldsymbol{v}_\infty^2 S_{\text{ref}}} , \\
C_M &= \sum_{i \in \mathcal{V}(\partial\Omega_w)} \frac{p_i \boldsymbol{d}_M \cdot \left(\boldsymbol{x}_i - \boldsymbol{O}_{\text{ref.}}\right) \times \boldsymbol{n}_i}{\frac{1}{2}\rho_\infty \boldsymbol{v}_\infty^2 S_{\text{ref}} L_{\text{ref}}} .
\end{aligned} \qquad (87)
$$

were $\boldsymbol{d}_D$ is a unit vector in the direction of the farfield velocity, $\boldsymbol{d}_D = -\boldsymbol{v}_\infty/|\boldsymbol{v}_\infty^2|$, $\boldsymbol{d}_L$ is a unit vector orthogonal to $\boldsymbol{d}_D$ and, $\boldsymbol{d}_M$ is a unit vector orthogonal to $\boldsymbol{d}_D$ and $\boldsymbol{d}_L$.

The values C_L^0 and C_M^0 are the lift and pitch-moment coefficients for the initial design. In expression (86), we take the square of the deviation of lift and pitch with respect to the initial design in order to penalize both an increase and decrease during the optimization. The real numbers $\{\lambda_U, \lambda_D, \lambda_L, \lambda_M\}$ are

Case	Objective	M_∞	Re_∞	f* [kHz]	β^* [m^{-1}]	X_{ms}	X_{me}
T11	E_1	0.734	$1.7\,10^7$	15.5	0	0.043	0.45
T12	E_1	0.734	$6.5\,10^6$	11	500	0.043	0.45
T21	E_1	0.68	$1.6\,10^7$	16.5	0	0.039	0.45
T31	J_C	0.734	$1.7\,10^7$	15.5	0	0.043	0.45
T32	J_C	0.734	$6.5\,10^6$	11	500	0.043	0.45

TABLE 5. Optimization tests description.

scaling factors calculated as

$$\lambda_U = \frac{1}{10E_1^0}, \quad \lambda_D = \frac{1}{10C_D^0}, \quad \lambda_L = \frac{10}{\left(C_L^0\right)^2}, \quad \lambda_M = \frac{10}{\left(C_M^0\right)^2}. \tag{88}$$

The tests are summarized in Table 5. For the case T21, without second order artificial viscosity (VIS2=0) was used in order to get better accuracy (see Figure 8). The thermodynamical properties for the different cases correspond to two different altitudes such that the TX1-cases are given at 0 meter ASL, and the TX2-cases are given at 9600 meter ASL.

5.2. *Analysis of the disturbance growth*

The objective function in the results shown here, is given as the total disturbance kinetic energy of a single disturbance, expression (29) in which $K = 1$. A stability analysis of a large number of modes with different frequencies $f^\star$, and spanwise wave numbers β^* corresponding to different wave angles, is performed prior to each optimization case, on the original design and the chosen flow conditions. The wave angle is defined as the angle between the wave number vector $\mathbf{k}$ and the inviscid streamline. The corresponding N-factors are calculated from these results, and the mode chosen to be used in the optimization which has the largest N-factor value with respect to all other modes, in the computational domain. The reason of this particular choice is that it has been shown in previous studies on optimal control, see Pralits *et al.* (2002) and Pralits & Hanifi (2003), that a control that successfully decrease the growth of a single disturbance also have a damping effect on other instability waves of the same type. It is common in transition prediction, to compute the envelope or envelopes (EoE) of the N-factor curves (i. e. envelope over both frequency and spanwise wave number). Transition is then assumed to occur at the position where the EoE curve first attains an empirically determined value. This curve also serves as a measure of the efficiency of a control or design, computed by minimizing a single disturbance, on a large number of disturbances.

Results of the analysis discussed here is shown in figure 9. The design is the medium mesh with a free stream Mach number $M_\infty = 0.734$, Reynolds number $Re_\infty = 6.5\,10^6$, and angle of attack $\alpha = 2.1875$ degrees. A total of 165 modes
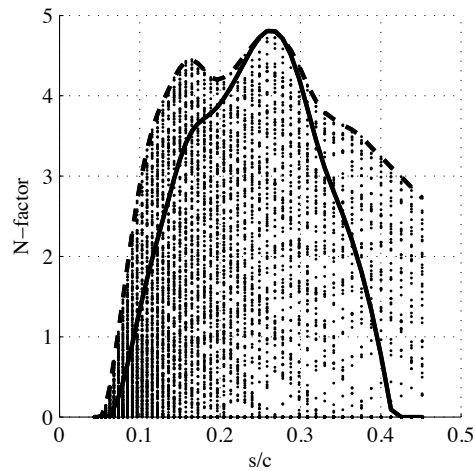
FIGURE 9. N-factor values for 165 modes (dots) with dimensional frequency $f^* = [5, 20]$ kHz ($\Delta f^\star = 1$ kHz), spanwise wavenumber $\beta^* = [0, 2500]$ m^{-1} ($\Delta \beta^\star = 250$ m^{-1}). From these values is the mode used in the optimization (solid) chosen, and the envelope of envelopes (EoE) (dash) calculated. The flow in this case is characterized by $Re_\infty = 6.5\,10^6$, $M_\infty = 0.734$, $\alpha = 2.1875$ degrees.

have been analyzed with dimensional frequency $f^\star = [5, 20]$ kHz ($\Delta f^\star = 1$ kHz), and spanwise wave number $\beta^\star = [0, 2500]$ m^{-1} ($\Delta \beta^\star = 250$ m^{-1}). This choice of spanwise wave number corresponds to wave angles between zero and 85 degrees. The corresponding N-factor values of all modes are given by dots. The mode chosen to be used in the optimization is given by the solid line and the EoE curve by the dash line. The values of $f^\star$ and $\beta^\star$ given here are used for all EoE analysis made in this report.

5.3. *Reduction of disturbance kinetic energy under volume constraints*

5.3.1. $M_\infty = 0.734$, *cases T11 and T12*

Results are shown here for the case of minimizing the disturbance kinetic energy of a single disturbance with the initial volume of the airfoil kept constant. Computations are performed for a given Mach number $M_\infty = 0.734$ and two different Reynolds numbers. The latter two correspond to 0, and 9600 meter ASL, and the cases are denoted T11 and T12, respectively. The convergence history is given in figure 10 for the T11 case. The objective function and gradient norm is given as a function of the iteration number. The optimization was stopped because the BLE could not converge for the design after the last iteration. This occurred as the changes in the geometry caused the shock wave to move upstream $x/c \approx 0.42$, into the domain in which the objective
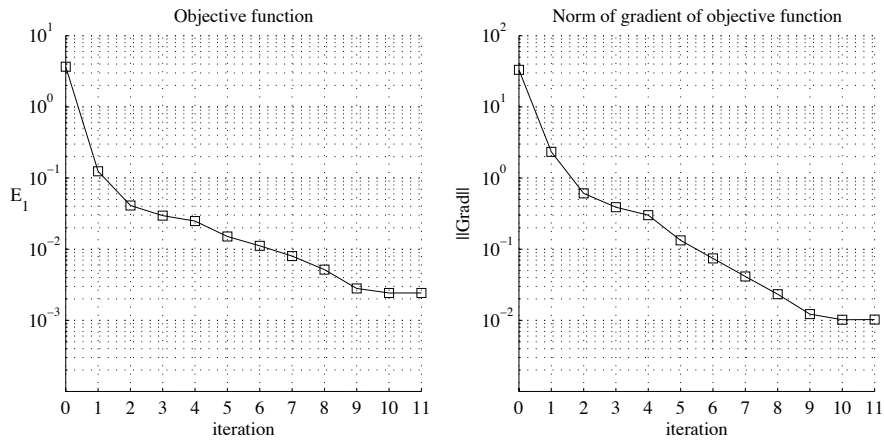
FIGURE 10. T11 - Objective function and norm of its gradient.
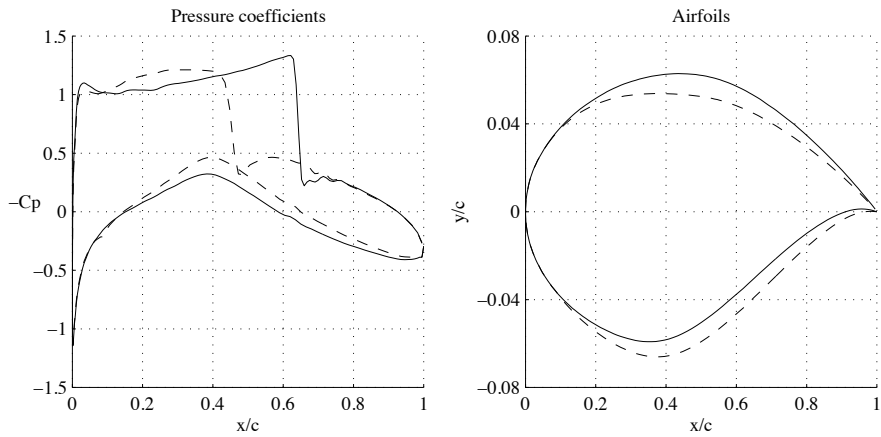
FIGURE 11. T11 - Pressure coefficients and shapes at initial
(solid) and final design (dash).

function is evaluated (between $x/c = 0.043$ and $x/c = 0.45$). This can be seen in figure 11, where the pressure coefficient and geometry for the initial and final design are plotted. At final design, the central upper part of the wing is thinner, measuring the thickness as the distance of a point on the airfoil to the chord. Therefore, because of the fixed region around the leading edge, the region between 4.3% of the chord length, from the leading edge, up to about 30% of the chord length, situated on the upper part, has a higher curvature at final design than at initial design.

An increase of the curvature of a wall boundary is known to reduce the pressure in the fluid flow. This may be the effect that can be observed in
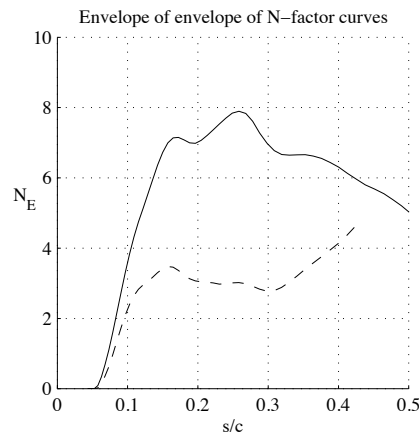
Figure 12. T11 - Envelope of envelopes of N-factor curves. Comparison between initial (solid) and final design (dash).

figure 11 where the pressure coefficient at final design has decreased ($-C_p$ is increased) in the region between 10% of the chord length, from the leading edge, up to about 30% of the chord length, in comparison to the initial design. In this way a pressure gradient is obtained that damps the growth of disturbances as it is explained below. However, the faster decrease of the pressure may be responsible for the shock moving upstream. Note that the deformation of the lower part of the wing is only due to the constraint that imposes a constant volume.

The effect on the disturbance growth can be seen in figure 12 where the EoE curves have been plotted for the initial and final design. A large damping of all modes has been achieved. This can be explained by the change in pressure gradient from adverse to favorable, in a large part of the region where the disturbances are amplified. The disturbance growth increases in this region due to the zero or weak adverse pressure gradient just upstream of the shock wave in the case of the final design.

The convergence history is given in figure 13 for the lower Reynolds number case (T12). The decrease of the objective function is of two orders of magnitude, smaller than it is for the case T11, figure 10, but the norm of the gradient is decreased by four order of magnitude, which is larger than the decrease achieve in case T11. The computation is here terminated as no further descent direction could be found. The magnitudes of the deformations of the airfoil are smaller compared to the case T11, shown in figure 11, but a similar trend is observed. The favorable pressure gradient, which can cause a decrease of the energy of the disturbances, may be caused by a local increase of the curvature on the upper part of the wing, between 4.3% and 30% of the chord length from the leading edge. As a consequence, the shock is moved upstream. The effect on the disturbance growth can be seen in figure 15 where the EoE curves have
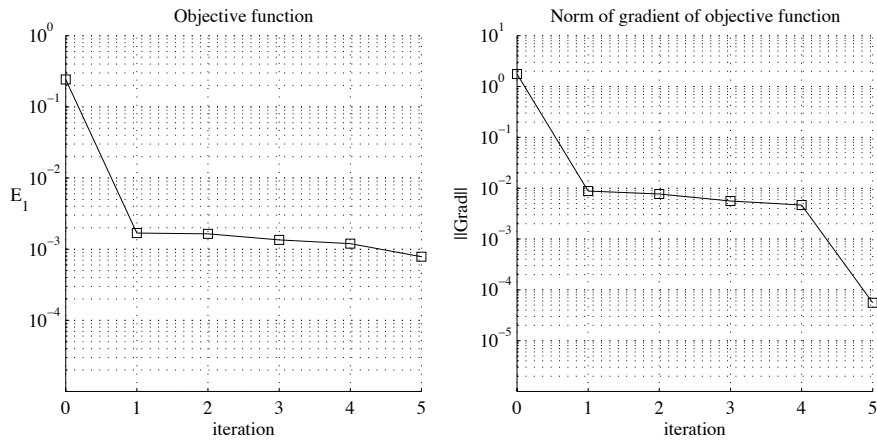
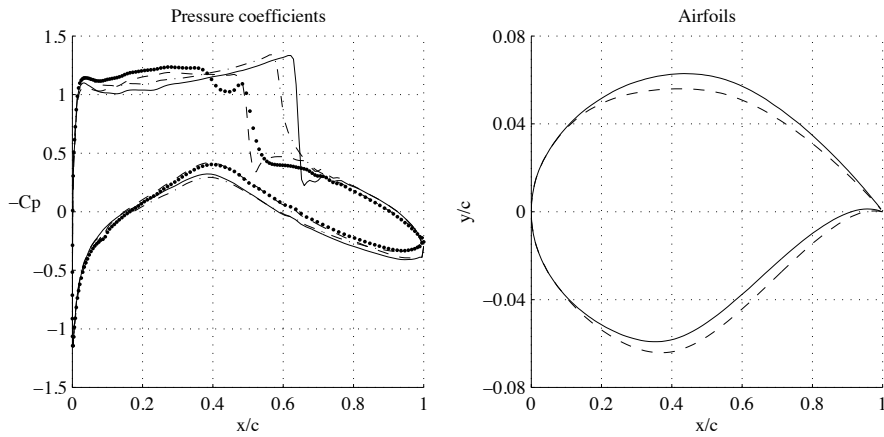FIGURE 13. T12 - Objective function and norm of its gradient.

FIGURE 14. T12 - Pressure coefficients and shapes at initial
design for Euler (solid) and RANS (dash-dot), and final design
for Euler (dash) and RANS (dot).

been plotted for the initial and final design. A large decrease in disturbance
growth is obtained using the optimized design, similar to the one found for the
high Reynolds number case (T11). Also this is due to the change in pressure
gradient from an adverse to favorable in the upstream part of the domain
where the disturbances become unstable. The shock wave has not moved as far
upstream and the boundary layer and stability analysis can therefore be made
further downstream, also on the optimized airfoil.

An attempt has been made to use the N-factor results of the initial and
final design in order to determine the respective transition location. These
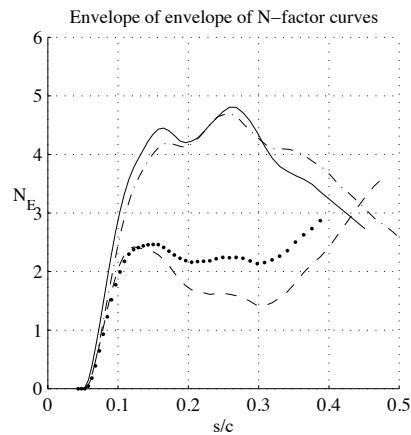
Figure 15. T12 - Envelope of envelopes of N-factor curves. Comparison between initial (solid) and final design (dash). A comparison is also made between the initial (dash-dot) and final (dot) design, when the pressure distribution is given by the solution of the Reynolds Averaged Navier Stokes equations.

results have been used as input to RANS calculations of the initial and final design in order to evaluate the change in the viscous drag. Values of the drag, lift and pitch coefficients for the initial and optimized designs are summarized in Table 6. The viscous drag is reduced by 13 drag counts, and, as it could be expected from previous observations about the position of the shock, the wave drag is also decreased, by 40 drag counts[5]. However, this is a byproduct of the reduction of the disturbance energy. Large changes in the lift and the pitch are also observed. These by-effects are controlled by imposing constraints in the cases T31 and T32, see (§5.4).

The results from the RANS calculations are in addition used to see the difference in N-factors computed using the pressure distributions from the Euler-, and RANS solutions. The transition position on the upper side of the initial design was taken as the streamwise position corresponding to the maximum value of the EoE curve of the N-factors computed using the pressure distribution from the Euler solution. The value is $s/c \approx 0.26$, see figure 15. As the EoE curve of the final design was lower in magnitude compared to the initial one, the transition location of the final design was set as the downstream position of the computational domain of the boundary layer and stability analysis. The same transition position was used on the lower side, both for the initial and final design. It should be noted that the transition location for the initial design is not based on experimental results. A common reference for the RAE2822

---

[5]One drag count is 10^{-4}

Coeff.	Case	RANS			Euler
		total	viscous	pressure	pressure
C_D	Initial	2.3×10^{-2}	4.8×10^{-3}	1.8×10^{-2}	1.3×10^{-2}
	T12 (Final)	1.6×10^{-2}	3.5×10^{-3}	1.3×10^{-2}	7.9×10^{-3}
	T32 (Final)	1.8×10^{-2}	3.7×10^{-3}	1.4×10^{-2}	8.3×10^{-3}
C_L	Initial	8.4×10^{-1}	-7.9×10^{-5}	8.4×10^{-1}	8.4×10^{-1}
	T12 (Final)	7.0×10^{-1}	-5×10^{-5}	7.0×10^{-1}	7.0×10^{-1}
	T32 (Final)	8.5×10^{-1}	-7×10^{-5}	8.5×10^{-1}	8.5×10^{-1}
C_M	Initial	3.2×10^{-1}	$-$	$-$	3.4×10^{-1}
	T12 (Final)	2.4×10^{-1}	$-$	$-$	2.6×10^{-1}
	T32 (Final)	3.1×10^{-1}	$-$	$-$	3.4×10^{-1}

TABLE 6. Summary of aerodynamic coefficients at initial and final design for T12 and T32, using Euler and RANS flow analysis.

airfoil is Cook & McDonald (1979), in which the boundary layer was tripped at 3% chord in the experiments in order to have a well defined turbulent portion.

The pressure coefficients obtained from the solution of the RANS for the initial and final design is found in figure 14. The largest difference compared to the Euler solution occur at the position of the shock wave. Upstream of this position however, the difference between the Euler and RANS solution is smaller, which can also be seen in figure 15, where the EoE curves of the two cases are compared. In the comparison of the pressure coefficients between the Euler and RANS computations of the final design, one can note the difference in the region between $x/c \approx 0.4$ and $x/c \approx 0.5$. Results of the velocity field from the RANS calculation (not shown here), show that separation occurs in this region. As this can not be accounted for in the boundary layer equations used here, the EoE curve computed using the pressure distribution from the RANS calculation is not performed downstream of $x/c \approx 0.4$, see figure 15.

5.3.2. $M_\infty = 0.68$, case T21

Results are shown here for the case of minimizing the disturbance kinetic energy of a single disturbance with the initial volume of the RAE2822 airfoil kept constant. Computations are performed for Mach number $M_\infty = 0.68$ at 0 meter ASL. The shock wave shown in the T11-, and T12 cases is not present in this case, see figure 17. The convergence history is given in figure 16. The objective function and the norm of the gradient are reduced of about three orders of magnitude. The pressure coefficients, and the geometries, at initial and final design, are found in figure 17. Alike the previous cases, the changes in the geometry of the upper part of the airfoil influence the pressure distribution in a way that is favorable to decrease the disturbance energy. However, the
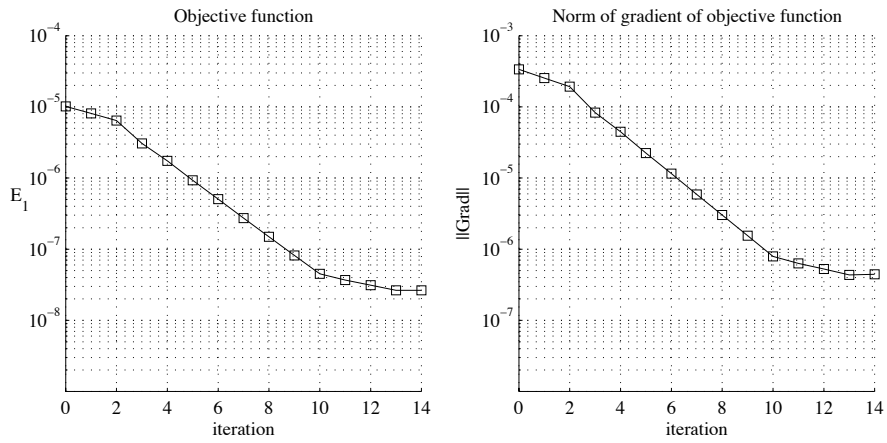
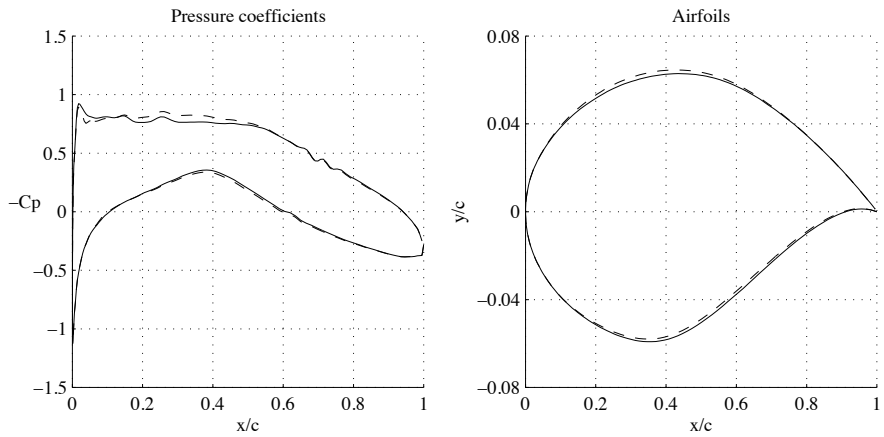FIGURE 16. T21 - Objective function and norm of its gradient.

FIGURE 17. T21 - Pressure coefficients and shapes at initial
(solid) and final design (dash).

deformation of the airfoil is of a different nature. Compared to the cases T11
and T12, the upper part of the airfoil is thicker at final design than at initial
design, which creates a region of higher curvature at about 40% of the chord
length away from the leading edge. This is further downstream compared to
where it appeared in the cases T11 and T12. The effects of these deformations
can be observed in changes of the pressure coefficient.

The difference between the test cases is better understood looking at the
envelope of envelopes (EoE) curves of the N-factors. In case T11, the dist-
urbances grow fastest in a region between $x/c = 0.2$ and $x/c = 0.3$, as seen
in figure 12. In the case T21, the growth of disturbances continues increasing
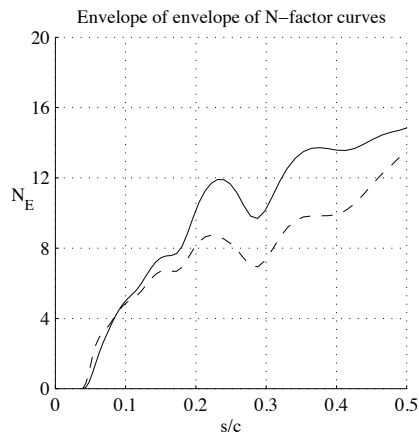
FIGURE 18. T21 - Envelope of envelopes of N-factor curves. Comparison between initial (solid) and final design (dash).

outside of the domain of integration of the objective function (29), that is for $x/c > 0.45$, figure 18. As a consequence, in case T11, damping the growth of disturbances in the near region of the leading edge has a major effect, but in case T21 the damping may be favored as far downstream as $x/c = 0.45$. A decrease in disturbance amplification has been achieved for all modes in the major part of the computational domain. This is due to change in the pressure distribution from a weak adverse to a zero or weakly favorable in the region where the disturbances become unstable, see figure 17. Note however, that in the upper most streamwise region, first an increase in the adverse pressure gradient occur. This is seen in the EoE curves which are actually larger between $x/c \approx 0.05$ and $x/c \approx 0.1$ compared to the initial design. Another thing to note is the "smoothing" of the pressure distribution in the region where the disturbances are amplified. The vanishing of these wiggles is also seen in the EoE curve plotted for the final design.

5.4. *Reduction of disturbance kinetic energy and wave drag under volume constraints while penalizing lift and pitch*

Results are shown here for the case of simultaneously minimizing the disturbance kinetic energy of a single disturbance, and the wave drag. The initial volume is kept constant during the optimization and changes in the lift, and pitch-moment coefficients with respect to the initial design are penalized, see expression (86). Computations are performed for a given Mach number $M_\infty = 0.734$ and two different Reynolds numbers. The latter two correspond to 0, and 9600 meter ASL, and the cases are denoted T31 and T32, respectively. The objective function and gradient norm of case T31 are given as functions of the iteration number in figure 19. The different components of the objective function are plotted in figures 20, and 21. The objective function is decreased
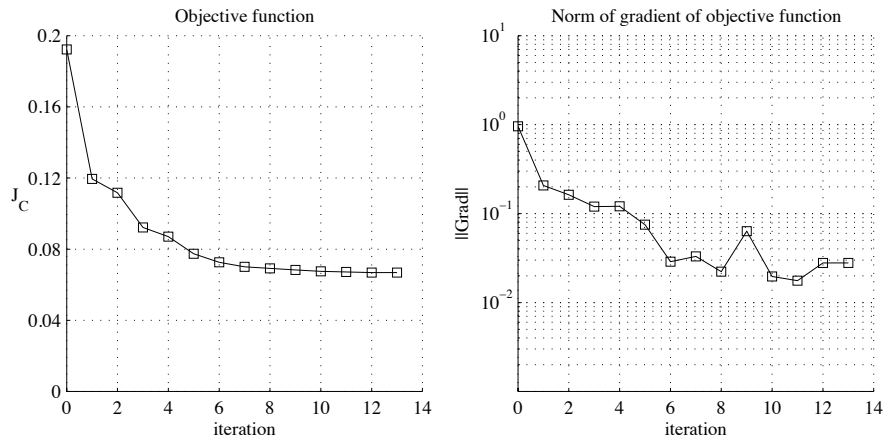
FIGURE 19. T31 - Objective function and norm of its gradient.

in each step of the optimization even though the component of the wave drag is increased between iteration number 2 and 4, compared to iteration number 1. The reason is that in this interval, the deviation of lift-, and pitch moment coefficients is decreased. A reduction has been obtained at the last iteration, in both disturbance kinetic energy and wave drag, while the lift-, and pitch moment coefficients are kept within a few percent. Comparisons between the pressure coefficients, and geometries of the initial and final design are given in figure 22. The change in pressure distribution occurs mainly on the upper side of the airfoil, where the shock wave has moved upstream and weakened. In comparison with T11, which has the same initial conditions, the displacement of the shock in T31 is smaller, but, the changes in T31 reflect the conservation of the pitch moment and lift coefficients. The effect on the disturbance growth can be seen in figure 23 where the EoE curves have been plotted for the initial and final design. A damping of the disturbance growth is obtained in a large part of the computational domain using the final design. It is clear looking at figure 22, that the adverse pressure gradient of the initial design in the upstream region where the disturbances become unstable, has changed into a zero or weakly favorable in the final design. Close to the shock wave of the final design, which has now moved further upstream, the flow is decelerated. This can be seen in the EoE curve where the value increases rapidly above that of the initial design.

The convergence history for the lower Reynolds number case (T32) is found in figures 24–26, and is similar to the one found for the case T31. The wave drag experiences an increase during a few optimization steps also here, while the deviation of lift, and pitch-moment coefficients decreases. In figure 27, a comparison is made between the pressure coefficient and geometry of the initial
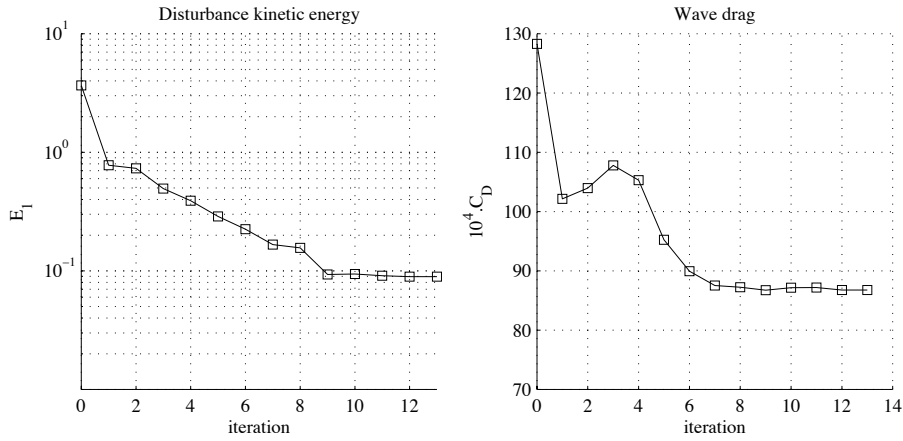
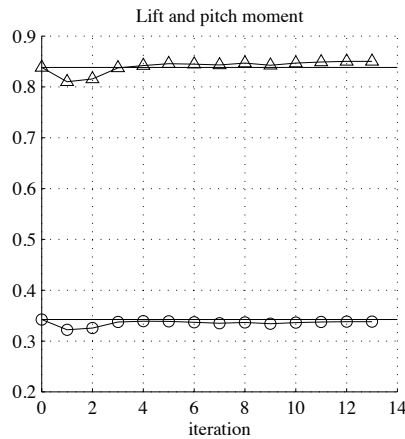FIGURE 20. T31 - Disturbance kinetic energy and wave drag.

FIGURE 21. T31 - Lift (triangle-solid) and pitch moment (circle-solid) coefficients. The values at initial design are indicated at each step (solid).

and final design. In comparison with case T12, which has the same initial conditions, the displacement of the shock is smaller but the pressure distribution in T32 minimizes changes in the coefficients of lift and pitch moment. The EoE curves computed using the pressure distribution from the Euler solution are used, as in case T12, to set the transition locations in two RANS calculations. The transition position on the upper side of the initial design was taken as the streamwise position of the maximum value of the EoE curve of the N-factors computed using the pressure distribution from the Euler solution ($s/c \approx 0.26$,
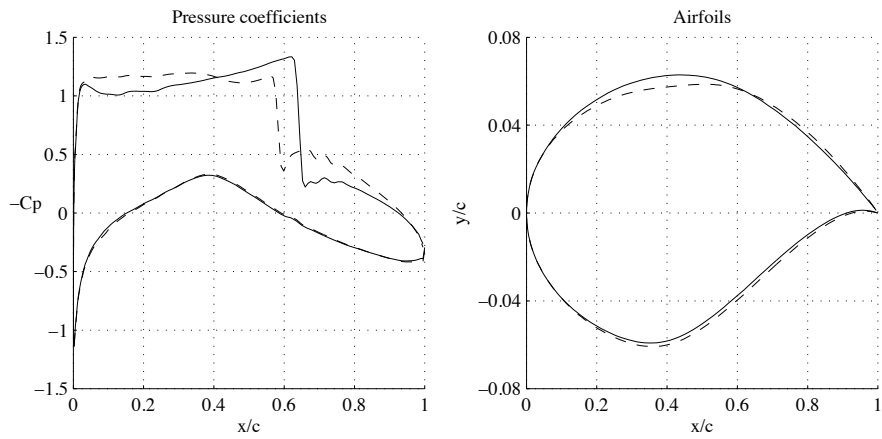
FIGURE 22. T31 - Pressure coefficients and shapes at initial (solid) and final design (dash).
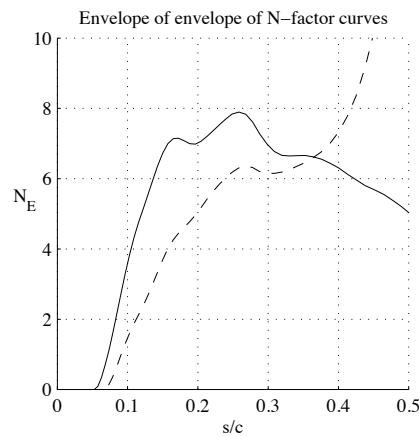
FIGURE 23. T31 - Envelope of envelopes of N-factor curves. Comparison between initial (solid) and final design (dash).

see figure 28). The maximum value of the EoE curve computed for the final design is below the value found for the initial one. The transition location on the upper side of the final design is therefore set as the downstream position of the computational domain of the boundary layer equations. The same transition position was used both for the initial and final design on the lower side. The major differences in the pressure distribution between the Euler and RANS calculation occur in the region around the shock wave. Upstream of the shock the difference is smaller, both for the initial and final design. This can also be seen in the comparison of the EoE curves found in figure 28. A decrease
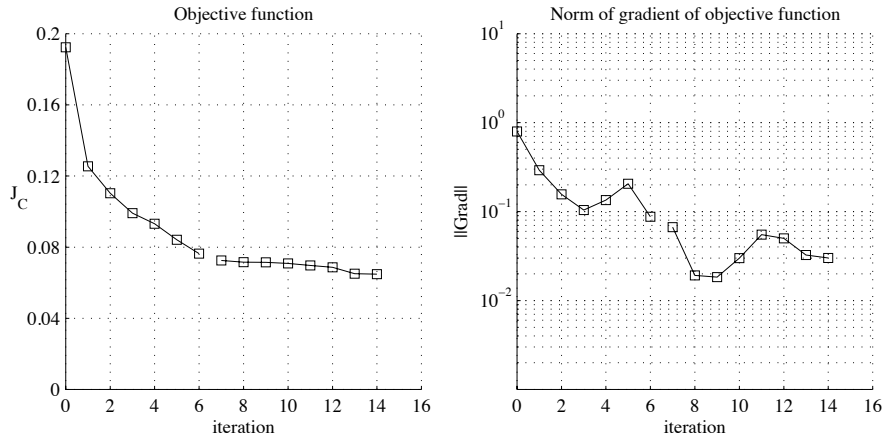
FIGURE 24. T32 - Objective function and norm of its gradient.

occur in the N-factor values in both results showing the EoE curves of the final design. This can be explained by the change in pressure gradient from adverse to zero or favorable, in a large part of the region where the disturbances are amplified.
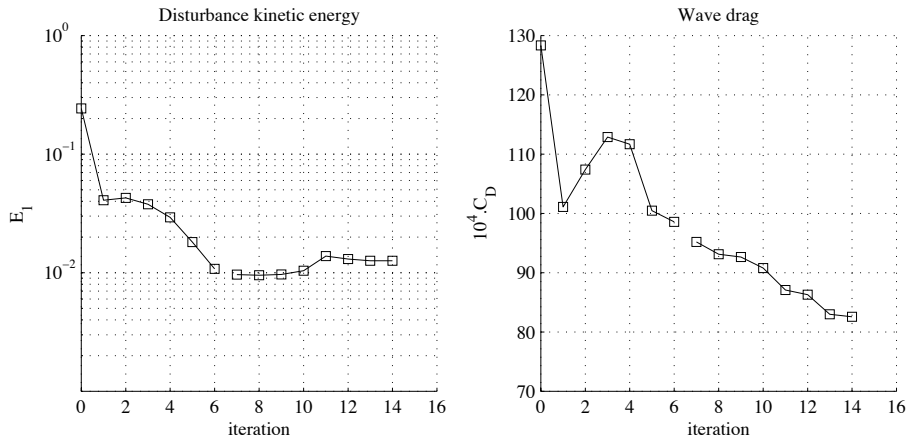

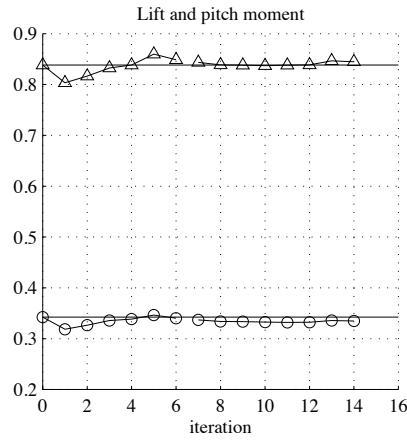FIGURE 25. T32 - Disturbance kinetic energy and wave drag.

FIGURE 26. T32 - Lift (triangle-solid) and pitch moment (circle-solid) coefficients. The values at initial design are indicated at each step (solid).
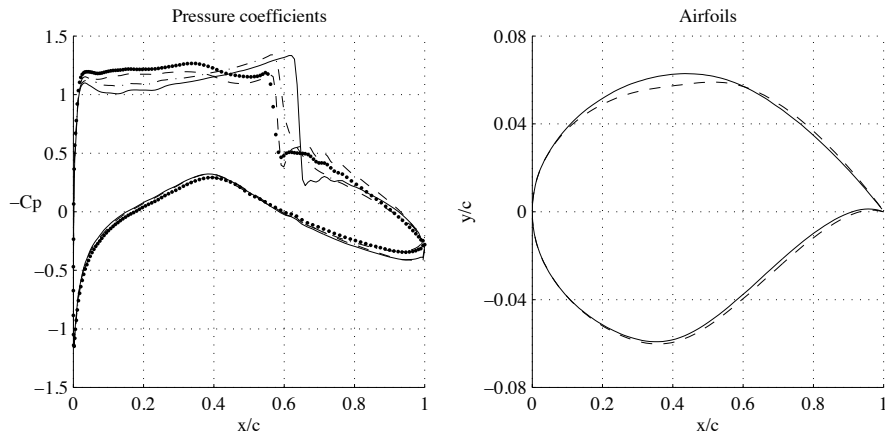

FIGURE 27. T32 - Pressure coefficients and shapes at initial design for Euler (solid) and RANS (dash-dot), and final design for Euler (dash) and RANS (dot).

6. Summary and discussion

Theory and results have been presented for an approach to perform shape optimization with the aim of transition delay, and thus a decrease of the viscous drag. The location of laminar-turbulent transition is analyzed using linear stability theory, in which perturbations with infinitely small amplitude are superimposed on the laminar mean flow. It is then assumed that transition will occur at the location where the total amplification of disturbances, with respect
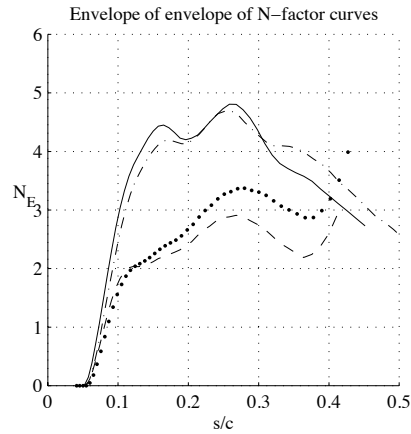
Envelope of envelope of N–factor curves

FIGURE 28. T32 - Envelope of envelopes of N-factor curves. Comparison between initial (solid) and final design (dash). A comparison is also made between the initial (dash-dot) and final (dot) design, when the pressure distribution is given by the solution of the Reynolds Averaged Navier Stokes equations.

to the first streamwise position where the disturbance starts to grow, attains an empirically determined value, whose logarithm is generally denoted by N. The inviscid flow is obtained by solving the Euler equations for compressible flows, and the viscous mean flow is obtained from the solution of the boundary layer equations for compressible flows on infinite swept wings. The evolution of convectively unstable disturbances is analyzed using the linear parabolized stability equations (PSE).

In the present approach, an iterative gradient based optimization procedure is used with the aim of minimizing an objective function based on the disturbance kinetic energy. Tests are carried out starting from the RAE2822 airfoil and are formulated to produce a reduction of the disturbance kinetic energy while maintaining a fixed volume, angle of attack, region around the leading edge and trailing edge position. Flow conditions include transonic and subsonic cases, with Reynolds number of 6.5, and 17 millions. In some cases the objective function is formulated to simultaneously reduce the wave drag and the disturbance kinetic energy while maintaining lift and pitch moment coefficients near their values at initial design. The normal displacements of the nodes on the airfoil are solution of a quadratic programming problem minimizing the variational form of the discrete Poisson problem and including linear constraints. Such a parameterization ensures smoothness of the geometries for each design generated by the quasi-Newton optimization algorithm (see Byrd 1994) and enables to define complex sets of admissible shapes as needed when coupling the three state equations. It has been shown that the gradient of the

objective function with respect to the design variables can be evaluated from the solution of adjoint of the Euler, boundary layer and parabolized stability equations. Using the adjoint equations, as opposed to other perturbation techniques, constitutes an efficient way to evaluate functional gradients when the number of design variables is large compared to the number of objective functions.

The work presented here is an ongoing project with improvements to be made in order to increase the existing computational efficiency and accuracy. It is further possible to include additional physical modeling in order to generalize the technique for more complex flow situations. As discussed herein, there are issues related to grid resolution and the approach taken to derive the adjoint equations. From a physical point of view, in order to obtain a converged result, different grid resolutions might be required for the Euler, boundary layer and stability equations. As shown here, the medium RAE2822 grid has a resolution which is fine with respect to what is needed for the Euler solution and coarse with respect to the stability solution. However, further refinement would not give large improvements in the physical results. For the evaluation of the gradient of the disturbance kinetic energy with respect to the pressure distribution on the other hand, the resolution plays an important role, as the ABLE and APSE are derived using the continuous approach. For this reason effort must be put into either deriving these equations using the discrete approach or to improve on the interpolation technique shown here.

There are modifications which can be made in order to approach a more realistic situation. One is to include the disturbance growth also on the lower side of the wing in the objective function, as transition occurs on both sides of the wing. As the objective function of the total disturbance kinetic energy is given as the sum of K convectively unstable disturbances, test can also be made in order to evaluate this effect. Another extension, which can include both of the above, is to use multiple design points in the optimization. In such case the objective function is the sum of a chosen cost function at e. g. different Mach numbers and/or different disturbances.

With the approach taken here there are some limitations which could be overcome using additional physical modeling. As no iterative coupling exist between the pressure distribution and the thickness of the boundary layer, this constitutes an approximation. In addition, the boundary layer calculated here is assumed laminar, and the effect of the increased thickness of the turbulent boundary layer due to transition is not accounted for. Separation is another issue which is not taken into account, and can be important especially for applications with large angle of attack. Several studies have been made on this topic for the boundary layer and stability analysis and might be possible to include in the current project. Another option that should be tested in order to avoid large adverse pressure gradients which might cause separation in the downstream domain, is to minimize an objective function including both E_K and E_f. The idea to include also the disturbance kinetic energy at a

downstream position (E_f), is based on the knowledge that an adverse pressure gradient has a destabilizing effect on the disturbance growth. Instead of using the Euler equations an extension is to use the Reynolds Averaged Navier-Stokes equations (RANS). This development should include the adjoint of the RANS equations.

Even though the Euler and adjoint Euler equations can be derived and solved for complete three-dimensional flows, the boundary layer and stability equations used here are given for, at most, infinite swept wing flows. The absence of variation of the viscous mean flow in the spanwise direction in the BLE and PSE means that e. g. tapered wings can not be analyzed without further approximations. To proceed to fully three-dimensional cases, it therefore has to be decided what approximations to make, or if effort should be spent on solving the BLE and PSE for complete three-dimensional flows.

The delay of transition is a benefit if accounting for all other aerodynamic properties of the wing, which are the wave drag, lift and moments coefficients. Reducing the wave drag is as important as the delay of transition when optimizing the airfoil at cruise speed. The latter can be achieved by formulating the objective function as a weighted sum of the wave drag and the disturbance kinetic energy. Lift and pitch moment can also be maintained near to their value for the initial design by adding terms to the objective function that penalize variations of these coefficients. However, in real life applications the interest is to maintain the lift above a minimum level while fixing the moments to their value at the original design. Imposing bound constraints in this non linear optimization problem would require to use more advanced method than the penalization technique that has been use in this study.

Acknowledgment

References

AIRIAU, C., BOTTARO, A., WALTHER, S. & LEGENDRE, D. 2003 A methodology for optimal laminar flow control: Application to the damping of Tollmien-Schlichting waves in a boundary layer. *Phys. Fluids* **15**, 1131–1145.

AMOIGNON, O. 2003 Adjoint-based aerodynamic shape optimization. Licentiate thesis to be published, Department of Information Technology, Division of Scientific Computing, University of Uppsala.

ANDERSON, W. & BONHAUS, D. 1999 Airfoil design on unstructured grids for turbulent flows. *AIAA Journal* **37** (2), 185–191.

ARNAL, D. 1993 Boundary layer transition: Predictions based on linear theory. Special course on 'progress in transition modeling', March-April 1993. AGARD-R-793, 2-1–2-63.

BARTH, T. J. 1991 Aspects of unstructured grids and finite-volume solvers for the Euler and Navier–Stokes equations. In *Special Course on Unstructured Methods for Advection Dominated Flows*, pp. 6–1–6–61. AGARD Report 787.

BAYSAL, O. & GHAYOUR, K. 2001 Continuous adjoint sensitivities for optimization with general cost functionals on unstructured meshes. *AIAA Journal* **39** (1), 48–55.

BERGGREN, M. 2003 Edge-based mesh movement strategies. Unpublished preprint, Sandia National Laboratories.

BERTOLOTTI, F. P., HERBERT, T. & SPALART, S. 1992 Linear and nonlinear stability of the Blasius boundary layer. *J. Fluid Mech.* **242**, 441–474.

BURGREEN, G. 1994 Improving the efficiency of aerodynamic shape optimization. *AIAA Journal* **32** (1), 69–76.

BYRD, R. 1994 A limited memory algorithm for bound constrained optimization. *Tech. Rep.* NAM-08. Northwestern University, Department of Electrical Engineering and Computer Science, Evanston Il 60208.

BYRD, R., LU, P., NOCEDAL, J. & ZHU, C. 1995 A limited memory algorithm for bound constrained optimization. *SIAM J. Sci. Comput.* **16**, 1190–1208.

COOK, P. & MCDONALD, M.A.AND FIRMIN, M. 1979 Aerofoil RAE 2822 – pressure distributions, and boundary layer and wake measurements. Experimental data base for computer program assessment. AGARD-AR-138, a6.

ELIASSON, P. 2001 Edge, a Navier–Stokes solver, for unstructured grids. *Tech. Rep.* FOI-R–0298–SE. Swedish Defence Research Agency, Stockholm.

ELLIOT, J. 1998 Aerodynamic based on the Euler and Navier–Stokes equations using unstructured grids. PhD thesis, MIT Dept. of Aero. and Astro.

ENOKSSON, O. 2000 Shape optimization in compressible inviscid flow. Licenciate Thesis LiU-TEK-LIC-2000:31, institute of Technology, Lindkpings University, Dept. of Math., ISBN 91-7219-780-3 ISSN 0280-7971.

FRANK, P. & SHUBIN, G. 1992 A comparison of optimization-based approaches for a model computational aerodynamics design problem. *Journal of Computational Physics* **98**, 74–89.

GILES, M. & PIERCE, N. 2000 An introduction to the adjoint approach to design. *Flow, Turbulence and Control* **65**, 393–415.

GREEN, B. E. & WHITESIDES, J. L. 1996 A method for the constrained design of natural laminar flow airfoils. *AIAA Paper* (96-2502).

HANIFI, A., HENNINGSON, D. S., HEIN, S. & BERTOLOTTI, F. P.AND SIMEN, M. 1994 Linear non-local instability analysis - the linear NOLOT code. *FFA TN* **1994-54**.

HERBERT, T. 1997 Parabolized stability equations. *Annu. Rev. Fluid Mech.* **29**, 245–283.

VAN INGEN, J. L. 1956 A suggested semiempirical method for the calculation of the boundary layer transition region. *Tech. Rep.* VTH-74. Department of Aeronautical Engineering, University of Delft.

JAMESON, A. 1988 Aerodynamic design via control theory. *Journal of Scientific Computing* **3**, 233–260.

JAMESON, A. 1997 Optimum aerodynamic design using the Navier-Stokes equations. *AIAA Paper no 97-0101* 35th Aerospace Sciences Meeting and Exhibit., Reno, Nevada.

JOSLIN, R. 1998 Overview of laminar flow control. *Tech. Rep.* 1998-208705. NASA, Langley Research Center, Hampton, Virginia.

LEE, J.-M., SCHRAGE, D. P. & MAVRIS, D. N. 1998 Development of subsonic transports with laminar flow wings. *AIAA Paper* (98-0406).

LIGHTHILL, M. J. 1945 A new method of two-dimensional aerodynamic design. *Tech. Rep..* ARC, rand M 2112.

LIONS, J. 1971 *Optimal Control of Systems Governed by Partial Differential Equations*. Springer-Verlag,New York, translated by S.K. Mitter.

MALIK, M. R. 1989 Prediction and control of transition in supersonic and hypersonic boundary layers. *AIAA J.* **27**, 1487–1493.

MALIK, M. R. & BALAKUMAR, P. 1992 Nonparallel stability of rotating disk flow using PSE. In *Instability, Transition and Turbulence* (ed. M. Hussaini, A. Kumar & C. Streett), pp. 168–180. Springer.

MANNING, V. M. & KROO, I. M. 1999 Multidisciplinary optimization of a natural laminar flow supersonic aircraft. *AIAA Paper* (99-3102).

MOHAMMADI, B. 1997 A new optimal shape procedure for inviscid and viscous turbulent flows. *Int. J. Numer. Meth. Fluids* **25**, 183–203.

NOCEDAL, J. & WRIGHT, S. 1999 *Numerical Optimization*. Springer Series in Operations Research, iSBN:0-387-98793-2.

PIRONNEAU, O. 1973 On optimal profiles in Stokes flow. *J. Fluid Mech.* **59**, 117–128.

PRALITS, J. O. 2001 Towards optimal design of vehicles with low drag: Applications to sensitivity analysis and optimal control. Licentiate thesis KTH/MEK/TR-01/07. Royal Institute of Technology, SE-172 90 Stockholm, Sweden.

PRALITS, J. O., AIRIAU, C., HANIFI, A. & HENNINGSON, D. S. 2000 Sensitivity analysis using adjoint parabolized stability equations for compressible flows. *Flow, Turbulence and Combustion* **65**, 321–346.

PRALITS, J. O. & HANIFI, A. 2003 Optimization of steady suction for disturbance control on infinite swept wings. *Phys. Fluids* **15** (9).

PRALITS, J. O., HANIFI, A. & HENNINGSON, D. S. 2002 Adjoint-based optimization of steady suction for disturbance control in incompressible flows. *J. Fluid Mech.* **467**, 129–161.

REUTHER, J. 1999 Constrained multipoint aerodynamic shape optimization using an adjoint formulation and parallel computers, part 1. *J. Aircraft* **36** (1), 51–60.

SCHUBAUER, G. B. & SKRAMSTAD, H. K. 1948 Laminar-boundary-layer oscillations and transition on a flat plate. *NACA Tech. Note No. 909* .

SIMEN, M. 1992 Local and non-local stability theory of spatially varying flows. In *Instability, Transition and Turbulence* (ed. M. Hussaini, A. Kumar & C. Streett), pp. 181–201. Springer.

SMITH, A. M. O. & GAMBERONI, N. 1956 Transition, pressure gradient and stability theory. *Tech. Rep.* ES 26388. Douglas Aircraft Co.

SOEMARWOTO, B. 1996 Multi-point aerodynamic design by optimization. PhD thesis, Delft University of Technology, Faculty of Aerospace Engineering, P.O. Box 5058, 2600 GB Delft, Netherlands, iSBN 90-5623-051-4.

Sung, C. & Kwon, J. 2000 Accurate aerodynamic sensitivity analysis using adjoint equations. *AIAA Journal* **38** (2), 243–250.

Wallin, S. & Johansson, A. V. 2000 An explicit algebraic Reynolds stress model for incompressible and compressible turbulent flows. *J. Fluid Mech.* **403**, 89–132.

Zhu, C., Byrd, R., Lu, P. & Nocedal, J. 1994 L-BFGS-B: Fortran subroutines for large scale bound constrained optimization. *Tech. Rep.* NAM-11. EECS Department, Northwestern University.

Zurigat, Y. H., Nayfeh, A. H. & Masad, J. A. 1990 Effect of pressure gradient on the stability of compressible boundary layers. *AIAA Paper* (90-1451), 21st Fluid Dynamics, Plasma Dynamics and Lasers Conference, Seattle, WA.